Study of the Martian Upper Atmosphere using Radio Tracking Data

by

Erwan Mazarico

M.S. Planetary Sciences, Massachusetts Institute of Technology, USA, 2004
Diplôme d'Ingénieur, École Nationale Supérieure de l'Aéronautique et de l'Espace, France, 2004

Submitted to the Department of Earth, Atmospheric, and Planetary Sciences
in partial fulfillment of the requirements for the degree of

Doctor of Philosophy

at the

MASSACHUSETTS INSTITUTE OF TECHNOLOGY

February 2008

Author: ……
Department of Earth, Atmospheric, and Planetary Sciences
January 11, 2008

Accepted by: …….
Maria T. Zuber
E. A. Griswold Professor of Geophysics
Thesis Advisor

Accepted by: …….
Thomas A. Herring
Professor of Geophysics
Graduate Officer, Department of Earth , Atmospheric, and Planetary Sciences

[THIS PAGE INTENTIONALLY LEFT BLANK]

Study of the Martian Upper Atmosphere using Radio Tracking Data

by

Erwan Mazarico

Submitted to the Department of Earth, Atmospheric and Planetary Sciences
on January 11, 2008, in partial fulfillment of the requirements for the degree of
Doctor of Philosophy in Planetary Sciences

Abstract

Since the first *in situ* observations of the Martian atmosphere were made by the twin Viking landers, we have learned considerably more about its composition, dynamics and variability. Not only did the new data on global atmospheric densities generate opportunities to understand the atmospheric composition of early Mars and supply constraints at the upper limit of General Circulation Models, it is critical for the design and planning of future exploration missions.

We can complement the successes of remote sensing and accelerometer investigations by using radio tracking data that have not been studied from an atmospheric science perspective, or are available for the first time. Due to the very low density of the higher layers atmosphere, the estimation of the drag acceleration using Precision Orbit Determination is a challenge. We developed new numerical models of the non-conservative forces acting on the spacecraft. In particular, the spacecraft cross-sectional area is calculated using improved spacecraft macro-models which include inter-plate shadowing. These improvements in the force modeling enable a more robust estimation of the atmospheric density. The density structure from the middle atmosphere up to the exosphere is studied using radio tracking data from the Mars Odyssey and the Mars Reconnaissance Orbiter spacecraft. Measurements in the Martian middle atmosphere, near 100–110 km, are obtained from the aerobraking phase of the Mars Odyssey spacecraft; we obtain periapsis density estimates consistent with the Accelerometer Team, and estimate scale heights representative of the drag environment from an operational point of view. The orbit of Mars Odyssey during its mapping and extended phases allows us to probe very high in the exosphere, near 400 km altitude. In the retrieved density time series, we observe some of the features of solar forcing and seasonal cycle predicted by different atmospheric models. The most recent radio tracking data, from the Mars Reconnaissance Orbiter mapping mission, enables a monitoring of densities near 250 – 300 km at higher temporal and spatial resolutions, allowing a more detailed study than previously possible.

Thesis Advisor: Maria T. Zuber, Ph.D.
Title: E. A. Griswold Professor of Geophysics

Etude de la Haute Atmosphère Martienne à partir de données radio

par

Erwan Mazarico

Soumis au Département de Sciences Terrestres, Atmosphériques et Planétaires
le 11 Janvier 2008, comme exigence partielle du
Doctorat en Planétologie

Résumé

Depuis les premières observations in situ de l'atmosphère martienne par les deux sondes Viking, nous avons énormément appris sur sa composition, sa dynamique et sa variabilité. Les nouvelles données sur la densité atmosphérique globale donnent non seulement des pistes pour comprendre la composition atmosphérique du passé de Mars mais fournissent également des contraintes pour les modèles numériques de circulation atmosphérique, ce qui sera crucial pour la planification des futures missions d'exploration.

Nous proposons d'utiliser les données radio qui n'ont pas été étudiées du point de vue atmosphérique ou qui sont disponibles pour la première fois afin de complémenter les succès de la télédétection et des accéléromètres. A cause de la très faible densité des couches supérieures de l'atmosphère, l'estimation de l'accélération de traînée (friction atmosphérique) avec la méthode de Détermination Précise d'Orbite est un défi. Nous avons développé de nouveaux modèles numériques pour les forces non conservatrices qui agissent sur les satellites. En particulier, la surface projetée est calculée à l'aide de meilleurs modèles physiques qui incluent les effets de l'ombrage entre différentes plaques. Ces améliorations dans la modélisation des forces permettent des estimations plus robustes de la densité atmosphérique. La structure de l'atmosphère depuis les strates intermédiaires jusqu'à l'exosphère est étudiée en utilisant les données radio des satellites de la NASA 'Mars Odyssey' et 'Mars Reconnaissance Orbiter'. Des mesures dans l'atmosphère intermédiaire de Mars – vers 100-110 km – sont obtenues durant la phase d'aérofreinage de Mars Odyssey ; les résultats de densité au périapse sont comparables à ceux obtenus par l'accéléromètre, et des hauteurs d'échelle représentatives de l'environnement frictionnel d'un point de vue opérationnel. L'orbite de Mars Odyssey pendant sa mission principale et ses extensions nous permet d'étudier la haute exosphère, vers 400 km d'altitude. Dans les densités obtenues, nous observons les effets du forçage solaire et du cycle saisonnier prédits par différents modèles atmosphériques. Les données radio les plus récentes de Mars Reconnaissance Orbiter permettent d'observer les densités autour de 250-300 km avec de meilleures résolutions temporelles et spatiales, et donc une étude plus détaillée que ce qui était possible jusqu'à maintenant.

Sous la direction de : Maria T. Zuber, Ph.D.
Titre : Professeur 'E. A. Griswold' en Géophysique

Estudi de l'alta atmosfera marciana utilitzant dades de ràdio-seguiment

per

Erwan Mazarico

Entregada al Departament de Ciències Planetàries, Atmosfèriques i de la Terra l'11 de gener de 2008, en compliment parcial dels requeriments per a la titolació de Doctor en Ciències Planetàries

Resum Executiu

Des que les sondes bessones Viking van aterrar al planeta Mart i hi feren les primeres observacions *in situ* de l'atmosfera d'aquell planeta, hem ampliat considerablement els nostres coneixements sobre la seva composició, dinàmica i variabilitat. Aquestes dades foren i continuen essent crítiques per al disseny i planificació de futures missions d'exploració; a més ens permeten entendre la composició atmosfèrica de Mart en el passat llunyà (fa tres o quatre mil milions d'anys) i ens ajuden a acotar els límits superiors dels Models de Circulació General, que són models numèrics de l'atmosfera.

Els èxits obtinguts a través dels sensors remots i les investigacions amb acceleròmetres es poden complementar amb l'ús de dades de ràdio-seguiment que fins ara no s'han estudiat des d'un punt de vista de ciència atmosfèrica, o que bé s'estudien ara per primera vegada. A causa de les baixíssimes densitats de les capes altes de l'atmosfera marciana, resulta força complicat calcular l'acceleració deguda a la resistència aerodinàmica fent servir les tècniques de reconstrucció orbital dels satèl.lits. El que hem desenvolupat en aquest projecte són uns nous models numèrics de les forces no-conservatives que actuen sobre la nau espacial. En particular, calculem l'àrea seccional de la nau a través d'un millor macro-model de la nau, que té en compte les obstruccions entre els seus diversos panells. Aquests avenços en el càlcul de les forces ens permeten fer una estimació més precisa de la densitat atmosfèrica. També hem estudiat l'estructura de la densitat des de l'atmosfera intermitja fins a l'exosfera mitjançant dades de ràdio-seguiment obtingudes per les sondes Mars Odyssey i Mars Reconnaissance Orbiter. L'atmosfera intermitja marciana, que es troba a uns 100-110km d'altura, fou mesurada durant la fase d'aerofrenada de la sonda Mars Odyssey; basant-nos en això, hem aconseguit càlculs de la densitat atmosfèrica a la periapsi, que són consistents amb el que suggereixen els acceleròmetres, i estimacions de les distàncies característiques de resistència aerodinàmica típiques des d'un punt de vista operatiu. L'òrbita de la Mars Odyssey durant la fase de rastreig ens va permetre prendre lectures a grans altures dintre de l'exosfera, prop dels 400km. En l'historial temporal de les dades de densitat que es van obtenir, hi hem observat alguns trets característics del forceig solar i els cicles estacionals que prediuen diversos models atmosfèrics. Les dades de ràdio-seguiment més recents, de la missió de rastreig Mars Reconaissance Orbiter, ens han permès capturar lectures de densitat prop dels 250-300km d'altura a unes resolucions espacials i temporals encara més elevades, cosa que ens ha donat la possibilitat de realitzar uns estudis molt més detallats que els que s'havien fet amb anterioritat.

Supervisor de la Tesi: Dra. Maria T. Zuber, Ph.D.
Títol Acadèmic: Professora E. A. Griswold de Geofísica

(JOSEP DORCA-LUQUE)

利用无线电跟踪数据研究火星上部大气

by

Erwan Mazarico
马欧文

Submitted to the Department of Earth, Atmospheric and Planetary Sciences
on January 11, 2008, in partial fulfillment of the requirements for the degree of
Doctor of Philosophy in Planetary Sciences

摘要

自从斯堪的纳维亚双子登陆车第一次观察到火星星大气开始，我们已经深入地了解了火星大气的成分，动力学，以及它的变异性。火星大气密度的新数据不仅给我们提供了理解早期火星大气成分的机会，为大气数值模型设定了上限，而且它对于将来火星探测任务的设计和计划也是至关重要的。

我们可以利用无线电跟踪数据来补助遥感技术和加速计研究的成功之处。这种数据是第一次用于大气科学的研究。因为更高层大气的密度非常低，利用人造卫星轨道摄动来估计大气摩擦加速度是一个挑战。我们利用作用到太空船的非保守力开发了一种新的数字模型。特别地，我们可以利用包含内部阴影的物理模型来计算太空船重叠的面积。这些在力学模型的提高能够使我们得到更加可信地估计火星大气密度。

我们利用来自冒险者和探索者火星探测器跟踪数据研究了火星大气从中层到外层的密度结构。火星中层大气（接近100到110公里）的测量数据来自冒险者的航空制动相位；我们得到的近拱点密度估计和加速器的测量结果一致，并且从操作的观点来看，我们估计的衰减特征高度代表了拖拽环境。冒险者在它主要和延伸任务中的轨道可以让我们探测到外大气层更高的地方（接近400公里的高度）。在密度时间序列中，我们观测到了由不同的大气模型预测的太阳风和季节周期的一些特性。来自探索者火星探测器最新的无线电跟踪数据可以检测到在250到300公里的更高时空分辨率的火星大气密度，必将可用于比以往更加详细的研究。

导师： 玛丽亚 朱波儿 博士
头衔：E. A. Griswold 地球物理教授

(CHANG LI 李昶)

利用無線電追蹤資料研究火星上部大氣

by
Erwan Mazarico
馬歐文

Submitted to the Department of Earth, Atmospheric and Planetary Sciences
on January 11, 2008, in partial fulfillment of the requirements for the degree of
Doctor of Philosophy in Planetary Sciences

摘要

自從維京雙子登陸車第一次現地觀察到火星大氣開始，我們已經深入地瞭解了火星大氣的成分，動力學，以及它的變異性。火星大氣密度的新資料不僅給我們提供了理解早期火星大氣成分的機會，爲大氣數值模型設定了上限，而且它對於將來火星探測任務的設計和計畫也是至關重要的。

我們可以利用無線電追蹤資料來補助遙感技術和加速計研究的成功之處。這種資料是第一次用於大氣科學的研究。因爲更高層大氣的密度非常低，利用人造衛星軌道攝動來估計大氣摩擦加速度是一個挑戰。我們利用作用到太空船的非保守力開發了一種新的數值模型。尤其，我們可以利用包含內部陰影的物理模型來計算太空船重疊的面積。這些力學模型的改善能夠使我們更可靠地估計火星大氣密度。

我們利用來自冒險者和探索者火星探測器追蹤資料研究了火星大氣從中層到外層的密度結構。火星中層大氣（接近100到110公里）的測量資料來自冒險者的航空制動相位；我們得到的近拱點密度估計和加速器的測量結果一致，並且從操作的觀點來看，我們估計的衰減特徵高度代表了拖拽環境。冒險者在它主要和延伸任務中的軌道可以讓我們探測到外大氣層更高的地方（接近400公里的高度）。在密度時間序列中，我們觀測到了由不同的大氣模型預測的太陽風和季節週期的一些特性。來自探索者火星探測器最新的無線電追蹤資料可以檢測到在250到300公里的更高時空解析度的火星大氣密度，必將可用於比以往更加詳細的研究。

導師： 瑪麗亞 朱波兒 博士
頭銜：E. A. Griswold 地球物理教授

(CHANG LI 李昶, CHIN-WU CHEN 陈劲武)

Untersuchung der oberen Marsatmosphäre mittels Radio-Tracking-Daten

von

Erwan Mazarico

Am 11. Januar 2008 der Abteilung für Erd-, Atmosphären- und Planetarwissenschaften übermittelt, in teilweiser Erfüllung der Anforderungen zur Erreichung des Grades Doktor der Philosophie in Planetarwissenschaften

Zusammenfassung

Seitdem die ersten *in situ* Messungen der Marsatmosphäre durch die beiden Viking Lander gemacht wurden, haben wir wesentlich mehr über Zusammensetzung, Dynamik und Variabilität des Mars gelernt. Die neuen Daten über die globale atmosphärische Dichte ermöglichen es nicht nur, die atmosphärische Zusammensetzung des frühen Mars zu verstehen und die Grenzen im oberen Bereich des "General Circulation" Modells zu erkennen, sondern sie sind auch von entscheidender Bedeutung für die Gestaltung und Planung zukünftiger Erkundungsmissionen.

Wir erweitern die Erfolge der Fernerkundungs- und Beschleunigungsmesser-untersuchungen unter zu Hilfenahme von Radio-Tracking-Datensätzen, die bisher noch nicht unter einem atmosphärischen Gesichtspunkt untersucht wurden, beziehungsweise zuvor nicht zur Verfügung standen. Aufgrund der sehr geringen Dichte der höheren Schichten der Atmosphäre ist die Schätzung der Beschleunigung der atmosphärischen Reibung mit der "Präzisions Orbit Bestimmungs"-Methode eine Herausforderung. Wir entwickelten neue numerische Modelle für nicht-konservative Kräfte, die auf das Raumfahrzeug wirken. Insbesondere der Raumsonden Querschnitt wird hier unter Verwendung eines verbesserten physikalischen Modells berechnet, welches auch gegenseitige Beschattung der Platten berücksichtigt. Diese Verbesserungen ermöglichen eine robustere Schätzung der atmosphärischen Dichte im Kräfte-Modell. Die Struktur der Dichte von der Mittel-Atmosphäre bis hin zur Exosphäre wird mit Radio-Tracking-Daten untersucht, die von den Raumsonden Mars Odyssey und Mars Reconnaissance Orbiter stammen. Messungen in der Mittel-Atmosphäre des Mars, bei 100-110 km, stammen aus den Luftbrems-Phasen der Mars Odyssey. Wir erhalten periaptische Dichteschätzungen, die im Einklang mit den Beschleunigungsmesserdaten stehen und schätzen Höhenlinien mathematisch derart ab, so dass sie als repräsentativ für die Luftwiderstandsumbgebung gesehen werden können. Die Umlaufbahn der Mars Odyssey während ihrer Kartierungsphase und ihren erweiterten Phasen ermöglicht es uns sehr hoch in der Exosphäre Messungen zu machen, und zwar in einer Höhe von nahezu 400km. In den ermittelten Dichte-Zeitmessungen können wir einige der Auswirkungen von Solarkraft und jahreszeitlich bedingten Zyklen beobachten, die von verschiedenen atmosphärischen Modellen vorhergesagt werden. Die jüngsten Radio-Tracking-Daten von Mars Reconnaissance Orbiter ermöglichen Bestimmung der Dichten in 250 bis 300 km Höhe in höherer zeitlicher und räumlicher Auflösung, was detailliertere Studien als je zuvor erlaubt.

Dissertations Berater: Maria T. Zuber, Ph.D.
Titel: E. A. Griswold Professor für Geophysik

(DANIELLE WENEMOSER)

לימוד של האטמוספירה העליונה של מאדים בעזרת מעקב רדיו

מאת ארוואן מאזאריקו

מאז התצפיות המקומיות (in situ) של האטמוספירה של מאדים שבוצעו על-ידי הנוחתים ויקינג 1 ו-2, למדנו רבות על ההרכב הכימי, הדינמיקה והשונות שלה. לא בלבד שהנתונים החדשים על צפיפות אטמוספירית גלובלית יוצרים הזדמנויות להבין את ההרכב הכימי של מאדים הקדום ולספק אילוצים לגבול העליון של מודלים כלליים לסירקולציה, הם גם חיוניים לתכנון של משימות חקר עתידיות.

אנחנו יכולים להוסיף על ההצלחות של מחקרי חישה מרחוק ומדי-תאוצה על-ידי שימוש במאגר נתונים של מעקב רדיו שעדיין לא נחקר מנקודת מבט של מדעי האטמוספירה ונתונים שזמינים בפעם הראשונה. עקב הצפיפות הנמוכה מאד של השכבות העליונות של האטמוספירה, ההערכה של תאוצת הגרירה בעזרת קביעת מסלול מדוייקת היא אתגר. אנו פיתחנו מודלים נומריים חדשים של הכוחות הלא-משמרים הפועלים על החללית. במיוחד, שטח החתך של החללית מחושב בעזרת מקרו-מודלים משופרים של החללית שכוללים הצללה בין-לוחית. שיפורים אלה במידול הכוחות מאפשרים הערכה מדוייקת יותר של צפיפות האטמוספירה.

מבנה האטמוספירה, מהאטמוספירה התיכונה עד האקזוספירה, נלמד בעזרת מעקב רדיו מהחלליות "מארס אודיסי" ו"מארס רקוניסנס אורביטר". מדידות של האמוספירה התיכונה של מאדים, באיזור 100-110 ק"מ, מושגות מהשלב המוקדם (אירו-ברייקינג) של החללית מארס אודיסי; קיבלנו תוצאות של צפיפות בפאריפסיס התואמות את התוצאות של צוות מד-התאוצה, והערכות של גובה סקאלה מייצגות את סביבת הגרירה מנקודת מבט תיפעולית. המסלול של מארס אודיסי בשלב המיפוי ובשלבים מאוחרים יותר מאפשר לנו לבחון באיזור גבוה מאוד באקזוספירה, בגובה של כ-400 ק"מ. בסדרות-הזמן המתקבלות של הצפיפות, אנחנו רואים חלק מהתופעות של אילוץ סולארי ומחזוריות עונתית שנחזו על-ידי מודלים אטמוספיריים שונים. הנתונים החדשים ביותר של מעקב-רדיו, מהחללית מארס רקוניסנס אורביטר מאפשרים מעקב של צפיפויות בקרבת גובה 250-300 ק"מ ברזולוציה גבוהה יותר במרחב ובזמן, מה שמאפשר מחקר מפורט יותר משהיה אפשרי עד כה.

מנחה: מריה זובר, פרופסורית ע"ש גריסוולד לגיאופיזיקה

Tanulmány a Mars Atmoszférájának Felső Rétegéről, Rádiójelzési Adatok Felhasználása Által

Erwan Mazarico

bemutatja az MIT Planetológia, Föld és Atmoszféra Tudomány Karának, 2008. Január 11-én, a Planetológia Doktori címhez fűződő követelmények parciális megfelelése céljából

Kivonat

Az első *in situ* megfigyelések óta, amelyeket a Viking ikerleszálló egységek készítettek, a Mars atmoszférájának összetételére, dinamikájára és változékonyságára vonatkozó ismereteink jelentős módon bővültek. Az új, globális atmoszféra sűrűségi adataink lehetőséget nyújtanak arra, hogy egyrészt jobban megismerjük a 3-4 milliárd évvel ezelötti Mars atmoszférájának összetételét és új felső határértékekkel szolgálhassunk az Általános Keringési Modellek számára; de ezeknek az adatoknak másrészt kritikus fontosságuk van eljövendő űrkutatási missziók részére is.

A távolból irányItott érzékelők és gyorsulásmérők által folytatott vizsgálatok sikereit most kiegészíthetjük olyan rádiójelzési adatok felhasználásával, amelyeket eddig vagy nem tanulmányoztunk atmoszférikus tudományok szempontjából, vagy pedig eddig egyszerűen nem álltak rendelkezésünkre. A súrlódási gyorsulás felmérése az Orbitális Műhold Értékelési módszer szerint kihIvást jelent a Mars atmoszférájának felső rétegeire jellemző alacsony sűrűség miatt. E tanulmány során új számszerű modelleket fejlesztettünk ki, amelyek az űrhajókra ható súrlódási erőkre összpontosítanak. Az űrhajó keresztmetszete területének felmérése manapság tökéletesített, űrhajó makro-modellek felhasználása által történik, amelyek a lemezek közötti árnyékolást is figyelembe veszik. Ezen erőmodellációs tökéletesítések megbizhatóbb sűrűségi becsléseket eredményeznek. Az atmoszféra középrétegétől az exoszféra felé terjedő sűrűségi struktúra tanulmányozását a Mars Odyssey és Mars Reconnaisance űrhajók által szerzett rádiójelzési adatok teszik lehetővé. A Mars belső rétegére vonatkozó mérések, 100-110 km távolságban, a Mars Odyssey aero-fékezési fázisa által lehetségesek amelyek által a Gyorsulási Mérőtől szolgáltatott értékekkel konszisztens, periapszisokra vonatkozó sűrűségi becslésekhez jutunk.. Az adatok új, az atmoszféra struktúrájára jellemző paraméterek becslését is lehetővé teszik amelyek megegyeznek az operacionális perspektivával. A Mars Odyssey alap- és meghosszabbított küldetési ideje alatt leírt orbitája az exoszférára (400 km körül) vonatkozó értékeléseket teszi lehetővé. Az idő szerinti sűrűségi adatokban, a különböző atmoszféra modellek által kivetített szoláris ingadozási és időszakos ciklikussági jelenségek figyelhetők meg. A Mars Reconnaissance Orbiter-ről származó legújabb rádió adatok lehetővé teszik a 250-300 km-hez közeli sűrűségek, magasabb idő és tér rezoluciós megfigyelését, amely a még kimerítőbb tanulmányokra ad lehetőséget.

Tézis Tanácsadó: Dr. Zuber T. Mária
CÍm: E. A. Griswolt Geofizika Professzora

(TIMEA PAL)

Studio dell'atmosfera superiore di Marte mediante l'uso di Radio Tracking Data

A cura di:
Erwan Mazarico

Presentata al Dipartimento di Scienze Atmosferiche e Planetarie,
11 Gennaio 2008, come parte degli adempimenti richiesti per il titolo di
Dottore di Filosofia in Scienze Planetarie

Abstract

A partire dalle prime osservazioni in situ dell'atmosfera di Marte effettuate dalle sonde gemelle Viking, abbiamo imparato sempre più della composizione, della dinamica e variabilità del pianeta. I nuovi dati sulla densità dell'atmosfera globale introducono nuove opportunità per capire la composizione dell'atmosfera primordiale di Marte e forniscono nuove condizioni al contorno per il limite superiore dei Modelli di Circolazione Globale (General Circulation Models), non solo, rappresentano un punto chiave per la progettazione e la pianificazione di future missioni di esplorazione.

Siamo in grado di integrare i successi del telerilevamento e di indagini accelerometriche usando i *radio tracking dataset*, non ancora studiati nell'ambito delle scienze atmosferiche, o che sono disponibili solo adesso per la prima volta. A causa dell' estrema bassa densità degli strati superiori dell'atmosfera, la stima dell'accelerazione di frizione, utilizzando una metodologia basata sulla ricostruzione dell'orbita dei satelliti è una sfida. Abbiamo quindi sviluppato nuovi modelli numerici delle forze non conservative che agiscono sulla sonde spaziali. In particolare, l'area della sezione trasversale della sonda è calcolata utilizzando modelli fisici di sonda spaziale migliorati, che comprendono l'effetto "ombra tra piastra". Questi miglioramenti nella modellazione delle forze consentono una stima più robusta della densità atmosferica. La struttura della densità dall'atmosfera intermedia fino alla esosfera è studiata utilizzando radio tracking data provenienti dalle sonde "Mars Odyssey" e "Mars Reconnaissance Orbiter". Alcune misurazioni nell'atmosfera intermedia marziana, approssimativamente a 100-110 km, sono ottenuti dalla fase di aereo freno della sonda Mars Odyssey; si ottengono stime della densità periasse coerenti con quelle ottenute da strumenti accelerometrici, e stime dell'altezza caratteristica di decadimento dell'ambiente di frizione rappresentative da un punto di vista operativo. L'orbita di Mars Odyssey durante la sua mappatura e le sue fasi estese ci permette di sondare molto in alto nel esosfera, fino a quasi 400 km di altitudine. Nelle serie temporali ricostruite di densità, osserviamo alcune delle caratteristiche delle forze provenienti dal sole e del ciclo stagionale, già previste da diversi modelli atmosferici. I più recenti *radio tracking data*, dalla missione di mappatura della sonda Mars Reconnaissance Orbiter consentono un monitoraggio della densità fino a 250 - 300 km ad una risoluzione temporale e spaziale più alta, che consente uno studio più approfondito rispetto al passato.

(CHIARA LEPORE)

라디오 추적 자료를 이용한 화성 상부 대기에 관한 연구

by

Erwan Mazarico

Submitted to the Department of Earth, Atmospheric and Planetary Sciences
on January 11, 2008, in partial fulfillment of the requirements for the degree of
Doctor of Philosophy in Planetary Sciences

초록

두 바이킹 탐사선에 의해 처음으로 화성대기의 직접 관측이 이루어진 이래, 그 조성, 역동성 그리고 가변성에 있어 상당히 많은 부분이 알려져왔다. 전체 대기 밀도에 관한 이러한 새로운 자료는 초기 대기 조성을 이해하기 위한 기회와 일반순환모델(General Circulation Models)의 상한을 제공했을 뿐 아니라, 장래 탐사 임무의 밑그림과 계획에 중요하다.

대기과학적 관점에서 연구가 되어오지 않았으며 처음으로 이용되는 라디오 추적 자료는 원격탐사와 가속도계 조사의 성과를 보완할 수 있다. 상층대기의 저밀도성 때문에, 정밀궤도결정(Precision Orbit Determination)에 의한 끌림가속도의 추정은 어려운 문제이다. 우리는 탐사선이 받는 비보존적 힘에 대한 새로운 수치모델을 개발하였다. 특히, 탐사선의 단면적은 탐사선 일부의 빛 차단 현상을 포함한 개선된 탐사선 입체 모델을 이용하여 얻어진다. 이러한 힘에 대한 개선된 모델로 대기밀도를 보다 정밀하게 추정할 수 있다. 중층대기에서 외기권까지의 밀도 구조 연구는 화성 오딧세이(Mars Odyssey)와 화성 리커네이선스 오비터(Mars Reconnaissance Orbiter)로부터 얻어진 라디오 추적 자료를 사용한다. 약 100-110km 까지의 중층대기 측정은 화성 오딧세이 에어로브레이킹(aerobraking) 단계에서 수행된다; 가속도계 결과와 일관되게 근점에서의 밀도 추정치를 얻으며, 운용상 관점에서 끌림환경을 대표하는 규모고도(scale heights)를 추정한다. 탐색(mapping)과 그 이후 과정 동안의 오딧세이 궤도는 400km 고도 근처의 외기권 상층부 탐사를 가능케한다. 이렇게 얻어진 밀도 시계열 자료에서, 다른 대기 모델에 의해 예측된 태양에너지 흡수와 주기적 현상의 몇몇 특징을 관찰한다. 화성 리커네이선스 오비터 탐사로부터 얻어진 가장 최신의 라디오 추적 자료를 가지고 보다 높은 시공간 해상도로 대략 250-300km 에서의 밀도를 관찰할 수 있으며, 이로서 이전보다 더욱 심도있는 연구를 할 수 있다.

Thesis Advisor: Maria T. Zuber, Ph.D.
Title: E. A. Griswold Professor of Geophysics

(KANG HYEUN JI, 지강현)

Un Studiu al Stratelor Superioare ale Atmosferei Planetei Marte Utilizând Date Radio de Semnalare

Autor
Erwan Mazarico

Prezentat Departamentului de Ştiinţe a Pământului, Atmosferei şi a Planetelor în data de 11 Ianuarie, 2008, în realizare parţială a cerinţelor pentru obţinerea titlului de Doctor al Ştiinţelor Planetare

Rezumat

De la primele observaţii in situ ale atmosferei planetei Marte de către cei doi landeri Viking, cunoştinţele noastre despre compoziţia, dinamismul şi variabilitatea planetei s-au îmbunătăţit în mod semnificativ. Noile informaţii despre densitatea atmosferică globală au creat oportunităţi nu numai pentru o mai bună înţelegere a compoziţiei atmosferice a planetei Marte cu 3-4 miliarde de ani în urmă şi pentru stabilirea valorilor limită pentru Modelele de Circulaţie Generală, dar au fost critice şi pentru planificarea misiunilor de explorare care au urmat.

În prezent, succesul metodelor de semnalare de la distanţă şi a investigaţiilor de accelerometrare pot fi complementate prin folosirea datelor de semnalare radio care fie nu au fost studiate din perspective ştiinţelor atmosferice, fie nu au fost disponibile mai devreme. Din cauza densităţii foarte scăzute al stratelor superioare ale atmosferei, estimarea acceleărării de fricţiune prin folosirea Reconstrucţiilor Orbitare prin Satelit a rămas dificilă. Prin această lucrare, s-au dezvoltat noi metode numerice de modelare a forţelor de fricţiune care actionează asupra navelor spaţiale. Suprafaţa cros-sectională a navelor spaţiale se calculează prin folosirea unor modele macro îmbunătăţite, care iau în considerare şi suprafaţa proiectată. Asemenea progrese pemit o estimare mai robustă a densităţii atmosferice. Structura de densitate a stratelor atmosferice de la stratul intermediar până la exosferă se studiază utilizând date de semnalare radio obţinute de la navele Mars Odyssey şi Mars Reconnaissance Orbiter. Estimările din stratul atmosferic intermediar, de la o altitudine de 100-110 de km, ce se obţin prin folosirea fazei de aero-frânare a navei Mars Odyssey putem obţine estimări de densitate din punctele periapsice care sunt consistente cu cele furnizate de Instrumentul de Accelerometrare. De asemenea, noile date ne permit şi noi estimări parametrice a structurii atmosferale, consistente cu perspective operaţională. Orbita navei Mars Odyssey pe durata misiunii principale de reprezentare şi a misiunii suplimentare ne permit să conducem investigaţii la o altitudine foarte ridicată, de la o altitudine de 400 de km. În seriile de date temporale se pot observa unele trăsături de variaţii solare şi ciclicităţi sezonale proiectate de diferite modele ale atmosferei. Cele mai recente date radio obţinute prin misiunea de explorare a navei Mars Reconnaissence Orbiter permit monotorizări a densităţilor de la o altitudine de 250-300 de km, la rezoluţii spaţiale şi temporale mai ridicate, oferindu-ne posibilitatea de a efectua studii mult mai detaliate decât în trecut.

Îndrumător de Lucrare: Maria T. Zuber, PhD
Titlu: Profesor E. A. Griswold de Geofizică

(TIMEA PAL)

Estudio de la atmósfera superior de Marte con datos de radio-seguimiento
por

Erwan Mazarico

Presentado en el Departamento de Ciencias Planetarias, de la Tierra, y de la Atmósfera
El 11 de enero de 2008, en cumplimiento parcial de los requisitos para el grado de
Doctor en Ciencias Planetarias

Resumen

Desde las primeras observaciones *in situ* de la atmósfera de Marte por las dos naves espaciales Viking, hemos aprendido considerablemente más acerca de su composición, dinámica, y variabilidad. Estos datos nuevos iluminaron la composición de la atmósfera durante las primeras épocas de la historia de Marte, y además fueron utilizados para fijar parámetros en Modelos de Circulación General, y que son esenciales para el diseño y planificación de futuras misiones.

Podemos complementar los éxitos de la observación remota e investigaciones con con acelerómetros, utilizando datos de radio-seguimiento que antes no fueron consultados para estudiar la atmósfera, o son disponibles por la primera vez. Debido a la densidad naja de las altas capas atmósfericas, la estimación de la aceleración de arrastre atmósferico utilizando Determinación Precisa de Orbitas es un gran desafío. Hemos desarrollado nuevos modelos numéricos de fuerzas non-conservadoras actuando sobre la nave espacial. En particular, el área de sección transversal está calculada usando nuevos modelos físicos de la nave espacial que incluyen el efecto de sombra. Estos mejoramientos en la modelización de fuerzas permiten una estimación más precisa de la densidad atmósferica. La densidad, desde niveles del medio de la atmósfera hasta la exosfera, esta investigada usando datos de radio-seguimiento de las naves Mars Odyssey y Mars Reconnaissance Orbiter. Observaciones en altitudes del medio de la atmósfera cerca de 100-110 km fueron obtenidos durante la etapa de aerofrenado de la nave Mars Odyssey. Hemos obtenido estimaciones de la densidad en periapsis que son similares a los del equipo instrumental del acelerómetro, y de la escala de altura eficaz de un punto de vista operacional. La órbita de Mars Odyssey durante sus etapas cartográficos y extendidos nos permitió hacer una investigación en altitudes muy altas en la exosfera, cerca de 400 km. En la evolución de la densidad, hemos observado algunos de los efectos de la influencia solar y ciclos estacionales, predichos por los diferentes modelos atmósfericos. Los últimos datos de radio-seguimiento de la misión cartográfica del Mars Reconnaissance Orbiter posibilitan la observación durante intervalos largos de la densidad cerca de 250 - 300 km con mayor resolución espacial y temporal, permitiendo una investigación más detallado qua antes no fue posible.

Asesor de Tesis: Maria T. Zuber, Ph.D.
Título: E. A. Griswold Profesor de Geofísica

(WESLEY A. WATTERS FARFÁN)

[THIS PAGE INTENTIONALLY LEFT BLANK]

[THIS PAGE INTENTIONALLY LEFT BLANK]

Dedication

A mes parents,
Hélène et Floréal,

[THIS PAGE INTENTIONALLY LEFT BLANK]

Acknowledgements

In addition to the challenge of doing a Ph.D., I feel that my time at MIT was a very special moment and an important experience. It brought me new perspectives, both at work and outside. The very international environment, in the EAPS Department, at MIT and in Cambridge, was tremendous. In France, I never had the opportunity of meeting so many people from all continents. My first time in the United States and almost out of Europe was to come and study here. The change was significant, and it is hard to remember the mindset I had when I first came here, in late August 2002. Since then, my horizons expanded!

When I came to MIT, I was still officially a student at a top French engineering school. That school, SUPAERO (Ecole Nationale Supérieure de l'Aéronautique et de l'Espace, or National Engineering School for Space and Aeronautics), allowed its top students to spend their last year in a foreign university. I grabbed that opportunity to come here and conduct scientific research. At the time, I was becoming very reluctant to work for the industry, and it felt like my childhood dream of space and learning about the Solar System would not be fulfilled by getting a 'normal job'. Maria Zuber, whom I would like to very sincerely acknowledge first, gave that 'random guy' the ticket to a two-year Master of Science in Planetary Sciences. That was something already! When came the time to seriously prepare the projects for the dreaded General Exams, I was considering continuing to Ph.D., until I found out that I had actually been admitted in the Ph.D. program from the start! So I stayed, took my Exams and made it through, even though the memories of that period are obviously not the best. Like (almost) any graduate student I know, I had my periods of doubt, but as they say there is light at the end of the tunnel. Maria was so encouraging in our meetings, even when the results I was presenting were not very convincing to me, that I am grateful to her for making sure I stayed on the right path and focus.

Precision Orbit Determination is not an easy field to discover and master. My engineering background certainly helped me to understand the limitations and intricacies of spacecraft modeling, but it took an incalculable number of trials and errors to overcome the successive obstacles, and finally get it right. In that respect, Frank Lemoine helped me a great deal, and he is also to blame for me finishing this Thesis. In addition to sometimes lengthy email conversations and chats at conferences, I made several short stays at the Goddard Space Flight Center, to meet with him and Dave Smith. Dave and Maria, who worked and work together on an incredible number of space missions, wanted to use the tracking data of Mars orbiters to learn about the atmospheric density. The funding for my Ph.D. came from their Mars Critical Data Products proposal. In the first couple of years, it seemed almost impossible to obtain reasonable and robust values. But after many meetings and conversations with them, and a lot of work, everything seems to have come together. The last semester was especially exciting, as the quality of the results was much improved and their implication unexpectedly significant. I also need to thank the professors to whom I talked and who gave me insight in understanding my results and trying out new things. In particular, Tom Herring and Alan Plumb who agreed to be on my Thesis Committee. I would also like to thank Dave Rowlands (GSFC) for answering my questions about the GEODYN source code, Greg Neumann (GSFC) in particular for providing me with MOLA data and for interesting conversations, Richard Simpson (Stanford) for archiving the Mars Odyssey radio tracking data on the NASA PDS server even though there was no official Radio Science mission, and Sami Asmar (JPL) for anwering important technical questions.

On a more personal note, I wish to thank all my friends for their support over all those years. I will not name them for fear of embarrassing myself by forgetting one, and they know who they are. In addition to those on the other side of the pond, of whom I definitely saw too little recently, I met new and amazing people. Being around people from all those different nationalities also reignited my interest in languages. I had studied several languages in France already, and took on Mandarin Chinese over the past two years. The classes at MIT were excellent and my level did impress some of my Chinese and Taiwanese friends, even though it is fading quite fast because of the past few months

when I was busy writing this Thesis. It was a lot of fun, and prompted me to ask a few friends to translate the Thesis abstract into their own mothertongue. Kudos to them! There are 12 versions of the abstract, in a variety of alphabets and writing systems.

Special roommates made daily life never boring, and labmates and fellow students made EAPS an enjoyable place to study. Maybe it is a bit chauvinistic to say that, but I feel that this Department has an especially good student community. And how could I forget the weekly student seminars, with the Bertucci's pizzas.

MIT and Cambridge slowly became like home, and now that I know Cambridge and Boston so much better than Paris, it will be hard to leave. But the people and memories associated with those places will stay with me as I move to the next stages.

That is one of the important side-effects of studying at MIT: it is one of the few places in the world where you get to be surrounded at all times by so many outstanding people. And of course, there is also "that other university down the river" (Harvard) where my girlfriend Sophia studies Architecture. Oddly enough, before dreaming of being an astronaut around 12, I wanted to be an architect (LEGO's are probably to blame). Then the space virus caught me. But in the past year and a half, I have had the chance to see and talk about architecture again! That made for interesting breaks (for me only though!), and in a way forced me to work even more (M.Arch. students are the most dedicated and hard-working that I know). Sophia is the reason I stayed sane in the past few months. Her support made the end of the Ph.D. a totally painless experience. I also had a lot of fun with her: touring the National Parks of the American West the past summer along with my brother Guillem; discovering Hong Kong over this summer; and making frequent short cultural-oriented trips to New York. And more adventures await!

My family in France saw little of me in the past five years. I generally came back just twice a year, and it was not always possible to see everyone in my extended family. But those vacations were better than ever, as it provided a complete break from Boston. I did not see too much of my parents and brother either, although we kept in close contact by phone. I know they are proud of me graduating, and becoming the first Dr. Mazarico.

Their support over my whole time here was the most important and needed, and I truly could not have made it without them. Merci!

As a note for the future, I am excited about the prospects of continuing planetary exploration. The lunar exploration is pacing up again, and I am eager to work on that next. I am more convinced than ever that Planetary Sciences, if not the coolest, is the greatest field to be in today. In my mind, its seemingly negligent disinterest in worldly matters is just a temporary illusion, as the future of mankind lies in the stars. Here is my small contribution to it.

To end with a quote, the one that inspired everything:

"That's one small step for a man, one giant leap for mankind."
Neil Armstrong
July 21, 1969
Mare Tranquillitatis, Luna

[THIS PAGE INTENTIONALLY LEFT BLANK]

[THIS PAGE INTENTIONALLY LEFT BLANK]

Table of Contents

Chapter 3 – Atmospheric density during the aerobraking of Mars Odyssey from radio tracking data

Chapter 4 – Atmospheric Density at 250km altitude with Mars Reconnaissance Orbiter Radio Science

[THIS PAGE INTENTIONALLY LEFT BLANK]

List of Tables

[THIS PAGE INTENTIONALLY LEFT BLANK]

List of Figures

Chapter 1 – Introduction

Chapter 2 – Martian exospheric density using Mars Odyssey radio tracking data

Chapter 3 – Atmospheric density during the aerobraking of Mars Odyssey from radio tracking data

Chapter 4 – Atmospheric Density at 250km altitude with Mars Reconnaissance Orbiter Radio Science

Chapter 5 – Non-conservative force modeling: self-shadowed cross-sections

Chapter 6 – Non-conservative force modeling: high-resolution albedo radiation pressure

Chapter 7 – Conclusion

no figure

[THIS PAGE INTENTIONALLY LEFT BLANK]

Chapter 1

Introduction

1.1 Motivation

In recent years, the planet Mars has been explored by a number of manmade spacecraft. Both landers and orbiters have explored the red world in search of clues to understand that world once thought to harbor advanced life. In addition to the geological study of the surface and subsurface, NASA's recent "follow the water" strategy has put an emphasis on the Martian atmosphere. It is also important to understand its current state to investigate the more distant past, so current atmospheric escape is one of the natural foci of study.

Relatively few spacecraft have returned data on the Martian exosphere. Figure 1.1 shows the coverage in season and solar activity of the measurements made by Mariner 4, 6, 7 and 9, Viking 1 and 2, Mars Pathfinder, Mars Global Surveyor (MGS), Mars Odyssey (ODY) and Mars Reconnaissance Orbiter (MRO). This uppermost layer of the Martian atmosphere is the region where atmospheric escape occurs. No spacecraft mission dedicated to the study of the upper atmosphere (i.e., aeronomy) has ever been sent to Mars, although two 'Scout' mission proposals are currently being developed. The atmospheric instruments of current orbiters (Mars Odyssey, Mars Express and Mars Reconnaissance Orbiter, and until end 2006 Mars Global Surveyor) are designed to probe the lower atmosphere in great detail, but not the upper layers. In this Thesis, we estimate the total atmospheric neutral density at high altitude (100-110km, ~250km and ~390km). Our measurements are indirect estimates based on the reconstructed trajectories of two spacecraft (Mars Odyssey and Mars Reconnaissance Orbiter), through Precision Orbit Determination using radio tracking data.

1.2 The Martian atmosphere

1.2.1 General presentation

On the Martian surface, the atmospheric pressure is less than 1 percent of that of the Earth. It varies significantly over the course of a Martian year, because of the large eccentricity of the orbit of Mars around the Sun (~0.094 compared to 0.017 for the Earth) and a seasonal cycle of mass exchange between the North and South polar caps. Composed mostly of CO_2, the Mars atmosphere is buffered by its two seasonal CO_2 polar caps, which overlay residual water ice caps. The asymmetry of the seasons makes the Southern CO_2 polar recede much more during the Southern summer, leading to a larger global pressure in Southern summer than in Northern summer (and 2 minima in spring and autumn).

Contrary to the Earth, the atmosphere of Mars is very dusty. The dust particles lifted in the atmosphere increase considerably its heat capacity and solar radiation absorption coefficient. As a result, the Martian atmosphere is subject to background aerosol heating (Bougher et al. [2000]). Moreover, large global dust storms (up to two per year, although with important inter-annual variability) can enhance significantly the temperature of the lower atmosphere. Recent observations of the global summer 2007 dust storm by the Mars Climate Sounder (MCS) instrument (Kass et al. [2007]) onboard the Mars Reconnaissance Orbiter (MRO) measured increases of up to 40K in the lower atmosphere. In addition to having profound effects on the circulation dynamics and the structure of the lower atmosphere, the large increases in dust opacity also affect the upper atmosphere (the focus of this Thesis). The dust particles do not reach thermospheric heights (>110km, Bougher et al. [1999]), but by warming up the lower atmosphere, the atmospheric column is inflated and all the isodensity levels shift upwards.

Numerical computations using General Circulation Models (GCMs) showed that the large topographic dichotomy between the low Northern hemisphere and the high Southern hemisphere (Smith et al. [1999]) plays a major role in the circulation of the atmosphere and in particular in the different convection patterns between Southern summer and Northern summer. In addition, the interaction of the atmospheric circulation with the topography gives rise to atmospheric waves (called gravity waves). Other processes that can give rise to waves are illustrated in Figure 1.2, as well as their effect on the coupling between lower and upper atmosphere. As noted by Withers et al. [2003], given the latitudinal variations in the topography zonal harmonics, atmospheric waves with wavenumbers of 2 and 3 are favored. These waves can interact with another type of periodic density variation: the diurnal and semidiurnal thermal tides due to the solar radiation forcing. This interaction can generate additional oscillation modes (Figure 1.3, Forbes et al. [2002]). In particular, vertically-propagating waves with long vertical wavelengths can reach very high altitudes. Their propagation depends on the vertical wind profile, and on various dissipation mechanisms (radiative cooling, wave-wave coupling, shear instabilities, viscous effects, ion drag, wave breaking). Bougher et al. [1997] and Withers et al. [2003] noted that semidiurnal tides can be excited during the storm season (Southern summer) by the atmospheric dust; the large vertical extent of the region over which forcing occurs favors waves with long vertical wavelengths (Bougher et al. [1993]). However, the dust distribution itself is not likely to generate atmospheric waves because it varies on short timescales. Forbes and Hagan [2000] also described the diurnal Kelvin wave, which has a nearly-infinite vertical wavelength, though is still dissipatve because it is close to resonance with the Martian atmosphere (Zurek and Leovy [1981]).

1.2.2 The upper atmosphere

The region defined as the ‘upper atmosphere’ varies significantly depending on the interest. Scientists studying the Martian weather may put the lower limit of the upper atmosphere at about 50 kilometers. Our focus on the atmospheric density environment of the Mars Odyssey and the Mars Reconnaissance Orbiter spacecraft, orbiting near 400km and 250km, respectively, naturally leads us to choose a different definition. The whole homosphere is considered as ‘lower atmosphere’, and the densities obtained during the Mars Odyssey aerobraking near 100–110km are considered the ‘middle atmosphere’. Below ~115-130km (depending on season), the various constituents of the atmospheric gas are well-mixed and have a mixing ratio constant with height. Above this ‘homosphere’ lies a ‘heterosphere’ in which the molecular species are not well-mixed; due to the low density, the collisions which homogenize the temperatures of interacting molecules are much less frequent. Individual atmospheric species follow their own photochemistry, and diffuse upwards with specific scale heights.

In the thermosphere (region above ~100km where the temperature increases with height) and the exosphere (region above ~200km where particles have ballistic trajectories and can potentially escape the atmosphere), the absorption of UV (Ultra-Violet, λ~300–400nm) and EUV (extreme UV, λ~80–120nm) light is an important source of energy. The exosphere is nearly isothermal (temperature reaching its maximum near the exobase), and its structure is largely controlled by solar heating. The 11-year solar cycle results in a two-fold change in the EUV flux, which corresponds to a factor of 3.5 in the flux at 10.7cm, aka $F_{10.7}$, a proxy historically used in atmospheric models (Bougher and Robble [1991]). Because of the larger distance to the Sun, the solar radiation flux at Mars is about twice as low as on the Earth. This is partially compensated by the higher heating efficiency of the incoming EUV radiation (~22% compared to ~15% for the Earth, Bougher et al. [1999]); the rest of the absorbed EUV radiation is either lost directly as UV

airglow, or is transformed into chemical energy and later released at lower altitudes where it does not sensibly affect the energy balance. Unlike the Earth, the flux received at Mars also varies by ~40% on a yearly timescale because of the eccentricity of the planet's orbit. In addition, the lack of a magnetic field precludes auroral processes from heating the upper atmosphere to very high temperatures as on the Earth (>1400K).

To balance this heating, the dominant cooling mechanism is the radiation to space of infrared (IR) light (Bougher et al. [1999]). The majority of the energy radiated at infrared wavelengths in the upper atmosphere is due to the 15μm vibrational CO_2 band, but the low abundance of atomic oxygen (O) does not provide a catalytic effect (quenching of CO_2) as on Venus (where it reduces significantly the exospheric temperature and its variations over the solar cycle despite the close distance to the Sun). The Martian atmosphere is depleted in oxygen (Bougher and Robble [1991]) due to its greater distance from the Sun, which reduces CO_2 photolysis, a source of O atoms (Bougher et al. [1999]). Figure 1.4 shows the number density profile of various atmospheric species up to 360km; atomic oxygen does not become dominant until 200-230km depending on solar activity. On Mars, molecular thermal conduction seems to regulate the exospheric temperature (Bougher and Robble [1991]). Because of the lower gravity on Mars and the resulting atmospheric scale heights, the altitude range corresponding to the densities at which the EUV heating operates is in a region where molecular conduction is effective (Figure 1.5).

There can be significant differences between the dayside and the nightside thermospheres, although there is no effective isolation because of the rapid rotation (a day on Mars, called a 'sol', lasts ~ 24h37min), unlike Venus. The exospheric temperature is dependent on the local solar time, and reaches a peak near 3pm and a minimum near 5am (Bougher et al. [1993], Bruinsma and Lemoine [2002]).

On the Earth, the propagation of atmospheric waves to high altitudes is overwhelmed by the strong diurnal forcing of the EUV heating on the density structure, especially at high solar activity (Hong and Lindzen [1976]). The UV spectrometer on Mariner 9 identified dayside exospheric temperature enhancements due to wave activity during a global dust storm (Stewart et al. [1972]), even near solar maximum (Bougher and Shinagawa [1998]). Of special interest in this Thesis because the two spacecraft studied have Sun-synchronous orbits (i.e., the surface seen at nadir is at a constant solar time), some non-migrating waves (which appear as stationary, longitude-dependent features at fixed solar time) have minimal dissipation as they propagate to the lower thermosphere (Forbes and Hagan [2000]). Potentially, under the right conditions (e.g., dayside, low solar activity, Southern summer), they could be observed in the exosphere (Bougher et al. [1993]).

1.3 Radio Science and Precision Orbit Determination

1.3.1 Data and method

Orbital spacecraft are typically tracked daily by large antennae on the Earth. In addition to receiving the scientific data through telemetry, the tracking is critical for navigation purposes. Navigation Teams reconstruct the spacecraft trajectory over short time periods (called an ‘arc’), plan for necessary orbital maneuvers and predict future positions to reiterate this task. Doppler shifts in the received radio signals and travel times are used to constrain the trajectory and explain it using a set of pre-established (*a priori*) physical models. During this process, called Precision Orbit Determination (POD), model parameters are adjusted to converge to the ‘best-fit trajectory’, i.e. the trajectory for which the measurement residuals (difference between the actual observation and the model-predicted value) are

smallest. For every arc, partial differential equations can be created for any model parameter. Many of such 'normal equations' can then be combined to obtain accurate estimates of low-signal parameters. Except for the Earth where *in situ* measurements are available, all the high-resolution gravity fields of Solar System bodies were created with this technique. The parameters adjusted in individual arcs can also lead to valuable measurements without this inversion step. In this Thesis, we use the GEODYN II software package (Pavlis et al. [2006]), developed at the NASA Goddard Space Flight Center (GSFC). We are particularly interested in the adjustment of the atmospheric drag scale coefficient. Using it to scale the density value predicted by an *a priori* atmospheric model, we obtain what are effectively indirect density measurements. Their temporal and spatial resolutions are directly dependent on the duration over which the drag coefficient is estimated. This is of course related to the signal-to-noise ratio, limited by the number of data points available during POD and the observation geometry (orbit, Earth position, etc.). In this Thesis, we show that we can obtain reasonable and robust time series of the density at the orbital altitudes of the two spacecraft studied.

1.3.2 Previous results

Despite being an old idea in satellite geodesy, with the first density measurements inferred from satellite drag dating back to the early 1960s (Jacchia and Slowey [1962]), at the time this Thesis was started the use of Precision Orbit Determination (POD) to study the atmospheric environment of Mars-orbiting spacecraft was just becoming possible. With the radio tracking data of MGS during the Science Phasing Orbit in 1998, Tracadas et al. [2001] used orbit reconstruction to infer atmospheric densities at high altitude (170-180 km). Bruinsma and Lemoine [2002] used the drag coefficients obtained during MGS mapping phase to measure the density near 400 km and improve the atmospheric model of Stewart [1987]. However, their density estimates had large uncertainties

and poor temporal resolution. Since then, with the improvement of *a priori* models (especially the gravity field), the recovery of density measurements has been more accurate. Density results based on MGS and Mars Odyssey tracking data were briefly discussed by Konopliv et al. [2006]. Forbes et al. [2006] conducted a dedicated atmospheric study of the Martian exosphere at the same time as work in the current Thesis (Mazarico et al. [2007], Chapter 2). The orbital altitude of MGS was just 20 kilometers lower than Mars Odyssey, but this altitude difference appears to be significant: densities measured with Mars Odyssey tracking data do not exhibit correlations with the solar rotation as clearly as in the case of MGS.

1.4 Goal and Outline of the Thesis

The goal of this Thesis is to study the available radio tracking datasets which have not been previously studied from the perspective of atmospheric density. It is important to make use of these data for two main reasons.

First, scientifically, to better understand the Martian atmosphere itself. The lower atmosphere is being examined in detail and has now been under continuous scrutiny for nearly a decade. On the other hand, the upper atmosphere has not been studied as thoroughly. While the interest in the lower atmosphere is obvious and natural, the upper atmosphere also has a great deal to say about Mars. The exosphere, where most of the measurements presented in the following Chapters were done, is the region where atmospheric escape occurs. The current escape rate is difficult to measure, but can be constrained by exospheric density measurements. Moreover, computer simulations can be effective tools to assimilate those density measurements. In recent years, the GCMs have greatly expanded upwards, from below 80km (Wilson and Hamilton [1996], Forget et al. [1999]) to more than 300km (Bougher et al. [2000], Forget et al. [2007]). However, they are still based on a very limited number of measurements. Data

from Mars Odyssey and the Mars Reconnaissance Orbiter can help bring new constraints near their orbital altitude (~250km for MRO and ~390km for Mars Odyssey). In addition to opening these perspectives, we interpret the obtained measurements and compare them to previous measurements and model predictions.

Second, the atmospheric drag environment of the orbiting spacecraft is important for Navigation purposes. It can help improve the orbit predictions needed to plan orbital maneuvers and instrument usage, and they can be important for the design of future missions (in particular, aerobraking upon arrival and quarantine after mission completion).

In Chapter 2, we present the density results obtained from radio tracking data of Mars Odyssey during its mapping phase and the subsequent extended mission. These data came first chronologically, but were actually the most challenging. With an orbit periapsis near 390km, the densities are very small. The signal-to-noise ratio of the measured densities is weak, and the relatively small 20km altitude difference with the Mars Global Surveyor (MGS), from which densities were also obtained, is sensible.

In Chapter 3, we use the Mars Odyssey tracking dataset during its aerobraking phase. During this short period of a few months, the spacecraft had a very eccentric orbit with much lower periapses (100–110km). Although the accelerometer experiment could observe atmospheric waves thanks to its much higher temporal resolution, this study is valuable to compare the density structure to the effective structure sampled, from a purely navigational perspective.

In Chapter 4, we used data from the Mars Reconnaissance Orbiter during the first year of its primary science phase. Using the same technique as in Chapter 2 but with a more recent gravity field and improved force models, we measured the density near 250km. The lower altitude results in a much higher density level, which enables us to obtain density estimates at significantly better temporal and

spatial resolution. Although the time period corresponds to low solar activity, we observe the effects of a global dust storm on exospheric density and temperature. Moreover, we observe clear density longitudinal variations. Based on earlier work subsequent to observations by the MGS and Mars Odyssey accelerometer experiments near 100-130km, we interpret these features near 250km as non-migrating atmospheric waves.

Chapters 5 and 6 are more technical and present in detail two improvements implemented in the POD program used (GEODYN II, Pavlis et al. [2006]). In Chapter 5, we describe a new algorithm to compute the spacecraft cross-sectional areas entering the calculations of all the non-conservative surface accelerations (solar radiation, albedo and thermal planetary radiation, atmospheric drag). In Chapter 6, we introduce a high-resolution model for the albedo radiation pressure acceleration, made possible by recent albedo data from the Mars Orbiter Laser Altimeter (MOLA) instrument on MGS. Both these models are tested with the MRO spacecraft using real data. In addition, they were used in Chapter 4.

Finally, Chapter 7 gives an overview of the results presented in the Thesis, and discusses possible future directions of research.

1.5 References

Bougher S. W. and R. G. Roble (1991), Comparative terrestrial planet thermospheres: I - Solar cycle variation of global mean temperatures, Journal of Geophysical Research, 96, 11045.

Bougher S. W., C. G. Fesen, E. C. Ridley and R. W. Zurek (1993), Mars mesosphere and thermosphere coupling: Semidiurnal tides, Journal of Geophysical Research, 98(E2), pp. 3281–3295.

Bougher S. W., J. Murphy and R. M. Haberle (1997), Dust storm impacts on the mars upper atmosphere, Advances in Space Research, 19, pp. 1255–1260.

Bougher S. W. and H. Shinagawa (1998), The Mars thermosphere-ionosphere: Predictions for the arrival of Planet-B, Earth, Planets, and Space, 50, pp. 247-257.

Bougher, S. W., S. Engel, R. G.Roble and B. Foster (1999), Comparative terrestrial planet thermospheres 2. Solar cycle variation of global structure and winds at equinox, Journal of Geophysical Research, Volume 104, Issue E7, pp. 16591–16611.

Bougher, S. W., S. Engel, R. G. Roble, and B. Foster (2000), Comparative terrestrial planet thermospheres 3. Solar cycle variation of global structure and winds at solstices, Journal of Geophysical Research, 105(E7), pp. 17669–17692.

Bruinsma S. and F. G. Lemoine (2002), A preliminary semiempirical thermosphere model of Mars: DTM-Mars, Journal of Geophysical Research, 107(E10), 5085.

Forbes J. M. (2000) , Wave Coupling in Terrestrial Planetary Atmospheres, In: Mendillo, M., Nagy, A., Waite, J.H. (Eds.), Atmospheres in the Solar System: Comparative Aeronomy, AGU Geophysical Monograph, 130, Washington, DC.

Forbes J. M. and M. E. Hagan (2000), Diurnal Kelvin wave in the atmosphere of Mars: Towards an understanding of ‘stationary’ density structures observed by the MGS accelerometer, Geophysical Research Letters, 27, pp. 3563–3566.

Forbes J. M., A. F. C. Bridger, S. W. Bougher, M. E. Hagan, J. L. Hollingsworth, G. M. Keating and J. Murphy (2002), Nonmigrating tides in the thermosphere of Mars, Journal of Geophysical Research, 107(E11), 5113.

Forbes, J. M., S. Bruinsma, and F. G. Lemoine (2006), Solar rotation effects in the thermospheres of Mars and Earth, Science, 312, 1366 – 1368.

Forget F., F. Hourdin, R. Fournier, C. Hourdin, O. Talagrand, M. Collins, S. R. Lewis, P. L. Read and J.-P. Huot (1999), Improved general circulation models of the Martian atmosphere from the surface to above 80km, Journal of Geophysical Research, 104, pp. 24155–24175.

Forget, F., E. Millour, F. González-Galindo, A.Spiga, S. R. Lewis, L. Montabone, P. L. Read, M. A. López-Valverde, G. Gilli, M.-C. Desjean, J.-P. Huot and the MCD/GCM development team (2007), The new (version 4.2) Mars Climate Database, Seventh International Conference on Mars, Abstract 3098.

Hong S. S. and R. S. Lindzen (1976), Solar Semidiurnal Tide in the Thermosphere, Journal of the Atmospheric Sciences, 33, pp. 135–153.

Jacchia, L. G. and Slowey, J. (1962), Accurate Drag Determinations for Eight Artificial Satellites; Atmospheric Densities and Temperatures, SAO Special Report, 100.

Kass D. M., D. McCleese, T. Schofield, A. Kleinboehl, R. Zurek, N. Bowles (2007), MCS Views of the 2007 Global Dust Storm, American Astronomical Society, DPS meeting 39, Abstract 17.02.

Konopliv, A. S., C. F. Yoder, E. M. Standish, D.-N. Yuan, and W. L. Sjogren (2006), A Global Solution for the Mars Static and Seasonal Gravity, Mars Orientation, Phobos and Deimos Masses, and Mars Ephemeris, Icarus.

Mazarico E., M. T. Zuber, F. G. Lemoine, and D. E. Smith (2007), Martian exospheric density using Mars Odyssey radio tracking data, Journal of Geophysical Research, 112, E05014, doi:10.1029/2006JE002734.

Pavlis, D. E., S. G. Poulose and J. J. McCarthy (2006), GEODYN operations manuals, contractor report, SGT Inc., Greenbelt, Maryland.

Smith, D. E., M. T. Zuber, S. C. Solomon, R. J. Phillips, J. W. Head, J. B. Garvin, W. B. Banerdt, D. O. Muhleman, G. H. Pettengill, G. A. Neumann, F. G. Lemoine, J. B. Abshire, O. Aharonson, C. D. Brown, S. A. Hauck, A. B. Ivanov, P. J. McGovern, H. J. Zwally, T. C. Duxbury (1999), The global topography of Mars and implications for surface evolution, Science, 284, pp. 1495-1503.

Stewart A. I., C. A. Barth, C. W. Hord and A. L. Lane (1972), Mariner 9 Ultraviolet Spectrometer Experiment: Structure of Mars's Upper Atmosphere, Icarus, 17, pp. 469–474.

Stewart, A. I. F. (1987), Revised time dependent model of the Martian atmosphere for use in orbit lifetime and sustenance studies, Tech. Rep. JPL PO NQ-802429, University of Colorado.

Tracadas P. W., M. T. Zuber, D. E. Smith, and F. G. Lemoine (2001), Density structure of the upper thermosphere of Mars from measurements of air drag on the Mars Global Surveyor spacecraft, Journal of Geophysical Research, 106(E10), pp. 23349–23358.

Wilson R. J. and K. Hamilton (1996), Comprehensive Model Simulation of Thermal Tides in the Martian Atmosphere, Journal of the Atmospheric Sciences, 53, pp. 1290–1326.

Withers P., S. W. Bougher and G. M. Keating (2003), The effects of topographically-controlled thermal tides in the martian upper atmosphere as seen by the MGS accelerometer, Icarus, 164, pp.14–32.

Zurek, R. W. and C. B. Leovy (1981), Thermal tides in the dusty Martian atmosphere: A verification of theory, Science, 213, pp. 437–439.

1.6 Figures

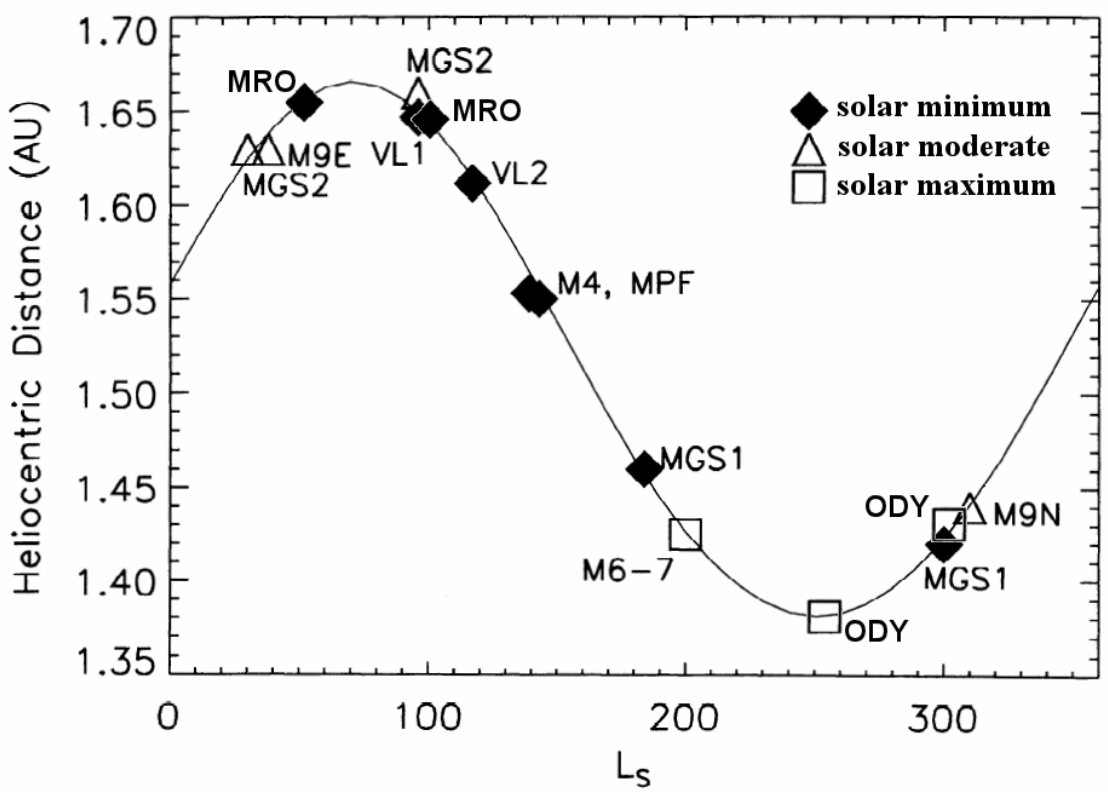

Figure 1.1 Seasonal and solar cycle sampling of the upper atmosphere to date: Mariner 4, 6, 7 and 9 (M4, M6, M7; M9 nominal and extended); the Viking 1 and 2 landers (VL1, VL2); Mars Pathfinder (MPF); Mars Global Surveyor aerobraking phase 1 (MGS1) and phase 2 (MGS2); Mars Odyssey aerobraking (ODY) aerobraking; Mars Reconnaissance Orbiter (MRO) aerobraking. Multiples indicate conditions at beginning (left) and end (right) of mapping. This chart does not include the density measurements inferred from radio tracking data of MGS (several Martian years), Mars Odyssey (Chapter 2 and 3) and MRO (Chapter 4). Mars Express remote sensing observations are also shown. (Figure adapted from Bougher et al. [2000])

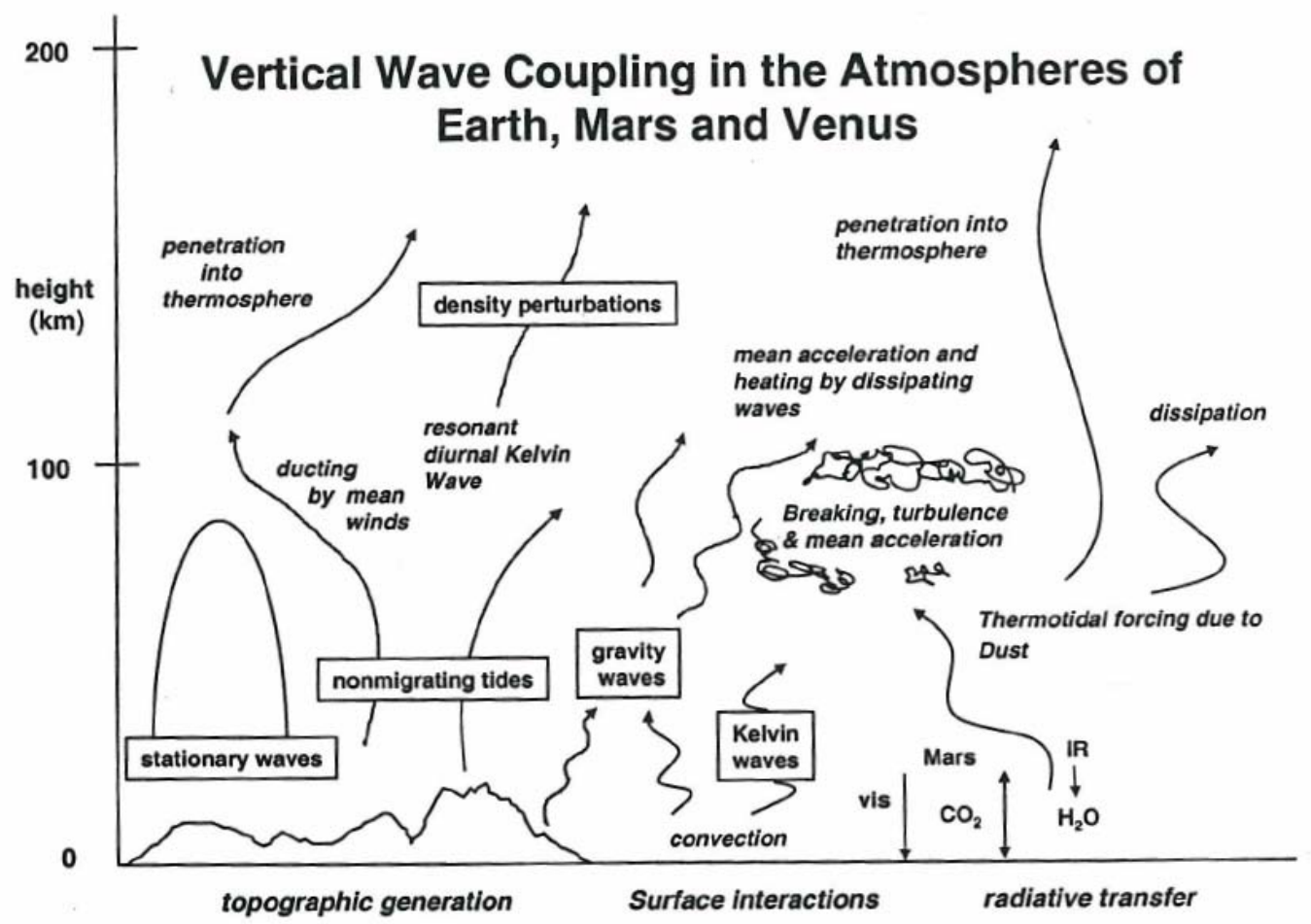

Figure 1.2 The various processes responsible for wave formation and coupling between lower and upper atmosphere of Mars (adapted from Forbes [2000]).

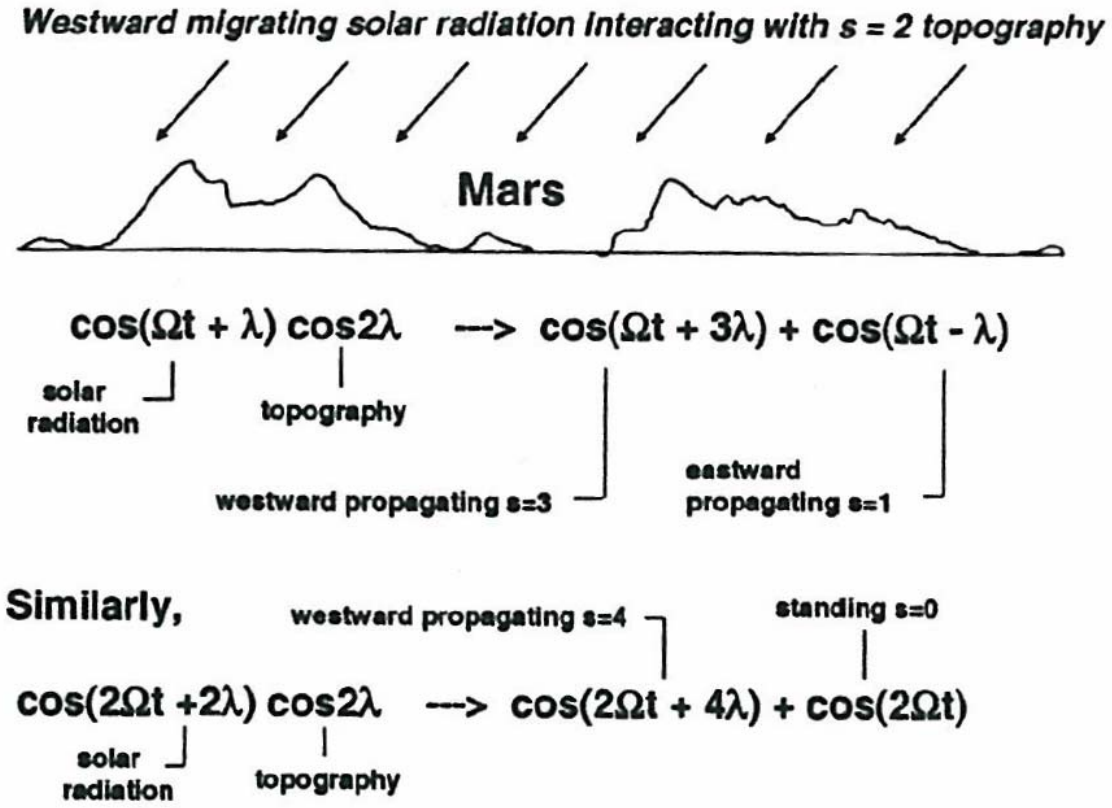

Figure 1.3 Figure from Forbes [2000]: "Schematic illustrating how solar radiation, interacting with topography dominated by zonal wavenumber s = 2 on a rotating planet, generates various wavenumber diurnal and semidiurnal oscillations, which give rise to longitude-dependent ("non-migrating") tidal oscillations".

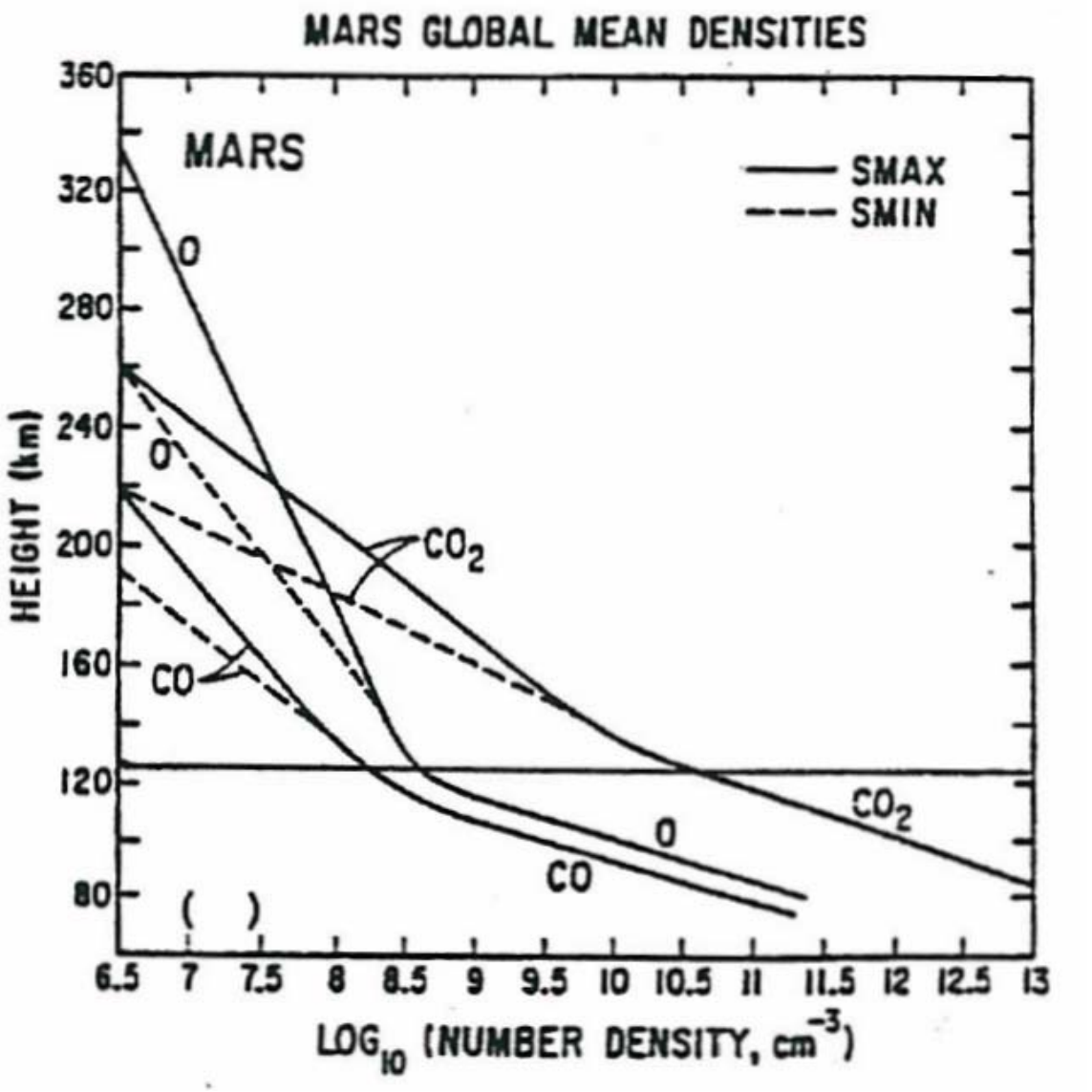

Figure 1.4 One-dimensional global mean density profiles for Mars during solar minimum (SMIN) and solar maximum (SMAX). The horizontal line separates the fully-mixed region (below) from the diffusive separation region. (from Bougher and Roble [1991])

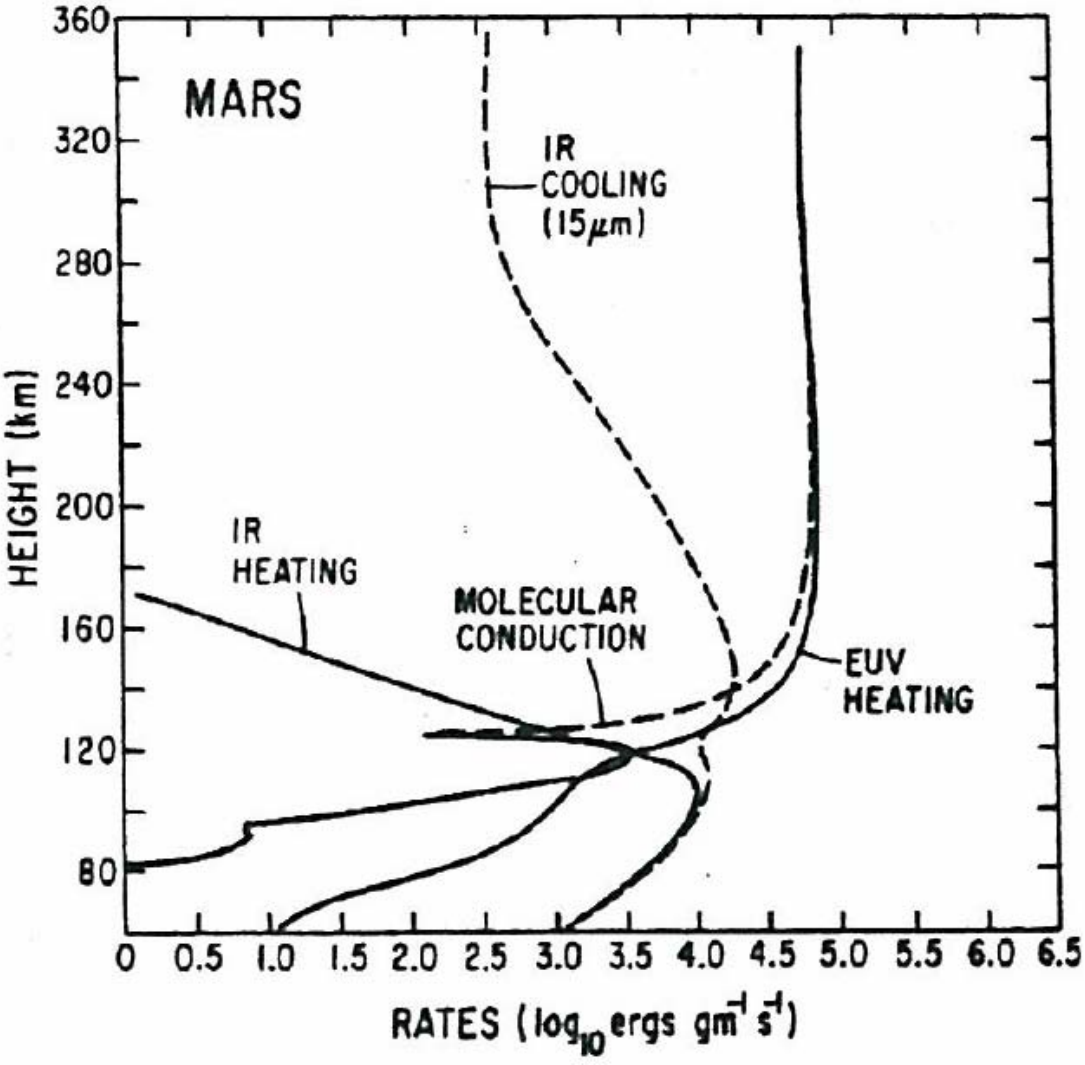

Figure 1.5 Heating and cooling rates in the Martian upper atmosphere (from Bougher and Roble [1991]).

[THIS PAGE INTENTIONALLY LEFT BLANK]

Chapter 2

Martian exospheric density using Mars Odyssey radio tracking data[1]

2.0 Abstract

We present measurements of the density of the Martian atmosphere at ~ 400 km altitude. Our analysis used radio tracking data to perform Precise Orbit Determination on the Mars Odyssey spacecraft between March 2002 and November 2005. Recent improvements in a priori physical models make it possible to isolate the contribution of the atmospheric drag from the various forces acting on the spacecraft. For each spacecraft trajectory segment (arc), we adjusted an atmospheric drag coefficient (C_D), which scales the a priori model density. From the drag coefficient we obtained a time series of the measured density. These measurements at the Mars Odyssey orbiting altitude are close to noise level, and the various tests we conducted show the robustness of the measurements. We obtained a better agreement with the atmospheric model used (Stewart 1987) during the second Martian year, when solar activity is lower. Using various simple exponential atmosphere models, we estimated the scale height near the spacecraft periapsis, and found values between 25 and 50 km, in the lower range of expected values, and used exospheric temperature estimates to assess the role of EUV heating of the upper atmosphere. We did not observe one-to-one correlation between solar activity and exospheric density, but we detected a solar rotation periodicity in our measurements.

[1] This chapter was published in the *Journal of Geophysical Research – Planets*. It appeared in the May 2007 printed issue (Volume 112, Issue E11, pp.5014–+), and its DOI reference is: 10.1029/2006JE002734

Mazarico, E., M. T. Zuber, F. G. Lemoine and D. E. Smith, "Martian exospheric density using Mars Odyssey radio tracking data," *Journal of Geophysical Research*, 112, 5014, 2007.

2.1 Introduction

In this analysis we use measurements of dynamic pressure on the Mars Odyssey spacecraft to recover atmospheric drag during the mission's mapping phase. From the measured drag we determine the density of the Martian upper atmosphere at an altitude of 400 kilometers. From an engineering perspective, drag measurements are important for spacecraft navigation and can become critical for lander entry design. In the upper atmosphere, the short- and long-term density variations due to the solar, seasonal and diurnal cycles and dust storms can be significant. In addition to operational navigation, density measurements at high altitudes can also prove valuable in terms of planetary protection. Additional density measurements at high altitudes can also help define appropriate quarantine orbits, on which to place spacecraft at the end of their mission, to prevent them from colliding with Mars on decadal timescales (Category III missions, NASA Procedural Requirements NPR 8020.12C). Measurements near 400km are essential, given that the current plan for the Mars Global Surveyor quarantine is to raise its orbiting altitude to 405km (Mars Global Surveyor Mission Plan, Section 2.2.5). Scientifically, current atmospheric modeling efforts push General Circulation Models (GCMs) to include increasingly greater portions of the Martian atmosphere (Haberle et al. [1999]; Justus et al. [2002]; Bougher et al. [2004]; Lewis and Barker [2005]; Angelats i Coll et al. [2005]; Bougher et al. [2006]), which approaches the altitude of the measurements presented here. Thus from both scientific and practical standpoints the variability of the atmosphere needs to be better assessed. Radio occultations by Mars Global Surveyor (MGS) have provided several thousands density profiles in the lower atmosphere (Hinson et al. [1999]; Tyler et al. [2001]). Data measurements that can be used as upper boundary conditions for GCMs are critical but sparse below 200 km, and almost nonexistent above. Important data has been acquired by accelerometers during the aerobraking phases of MGS and Mars Odyssey, at lower altitudes (100-170 km,

Keating et al. [1998]; Tolson et al. [2005]; Withers et al. [2003]; Withers [2006]). Measurements below 220 km are also possible with remote sensing techniques (limb scanning, air glow, electron reflectometry, stellar occultations). As noted by Bruinsma and Lemoine [2002], drag measurements by Mars Odyssey made at 400 km can be valuable for a better understanding of the Martian thermosphere, as a complement to existing datasets. In this work, we retrieve atmospheric densities at the orbital altitude of Mars Odyssey, using X band radio tracking data and Precision Orbit Determination (POD thereafter). This has been done extensively with Earth-orbiting satellites (e.g., Jacchia and Slowey [1962]), and more recently by Konopliv et al. [2006] and Forbes et al. [2006] for Mars. After introducing the data and methods used to estimate the density (Section 2.2), we present the analysis of the tracking data (Section 2.3), the results and their significance (Section 2.4) for Martian atmosphere structure.

2.2 Data and Methods

The Mars Odyssey spacecraft was launched in April 2001 and performed its insertion maneuver into Mars orbit October of that year. As for the earlier Mars Global Surveyor mission, Mars Odyssey underwent a period of aerobraking (Mase et al. [2005]; Smith and Bell [2005]; Tolson et al. [2005]; Withers [2006]) to transform its initial polar, elliptical orbit to a circular mapping orbit at an altitude of ≈ 400 km. The spacecraft advantageously used the atmospheric drag near the periapsis (≈110 km) of its initial elliptical orbit to remove energy from the orbit and progressively decrease the apoapsis. Odyssey's aerobraking phase was completed on February 19, 2002, and science operations began shortly thereafter. Here, we use the available radio-tracking dataset during the nominal mission (March 2002 to August 2004) and extended mission (August 2004 to November 2005), i.e. about 2 Martian years total.

2.2.1 Mars Odyssey Orbit

Mars Odyssey has an orbit quite similar to Mars Global Surveyor: a retrograde polar orbit (i ≈ 93.1°) with a semi-major axis corresponding to a mean altitude near 400 km and an orbital period of just under 2 hours (≈118 minutes). With this inclination and an appropriate phasing, the orbit is nearly sun synchronous (fixed equator-crossing time), which allows for good solar energy input (the eclipse duration never exceeds 25% of the orbit). Although Odyssey's orbit is nearly circular, its eccentricity oscillates between 0 and 0.013 (average of ≈0.008) with a period of ≈74days (Pace et al. [2000]). The altitude of the spacecraft varies between 390 and 450km.

The Mars Odyssey orbit is ‘frozen’ (Cutting et al. [1978]), such that the periapsis is always located above the South Polar region, near 85°S. But contrary to MGS, the afternoon Local Mean Solar Time (LMST) drifted, from ≈4am/pm to ≈5am/pm between January 2002 and October 2003 (Mase et al. [2005], Figure 1). A maneuver on October 20, 2003 stabilized the LMST at 5am/pm and put Odyssey into its sun-synchronous configuration. Nevertheless, due to the eccentricity of Mars' heliocentric orbit, the Local True Solar Time (LTST) continued varying between ≈4pm and ≈6pm.

Odyssey's orbit experiences more significant changes in the sun beta angle ($\beta\odot$) than did MGS (Figure 2.1). $\beta_{\odot}$ is the angular separation between the Sun-Mars line and the orbit plane.

2.2.2 Radio Tracking Data

The radio signals received (uplink) and transmitted (downlink) by the Mars Odyssey Telecommunication system have frequencies at X band (7.2 GHz uplink, 8.4 GHz downlink).

In addition to a fully redundant electronics subsystem, the 1.3-m-diameter

parabolic high-gain antenna (HGA) is supplemented by a medium-gain antenna (MGA) and a low-gain antenna (LGA). When the spacecraft is in safemode, the LGA is used for reception (because of its large beamwidth) and the MGA for transmission. (There were two instances of safemode over the course of the primary science mission: 3 days in November 2002, 8 days in November 2003).

The HGA is mounted on a two-gimbal articulated arm, which enables it to point over a large solid angle. This permits nearly continuous tracking by the Deep Space Network (DSN, with stations in Goldstone, California; Canberra, Australia; Madrid, Spain) while maintaining a nominal spacecraft attitude and operating the science instruments.

The DSN ground stations act as very accurate and stable frequency sources which the spacecraft can use to generate the downlink radio signals. A frequency carrier can be generated onboard by an oscillator (SSO, Sufficiently Stable Oscillator), but its quality (i.e., stability) is poor compared to the USO (Ultra Stable Oscillator) onboard MGS and the Hydrogen-Maser clocks in the DSN facilities. The stability of the latter is of the order of 1 part in 10^{16} over a few hours. The radio signals generated with the SSO would not be appropriate for POD. The ratio of received and transmitted frequencies was chosen as a rational number (749/880), so that electronic frequency multipliers can generate the outgoing radio signal from the frequency of the incoming electromagnetic wave, enabling high-quality X-band tracking of Mars Odyssey. Although the frequencies used by MGS are slightly different, the uplink/downlink ratio is the same and the telecommunication subsystem is very similar to the one described by Tyler et al. [1992].

Two different types of measurements can be carried out to provide radio-tracking data to be used for the POD. The Doppler shift of the signal frequency is related to the relative velocity of the spacecraft in the line-of-sight. The high stability of the frequency source enables the measurement of line-of-sight velocity changes of the order of 10μm/s. 1-way (spacecraft to station) radio signals are not used to perform the POD because of the SSO. However, with the ‘turn-around’ capability,

2-way (station to spacecraft and back to the same station) and 3-way (station to spacecraft and back to a different station) 'Doppler measurements' are of good quality. Moreover, the frequency shift is averaged over 10 seconds to increase the signal-to-noise ratio. The travel time of the electromagnetic waves puts a constraint on the position of the spacecraft. Due to the fact that transmitted radio signals have a wavelength much shorter than the actual range to be measured, and that only the phase of the received signal can be measured, a series of square waves of decreasing frequency is transmitted. As a result, 'Range measurements' are sparser than the Doppler ones. The dataset of this study comprises of ≈ 3,500,000 Doppler and ≈ 155,000 Range observations.

2.2.3 Precision Orbit Determination

2.2.3.1 Force and Measurements Modeling

We used the software package GEODYN (Pavlis et al. [2006]) to process the radio-tracking data of Mars Odyssey over short trajectory segments (called 'arcs'). Arc duration is determined primarily by the data coverage, but is usually about 5 days (Lemoine [1992]). The spacecraft motion is integrated in a Cartesian frame from an initial state with a fixed-integration-step using a high-order Cowell predictor-corrector method. The initial state and various model parameters are adjusted by a Bayesian least-squares scheme until convergence is deemed satisfactory (typically a change in RMS, root-mean squares, smaller than 2% compared to the previous iteration). This is done using a number of physical models for the forces acting on the spacecraft and the corrections to apply to the radio observations.

The physical models included in GEODYN are the following:

- third-body gravitational perturbations, with ephemerides DE410 from JPL (Sun, planets, Moon) and Jacobson et al. [1989] (Phobos and Deimos).

DE410 is a successor model to DE403 (Standish et al. [1995]). It includes recent Mars orbiter data range and delta differential one-way range (D-DOR) data, which significantly improves the Mars ephemerides modeling;

- gravitational acceleration due to Mars – calculated from a high-resolution spherical harmonic expansion of the gravity field. We use the GSFC solution 'mgm1041c', calculated from MGS radio tracking data only (Lemoine et al. [2003]).
- relativity modeling in the force model (modification of the Mars central body term) and in the measurement model (for light time and range corrections, combined with the ephemerides);
- the Mars solid tide, which is explicitly modeled in the spacecraft acceleration calculation. We use the value of the tidal Love number k_2 of 0.055 (Smith et al. [2001]). More recent published values are in the range 0.153-0.163 (Yoder et al. [2003]; Smith et al. [2003]). However, due to Mars Odyssey nearly constant LMST, variations in the tidal force are expected to be small.
- DSN ground station position corrections due to solid tides and ocean loading;
- corrections to the radio signal due to its propagation through the troposphere, dependent on local weather;
- surface forces: radiation pressure (direct, reflected and planetary thermal) and atmospheric drag.

The reflected and thermal radiation forces are calculated using low-order zonal spherical harmonic expansions of seasonally-varying Martian albedo and emissivity maps (Lemoine [1992]). The atmospheric density model used is discussed in a later section (Section 2.4.1).

For radiation and atmospheric drag forces, cross-sectional areas of the spacecraft need to be calculated. We use a macromodel to represent the spacecraft (Marshall

and Luthcke [1994]), that consists of 10 plates with specific surface areas, orientations, and diffuse and specular reflectivities (6 for the spacecraft bus, 2 for the front/back of the HGA, 2 for the front/back of the solar panel).

The plates are oriented in inertial space according to the telemetered quaternions. During short telemetry data gaps, the orientation is interpolated, and a attitude model is used for longer gaps. The total surface acceleration is computed by summing the contributions of each plate from the source vector. For the atmospheric drag and direct solar radiation pressure, the source vectors are, respectively, the along-track and Sun directions. For the reflected and planetary thermal radiation pressures, the visible Martian surface is broken into multiple sources (Lemoine [1992]). GEODYN does not account for self-shadowing and radiation of the modeled plates. While the instantaneous self-shadowed area can reach as much as ≈10% of the total, its phasing with respect to the orbit perihelion (and maximum velocity) leads to only a ≈3 - 4% misestimate over a full orbit. The POD-adjusted drag coefficients can be modified a posteriori to account for this effect.

The attitude of the spacecraft is controlled using three momentum wheels. If spun appropriately, the whole spacecraft can point in the desired direction by simple conservation of angular momentum. These wheels need to be slowed down when they are rotating too fast. The non-symmetrical spacecraft configuration, with only one large solar panel and a telescopic boom for the GRS sensor, can also lead to perturbations to the spacecraft attitude that need to be corrected. Small thrusters are fired while despinning the wheels in order to keep the spacecraft fixed. The number of attitude thruster firings is generally low (about 1 per day), but as a desaturation maneuver is never perfectly decoupled (balanced), it results in a small acceleration and torque imparted to the spacecraft. Due to the low level of the atmospheric drag acceleration, it is necessary to estimate these ‘Angular Momentum Desaturation’ (AMD) accelerations to prevent contamination of our results.

2.2.3.2 Method

The ≈ 4 years of radio-tracking data we processed were divided into 235 trajectory arcs. The arc length is the result of a trade-off between having enough observations in order to have a stable and sensitive convergence while avoiding the accumulation of force model errors. Following Lemoine [1992], we favored an average length of ≈ 5 days. The exact start and stop times were chosen based on AMD timings and data coverage, and the actual arcs are 3 to 7 days long. Inasmuch as possible, we did not include extended periods where AMD accelerations had to be estimated without tracking data.

Among the various parameters adjusted by GEODYN, the drag coefficient (C_D) is the most critical in this study. It is an unconstrained scale factor of the atmospheric drag force adjusted to best fit the observations, and our density measurements depend directly on it (Section 2.2.4). Short arcs (one station pass, i.e. a few hours) and arcs with large data gaps lead to poor estimates and low signal-to-noise ratio. To stabilize the recovered C_D values, we chose to nominally adjust it only once per arc, even though it entails poor temporal resolution of our measurements. Indeed, if adjusted too frequently, non-atmospheric perturbations are likely to perturb the adjustment of C_D, which would result in erroneous results. In other (gravity-oriented) studies, C_D is usually evaluated more often, sometimes once per orbit, but in such a case it is often viewed as a way to account for mismodeled accelerations and not necessarily atmospheric drag. As shown later, we obtain robust results and rather little contamination from other perturbations. Indeed, although the level of atmospheric drag is usually much smaller than both the direct solar and albedo radiation pressures, it is only acting along-track, and is of comparable magnitude with the along-track components of the other non-conservative forces (the albedo radiation is mostly radial, and the direct solar radiation is typically radial and cross-track). This makes its estimation by POD

possible. As presented in Section 2.3 and 2.4, we obtain a consistent time series of drag coefficients and densities, although we are probably close to noise level.

2.2.3.3 Density Measurements from Mars Odyssey POD

The atmospheric drag acceleration implemented in GEODYN is:

$$a_{drag} = \frac{1}{2}\frac{\rho C_D V^2}{m}\sum_i A_i \vec{n}_i . \vec{n}_V$$

where V is the spacecraft velocity, n_V the along-track vector, A_i and n_i the surface area and normal vector of the macromodel plates facing n_V (i.e., whose angle with n_V is less than 90°) and m the mass of the spacecraft. The lateral wind and aerodynamic lift are not taken into account. The C_D factor in the equation above, commonly referred to as the 'drag coefficient', is the parameter adjusted by GEODYN. It does not only represent the aerodynamic drag coefficient of the spacecraft, but is also used to scale the model atmospheric density to achieve best-fit of the tracking observations:

$$\rho_{measured} = \frac{C_D}{C_C^{real}}\rho_{Stewart}$$

where C_D^{real} is the spacecraft aerodynamic drag coefficient. Given the hypersonic free-molecular flow regime of Mars Odyssey, C_D^{real} is close to 2.1 (calculated computationally by Takashima and Wilmoth [2002] with 2.9% uncertainty; also comparable to the value for MGS of 2.13 from Wilmoth et al. [1999]).

Thus, the drag coefficients obtained in Section 2.3.2 are not a direct scale factor of the model density: the measured density is the model density when C_D is equal to C_D^{real}, not 1. A change in C_D does not necessarily translate to a density variation.

2.3 Analysis of the tracking data

2.3.1 Convergence of orbital arcs

Within an orbital arc, a large number of orbits are poorly or not tracked, and regular desaturation maneuvers need to be evaluated. With arcs several days in length, the mean trajectory of the spacecraft can be well constrained. The initial state of the spacecraft was determined with formal relative standard deviations near 10^{-7}, which correspond respectively for position and velocity to better than 1m and 1mm/s, except for a small number of arcs in 2004. These formal uncertainties are commensurate with the a priori data weights used, which are based on the quality of the tracking (we chose 1m and 1mm/s for the Range and Doppler measurements respectively).

In addition to reducing the coverage (when viewed edge-on, the spacecraft is behind Mars half of the time), the observation geometry can worsen the quality of the Doppler measurements (when viewed face-on, the velocity vector has no line-of-sight component). Figure 2.2 presents the quality of the arc initial state determination (relative standard deviation) in terms of the major osculating orbital elements. The determinations are generally better than 1 part per million for the eccentricity and orders of magnitude less for the semi-major axis. We can also observe the negative correlation between the determination of the inclination *i* and that of *a* and *e* (respectively, semi-major axis and eccentricity): an edge-on geometry of the orbit when viewed from the Earth is more favorable for the estimation of *a* and *e*, whereas *i* is better constrained when the spacecraft trajectory is seen face-on.

The RMS of the Doppler and range residuals (differences between actual observations and model predictions after convergence of the arc) are of the order of 0.3 mm/s and 3 m, respectively (Figure 2.3). A few arcs show larger values, but that does not imply they are poorly constrained (Figure 2.2). During periods of

solar conjunction, the number of range measurements decreases significantly, dropping to zero near conjunction. The quality of the data is also affected and the POD is noisier, due in part to mismodeled signal distortion by solar plasma (near $DOY_{2002} \approx 220$ and $DOY_{2002} \approx 980$).

2.3.2 Drag Coefficient

Figure 2.4 shows the time series of the C_D and C_R coefficients estimated for each arc. For each arc, the C_D and C_R are unconstrained and adjusted, with other parameters, to achieve best-fit to the radio tracking observations. A small number of drag coefficients adjust to negative or anomalously high values. Those were discarded as non-physical, and are mostly due to poor adjustment by GEODYN because of large data gaps. The adjustments are totally independent from arc to arc, but clear trends are visible in both curves.

There is a high temporal correlation in our C_D estimates: a trend is clearly visible in arc-to-arc values. The few data points that fall far from that trend were removed at this point. We think that the consistency in the independently-adjusted C_D stems from a real signal, indicative of atmospheric changes. Indeed, formal C_D standard deviations are usually around 1% of the adjusted value, but increase to about 10% near $DOY_{2002} \approx 950$. The real uncertainties in the retrieved densities are difficult to assess, but given the robustness of the drag coefficient adjustments in both long and short arcs (Section 2.3.2.4), we believe that uncertainties about five times the formal ones would be reasonable.

2.3.2.1 C_R trend

An unconstrained scaling factor for the solar radiation pressure acceleration (C_R) was also adjusted by GEODYN. Its value is expected to be near unity because the solar flux is a constant once the eccentricity of Mars orbit has been taken into

consideration. But some mismodeled or unmodeled nonconservative forces (approximate surface properties, no interplate reradiation, no spacecraft thermal emission) are expected to be absorbed in the C_R estimate.

The adjusted C_R coefficients for Mars Odyssey show remarkable temporal consistency (Figure 2.4), with values close to unity, but follow a trend strongly correlated to the $\beta_\odot$ angle (Section 2.2.1, Figure 2.1). We have no definitive explanation for this trend, and as mentioned above, given our imperfect modeling of the non-conservative forces we do not expect to obtain a perfectly flat C_R time series. While the dependence of our recovered C_R on a parameter linked to the orbit geometry is troublesome because of its potential implications on our C_D results, we present below the results of robustness tests conducted to establish the independence of C_D and C_R and the robustness of the obtained C_D coefficients.

2.3.2.2 C_R=1 test

We did reprocess the whole dataset while fixing the C_R coefficient to 1. Given that the solar radiation acceleration is more than one order of magnitude larger than the atmospheric drag, this constraint imposes a relatively large acceleration to be adjusted in different ways by GEODYN (among others, the initial state and the C_D coefficient).

The changes induced in C_D (in percent) are presented in Figure 2.5. These can be large, and show that large forced changes in C_R impact the recovered C_D coefficient. However, it is important to note that in the time series of the magnitude of these changes, the earlier C_R / $\beta_\odot$ trend has disappeared. The angle between the solar radiation and atmospheric drag accelerations is, on average, $\beta\odot$. But both the large variations in $\beta_\odot$ and in the magnitude of the acceleration (scaled by C_R–1, almost always positive, meaning that the forcing is always in the same direction relative to the orbit and the drag) are not visible in the C_D changes (Figure 2.5), which cluster nearly randomly around a small mean (– 4%). In

addition, we note that the Doppler RMS generally increases by more than 20%, and is sometimes doubled. Thus, the mismodeled force responsible for the C_R trend cannot be accounted by a change in C_D when forced to, but only leads to poorer convergence when we fix C_R to 1.

This leads us to think that the unexplained and anomalous acceleration that contaminates C_R has no atmospheric origin; and that the large changes observed in C_D are the result of forcing GEODYN to account for that acceleration solely in the form of atmospheric drag. These changes, about 30% on average, may represent upper bounds on the uncertainties in C_D due to physical mismodelling. In addition, the formal covariance between C_D and C_R established by GEODYN within each arc is small, less than 10 percent, compared to values close to one when a correlation is expected (e.g., Cartesian components of the initial velocity or position of the spacecraft).

It is very unrealistic not to adjust the radiation coefficient, because of modeling uncertainties, and it is usually not done in practice. Thus, in order not to overconstrain the solution and to be able to distinguish between bad C_D estimates and artificial contamination due to fixed C_R, the following results are for unconstrained C_R coefficients. Constraining C_R also leads to significant increases in RMS.

2.3.2.3 Comparison with C_D obtained from another set of arcs

In Section 2.2.3, we mentioned that the arcs were created based on data coverage and thruster firing timings. Because of the very low level of drag acceleration that we need to discriminate, we evaluated the influence of our choice of arcs on the obtained values. The objective is to show that the frequent data gaps and the regular AMD estimates do not significantly influence the recovery of the C_D and C_R.

The arc lengths are different so the number of AMDs and gaps are different. The new arcs are not as 'good' as our primary choice, and sometimes include relatively long periods at the beginning of the arcs without data. The new C_D and C_R values are shown in Figure 2.6. The trend is unchanged, and the changes are of the same order of what could be expected from arc-to-arc atmospheric variability alone (about 50%; Figure 2.6, open symbols). In addition, the adjusted C_D values are closer when the arc overlap is more significant. The same is observed for the radiation coefficient C_R. We note that C_R is not as sensitive to the change in arc length as C_D, mainly because the solar radiation is a stronger acceleration, easier for GEODYN to adjust as it affects the overall convergence.

Thus, the contamination of our results due to arc length, epoch time and AMD acceleration estimation seems to be limited to an average ~20% in C_D. This indicates that the results are largely independent of the manner in which we chose the initial orbital arcs and provides additional support for the conclusion that the retrieved C_D values are representative of actual changes in atmospheric density.

2.3.2.4 Comparison with daily C_D coefficients

Our general ability to properly estimate the atmospheric density scale factor with GEODYN was assessed by increasing the temporal resolution and evaluating the stability of the recovered drag coefficients. We estimated C_D once per day instead of once per arc (i.e., 3 to 7 days). Due to data gaps inside the arcs, a non-negligible number of 1-day intervals were insufficiently constrained and resulted in anomalous coefficients (≈ 15% of the total number) that we discarded. Indeed, with large data gaps in a 24-h period, the drag acceleration adjustment is less constrained and is more subject to contamination by mismodeled forces. Nevertheless, the majority of coefficients fell within the range of C_D adjusted previously (Figure 2.7), and thus may represent actual atmospheric variability.

Here arc convergence is not affected, and the radiation coefficients unchanged. We tried reducing the adjustment intervals to values comparable to the orbital period (≈ 2 h), but that resulted in nearly random coefficients.

We used these more frequent drag coefficient estimates in order to estimate the intrinsic density variability (which can also be seen as an uncertainty) of our ≈ 5-day-averaged recovery. For each arc, we estimated the standard deviation of the daily estimates with respect to the C_D obtained over the entire arc (Figure 2.7, bottom). The observed variability is not due to computational issues. Indeed, in general, the variability within the long 5-day arcs is about 10%, although values below 50% are common (but do not seem correlated to either geometry or seasons), well above the level of uncertainties in the C_D values.

2.3.2.5 Periodicity within the C_D time series

We also checked for periodicities in the C_D time series, in order to detect the signature of the solar rotation in our measurements. That signature, in density, has been observed both on the Earth (with CHAMP) and on Mars (with MGS) by Forbes et al. [2006].

We expect to see that signature in the C_Ds as well, because they are adjusted from the Stewart model, which uses an 81-day averaging of actual solar flux (therefore removing the solar rotation periodicity from the model estimation; see Section 2.4.1 below). As noted by Withers and Mendillo [2005], due to the difference in the planets' orbital periods, the observed solar rotation seen from Mars should have a 26 day periodicity rather than 27 days observed on Earth.

We performed this analysis on drag coefficient residuals (actual C_D – C_D smoothed over 26 days). We used the daily estimates rather than the arc-long values whose 5 – 7 day sampling is not appropriate to detect a ≈ 26 day period.

The uneven sampling of the time series (which depends on the arcs themselves, i.e. data coverage) renders the use of an FFT problematic. By interpolating the

data at a frequency of a fraction of a day, we could obtain a power spectrum (Figure 2.8a), but it is hard to say whether it was contaminated by interpolation artifacts. Nevertheless, the most significant frequency seems to be ≈ 26 days, close to the solar rotation period.

To answer this issue of uneven sampling, we used Lomb's method (Lomb [1976]). We obtain a single significant frequency of ≈ 25.2 days (at 98.5% confidence) (Figure 2.8b, 2.8c). While this period is a lower than the expected solar rotation period, such a strong frequency in our data suggests we detect the effects of the solar input on Mars atmosphere.

This analysis demonstrates that our measure of the atmospheric drag obtained from the Mars Odyssey represents actual changes in the atmospheric density at the spacecraft altitude. In the next section, we discuss these results regarding the atmospheric structure near 400km. The atmospheric signal in the processed MGS tracking data (Forbes et al. [2006]) was very faint. Given the altitude difference (≈ 20km), the densities sampled by Mars Odyssey are 2 – 3 times smaller, and the Mars Odyssey atmospheric signal is closer to the noise level. Thus, the reader should keep in mind that even after much care in the processing of the tracking data with the state-of-the-art GEODYN program, not all the features we could expect can be observed in the obtained time series.

2.4 Atmospheric Results

2.4.1 Exosphere, Stewart model

With a mean altitude near 400 km, the spacecraft is in the heterosphere, where diffusion is the main transport process: air molecules do not interact much by collisions, and follow ballistic, orbital or escape trajectories. The distribution with altitude of each atmospheric species follows its specific photochemistry. This is in

contrast with the homosphere below, where all the species follow the same transport laws (collision), and the mixing ratios can be considered constant. The boundary between these two layers varies between 115 and 130-km altitude with the seasons and the solar activity (Stewart [1987], Bougher et al. [2000]). In the heterosphere, the temperature increases with altitude asymptotically up to a maximum value (the exospheric temperature) determined by the solar activity. The upper part of the heterosphere (above ≈ 250km for Mars) is called the exosphere, because light particles (mainly atomic hydrogen) can escape (Chassefière and LeBlanc [2004]). The heating of the exosphere by solar radiation is largely due to the EUV (Extreme UV) radiation. However, the radiation at 10.7cm wavelength, characterized by the $F_{10.7}$ index, has historically been used in atmospheric modeling. Indeed, both radiations originate from the same region of the Sun atmosphere (and show a good correlation) and the 10.7cm radiation can be readily measured on the ground (at the Penticton site in Canada).

The numerical value used for $F_{10.7}$ is actually an average over 3 solar rotations of the daily values. The main reason for doing this is that the $F_{10.7}$ index is measured on Earth, and depending on the Earth-Sun-Mars geometry the instantaneous value may not be relevant to the radiation environment on Mars.

The heterosphere itself can be subdivided into a thermosphere and an exosphere. In the exosphere where the Mars Odyssey spacecraft orbits during its science mission, molecules can escape the atmosphere (atomic H mainly through Jeans escape, Chassefière and LeBlanc [2004]), and light gases become significant. From the model presented below, in terms of number density, the major components near 400 km and for average conditions are He, H_2, H and O (Stewart [1987], Krasnopolsky [2002]). In terms of mass density, which is more relevant to the current study, the main contributors are O, He, N_2 and CO.

The atmospheric model used in GEODYN during POD is based on Stewart's thermospheric model (Stewart [1987]), with modifications (Lemoine et al. [2001]). The turbopause altitude is calculated using an empirical formula; the reference

6.1mbar altitude is corrected for time-dependent effects (seasonal global pressure variation, seasonal dust opacity variations of an average year); the solar activity ($F_{10.7}$) sets the exospheric temperature. L_S is the areocentric longitude of the Sun, used to refer to the Martian seasons; it varies between 0 and 360°. By convention, the first Mars year (MY) began on 11 April 1955, so the Mars Odyssey data used here is from late MY-25 to late MY-27.

The model atmospheric density can vary by nearly two orders of magnitude due to solar activity. The impact of the seasonal cycle is not as significant, and may be due largely to the varying heliocentric distance modulating the solar input in the atmosphere. With varying solar activity (heating from EUV photons), the temperature of the exosphere varies, and in turn the relative contribution of various atmospheric species is modified.

The Stewart model is based on scarce data near solar minimum; the main constraints on the atmospheric structure are the atmospheric composition profiles acquired by the mass spectrometers on the two Viking landers (Nier and McElroy [1977]). Mars Odyssey orbits at local solar times near 3 – 5 am/pm, where the atmospheric structure can differ from the global average. But most of the calculated partial densities are global mean values, although the atomic oxygen density does have a dependency on solar time. The exospheric temperature dependence on solar activity ($F_{10.7}$) is extrapolated from measurements at low solar activity ($F_{10.7}$<60 at Mars) using a linear regression.

Using a simple random error approach, we quantified the magnitude of the uncertainties in the model density. We first calculated its sensitivity to small variations in relevant (controlling) parameters for a range of L_S and $F_{10.7}$ indices. Using estimates of the uncertainties or intrinsic variations of these parameters (5% uncertainty in $F_{10.7}$, 10% for most of the other parameters), we obtained an overall density uncertainty (Figure 2.9). The solar activity, through $F_{10.7}$ and the exospheric temperature, is the main contributor (Stewart [1987]). However, in terms of seasonal and solar effects, the Stewart model exhibits large differences

when compared to more recent models, such as Mars-GRAM (Section 2.4.3).

2.4.2 Effective atmospheric sampling

As explained in Section 2.2.3.2, the temporal resolution of our measurements is of the order of several days, which prevents the precise study of short-lived phenomena. During one arc, the spacecraft orbits the planet several tens of times, so that no longitudinal localization of the measured density is possible. In addition, with the small amplitude of altitude variations (low eccentricity), the whole orbit contributes to the measured density. This globally averaged measurement is weighted towards the southern latitudes, due to Mars Odyssey's periapsis being located at ≈ 85°S. The flattening of the planet tends to extend the part of the orbit with largest atmosphere densities and drag force. The actual atmospheric drag is the density weighted by the square of the velocity of the spacecraft, which amplifies the simple altitude effect. We can calculate the effective density sampled by the spacecraft. However, we chose to present a density time series referenced to an altitude of 400km over the South Pole, for two reasons. First, over the course of the mapping mission, Mars Odyssey orbital parameters experience slight perturbations, undermining the direct interpretation of a time series of the effective sampled density. Second, that time series is actually very similar to a time series of the density above the South Pole, except for an offset due to the altitude difference.

It is also important to recall that the local solar time of the spacecraft is almost fixed and that we cannot separate the thermal tide effect from the mean density signal. The results presented here are indicative of the density in the spacecraft environment and not of an average density over the whole southern hemisphere.

The measurements are thus more suitable for the general monitoring of the atmospheric density at the spacecraft orbital altitude, and would not be appropriate for studies of the dynamics of the exosphere or small-scale structures.

2.4.3 Comparison of the results to the model

As shown on Figure 2.9, the measured densities are usually smaller than the model predictions. During the first Mars year of measurements (i.e. $DOY_{2002}<800$) the discrepancy is larger than what could be expected from model uncertainties calculated previously, arguing for erroneous modeling in that time period. In the second Mars year, the agreement is more satisfying, with differences generally of the order of ≈ 2 compared to up to an order of magnitude earlier.

In Section 2.4.1, we noted that the solar activity effects on density in the Stewart model is based on a fit from measurements near solar minimum. With a solar minimum in late 2006, the better agreement between model and measurements during the second half of the time series might not be surprising. The definite discrepancy observed in 2002-2003 might be due to mismodeling at higher solar activity. On Figure 2.9, we also plotted the density predictions by the Stewart 1987 model and the more recent Mars-GRAM 20012 (Justus and Johnson [2001]), with $F_{10.7}$ held constant at values representative of low, moderate and high solar activity. The two models display very different behavior with respect to solar and seasonal forcing. The density from the Stewart model is enhanced by a factor of $\approx$ 60 between solar minimum and solar maximum, whereas Mars-GRAM 2001 only shows a maximum fourfold increase. On the other hand, for a fixed $F_{10.7}$, the seasonal density variations are much larger in the Mars-GRAM model. Our density measurements are in general bounded by the predictions of both models.

The importance of solar input on the atmospheric density is illustrated in Figure 2.10, which plots the density versus L_S (season). Between $DOY_{2002} \approx 100$ and $DOY_{2002} \approx 800$ (MY-26), the $F_{10.7}$ index at Earth is moderate to high, with values between 100 and 200; it then slowly decreases to ≈ 80 near $DOY_{2002} \approx 1400$ (end

[2] Mars-GRAM models have not been integrated into GEODYN due to ITAR regulations on Mars-GRAM which would seriously restrict the distribution of GEODYN, in particular to its numerous foreign users.

of MY-27). The density differences between the two Martian years are more significant during the 0 – 180° period, where the contrast in $F_{10.7}$ from year to year is larger. In the second part, 180 – 360°, where solar activity levels in both Mars years are comparable, the measured densities show less variation.

During MY-27, Figures 2.9 and 2.10 also show that the measured seasonal density contrast is more than one order of magnitude. This is larger than the predictions from Stewart (for all $F_{10.7}$), but close to Mars-GRAM 2001 with moderate or low solar activity.

Even though our measurements do not agree completely with either model, it is interesting to see that our results concur with some aspects of each. Also, we find our results in better general agreement with Mars-GRAM 2001, more recent and based on more data (especially concerning light neutral gases which are major contributors in that part of the exosphere).

Because no global dust storm occurred during the timeframe of our measurements (the last having taken place in 2001, mid-MY-25), we could not conclude on correlation between dust opacity and exospheric density levels.

2.4.4 Scale Height estimates

The single coefficient adjusted by GEODYN to recover the density is not sufficient to obtain estimates of the atmospheric scale height at the spacecraft altitude. It adjusts an ‘average density’, resulting from the integrated atmospheric drag over a period of several days. The atmospheric structure assumed by the Stewart model enters the result, but does not put any constraint on the real atmosphere: the adjusted C_D has the value that best fits the observations, i.e., that minimizes the misrepresentation of the atmosphere by the model.

Nevertheless, analytical work (King-Hele [1987]) provides a way to estimate the scale height near the orbit periapsis, if we assume the atmosphere can be locally represented as a simple exponential atmosphere (a reasonable assumption for our

study). King-Hele showed that the density at a half-scale height above the periapsis altitude is largely insensitive to misestimates in the scale height H. An error of 25% produces a 1% density change at that altitude, and a 50% error a 3% change. Therefore, an estimate of the scale height can be obtained from the altitude of intersection of adjusted simple exponential profiles. Martian exospheric models predict a large range of scale heights near 400 km, between 30 and 90 km depending on the time of year (Culp and Stewart [1984]; Stewart [1987]; Justus et al. [2002]).

We reprocessed the whole Mars Odyssey dataset using simple exponential density models characterized by respective scale heights 30, 50, 70 and 90 km. The arcs using these various models are equivalent in terms of convergence and residual RMS, so that we average the scale heights obtained from the intersection of model pairs.

The values obtained are robust and consistent, which indicates that the assumption of an exponential isothermal atmosphere is reasonable. The scale heights are mostly between 25 and 45 km (Figure 2.11), in the lower range of what is estimated by the existing models. In particular, the Stewart model predicts values between 50 and 60 km. A smaller scale height is consistent with the generally lower density levels observed in the early part of our data span. However, in the second Mars year where the model and the measurements are roughly consistent, the scale height exhibits the same discrepancy, which is surprising and hard to explain.

2.4.5 Solar Rotation effects

In Section 2.3.2.5, we presented the detection of the solar rotation in the drag coefficient time series. The density time series also displays a ≈ 26 day periodicity. Using Lomb's method, two periods, ≈ 24 and ≈ 25.7 days, present a peak in the power spectrum, significant at >99% and >86% probability

respectively. Arc-to-arc variability and the superposition of longer (seasonal) periods to the solar rotation could explain the observed splitting in frequency.

2.4.6 Solar Activity effects

Unlike Forbes et al. [2006], we do not observe a very high correlation between the density residuals and the $F_{10.7}$ residuals (here, residuals are defined as the instantaneous value minus a smoothed value). When we fit a straight line to a scatter plot of density residuals versus $F_{10.7}$ residuals, we obtain a shallower slope than Bruinsma et al. [2006], with larger misfits. As a result, a linear regression using measured $F_{10.7}$ values only yields a rather weak correlation with the $F_{10.7}$ time series (≈ 0.6). The lower signal to noise ratio compared to MGS (Forbes et al. [2006]) might explain why, for the same change in $F_{10.7}$ from average condition, we do not observe as strong an increase in density. Nevertheless, we note that the residuals calculated using a smoothing period of 26 days (the effective solar rotation period at Mars) result in the best fit.

In Section 2.3.2.5, we presented the detection of the solar rotation in the drag coefficient. In addition to the atmospheric structure, the recovery of the scale height near 400km can provide constraints on the heating and cooling processes of the exosphere. We can obtain estimates of the exospheric temperature, T_{exo}, from the measured scale height H_{geodyn}, the modeled mean molecular weight (M_w) and known parameters (gravitational acceleration g, Boltzman constant k):

$$T_{exo} = \frac{M_w H_{geodyn} g}{k}$$

The obtained exospheric temperatures (100–200K) are low compared to Stewart [1987] (200–300K), because of the lower measured scale heights. These temperatures imply that a very efficient cooling process, such as the CO_2 cooling (Keating and Bougher [1992], Bougher et al. [1999, 2000], Forbes et al. [2006]), is counter-balancing the EUV heating. Moreover, we note that even though the

exospheric temperatures predicted are usually in the 200–300K range, the measurements on which the Stewart model is based are mostly inferences from plasma scale heights. Only two measurements from the Viking missions (both at very low solar activity) were used, which gave temperatures between 160 and 180K and between 110 and 130K respectively (Nier and McElroy [1977]).

The exospheric temperature time series has a general negative trend consistent with decreasing solar activity. This is due in part to the dependence of the estimated temperatures on the Stewart model, which was used to constrain the mean molecular weight. The correlation of the exospheric temperature with the modeled molecular weight is high (≈ 0.71). On the other hand, the molecular weight correlations are rather low. Nevertheless, our measurements show large improvements in correlation with both the mean molecular weight and the $F_{10.7}$ index when we use instantaneous $F_{10.7}$ values. The molecular weight correlation improves by 15% to 0.82. The correlation with $F_{10.7}$ (lagged to account for the Earth-Sun-Mars geometry, both in terms of angles and distances) increases from ≈0.34, when using $F_{10.7}$ values smoothed over 3 solar rotations, to ≈0.54. This better agreement of our measurements (obtained from smoothed $F_{10.7}$) with instantaneous $F_{10.7}$ values suggests that the temperature variations obtained from our scale height measurements capture some of the effects of varying solar radiation on the upper atmosphere.

An expected result is that the exosphere temperature seems to react rather slowly to solar EUV forcing. The RMS of the residuals after fitting T_{exo} vs $F_{10.7}$ with a straight line decreases significantly when both time series are smoothed: -25% when smoothing over 1 solar rotation, and an -52% when smoothing over 3 solar rotations. In addition, the dependence of T_{exo} on $F_{10.7}$ also becomes stronger: the slope of the linear fit increases by respectively 33 and 45%. The exosphere appears to be more responsive to long-period forcing.

2.5 Conclusion

After processing the X-band tracking data of the Mars Odyssey spacecraft, we recovered regular density measurements in the Martian exosphere over a period of two Martian years. Despite the very low levels of drag acceleration encountered, we showed through various tests that the values obtained with this technique are robust. Until recently, direct measurements near 400 km altitude were not possible. The use of Radio Science enables the monitoring of the atmospheric density over long timescales and on a global scale, at very high altitudes. The limited spatial and temporal resolutions of the results limit our measurements to global or hemispherical averages. However, this presents the advantage of maintaining a constant sampling area, and thus offers measurements consistent over time that can be directly compared temporally. In our measured density time series, we observe some important features, such as a solar rotation periodicity, and the agreement with exospheric model is reasonable. However, in this atmospheric study of the Mars Odyssey radio tracking data, the correlation of retrieved density and solar index $F_{10.7}$ is not as high as the one seen on MGS by Forbes et al. [2006], which could be explained by the Mars Odyssey orbit being ≈ 20 km higher.

2.6 References

Angelats i Coll, M., F. Forget, M. A. López-Valverde, and F. González-Galindo (2005), The first Mars thermospheric general circulation model: The Martian atmosphere from the ground to 240 km, Geophysical Research Letters, 32, 4201–+, doi:10.1029/2004GL021368.

Bougher, S. W., S. Engel, R. G. Roble, and B. Foster (1999), Comparative terrestrial planet thermospheres: 2. Solar cycle variation of global structure and

winds at equinox, Journal of Geophysical Research, 104, doi:10.1029/1998JE001019.

Bougher, S. W., S. Engel, R. G. Roble, and B. Foster (2000), Comparative terrestrial planet thermospheres: 3. Solar cycle variation of global structure and winds near solstices, Journal of Geophysical Research, 105, doi:10.1029/2000JE001232.

Bougher, S. W., S. Engel, D. P. Hinson, and J. R. Murphy (2004), MGS Radio Science electron density profiles: Interannual variability and implications for the Martian neutral atmosphere, Journal of Geophysical Research, 109, E03010, doi:10.1029/2003JE002154.

Bougher, S. W., J. M. Bell, J. R. Murphy, M. A. López-Valverde, and P. G. Withers (2006), Polar warming in the Mars thermosphere: Seasonal variations owing to changing insolation and dust distributions, Geophysical Research Letters, 32, L02203, doi:10.1029/2005GL024059.

Bruinsma, S., and F. G. Lemoine (2002), A preliminary semiempirical thermosphere model of Mars: DTM-Mars, Journal of Geophysical Research, 107, 15–1, doi:10.1029/2001JE001508.

Bruinsma, S., Forbes, J. M. and F. G. Lemoine (2006), Solar Flux variability and Mars' thermosphere densities derived from orbital tracking data, Second workshop on Mars atmosphere modeling and observations.

Crider, D. H., J. Espley, D. A. Brain, D. L. Mitchell, J. E. P. Connerney, and M. H. Acuña (2005), Mars Global Surveyor observations of the Halloween 2003 solar

superstorm's encounter with Mars, Journal of Geophysical Research, 110, 9–+, doi:10.1029/2004JA010881.

Culp, R. D. and Stewart, A. I. (1984), Time-dependent model of the Martian atmosphere for use in orbit lifetime and sustenance studies, Journal of Astronautical Sciences, 32, 329–341.

Cutting, E., J. C. Frautnick, and G. H. Born (1978), Orbit analysis for Seasat-A, Journal of Astronautical Sciences, 26, 315–342.

Forbes, J. M., S. Bruinsma, and F. G. Lemoine (2006), Solar rotation effects in the thermospheres of Mars and Earth, Science, 312, 1366 – 1368.

Haberle R. M., M. M. Joshi, J. R. Murphy, J. R. Barnes, J. T. Schofield, G. Wilson, M. Lopez-Valverde, J. L. Hollingsworth, A. F. C. Bridger, and J. Schaeffer (1999), General circulation model simulations of the Mars Pathfinder atmospheric structure investigation/meteorology data, Journal of Geophysical Research, 104, 8,957–8,974.

Hinson, D. P., R. A. Simpson, J. D. Twicken, G. L. Tyler, and F. M. Flasar (1999), Initial results from radio occultation measurements with Mars Global Surveyor, Journal of Geophysical Research , 104, 26,997–+.

Jacchia, L. G. and Slowey, J. (1962), Accurate Drag Determinations for Eight Artificial Satellites; Atmospheric Densities and Temperatures, SAO Special Report, 100.

Jacobson, R. A., S. P. Synnott, and J. K. Campbell (1989), The orbits of the satellites of Mars from spacecraft and earthbased observations, Astronomy and Astrophysics, 225, 548–554.

Justus, C. G., D. L. Johnson (2001), Mars Global Reference Atmospheric Model 2001 Version (Mars-GRAM 2001): Users Guide, Tech. Rep. NASA/TM-2001-210961.

Justus, C. G., B. F. James, S. W. Bougher, A. F. C. Bridger, R. M. Haberle, J. R. Murphy, and S. Engel (2002), Mars-GRAM 2000: A Mars atmospheric model for engineering applications, Advances in Space Research, 29, 193–202.

Keating, G. M., and S. W. Bougher (1992), Isolation of Major Venus Thermospheric Cooling Mechanism and Implications for Earth and Mars, Journal of Geophysical Research, 97, 4189-4197.

Keating, G. M., S. W. Bougher, R. W. Zurek, R. H. Tolson, G. J. Cancro, S. N. Noll, J. S. Parker, T. J. Schellenberg, R. W. Shane, B. L. Wilkerson, J. R. Murphy, J. L. Hollingsworth, R. M. Haberle, M. Joshi, J. C. Pearl, B. J. Conrath, M. D. Smith, R. T. Clancy, R. C. Blanchard, R. G. Wilmoth, D. F. Rault, T. Z. Martin, D. T. Lyons, P. B. Esposito, M. D. Johnston, C. W. Whetzel, C. G. Justus, and J. M. Babicke (1998), The Structure of the Upper Atmosphere of Mars: In Situ Accelerometer Measurements from Mars Global Surveyor, Science, 279, 1672–+.

King-Hele, D. (1987), Satellite Orbits in an Atmosphere: Theory and Applications, Blackie, Glasgow.

Konopliv, A. S., C. F. Yoder, E. M. Standish, D.-N. Yuan, and W. L. Sjogren (2006), A Global Solution for the Mars Static and Seasonal Gravity, Mars Orientation, Phobos and Deimos Masses, and Mars Ephemeris, Icarus.

Krasnopolsky, V. (2002), Mars' upper atmosphere and ionosphere at low, medium, and high solar activities: Implications for evolution of water, Journal of Geophysical Research, 107, 11–+.

Lemoine, F. G. (1992), The dynamics of orbitings satellites and gravity model development, Ph.D. thesis, University of Colorado at Boulder, Bouler, Colorado.

Lemoine, F. G (2003)., mgm1041c gravity field solution, Planetary Data System, Geosciences Node, http://pds-geosciences.wustl.edu/geodata/mgs-m-rss-5-sdp-v1/mors 1021/sha/.

Lemoine, F. G., D. E. Smith, D. D. Rowlands, M. T. Zuber, G. A. Neumann, D. S. Chinn, and D. E. Pavlis (2001), An improved solution of the gravity field of Mars (GMM-2B) from Mars Global Surveyor, Journal of Geophysical Research, 106, 23,359–23,376, doi:10.1029/2000JE001426.

Lewis, S. R. and P. R. Barker (2005), Atmospheric tides in a Mars general circulation model with data assimilation, Advances in Space Research, 36, 2,162–2,168, doi:10.1016/j.asr.2005.05.122.

Lomb, N. R. (1976), Least-Squares frequency analysis of unequally spaced data, Astrophysics and Space Science, 39, 447 – 462.

Marshall, J. A., and S. B. Luthcke (1994), Modeling radiation forces acting on TOPEX/Poseidon for precision orbit determination, Journal of Spacecraft and Rockets, 31, 99–105.

Mase, R. A., P. Antreasian, J. L. Bell, T. L. Martin-Mut, and J. C. J. Smith (2005), Mars Odyssey Navigation Experience, Journal of Spacecraft and Rockets, 42 (3), 386–393.

Nier, A. O., and M. B. McElroy (1977), Composition and structure of Mars' upper atmosphere - Results from the neutral mass spectrometers on Viking 1 and 2, Journal of Geophysical Research , 82, 4,341–4,349

Neumann, G. A., D. D. Rowlands, F. G. Lemoine, D. E. Smith, and M. T. Zuber (2001), Crossover analysis of Mars Orbiter Laser Altimeter data, Journal of Geophysical Research , 106, 23,753–23,768, doi:10.1029/2000JE001381.

Pace, G. D., D. A. Spencer, J. Harris, S. Saunders, G. Badhwar, P. Christensen, R. Barry, R. Gibbs, L. Adams, W. Sidney, P. Kallermeyn, and W. Boynton (2000), Mars Surveyor 2001 Mission Plan Revision B, Tech. rep., JPL.

Pavlis, D. E., S. G. Poulose and J. J. McCarthy (2006), GEODYN operations manuals, Contractor report, SGT Inc., Greenbelt, Maryland.

Smith, D. E., M. T. Zuber, and G. A. Neumann (2001), Seasonal Variations of Snow Depth on Mars, Science, 294, 2141–2146, doi:10.1126/science.1066556.

Smith, D. E., M. T. Zuber, M. T. Torrence and P. J. Dunn (2003), Estimating the k2 Tidal Gravity Love Number of Mars, AGU Fall Meeting Abstracts

Smith, J. C. and J. L. Bell (2005), 2001 Mars Odyssey Aerobraking, Journal of Spacecraft and Rockets, 42 (3), 406–415.

Standish, E. M., X. X. Newhall, J. G. Williams, and W. M. Folkner (1995), JPL Planetary and Lunar Ephemerides, DE403/LE403, Tech. Rep. JPL IOM 314.10-127, JPL.

Stewart, A. I. F. (1987), Revised time dependent model of the Martian atmosphere for use in orbit lifetime and sustenance studies, Tech. Rep. JPL PO NQ-802429, University of Colorado.

Takashima, N. and R. G. Wilmoth (2002), Aerodynamics of Mars Odyssey, Conference Paper, AIAA Atmospheric Flight Mechanics Conference and Exhibit, Monterey, California

Tolson, R. H., G. M. Keating, B. E. George, P. E. Escalera, M. R. Werner, A. M. Dwyer, and J. L. Hanna (2005), Application of Accelerometer Data to Mars Odyssey Aerobraking and Atmospheric Modeling, Journal of Spacecraft and Rockets, 42, 435–443.

Tyler, G. L., G. Balmino, D. P. Hinson, W. L. Sjogren, D. E. Smith, R. Woo, S. W. Asmar, M. J. Connally, C. L. Hamilton, and R. A. Simpson (1992), Radio Science Investigations With Mars Observer, Journal of Geophysical Research, 97, 7759–7779.

Tyler, G. L., G. Balmino, D. P. Hinson, W. L. Sjogren, D. E. Smith, R. A. Simpson, S. W. Asmar, P. Priest, and J. D. Twicken (2001), Radio science observations with Mars Global Surveyor: Orbit insertion through one Mars year in

mapping orbit, Journal of Geophysical Research , 106, 23,327–23,348, doi:10.1029/2000JE001348.

Wilmoth, R. G., D. F. Rault, F. M. Cheatwood, W. C. Engelund, and R. W. Shane (1999), Rarefied aerothermodynamic predictions for Mars Global Surveyor, Journal of Spacecraft and Rockets, 36, 314–322.

Withers, P. G., S. W. Bougher, and G. M. Keating (2003), The effects of topographically controlled thermal tides in the Martian upper atmosphere as seen by MGS Accelerometer, Icarus, 164, 14–32.

Withers, P. and M. Mendillo (2005), Response of peak electron densities in the martian ionosphere to day-to-day changes in solar flux due to solar rotation, Planetary and Space Science, 53 (14-15), 1401-1418.

Withers, P. G. (2006), Mars Global Surveyor and Mars Odyssey Accelerometer observations of the Martian upper atmosphere during aerobraking, Geophysical Research Letters, 33, doi:10.1029/2005GL02444.

Yoder, C. F., A. S. Konopliv, D. N. Yuan, and E. M. Standish (2003), Fluid Core Size of Mars from Detection of the Solar Tide, Science, 300, 299–303, doi:10.1126/science.1079645.

2.7 Figures

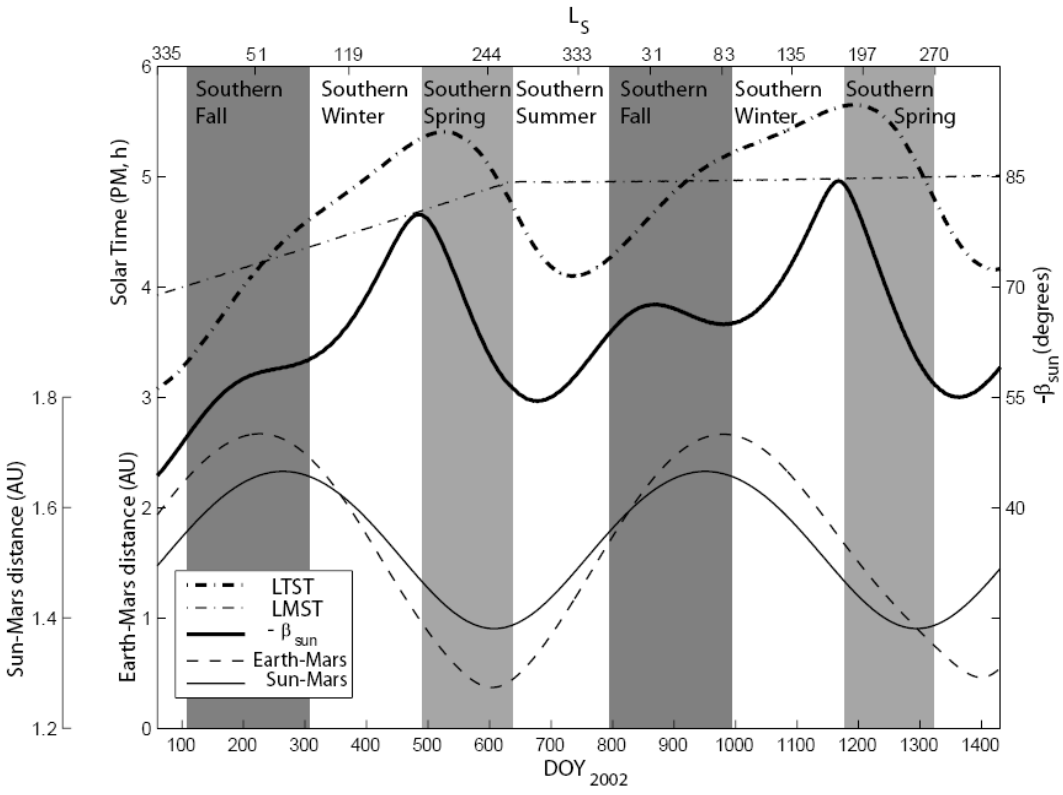

Figure 2.1 Near conjunction ($DOY_{2002} \approx 220$ and $DOY_{2002} \approx 980$) Mars appears close to the Sun and the quality and quantity of tracking decreases. The parameter is the elevation of the Sun with respect to the orbit plane, and controls the length of the eclipses of the Sun by Mars. The LTST (Local True Solar Time) is an important controlling parameter for the atmospheric density. The LMST (Local Mean Solar Time) is defined with respect to the fictitious Sun position if Mars' orbit was circular, and represents the average LTST over a Martian year.

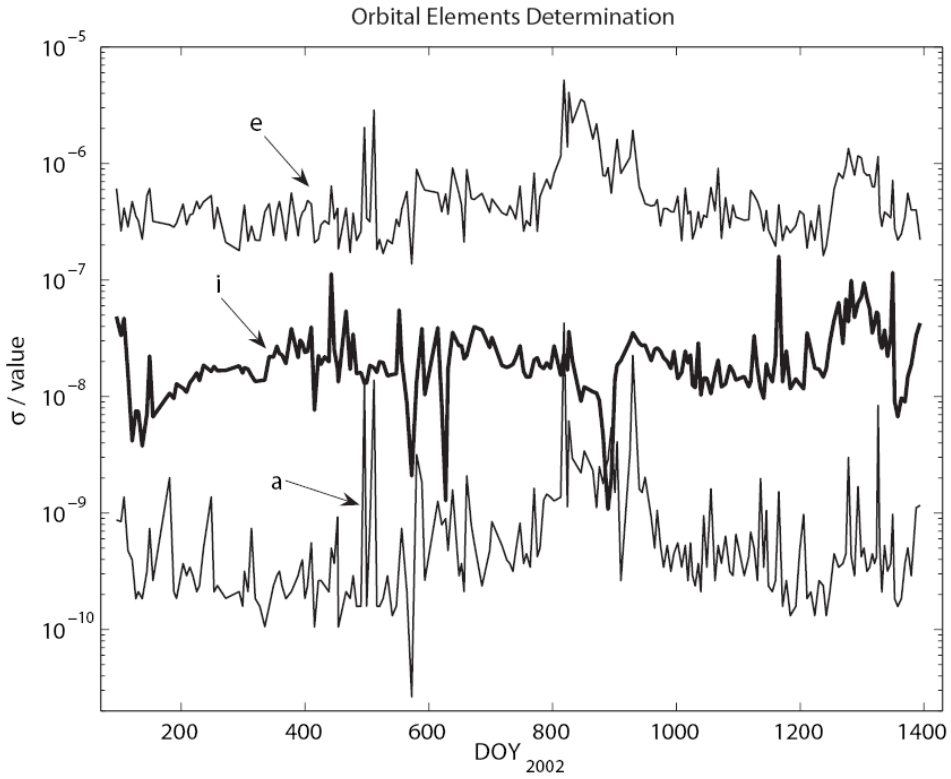

Figure 2.2 The relative standard deviation (σ/value) of several orbital elements of the spacecraft state at the initial timestep of each arc: the semi-major axis (*a*), eccentricity (*e*) and inclination (*i*).

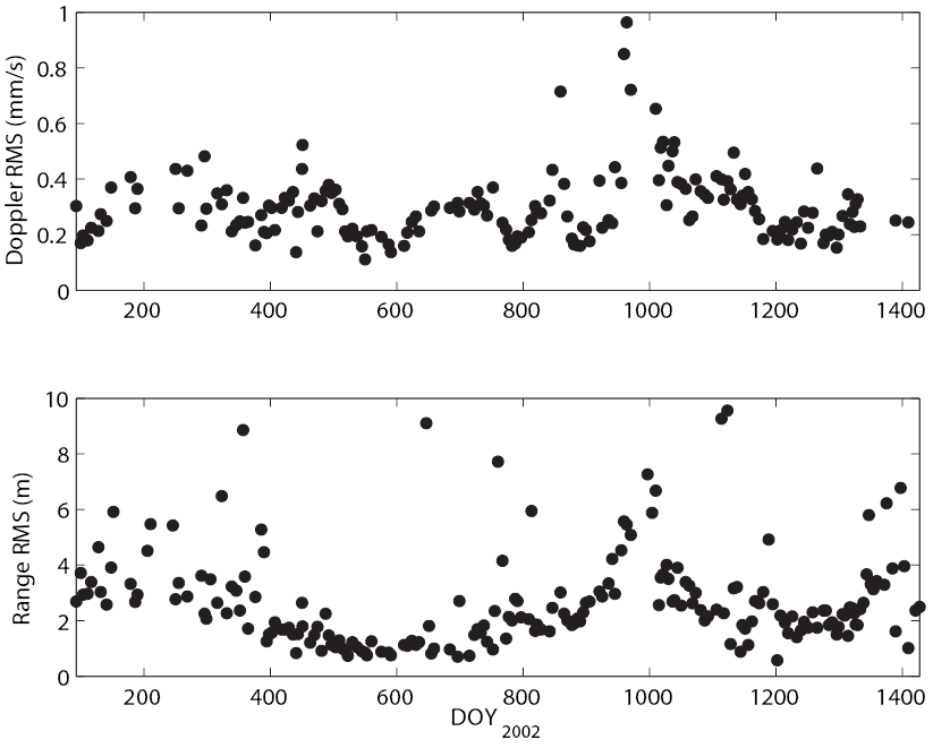

Figure 2.3 RMS of the observation residuals (i.e. the difference between data and the best-fit model trajectory reconstructions). Units are mm/s for Doppler residuals (top) and meters for range residuals (bottom). The range RMS is correlated with Earth-Mars distance, but the Doppler RMS is less sensitive to the geometry, except near solar conjunction ($DOY_{2002} \approx 220$ and $DOY_{2002} \approx 950$).

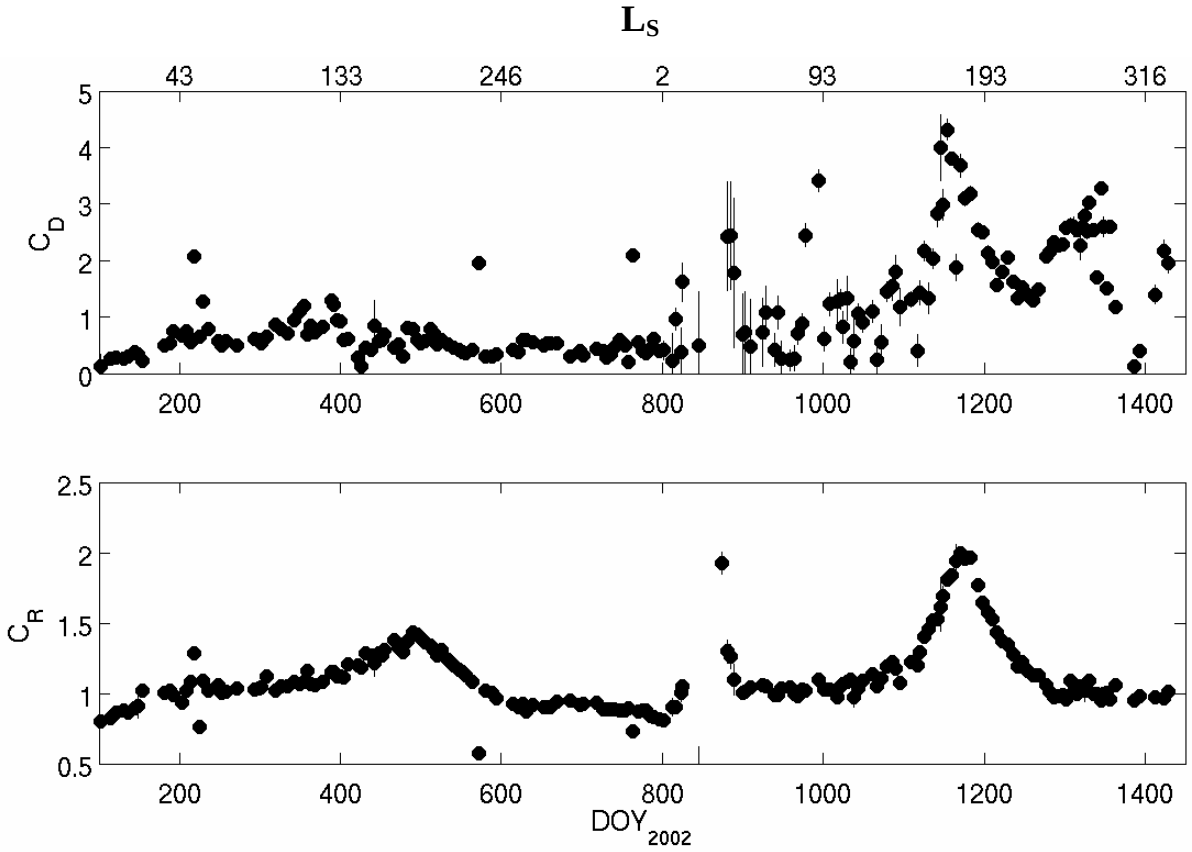

Figure 2.4 Time series of the drag and radiation coefficients adjusted by GEODYN. The uncertainties shown are 10 times the formal uncertainties calculated by the program GEODYN II, but they are still not visible for the majority of the results. The period DOY_{2002} ~ 800 – 1000 has larger uncertainties in both C_D and C_R due to bad orbit viewing geometry (the orbit is seen nearly face-on from Earth, so the line-of-sight component of the velocity is very small).

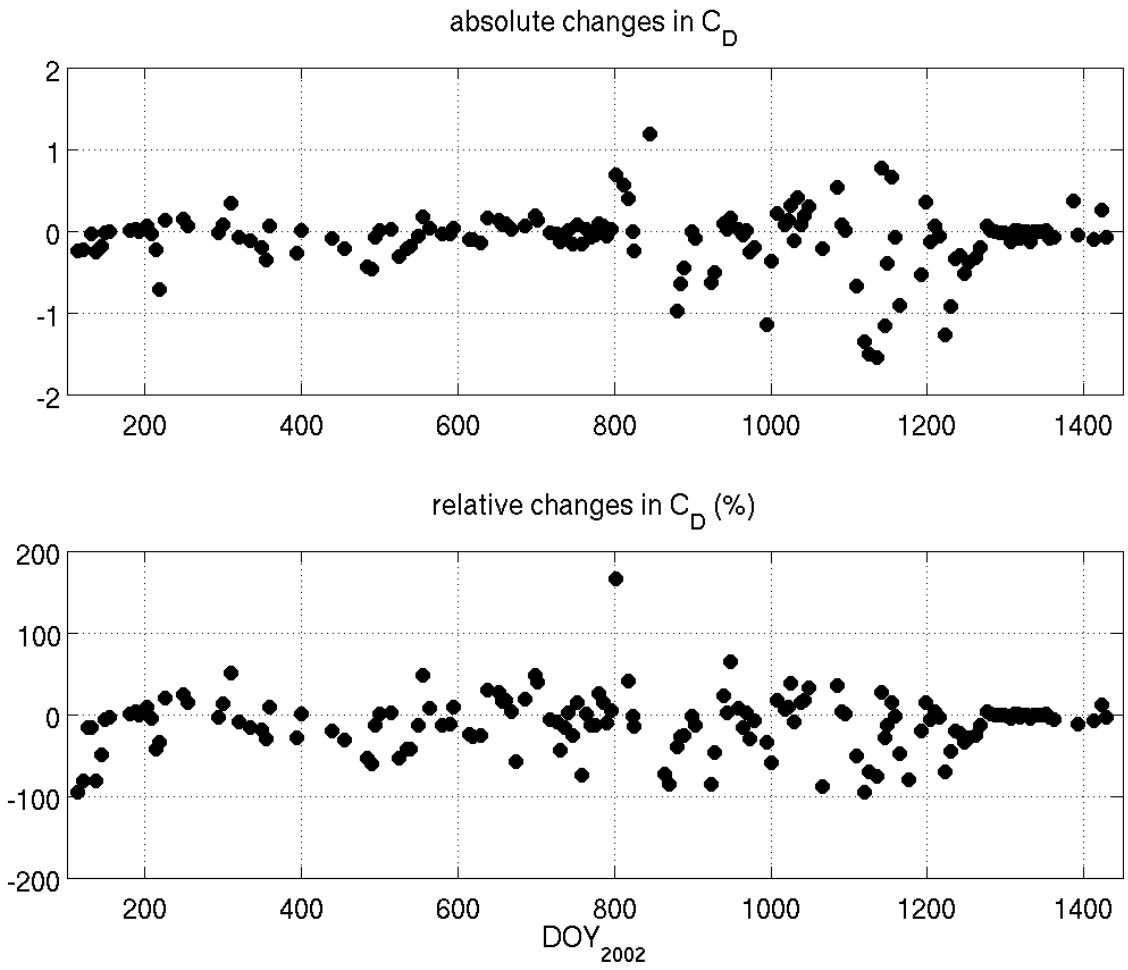

Figure 2.5 Absolute changes (top) and relative changes (bottom, in percent), in the drag coefficient C_D that result from constraining the radiation coefficient C_R to unity.

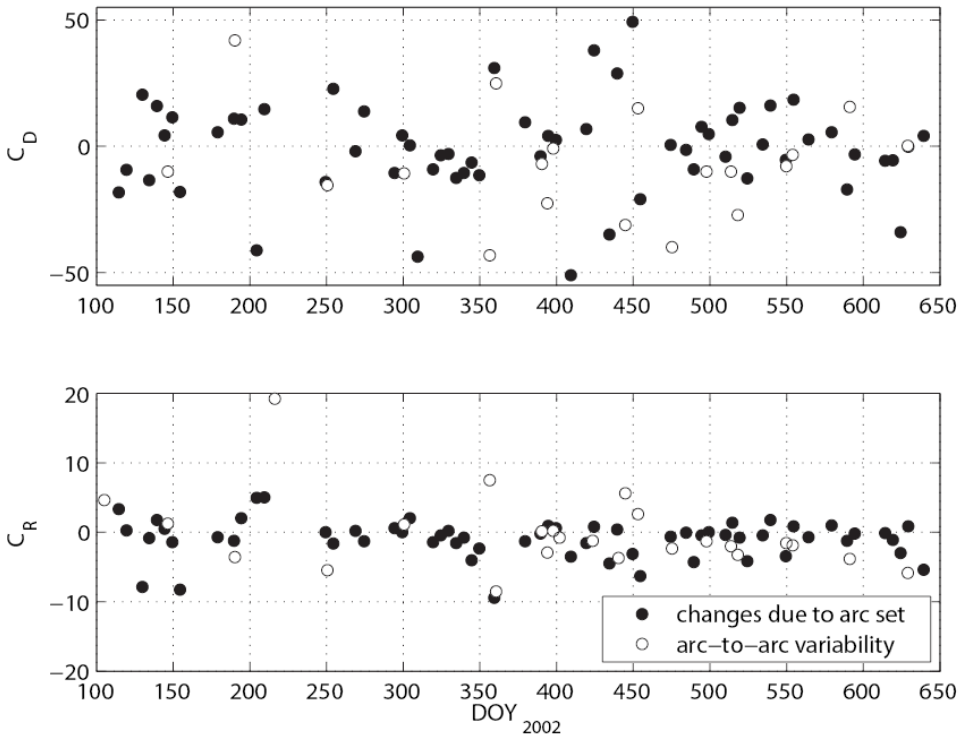

Figure 2.6 Changes in C_D and C_R due to a change of arc set (solid circles). For comparison, the arc-to-arc variability (within the primary set of arcs, and of very close arcs only) is also plotted.

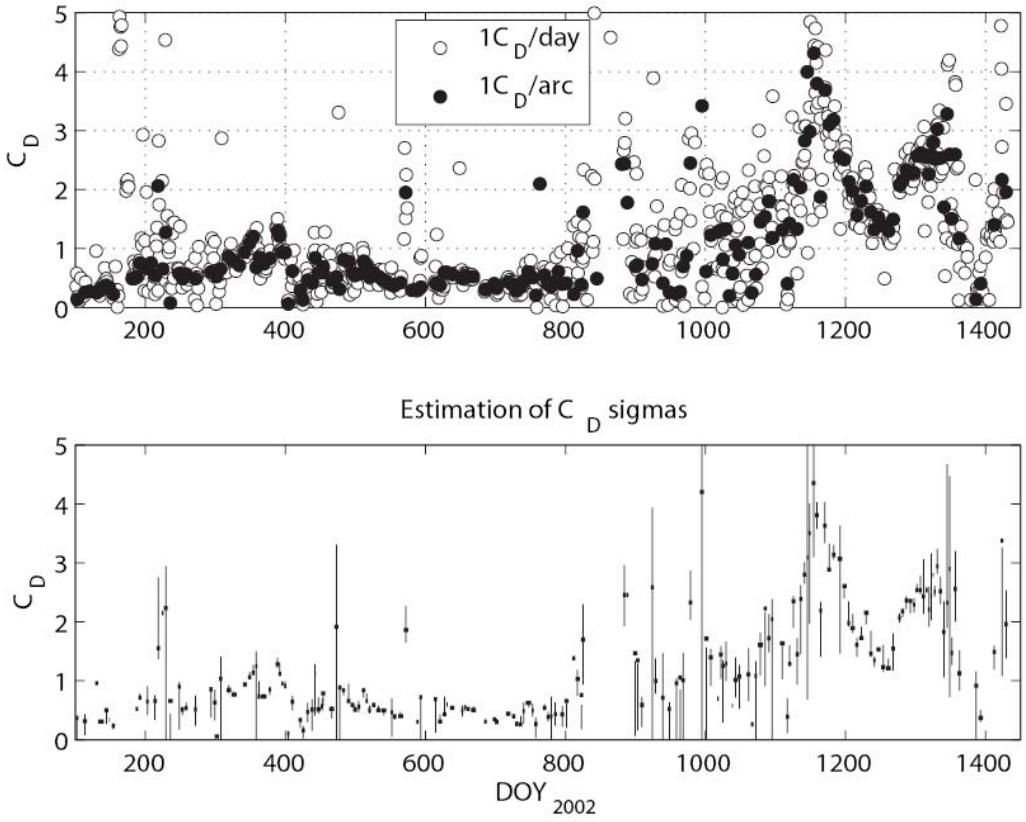

Figure 2.7 Top: daily estimates of the drag coefficient (open circles) show a significant scatter around the arc-long values (solid circles). Bottom: scattered daily values were used to evaluate the C_D variability versus time. The scatter provides a measure of the sensitivity of atmospheric density recovery to the length of the averaging window (arc).

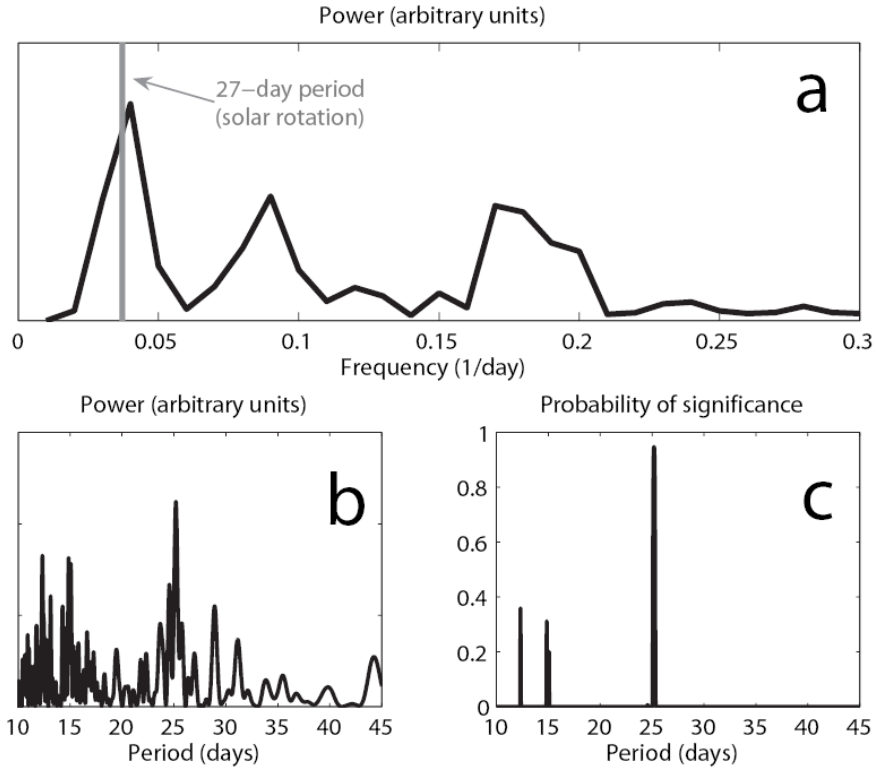

Figure 2.8 Frequency analysis of the C_D residuals: power spectrum using FFT, after interpolation to obtain an evenly-spaced time series (a); using Lomb's method for unevenly spaced data, power spectrum (b) and probability of peak significance (c).

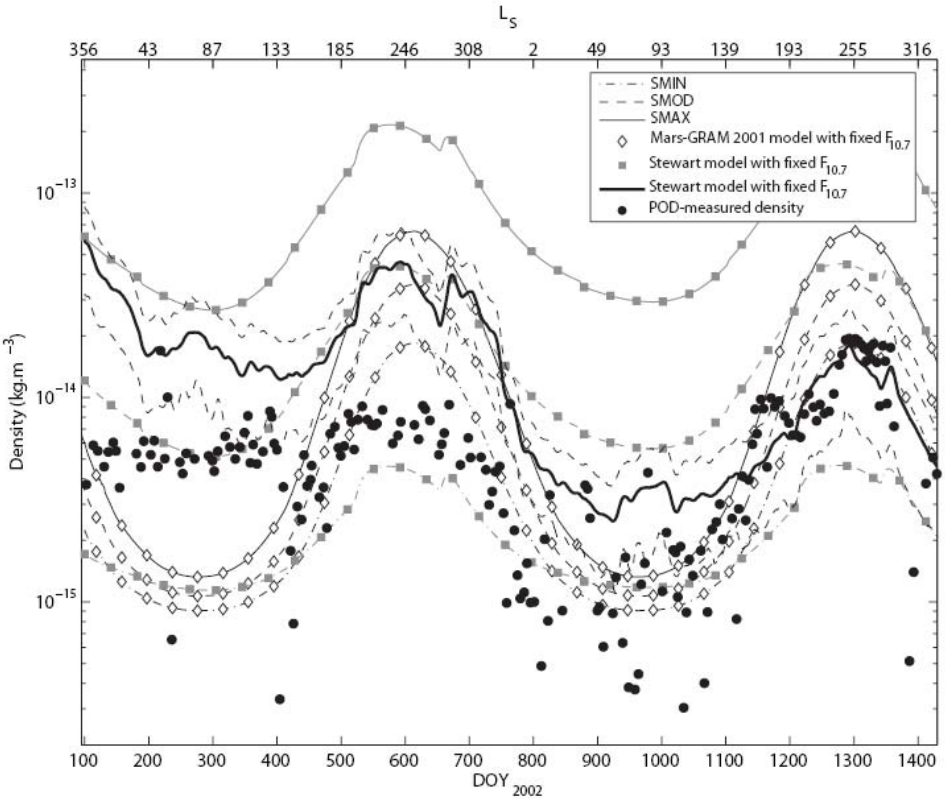

Figure 2.9 Time series of the measured atmospheric density. Each solid circle corresponds to an arc-long estimate. The model density and its calculated uncertainty (Section 4.1) are shown (dashed). In the background, we show densities predicted by two models with $F_{10.7}$ held constant at values representative of low (dot-dashed), moderate (dashed) and high solar activity (solid): the Stewart 1987 we used as an a priori (square) and Mars-GRAM 2001 (diamond).

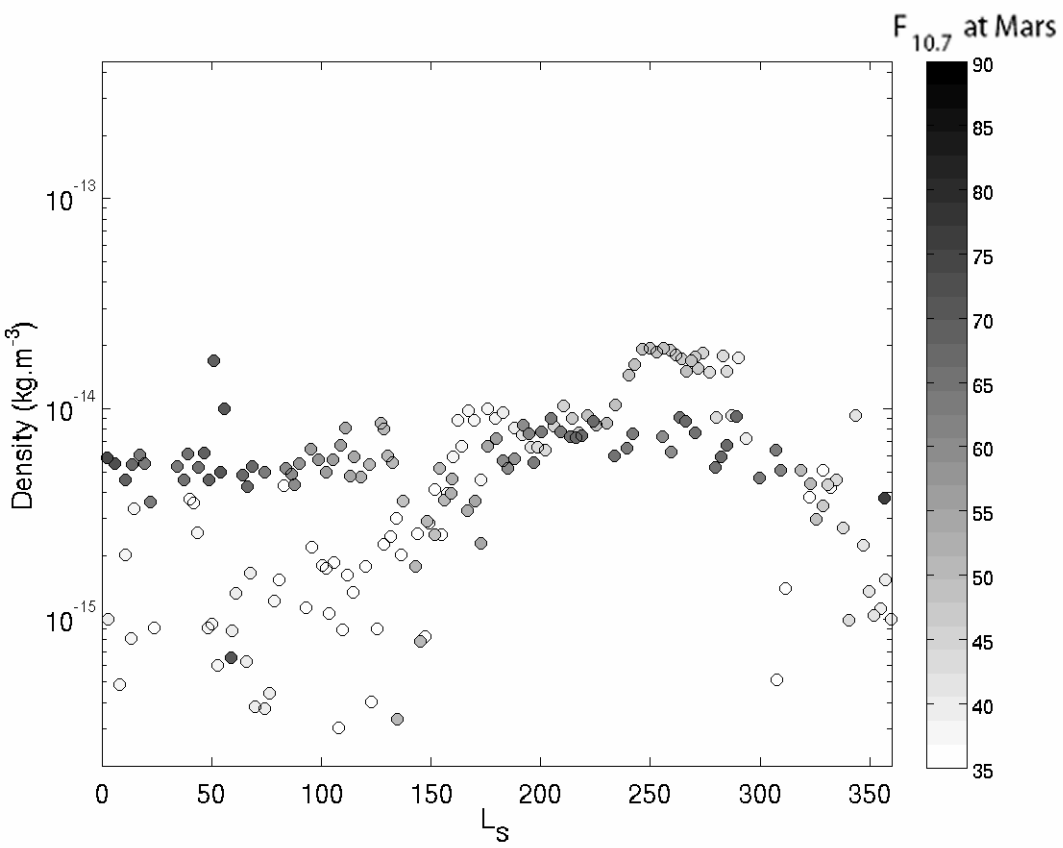

Figure 2.10 Measured density plotted versus the season (L_S). Darker shades indicate higher values of the solar index $F_{10.7}$ at Mars.

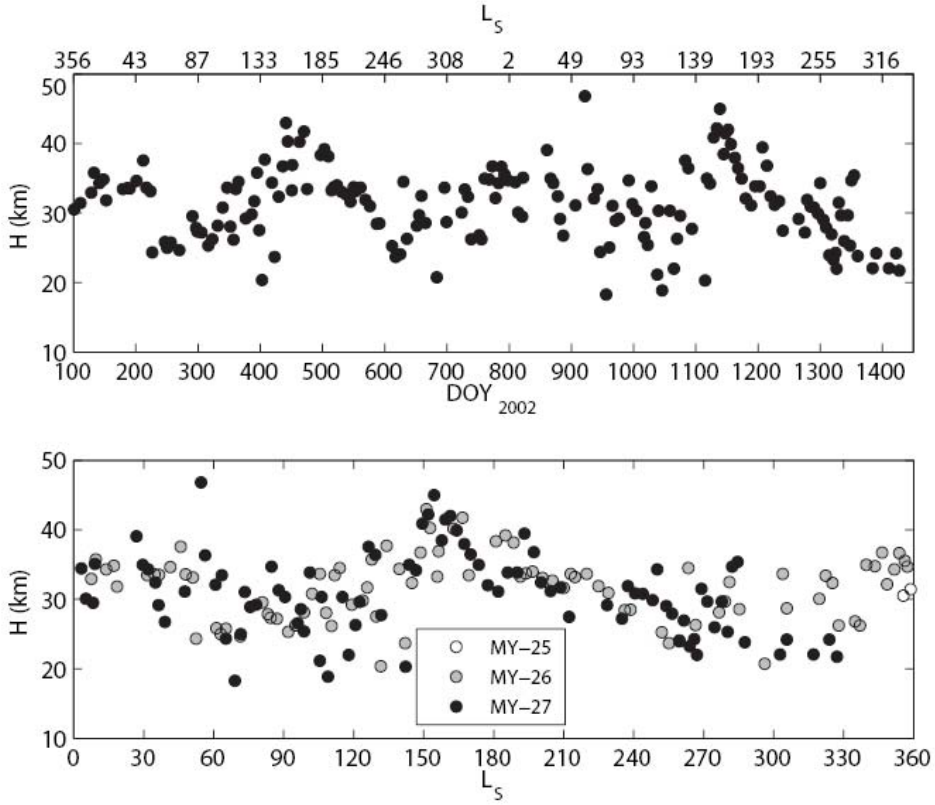

Figure 2.11 The estimated scale height (top) at the spacecraft periapsis ranges from ≈ 20 km to ≈ 50 km. When plotted against L_S (bottom), it appears that the scale height is quite repeatable from year to year.

[THIS PAGE INTENTIONALLY LEFT BLANK]

[THIS PAGE INTENTIONALLY LEFT BLANK]

Chapter 3

Atmospheric density during the aerobraking of Mars Odyssey from radio tracking data[1]

3.0 Abstract

We analyzed X-band radio tracking observations of the Mars Odyssey spacecraft during its aerobraking phase (October 2001 – January 2002). We used the precision orbit determination (POD) software GEODYN to estimate the spacecraft orbital energy lost during each periapsis pass due to atmospheric drag. We also recovered atmospheric density values at each periapsis, assuming simple exponential atmospheric models. Our measurements are in good agreement with the time series from the Odyssey accelerometer instrument, but they are dependent on the a priori scale height used. From the accelerometer-derived periapsis densities and the POD-derived frictional loss of orbital energy, we calculated new scale heights. Each represents the effective scale height of the atmosphere near periapsis for each aerobraking pass. Our results are consistently ≈1.7±0.7km greater than the published accelerometer values. The accelerometer measurements have higher spatial and temporal resolution when they are available, but these results provide a dataset useful for engineering and navigational purposes, to assess variability in the Martian middle atmosphere.

[1] This chapter was accepted for publication in the *Journal of Spacecraft and Rockets* in a Special Issue gathering several papers from presenters in the 2006 AIAA/AAS Astrodynamics Specialist Conference held in August 2006 in Keystone (Colorado, USA). The Special Issue is to be published shortly.

Mazarico, E., M. T. Zuber, F. G. Lemoine and D. E. Smith, "Atmospheric density during the aerobraking of Mars Odyssey from radio tracking data," *Journal of Spacecraft and Rockets*, accepted.

3.1 Introduction

In addition to the obvious scientific interest in understanding the density structure and variability of the middle atmosphere of Mars, there are strong engineering incentives to do so. Such knowledge is critical to lander entry, and to orbiter aerobraking operations. Given the numerous planned missions to Mars, and with the perspective of human exploration, significant effort has been invested into collecting data on Mars' atmospheric structure. Thus, the amount of data available for modeling and understanding the lower and middle atmosphere has increased considerably. In addition to radio occultation and remote sensing studies during the primary missions of the various spacecraft in orbit around Mars, accelerometer experiments have been conducted during aerobraking. Accelerometers on Mars Global Surveyor (MGS), Mars Odyssey and Mars Reconnaissance Orbiter (MRO) obtained density profiles at each passage through the denser layers of the atmosphere, from periapsis up to about 140 km altitude (Keating et al. [1999]; Withers et al. [2003]; Tolson et al. [2005]; Withers [2006a]).

Here, we present density measurements of the middle atmosphere of Mars using the radio tracking data of the Mars Odyssey spacecraft during its aerobraking phase (24 October 2001 to 11 January 2002). Mars Odyssey, launched on 7 April 2001, performed its Mars orbit insertion maneuver on 24 October 2001, achieving an initial 18.6-hour-long and highly elliptical orbit. Slowly, thanks to the atmospheric drag, the semi-major axis and the eccentricity of the orbit were decreased in order to reach the final, nearly-circular mapping orbit.

In this study we show that Precise Orbit Determination (POD) can be used during periods of high atmospheric drag to estimate the energy lost by friction and the atmospheric environment near periapsis. POD has been used in the past to conduct studies geared towards the Martian atmosphere (Tracadas et al. [2001]; Bruinsma and Lemoine [2002]; Forbes et al. [2006]; Mazarico et al. [2007];

Lemoine et al. [2007]), but previous studies used data at higher altitudes (MGS near 175 km and 400km; Mars Odyssey near 400 km).

The Mars Odyssey spacecraft also included an accelerometer that was used during the aerobraking phase to estimate atmospheric density to aid in spacecraft operations. A preliminary reexamination of the raw accelerometer data (Withers [2006b]) showed some differences in the recovered density values compared to initial values published by the Accelerometer Team (Keating et a. [2004]). Because POD uses an independent dataset, it can provide a complementary view of the atmospheric density environment. Here we present periapsis density and scale height results, assuming an exponential atmosphere with constant scale height. These results are used to assess atmospheric variability, which could be useful to make predictions when no accelerometer data are available.

3.2 Data and Methods

Compared to previous analyses performed during mission science phases (Forbes et al. [2006]; Mazarico et al. [2007]; Konopliv et al. [2006]), where the atmospheric drag acceleration is very small compared to radiation pressure accelerations (both direct and reflected by Mars), the drag acceleration levels during Mars Odyssey aerobraking are 4 to 5 orders of magnitude larger. This is, of course, due to the much lower altitude during this mission phase: the periapsis altitude is in general around 100-110km, compared to a mean mapping phase altitude of around 390-400km. During each passage through periapsis, the friction decreases the total energy of the spacecraft orbit. The change in energy corresponds to a change in orbital parameters (ideally, only the semi-major axis), shrinking the orbit (the very objective of aerobraking).

The Mars Odyssey orbit and the atmospheric density are thus closely related. While the accelerometer measurements do not invoke the particular geometry of the orbit (except through the spacecraft velocity, to transform the observed

acceleration into a density), it is possible to estimate the atmospheric density at periapsis from the trajectory alone.

3.2.1 Simple Timing Method

To illustrate that point, and to assess whether we could anticipate valuable results with a more precise approach, we conducted preliminary calculations of the periapsis density using two relatively straightforward methods. We first used theoretical results (King-Hele [1987]), which give a direct relationship between the eccentricity, the change in semi-major axis and the density at the periapsis. Our second method was more computational. For each aerobraking pass, we extracted positions of the Mars Odyssey spacecraft from the SPICE kernels on the NASA Planetary Data System (PDS). SPICE is a toolkit developed by the NASA NAIF (Navigation Ancillary Information Facility) to enable the used of spacecraft mission ancillary information. The various kernels provide data on position and ephemeredes (SP), instrument pointing (I), attitude (C) or events(E).

The orbital energy change was calculated from the semi-major axis values at the preceding and following apoapsides.

$$\Delta E_i = E_{i+1} - E_i = -\frac{GM}{2}\left(\frac{1}{a_{i+1}} - \frac{1}{a_i}\right). \quad (1)$$

During aerobraking, the loss of energy by atmospheric drag is much larger than changes in semi-major axis due to secular effects or orbit perturbations, so we have $\Delta E_i<0$. A simple atmospheric exponential density model

$$\rho(z) = \rho_0 \exp\left(-\frac{z - z_0}{H_0}\right) \qquad (2)$$

was used to obtain the energy lost by friction along the trajectory arc. Each discretized 1-second orbital segment contributed

$$\frac{1}{2} C_D A \rho(z) V(z)^2 .ds . \quad (3)$$

to the total dissipated energy E_{diss} (where *ds* is the length of the segment, *A* is the cross-sectional area of the spacecraft, C_D is the drag coefficient, and *V* is velocity). The atmospheric density, $\rho_{0,}$ at the reference height, z_0, was adjusted so that $\Delta E = E_{diss}$. The density at periapsis was then obtained.

As seen in Figure 3.1a, the densities obtained from both methods (with H_0=10km) are in general agreement with results from the accelerometer experiment, in terms of magnitude and trend. The densities are consistently underestimated by ~20% (Figure 3.1b), and larger discrepancies appear when the semi-major axis decreases (aerobraking pass number > 250). Nevertheless, it is sensible to expect more accurate estimates of the density during the Mars Odyssey aerobraking phase using POD than provided by oversimplified methods.

3.2.2 Precise Orbit Determination

3.2.2.1 Methods and Models

Compared to the previous methods, Precise Orbit Determination (POD) has the advantage of providing a rigorous framework with which to evaluate the contribution of atmospheric drag to orbit evolution, relative to those caused by other forces acting on the spacecraft. Physical models of the geometry, the forces, and the corrections to be applied to the tracking observations are used to integrate the trajectory of the spacecraft (called an 'arc'). The initial state of the spacecraft and various parameters describing those physical models are adjusted according to the differences (*residuals*) between actual observations and best-fit values inferred from the reconstructed trajectory. This process is iterated until an accurate fit is found, which minimizes the residuals of the observations. In this manner, POD can help disentangle atmospheric drag from contributions from other forces. We used the GEODYN program, developed at NASA Goddard Space Flight Center (GSFC; Pavlis et al. [2006]). GEODYN is an orbit determination least squares

batch filter that integrates the equations of motion and processes spacecraft tracking data to estimate geodetic parameters. On the force model side, gravitational accelerations of the Sun, Earth, Moon, planets, Phobos and Deimos are calculated based on the DE410 planetary ephemeredes (Standish et al. [2003]; Jacobson [1995]); for Mars itself, a degree and order 90 spherical harmonic model (the GSFC 'mgm1041c') is used (Lemoine [2007]); modeled non-conservative accelerations include direct solar radiation, albedo and thermal planetary radiation and atmospheric drag. GEODYN also applies corrections to the tracking data for relativity, for spacecraft antenna offset, for tropospheric delay due to ground station weather and for ground station position due to polar motion, solid tides and ocean loading. The values used for these parameters are the same as in studies of Mars Global Surveyor and Mars Odyssey mapping phase radio tracking data (Mazarico et al. [2007]; Lemoine et al. [2001]).

Compared to previous studies, we changed the *a priori* atmospheric model. Instead of using the Stewart model (Stewart [1987]), based on the dual snapshot Viking lander entry profiles, we used a simple exponential model, which is better adapted to the middle atmosphere. The scale height is set, but the *a priori* density of 2.10^{-8} kg.m^{-3} at a reference height of 110 km is adjusted by GEODYN, through the drag coefficient C_D.

3.2.2.2 Data

While there is no official Radio Science investigation on Mars Odyssey, the raw radio tracking data and the timings of the orbital maneuvers have fortunately been archived on the NASA PDS server by R.A. Simpson. We analyzed data between 02 November 2001 and 09 January 2002, *i.e.*, about 300 aerobraking passes (#12 to #313, referenced to #2 at ~21:05UTC on 24 October 2001). No radio tracking data were available between 31 December 2001 and 08 January 2002, corresponding to aerobraking passes #187 to #272.

The two types of observables in the tracking of the Mars Odyssey spacecraft are Doppler and Range measurements. In simple terms, Doppler observations constrain the velocity of the spacecraft relative to the tracking ground station, but only in the line-of-sight to the observing station on Earth. Range observations, usually sparser, measure the ground station to spacecraft distance. In the case of Mars Global Surveyor and Mars Odyssey (science phase), the uncertainty in those measurements is usually ~0.1 mm/s and 1 m, respectively. However, the aerobraking radio tracking data available are based on 1-s averages, instead of typical 10-s averages. Thus, the expected standard deviations on the Doppler measurements would be closer to ~0.3 mm/s (increase by a factor $\sqrt{10}$). On the other hand, as a consequence, the number of observations is comparatively much greater. During the ~2 months (68 days) of data processed in this study, there were ~4,000,000 Doppler and ~30,000 Range observations to compare to ~3,500,000 and ~155,000 respectively during ~4 years of the Mars Odyssey mission (Mazarico et al. [2007]). This large number is also due to a necessarily more comprehensive tracking during aerobraking, which is the most critical phase of the mission once in orbit around Mars.

The observation geometry of the orbit during aerobraking phase, as well as practical constraints on the spacecraft attitude during atmospheric passes, lead to poor periapsis tracking coverage (the high-gain antenna, HGA, was stowed on the spacecraft bus during drag passes). Only four passes were tracked during periapsis. In general, there was a data gap, extending around periapsis by ±20 minutes (minimum: 12 minutes, maximum: 30 minutes). To verify that the estimated C_D on the great majority of the arcs was not biased due to those data gaps, we artificially removed 40 minutes of data around the four periapsis with actual data. The drag coefficient adjusted by GEODYN changes by less than 0.1% in three cases, and by ~0.5% at maximum. Thus, this lack of coverage just near periapsis does not bias our results. On the other hand, without coverage near periapsis, we cannot constrain atmospheric model other than simple exponential

density models. Note that in order to be able to put any constraint on the atmospheric density, it is necessary to constrain the orbit both before and after the atmospheric drag pass occurs. Thus, any aerobraking pass that lacked tracking on either side (ingress or egress) was discarded.

3.2.2.3 Arcs

It proved difficult to perform the orbit determination on arcs several orbits in length because of frequent orbital maneuvers. During aerobraking, those maneuvers are generally short but quite numerous, and take place mostly near periapsis, and usually with no data coverage. Instead of letting GEODYN adjust every single thruster firing documented on the PDS, we grouped them in longer 'maneuvers'. To distinguish and estimate numerous second-long thruster firings could lead to a destabilization of the solution, so instead we estimated one single set of accelerations per periapsis maneuver. There are two short periods free of maneuvers, and longer arcs, each spanning ~10 orbits, yield reasonable estimates of density. In total, we created 179 separate arcs.

The processing of the arc is not as straightforward as during the mission mapping phase. The main difficulty comes from the initial state value. This initial "guess" to start the integration is based on the available SPICE kernels (reconstruction form the Navigation Team). Arcs starting near apoapsis made the POD program (GEODYN) over-correct the initial state after the first iteration and often lead to non-convergence. For this reason, we chose to start the arcs as close to Mars as possible, so that the uncertainties in the initial position, and hence in the adjustments, are necessarily smaller. In order to use as much tracking data as possible, the arcs were generally started shortly after the previous periapsis (once the altitude of the spacecraft was above the atmosphere contributing to the pass drag, taken to be ~300km). Similarly, they were stopped before entering the

atmosphere at the following aerobraking pass. Each arc thus lasted for a bit less than two orbital periods.

In addition, we generally performed initial convergence of the arcs assuming a fixed initial state. This enabled the removal of 'bad' data points, another source of solution instability. The constraints on the initial state were then loosened, and we obtained the adjusted values for the parameters of interest (below).

3.3 Results

3.3.1 Arc Convergence

The quality of the arc convergence can be assessed from the residuals. We obtain root mean squares (RMS) values of arc residuals of order of 5-10 mm/s. This is greater than common values for the higher-altitude science phase arcs of MGS and Mars Odyssey (where the RMS is less than 1 mm/s , Mazarico et al. [2007]; Konopliv et al. [2006]). Indeed, with more elliptical and higher-energy orbits, small changes in the adjusted orbital elements lead to more significant changes in position and velocity along the arc. Nevertheless, the arc convergence is stable, and estimates of the drag coefficient, the critical physical parameter for our purpose, are robust.

The magnitude of the solar radiation pressure forces (direct solar radiation and reflected solar radiation due to Mars albedo) are scaled by a radiation coefficient, C_R, which is also adjusted by GEODYN during the POD processing. The recovered coefficients are quite different from unity, as would be expected ideally. The 'contamination' of C_R entails insufficient force modeling; either the radiation pressure itself or other forces are wrongly accounted for by GEODYN. The Mars Odyssey spacecraft has only one solar panel, and the asymmetry in its geometry could enhance residual forces not properly modeled.

Our modeling of the radiation pressure is arguably not thorough. Indeed, the spacecraft attitude is not considered, because of important self-shadowing due to

the stowed HGA and frequent quaternion telemetry gaps not straightforward to interpolate. For those reasons, we fixed the cross-section to a value of 11 m^2. This is a fair assumption near periapsis because the spacecraft was controlled such that it presented the -Y face to the air flow. Outside of the atmosphere (which accounts for the major part of the orbit), the attitude of the spacecraft is not constrained as well, and using a constant cross-sectional area for the radiation force along the whole orbit might result in significant errors in its modeling. However, during aerobraking, over an entire orbit, the atmospheric drag is much stronger than the radiation pressure. (The opposite is true during normal science phase). In addition, radiation effects over a couple of orbits are not as important as in the case of long arcs at higher altitude.

The adjusted C_R values are generally low, meaning that the mismodeled forces that are contaminating the C_R recovery are small compared to the atmospheric drag. The inexact recovery of C_R is thus not a subject of worry for the quality of the adjusted C_D values,. To demonstrate this, we processed all the arcs both with C_R fixed to 1 and with C_R unconstrained. The ratio of the two obtained C_D series has a mean of exactly 1.0, and a standard deviation of only 0.5%.

The recovery of the magnitude of the orbital maneuvers is of the same order as the values reconstructed from the PDS. Given the important differences between modeled (one rather long and continuous acceleration) and actual (numerous short thruster firings) maneuvers, we did not expect perfect agreement. In any case, the magnitude of these maneuvers is generally rather small compared to the atmospheric drag acceleration, so the impact on the adjusted CD should also be small. We verified this by reprocessing the aerobraking tracking data constraining the accelerations to the PDS values, not allowing GEODYN to adjust them. The recovered CD values are very close to our previous results. The mean of the CD values changes by only 0.5%, with a 1.5% standard deviation.

3.3.2 Drag Coefficient

We obtain the density measurements at the periapsis from the C_D time series. The measured density at the reference height of 110 km is simply the drag coefficient multiplied by our *a priori* 2.10^{-8} kg.m^{-3}. We calculate the density at the periapsis altitude, where most of the atmospheric drag occurs (i.e., where the measurement is actually done, and meaningful), using the scale height of the simple exponential model used during POD.

3.4 Discussion

3.4.1 Density Comparison

For comparison with published density results during aerobraking, we only refer to densities at periapsis, because that is where the drag force acts on the spacecraft and thus where our measurements are significant. Furthermore, differences in scale heights between models would artificially increase the discrepancies between our measured values and the accelerometer-derived densities when referencing them to a common reference altitude. The periapsis is also a natural choice for comparison because the Accelerometer Team did not detail its definition of the reference ellipsoid for the altitude reference. A disadvantage of dealing with periapsis densities is that the plots presented here cannot be directly used to infer any temporal variation, because the periapsis altitude varies over time.

Figure 3.2a shows the densities at periapsis obtained from POD, the published values from the Accelerometer Team and the values obtained by P. Withers on preliminary reexamination of the same accelerometer data (Withers [2006b]). The POD approach shows a clearly improved agreement with accelerometer-derived results compared to the simple methods presented in Section II.B. Recovered densities are in closer agreement with the Accelerometer Team results than the

more recent calculations by P. Withers (derived from either the 1s-, 7s- or 39s-smoothed raw accelerometer data; the 7s and 39s averages are respectively appropriate for removing the influence of short-period spacecraft oscillations and smoothing out the atmospheric waves). The recovered density profiles change when the applied smoothing is varied. In particular, the 39-s densities can be 10% lower than the 1-s and 7-s samples. Therefore, we prefer using the 7-s estimates, which have the advantage of both giving periapsis densities very close to the 1-s values and showing the overall density structure (and not the waves or instabilities).

3.4.2 Scale Height Comparison

In Figure 3.2b, we plot the ratio of various densities with the Accelerometer Team results. The time series corresponding to the POD with a scale height of 10 km actually shows less scatter around unity than densities obtained from the 7s-smoothed data (itself closer to the previously published accelerometer results than the 1-s and 39-s cases). A scale height of 10 km corresponds to what is expected at that altitude from atmospheric models.

The density recovery is stable for shorter orbital periods, unlike the divergence observed earlier (Section II.B). The scatter around accelerometer-derived results is greatly reduced. When the model scale height is decreased (from 10 km to 5 km), the obtained densities increase, because the same amount of friction must be experienced along a much shorter arc length (most of the drag occurs within two or three scale heights above the periapsis). Likewise, increasing the scale height (from 10 km to 15 km) leads to smaller estimates of the density near periapsis. For an *a priori* scale height of 10 km, the density ratios, very close to 1 before the radio tracking data gap (orbit number < 186), are ≈0.8 afterwards. The scale height decreased from ≈10 km to ≈6 km. The evolution of important parameters is shown on Figure 3.3. Several of them do show correlation or anti-correlation with

the scale height obtained from the accelerometer experiment: latitude, local solar time, altitude. The changes in solar-zenith angle are rather small compared to those. With the POD method used here, the assumed scale height plays an important role on the measured density. Figure 3.4 shows the density ratios obtained from POD plotted against the scale height derived from the accelerometer experiment. From a nearly-random scatter around unity in Figure 3.2b, a clear linear trend appears, supporting the fact that the obtained ratio is closer to unity when the assumed scale height is closer to the actual scale height. GEODYN does not currently have the capability to dynamically adjust the scale height during the arc convergence. The variations shown on Figure 3.3 clearly show that assuming a constant scale height is not correct. However, the choice of reasonable time-variable values would suppose a good *a priori* knowledge of the atmosphere

In reality, POD analysis of the tracking data produces precise estimates of ΔE, the energy lost by friction over one orbit. This quantity does not depend on the *a priori* atmospheric models used, and we obtain reasonably close values after converging the same arcs with various scale heights. The relative uncertainty in ΔE is <5%, rising with time from 1±1% to 2±2% (Figure 3.7). For the most part, this increase is due to the decreasing orbit semi-major axis, and the decrease of the ratio lost frictional energy over total orbit energy.

On the other hand, as said above, the density is better constrained by the accelerometer, because of the high signal-to-noise ratio near periapsis. Thus, a new estimate of the scale height consistent with both the accelerometer periapsis density and the total frictional energy lost in an orbit can be obtained by solving for

$$H_{NEW} \text{ such that } \Delta E(\rho_{ACC}, H_{NEW}) = \Delta E(\rho_{POD}, H_{POD}) \qquad (4)$$

We use the periapsis density determined from the accelerometer data. We choose to use the Accelerometer Team results, for consistency reasons in the following comparison of our estimated scale heights with the Accelerometer Team scale

heights; and because the results obtained by Paul Withers did not take the dependence of C_D on density (transitional regime) into account. We were cautious of wave activity near periapsis for the evaluation of periapsis density.

In order to relate the frictional energy to orbital parameters and density and scale height at periapsis, we use simple orbital mechanics. On an orbit with semi-major axis *a* and eccentricity *e*, the distance to the center of the planet, *r*, is given by:

$$r(\theta) = \frac{a(1-e^2)}{1+e\cos(\theta)}, \quad (5)$$

where θ is the true anomaly ($\theta=0$ at periapsis). Over a short arc length $ds=r.d\theta$ at position θ, the energy lost due to friction is

$$dE(\theta) = \left(\frac{1}{2}C_D\rho(\theta)V(\theta)^2 A\right).ds = \frac{C_D A}{2}\left[\rho_0 \exp\left(-\frac{r(\theta)-r_0}{H_0}\right)\right].\left[GM\left(\frac{2}{r(\theta)}-\frac{1}{a}\right)\right].r(\theta)d\theta \quad (6)$$

When we integrate over θ from $-\pi$ to π (to obtain the total energy loss over one orbit), we obtain:

$$\Delta E = \frac{C_D AGM}{2}\rho_0 f(a,e,r_0,H_0), \quad (7)$$

with

$$f(a,e,r_0,H_0) = \int_{-\pi}^{\pi} \frac{1+2e\cos(\theta)+e^2}{1+e\cos(\theta)} \exp\left(-\frac{\frac{a(1-e^{2)}}{1+e\cos(\theta)}-r_0}{H_0}\right) d\theta \quad (8)$$

Thus, the new estimate of the scale height has to satisfy:

$$H_{NEW} \text{ such that } f(a,e,r_0,H_{NEW}) = \frac{\rho_{POD}}{\rho_{ACC}} f(a,e,r_0,H_{POD}) \quad (9)$$

For each aerobraking arc, we performed a least-square inversion to obtain the scale height that best fits the results obtained with all the probed *a priori* scale heights. The uncertainty was estimated from the scatter of scale heights inferred from individual *a priori* scale heights around that best-fit value (see Figure 3.5 for

explanation). The comparison between the POD and the accelerometer results is shown in Figure 3.6.

We processed the entire aerobraking dataset using 12 model scale heights (from 4 to 15 km, every kilometer), so that the uncertainties (σ_{POD}) are small: 350±150 m, with a maximum of 900 m. These uncertainties are mostly due to uncertainties in ΔE, and thus follow the same trend, increasing with time from 1.5±1% to 4±3% (Figure 3.7). They cannot be compared to the uncertainties published by the Accelerometer Team (σ_{ACC}), which measure the departure of the actual density profile from an exponential one. With POD it is not possible to obtain density measurements at high spatial and temporal resolution because of the scarcity of radio tracking data relative to the number of parameters that would need to be estimated. Thus, our uncertainties represent the level of confidence in the exponential profile scale height.

From Figure 3.6, it is clear that for the most part the obtained scale heights are larger than the published Accelerometer Team values. When plotted against each other (Figure 3.8), we observe an almost constant bias offset between the two series: our recovered scale heights are ≈1.7±0.7km larger. This suggests that ΔE would be consistently underestimated from the accelerometer data alone, by about ≈9±3.5%. Furthermore, about 86% of the Accelerometer Team scale heights do not fall within 3-sigma of our determined values.

It is important to note that when the assumption of an exponential atmosphere is verified (low σ_{ACC}), the scale heights obtained from both methods are in good agreement. All of the periapsis passes with $\sigma_{ACC}<\sigma_{POD}$ (nine total) had scale height differences less than σ_{POD}. About 95% of the periapses with $\sigma_{ACC}<2\sigma_{POD}$ (23 total) had scale height differences less then $2\sigma_{POD}$. This percentage decreases to ~68% for $\sigma_{ACC}<3\sigma_{POD}$ (38 total), but these numbers indicate that the scale heights recovered by POD are representative of the atmospheric density structure. When the atmosphere does not strictly follow an exponential profile, it still

provides a picture of the effective drag environment experienced by the spacecraft during periapsis.

When no accelerometer data are available, these estimates would provide better constraints on scale heights than the values derived from the accelerometer experiments. Indeed, if we use a simple exponential model, the POD scale heights will lead to the correct amount of orbital energy lost by friction, whereas lower scale heights (accelerometer) would underestimate it. The POD approach would be more appropriate to model the atmospheric structure from a navigation or orbit lifetime perspective. In the case of the Earth, early models based on satellite drag measurements (e.g., Jacchia models, Jacchia [1964]) are still used operationally by various organizations (US. Air Force Space Command, NASA Marshall Space Flight Center, Marcos [2006]; Marcos et al. [2006]). More recent models based on direct neutral density measurements (e.g., based on MSIS, Mass Spectrometer and Incoherent Scatter , Hedin et al. [1977]) are more expensive computationally and do not lead to better accuracy (Marcos [2006]). In terms of orbit lifetime, the MSIS model tends to postpone the reentry date (Pardini and Anselmo [2004]).

The density and scale heights near periapsis during the Mars Odyssey aerobraking can to first order be fitted linearly with latitude. The 1-σ fitting error for the scale height is about 13%, or 1.7 km, whereas for the density (in log scale) σ is close to 40%. Thus, if no accelerometer data is available, estimates of reasonable accuracy obtained from radio tracking data can be used to constrain the spacecraft drag environment.

3.5 Conclusion

We have demonstrated using observations from Mars Odyssey how Precision Orbit Determination can be used to build on results from the accelerometer instrument during aerobraking to understand better the density structure of the Martian atmosphere. Based on the X-band radio tracking data, we were able to tightly constrain the amount of energy lost by friction during each passage through periapsis. Although the density cannot be estimated directly because of the dependence of our results on the *a priori* atmospheric models used, the trajectory arcs prove useful to obtain improved estimates of the atmospheric scale height near periapsis. The effective atmospheric structure derived from POD consistently shows larger scale heights than those inferred from accelerometer data alone. This technique, which could be applied to other spacecraft with an accelerometer experiment (such as MGS and MRO), can be useful for engineering and navigation purposes. Indeed, the temporal resolution of our measurements (one per orbit) is very poor compared to the accelerometer (typically 1 per second), but the observations relate directly to the effective energy lost by the spacecraft drag passes. The radio science measurements constitute a dataset which could be used to estimate the effects of atmospheric drag on the orbit when no accelerometer data is available, and yield accurate atmospheric density estimates when the atmosphere is well approximated by an exponential density structure.

3.6 Nomenclature

A	=	spacecraft cross-section
a	=	semi-major axis
C_D	=	drag coefficient
C_R	=	radiation coefficient
e	=	orbital eccentricity
E_i	=	orbital energy of aerobraking orbit *i*
G	=	gravitational constant
θ	=	orbital true anomaly
H	=	atmospheric scale height
M	=	mass of Mars
ρ	=	atmospheric density
ρ_0	=	atmospheric density at the reference altitude z_0
r	=	distance to Mars center of mass
r_0	=	reference distance to Mars center of mass
σ_{ACC}	=	sigma for the atmospheric scale height published by the Accelerometer Team
σ_{POD}	=	uncertainty on the atmospheric scale height obtained from this study
z	=	altitude above reference ellipsoid
z_0	=	reference altitude above reference ellipsoid

3.7 References

Bruinsma, S., and F. G. Lemoine, "A preliminary semiempirical thermosphere model of Mars: DTM-Mars," Journal of Geophysical Research, 107, 2002.

Forbes, J. M., S. Bruinsma, and F. G. Lemoine, "Solar rotation effects in the thermospheres of Mars and Earth," Science, 312, 2006, pp.1366 – 1368.

Hedin, A. E., C. A. Reber, G. P. Newton, N. W. Spencer, H. C. Brinton, H. G. Mayr, and W. E. Potter, "A global thermospheric model based on mass spectrometer and incoherent scatter data: MSIS 2 composition", Journal of Geophysical Research, 82, 2148, 1977.

Jacchia, L. G., “Static-Diffusion Models of the Upper Atmosphere with Empirical Temperature Profiles”, SAO Special Report No. 170, 1964.

Jacobson, R. A., “Ephemerides of the Martian Satellites”, Tech. Rep. JPL IOM 312.1-95-142, JPL, 1995.

Keating, G. M., J. R. Murphy, R. F. Beebe and L. F. Huber, ODY-M-ACCEL-5-ALTITUDE-V1.0, NASA Planetary Data System, 2004.

Keating, G. M., S. W. Bougher, R. W. Zurek, R. H. Tolson, G. J. Cancro, S. N. Noll, J. S. Parker, T. J. Schellenberg, R. W. Shane, B. L. Wilkerson, J. R. Murphy, J. L. Hollingsworth, R. M. Haberle, M. Joshi, J. C. Pearl, B. J. Conrath, M. D. Smith, R. T. Clancy, R. C. Blanchard, R. G. Wilmoth, D. F. Rault, T. Z. Martin, D. T. Lyons, P. B. Esposito, M. D. Johnston, C. W. Whetzel, C. G. Justus, and J. M. Babicke, “The Structure of the Upper Atmosphere of Mars: In Situ Accelerometer Measurements from Mars Global Surveyor,” Science, 279, 1998, p.1672.

King-Hele, D., Satellite Orbits in an Atmosphere: Theory and Applications, Blackie, Glasgow, 1987.

Konopliv, A. S., C. F. Yoder, E. M. Standish, D.-N. Yuan, and W. L. Sjogren, “A Global Solution for the Mars Static and Seasonal Gravity, Mars Orientation, Phobos and Deimos Masses, and Mars Ephemeris,” Icarus, 2006.

Lemoine, F.G., “MGM1041c Gravity Model, Mars Global Surveyor Radio Science Archival Volume MGS-M-RSS-5-SDP-V1/mors_1021,” URL: http://pds-geosciences.wustl.edu/geodata/mgs-m-rss-5-sdp-v1/mors_1021/sha/ [cited 22 February 2007].

Lemoine, F. G., S. Bruinsma, D. S. Chinn and J. M. Forbes, “Thermospheric Studies with Mars Global Surveyor,” Journal of Spacecraft and Rockets, to be published in the same Special Issue.

Lemoine, F. G, D. E. Smith, D. D. Rowlands, M. T. Zuber, G. A. Neumann, D. S. Chin and D. E. Pavlis, “An improved solution of the gravity field of Mars (GMM-2B) from Mars Global Surveyor”, Journal of Geophysical Research, 106, 2001, pp. 23,359 – 23,376, 2001.

Marcos, F. A., “New Satellite Drag Modeling Capabilities”, 44th AIAA Aerospace Sciences Meeting, Reno, Nevada, January 9-12 2006.

Marcos, F. A., B. R. Bowman, and R. E. Sheehan, “Accuracy of Earth’s Thermospheric Neutral Density Models”, AIAA Astrodynamics Specialist Conference, Keystone, Colorado, August 21-24 2006.

Mazarico, E., M. T. Zuber, F. G. Lemoine and D. E. Smith, “Martian exospheric density using Mars Odyssey radio tracking data,” Journal of Geophysical Research, 112, 5014, 2007.

Pardini, C., and L. Anselmo, “On the accuracy of satellite reentry predictions”, Advances in Space Research, 34, 1038, 2004.

Pavlis, D. E., S. G. Poulose and J. J. McCarthy, “GEODYN operations manuals,” contractor report, SGT Inc., Greenbelt, Maryland, 2006.

Standish, D. E., X. X. Newhall, J. G. Williams and W. M. Folkner, “JPL Planetary and Lunar Ephemerides, DE410”, Tech. Rep. JPL IOM 312.N.03-007, JPL, 2003.

Stewart, A. I. F., “Revised time dependent model of the Martian atmosphere for use in orbit lifetime and sustenance studies”, Tech. Rep. JPL PO NQ-802429, University of Colorado, 1987.

Tolson, R. H., G. M. Keating, B. E. George, P. E. Escalera, M. R. Werner, A. M. Dwyer, and J. L. Hanna, “Application of Accelerometer Data to Mars Odyssey Aerobraking and Atmospheric Modeling,” Journal of Spacecraft and Rockets, 42, 2005, pp. 435–443.

Tracadas, P.W., M. T. Zuber, D. E. Smith and F. G. Lemoine, “Density Structure of the upper thermosphere of Mars from measurements of air drag on the Mars Global Surveyor spacecraft,” Journal of Geophysical Research, 106, 2001, pp. 23349 – 23358.

Withers, P. G., “Mars Global Surveyor and Mars Odyssey Accelerometer observations of the Martian upper atmosphere during aerobraking,” Geophysical Research Letters, 33, 2006. (Withers 2006a)

Withers, P. G., “Rapid data products from the ODY ACC experiment generated in support of MRO aerobraking,” URL: http://sirius.bu.edu/withers/odyaccresultformro_v1point0/ [cited 26 July 2006]. (Withers 2006b)

Withers, P. G., S. W. Bougher, and G. M. Keating, “The effects of topographically controlled thermal tides in the Martian upper atmosphere as seen by MGS Accelerometer,” Icarus, 164, 2003, pp. 14–32.

3.8 Figures

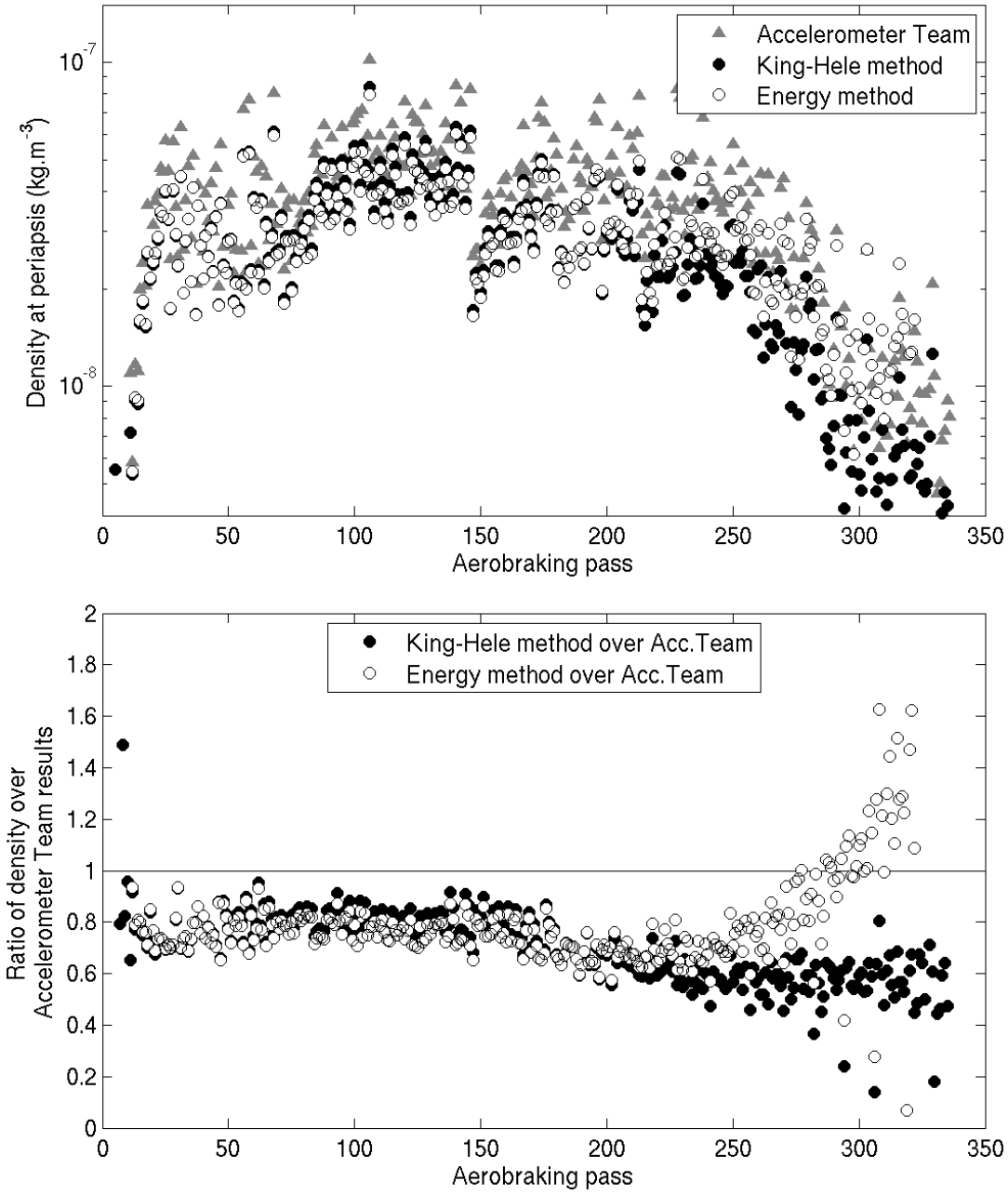

Figure 3.1 (a) Densities at Mars Odyssey periapsis obtained from the two simple methods presented in **Section 3.2.2**, and from the accelerometer experiment. **(b)** shows the ratio of results in (a) to the Accelerometer Team results.

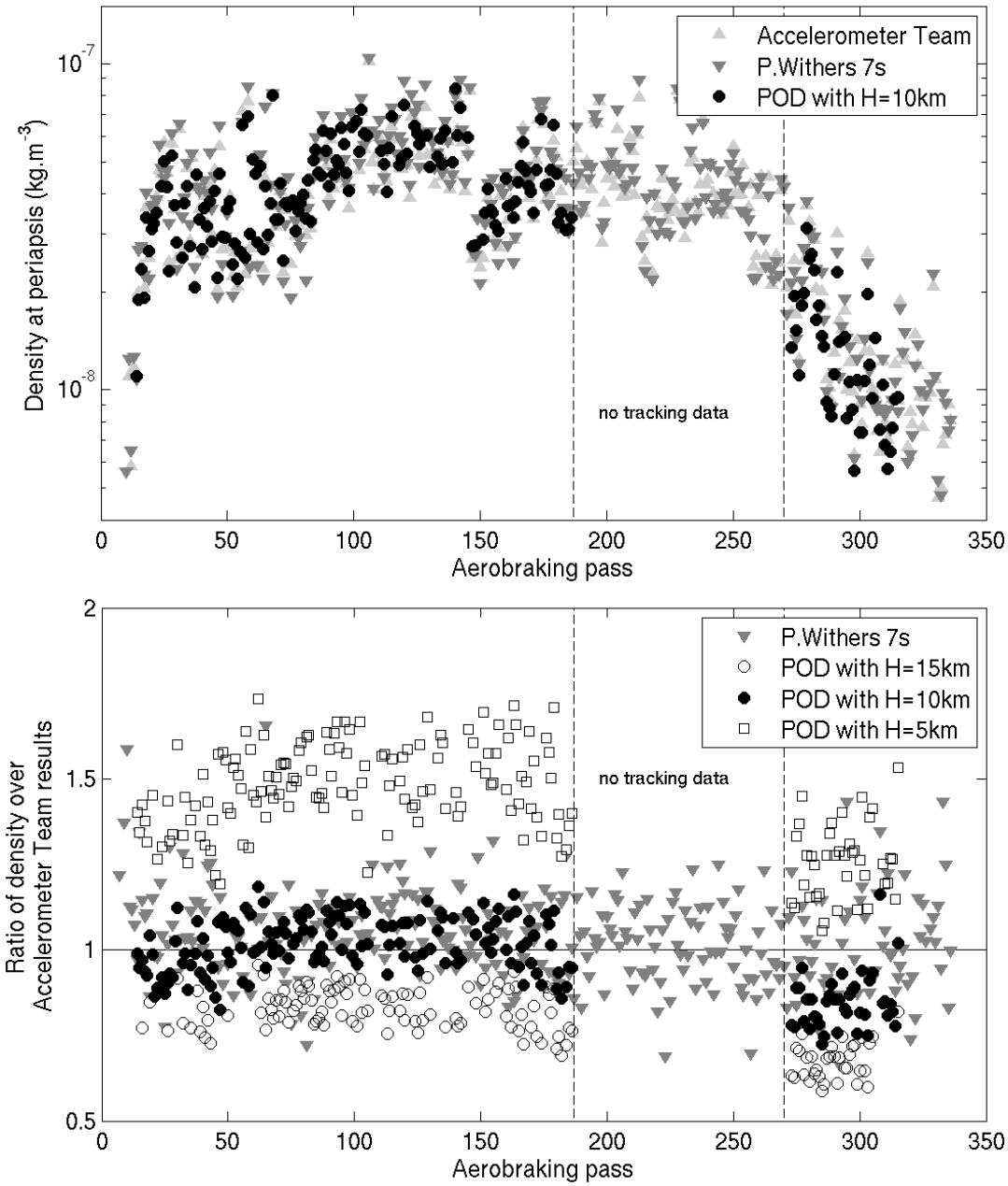

Figure 3.2 (a) Densities at periapsis obtained after POD on the available radio tracking data. Also shown are two results based on accelerometer data. **(b)** As in Figure 3.1b, the ratio of densities obtained from POD assuming various scale heights over the Accelerometer Team result. For reference, the figure also shows the ratio of results from reprocessed accelerometer data over the previously published values.

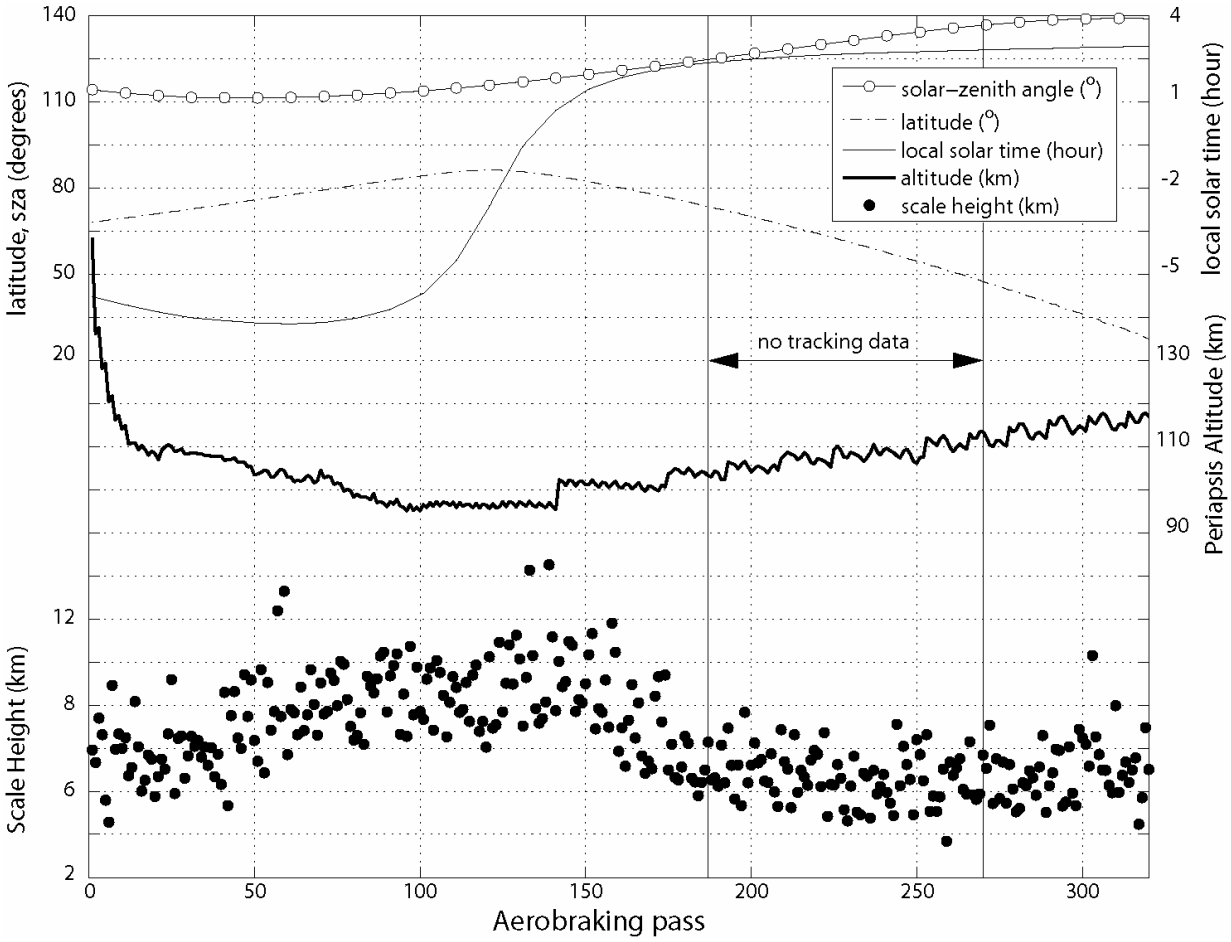

Figure 3.3 Scale height obtained from the Accelerometer Experiment (solid circles) versus orbit number. Also plotted are the parameters that influence the atmospheric scale height: solar-zenith angle, latitude, local solar time and altitude. The values are given at periapsis. The region of the atmosphere sampled changes significantly during the tracking data gap, going in latitudes from ≈70-80°N to ≈30-50°N.

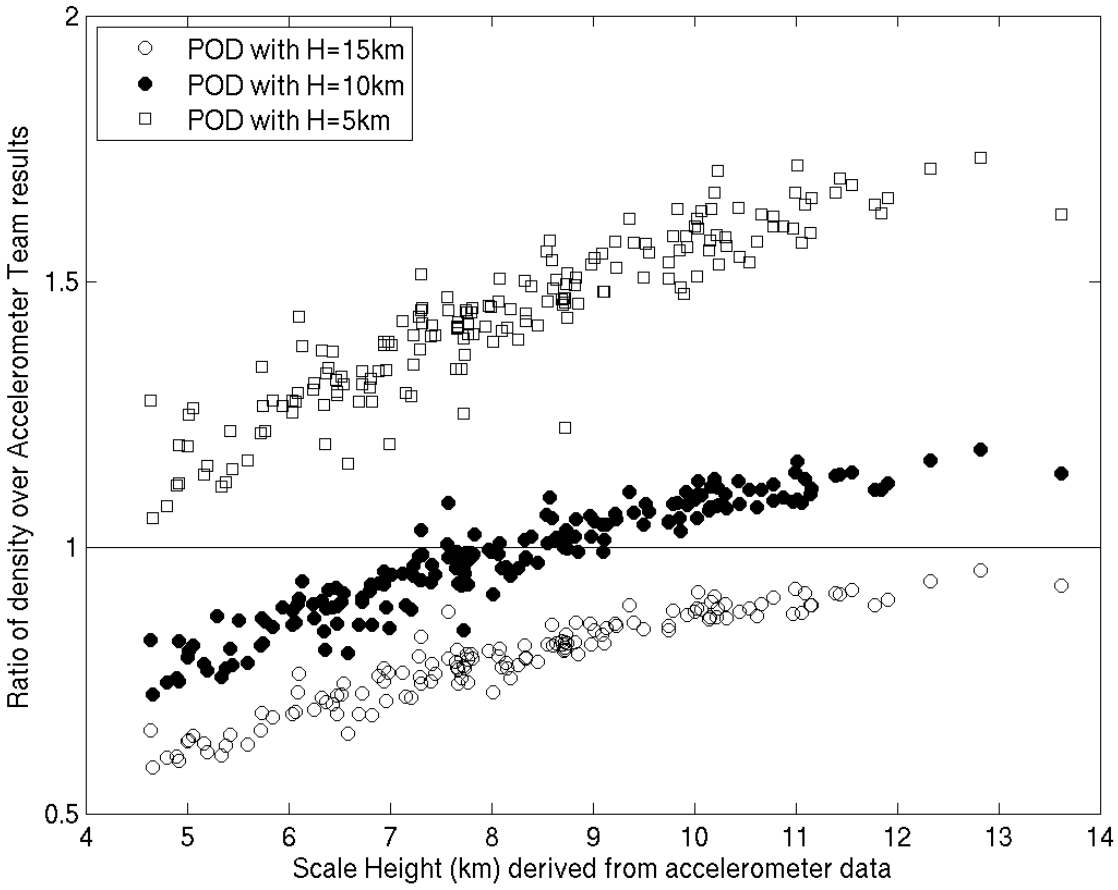

Figure 3.4 Ratio of densities obtained from POD (assuming scale heights of 5, 10 and 15 km) over the results from the Accelerometer Team, against the scale height estimated from accelerometer data.

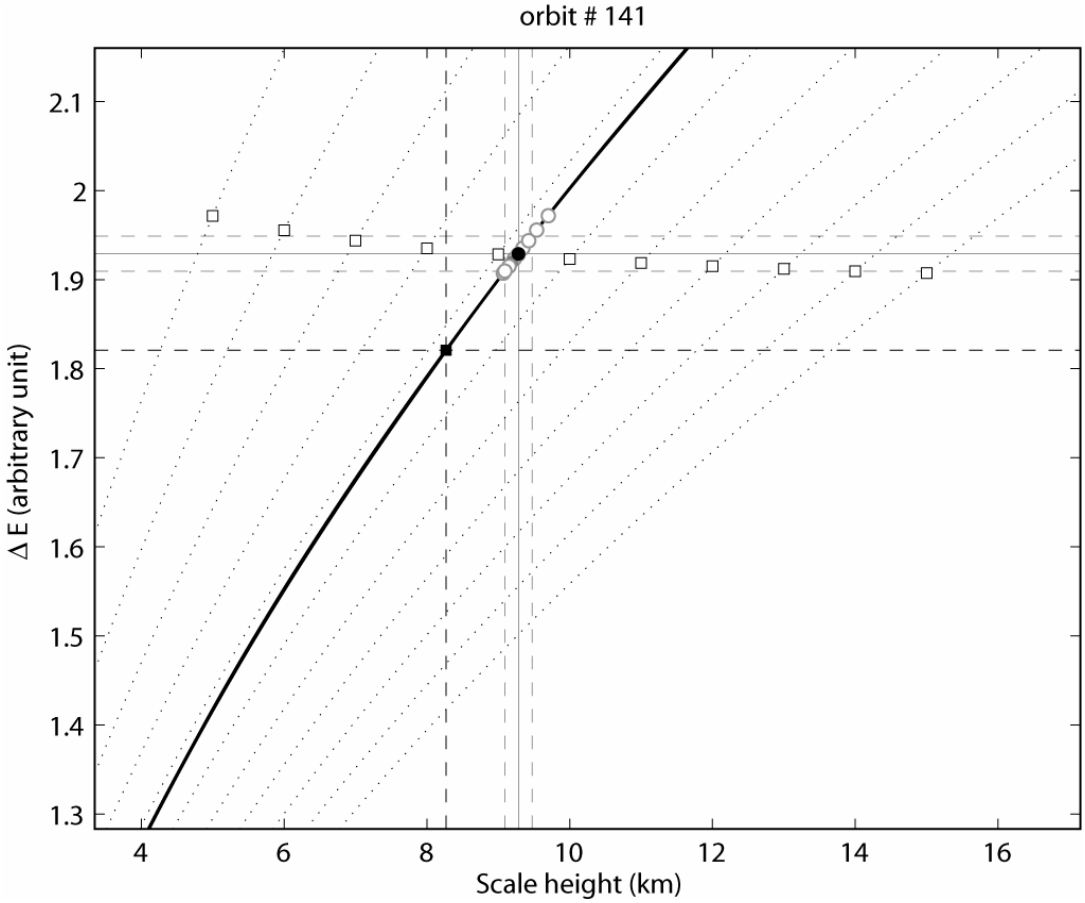

Figure 3.5 Technique used to obtain new estimates of the atmospheric scale height. This example is based on orbit #141. The various curves relate the frictional energy to the scale height, given a particular density at periapsis. The thick solid line shows such a curve with the density at periapsis measured by the accelerometer. The solid square is placed at the accelerometer-derived scale height, and gives the ΔE lost by friction that can be inferred from the accelerometer results. The dotted lines and open squares are the same, for the various GEODYN runs. Each GEODYN-measured ΔE is used to infer a new scale height (open circles) consistent with the accelerometer periapsis density. These new values are used to calculate a least-square best-fit (solid circle) and associated sigma (vertical dashed light-grey lines).

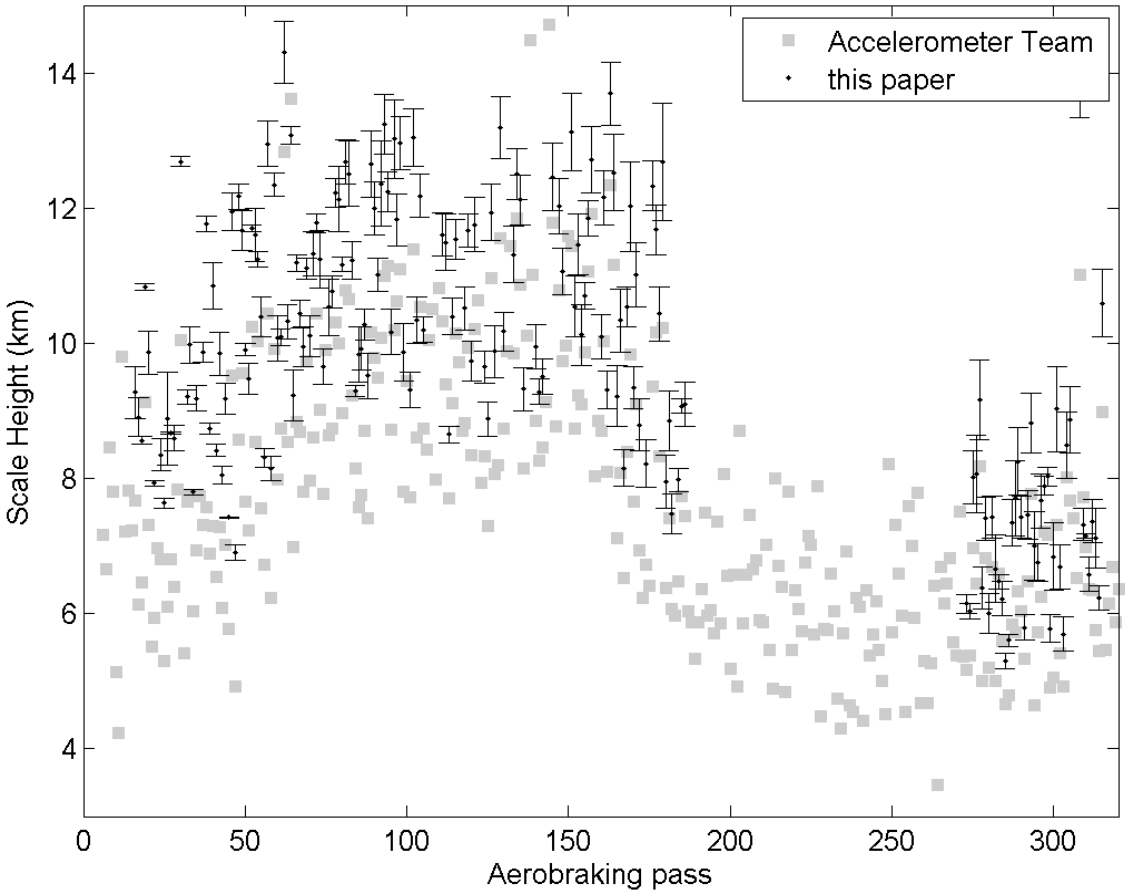

Figure 3.6 Scale heights obtained from POD, with their 1-sigma uncertainties, and scale height values inferred from the accelerometer experiment (light grey squares, uncertainties are not shown but are ≈1.9±1.6 km).

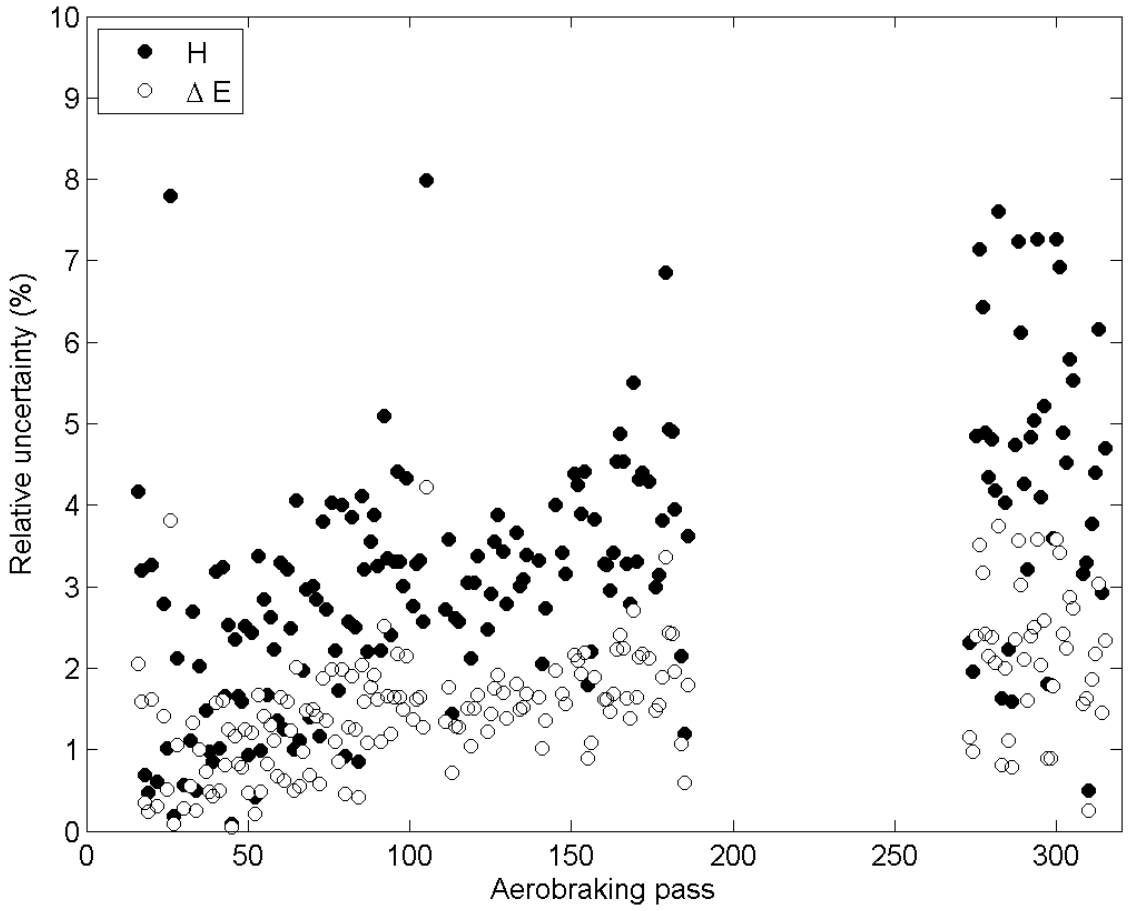

Figure 3.7 Relative uncertainties (in percent) of the recovered scale height (*H*, solid circles) and of the frictional energy lost during the aerobraking pass (*ΔE*, open circles).

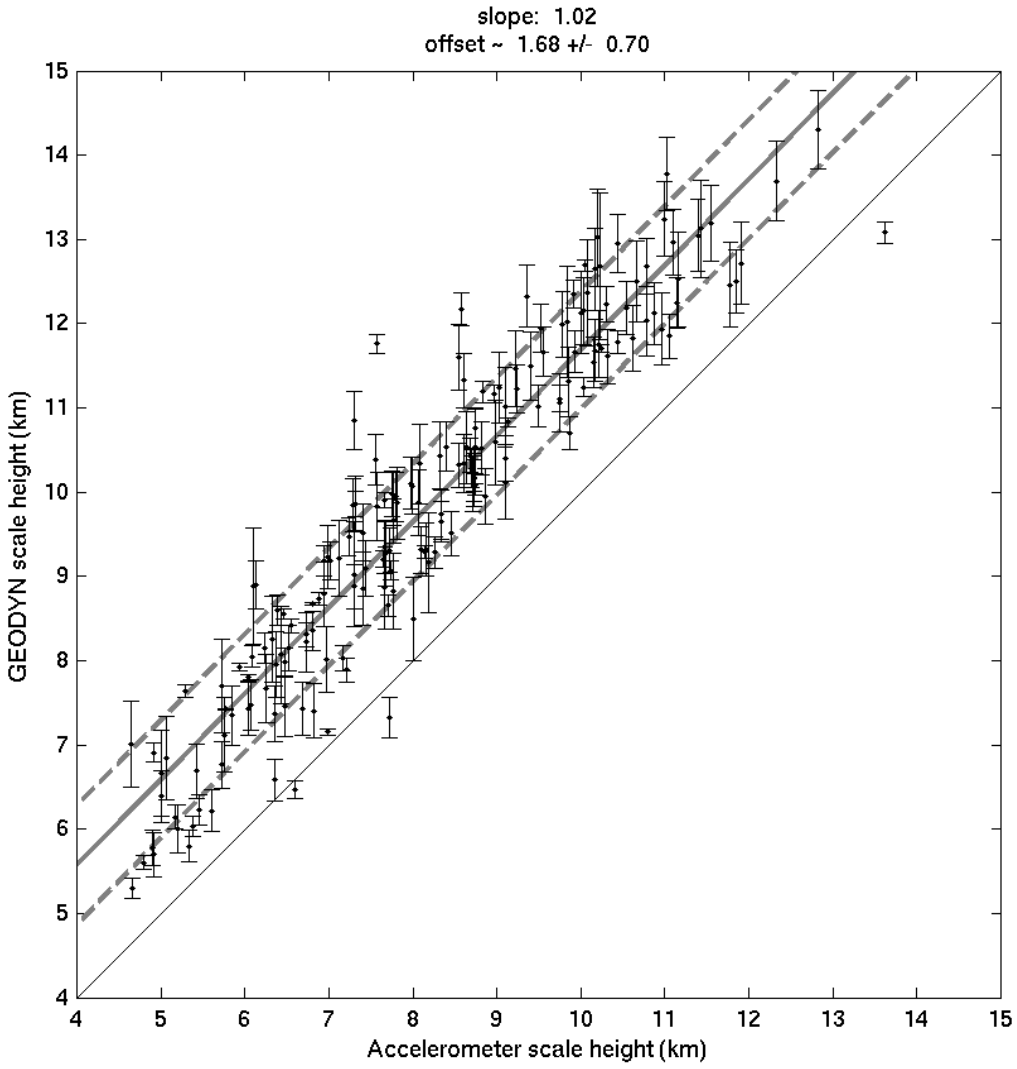

Figure 3.8 Comparison of the POD-obtained scale heights versus the published accelerometer team values. The thick dark grey lines represent the best linear fit (dashed lines show 1-sigma uncertainties). The thin solid dark line represents the 1:1 line. The scale heights obtained from the tracking data are biased by ≈+1.7km.

[THIS PAGE INTENTIONALLY LEFT BLANK]

Chapter 4

Atmospheric Density at 250km altitude with Mars Reconnaissance Orbiter Radio Science

4.0 Abstract

We present the atmospheric density results obtained from more than one Earth year of Mars Reconnaissance Orbiter spacecraft (MRO) radio tracking data. The stronger signature of atmospheric drag in the MRO Doppler data, compared to the Mars Global Surveyor and Mars Odyssey missions, enables density estimation at higher temporal frequency, up to once every 2 orbits (~4h). We processed the high quality, 1-second Doppler tracking data in short arcs using the GEODYN program, starting after the October 2006 solar conjunction. We first used long-arc durations (desaturation maneuvers are separated by 2 to 3 days), but the Doppler residual root mean square (RMS) started to deteriorate in April-May 2007. As a result, we shortened the arcs, allowing no data gap greater than 5 hours and no desaturation maneuver. The resulting Doppler residual RMS is low (0.7-0.8mm/s) and stable from arc to arc. To assess the robustness of the density measurements and to evaluate their temporal variability, we processed the tracking data using various adjustable physical parameters and different *a priori* atmospheric models (Stewart 1987 and the recent MCD4.2). We observed a large and sudden density increase starting June 2007 with the formation of a dust storm, also observed in the lower atmosphere by remote sensing instruments such as MCS on MRO and THEMIS on Mars Odyssey. We calculate the density variability at different timescales from a set of density time series (2, 3, 4 and 6 orbits). The scatter and formal uncertainty of the density measurements increase when we decrease the estimation periods. The highest estimation frequency is used to study the

longitudinal density structure. The current seasonal trend of increasing atmospheric density is clearly visible in our results, from 10^{-13}kg.m^{-3} in November 2006 to 8.10^{-13}kg.m^{-3} in June 2007 (at 250km altitude above the South Pole). Contrary to previous MGS and Odyssey results, we do not detect the solar rotation periodicity in the density time series, because of low solar activity and perhaps the temporal and spatial characteristics of the density sampling.

4.1 Introduction

In this paper, we study the upper Martian atmosphere using radio tracking data from the Mars Reconnaissance Orbiter (MRO). Until recently, Precision Orbit Determination (POD) was used during spacecraft Mars missions only to obtain the gravity field of the planet and other geophysical parameters. Previously, Radio Science atmospheric results were limited to occultation studies of the neutral atmosphere and of the ionosphere (Tyler et al. [2001], Hinson et al. [1999]). The Mars Global Surveyor (MGS) and the Mars Odyssey (ODY) spacecraft provided the first opportunities to measure the atmospheric density at very high altitude. With their long mission duration, they were also useful in characterizing the seasonal changes (Smith et al. [2001]) as well as the response of the upper atmosphere to the solar activity (Forbes et al. [2008]).

MRO orbits at a much lower altitude (~250km) than MGS and ODY (~400km), but it is still in the thermosphere/exosphere region. Measuring the neutral density with direct remote sensing methods is difficult at such an altitude, so indirect density estimations through the Precision Orbit Determination (POD) are valuable. For instance, spectrometer measurements can estimate the atomic hydrogen number density from Lyman alpha fluorescence, but physical models are necessary to obtain a total density.

The MRO spacecraft was launched in August 2005 and performed a large burn on March 10, 2006 for Mars Orbit Insertion. After a short period of aerobraking, the primary science phase began in early September 2006. The spacecraft carried a payload of numerous scientific experiments geared towards both the solid and the fluid Mars (Zurek et al. [2007]): the Mars Color Imager (MARCI) to conduct daily global surveys of the atmosphere at UV and visible wavelengths; the Mars Climate Sounder (MCS) to scan the atmosphere up to ~80km with limb and nadir views, and in particular the water vapor content; the Compact Reconnaissance Imaging Spectrometer for Mars (CRISM) to map the planet at moderate resolution (~200m/pixel) and regions of interest at high resolution (~20m/pixel) and to continue the observations made by TES and THEMIS on MGS and Mars Odyssey; the High Resolution Imaging Science Experiment (HiRISE), a 0.5m telescope to map a small portion of the surface at very high resolution (down to 0.25m/pixel), expanding on the work done by MOC on MOLA (Malin et al. [1992]); the Context Imager (CTX) to map 15-20% of the Martian surface during the primary mission at moderate resolution (<10m/pixel); the Shallow Radar (SHARAD), a ground penetrating radar (at 20MHz with a large 10MHz band pass) to study the subsurface ice detected by the Gamma Ray Spectrometer (GRS) on Mars Odyssey (Boynton et al. [2002]). Finally, it also includes a gravity field investigation package (Zuber et al. [2007a]). In addition to being used for geophysical purposes (mainly determining the Martian gravity field with better spatial resolution than what was possible with MGS and ODY, Zuber et al. [2007a]), high quality radio tracking data can provide constraints on the atmospheric drag environment the spacecraft experiences. An experimental Ka-band telecommunication engineering instrument was also launched, but no high quality Ka-band data were available for the current study due to technical difficulties which arose during aerobraking.

We perform Precision Orbit Determination on the MRO spacecraft in order to obtain density measurements at the orbiting altitude. The resulting time series can

provide constraints on modern General Circulation Models (GCMs). Exospheric densities are generally calculated by upward continuation of lower altitude densities using thermospheric models. We also investigate seasonal and solar effects for the period October 2006-September 2007. This was done near 400km altitude with MGS (Forbes et al. [2006]) and ODY (Mazarico et al. [2007]), and a concurrent use with new MRO measurements would be important. However, MGS was lost very early in the MRO mission, and the ongoing analysis of ODY tracking data shows that the density measurement quality has been poor since September 2006 due to orbit geometry. (From the Earth, the orbit during this period was oriented nearly face-on, which provides poor constraints on the along-track accelerations). We characterize a large density enhancement due to a dust storm in the summer of 2007 dust storm is characterized.. Finally, we use the high temporal and spatial resolution of our measurements to study the longitudinal structure of the exosphere.

4.2 Data, arcs and orbit

4.2.1 Data and arcs

In this section, we describe the dataset used to evaluate the density environment of the spacecraft.

To process the tracking data, the trajectory of the spacecraft is cut into a series of ‘arcs’. The timings and lengths of these arcs is entirely arbitrary, but is generally constrained by data coverage and thruster firings. The thruster firings, also called “Angle Momentum Desaturations” (AMD), are frequent, small orbital maneuvers that despin the spacecraft momentum wheels. Those wheels constitute the main component of the spacecraft attitude control system. They are used to stabilize the spacecraft attitude by balancing perturbating torques with wheel angular momentum. Eventually, they reach their angular velocity limit and need to be

'reset'. During that operation, the thrusters are fired in order to cancel the angular momentum created by the wheel despinning. Ideally, there is no net effect on the spacecraft linear and angular momenta, but in reality it results in a small (unknown) acceleration. It is thus preferable to eliminate these events, whenever possible, from orbit reconstruction. However, when those maneuvers are frequent (several times a day), they cannot be avoided during POD. More massive than earlier spacecraft (2180kg at launch, 1325kg after aerobraking), MRO is less sensitive to external perturbation torques. As a result, they only occur once every two or three days, allowing us to create arcs that do not have any AMD events. With MGS and ODY, long arcs (preferred in gravity studies to constrain the long-wavelength harmonics) were necessary to improve the signal-to-noise ratio (SNR) of the adjusted drag coefficients. But in the case of MRO, the density can be estimated at much shorter timescales, and long arcs are not more advantageous. Until March 2007, the MRO solar panels were constantly controlled to face the Sun and maximize the solar power input. Between early March and late June 2007, enough power could be generated keeping them fixed, which reduced the maneuver frequency to once every three days.

Early in the mission (April 2007), 2-3-day long arcs showed an increase in Doppler residual root mean square (RMS) that could be partially resolved by increasing the drag coefficient estimation frequency. Nevertheless, a second set of arcs was created, shorter and with no tracking data gap larger than 5 hours. A comparison between those two arc sets is made in Section 4.2.3.

The radio tracking itself is made through X-band Doppler and Range data, similarly to the MGS (Tyler et al. [2001]) and Mars Odyssey spacecraft (Mase et al. [2005]). In addition, the MRO spacecraft carries a Ka-band transponder as part of an engineering experiment, but after issues during the aerobraking phase, it has not been used during the primary science phase operations. The two downlink

frequencies could have been used to remove the ionospheric delay self-consistently. The data available to the Science Team consist of 1-second averaged arrival times (Range) and frequency residuals (Doppler). The Range data, always sparser than the range rate measurements, are very limited (Figure 4.1). There is a significant amount of 1-way (open-loop) Doppler data. Those data have a lower accuracy because they are synthesized onboard by the Ultra-Stable Oscillator (USO) instead of the controlled frequency source on Earth (generally H-maser clocks). On MRO, the USO has a stability of $\sim 10^{-12}$ over the 10-100s range (S. Asmar, personal communication), much greater than the $\sim 10^{-16}$ value for the H-maser clocks on the ground. For comparison, the USO of MGS and the Sufficiently-Stable Oscillator (SSO) of Mars Odyssey had Allan variances over the same range of respectively $\sim 10^{-13}$ and $\sim 10^{-11}$ (S. Asmar, personal communication). Nevertheless, they are useful in constraining the spacecraft trajectory when no other data are available. Before using the 1-way Doppler in POD, the arcs were first converged with only Range and 2- and 3-way (closed-loop) Doppler data. *A priori* uncertainties for the closed-loop Doppler, open-loop Doppler and Range were respectively set to 0.01 mm/s, 0.02 mm/s and 35.2 range units (~10m). Figures 4.1 and 4.2 show the distribution of tracking observations in types and ground station use for the two arc sets ("short" and "long").

In addition to the radio tracking data, other data types are necessary to perform Precision Orbit Determination: the planetary and moon ephemerides, telemetered quaternions of the spacecraft attitude, firing times of the attitude thrusters, weather data at the ground stations and $F_{10.7}$ proxy for solar activity. Those data were obtained either internally at GSFC or from the JPL MRO project and NAIF servers.

4.2.2 MRO: spacecraft and orbit geometry

The Mars Reconnaissance Orbiter carries a suite of scientific instruments comparable to those onboard the Mars Global Surveyor and the Mars Odyssey spacecraft. As these instruments are major drivers of the mission and orbit design, it is not surprising that their orbits share many similar features. The MRO orbit is quasi-frozen (its periapsis is fixed near the South pole, at ~86°S), retrograde polar and nearly sun-synchronous (constant local mean solar time, LMST, ~3pm) (Figure 4.3). The main difference between MRO and the previous Mars orbiters is its lower orbital altitude, a consequence of the spatial resolution requirements of the Hi-RISE high resolution imaging system onboard. The spacecraft periapsis is near 250km altitude, and the orbital period is ~112 minutes. The maximum orbital altitude difference, between periapsis and apoapsis, is about 60km, due to the low eccentricity (0.81±0.15%). This lower orbit is of great interest as it allows us to probe a different region of the Martian atmosphere than previous missions. While MGS and Mars Odyssey orbited high in the exosphere (Konopliv et al. [2006]), MRO is in the lower part of that uppermost layer of the neutral atmosphere.

Soon after the end of aerobraking and the beginning of the MRO primary science phase in October 2006, the spacecraft went into occultation by the Sun (superior conjunction). Little to no tracking could be analyzed for a period of about two weeks, and the data quality deteriorated shortly before and after the conjunction. Seen from the Earth, Mars was either directly behind the Sun (i.e., no radio link) or so close to the Sun that the signals propagated through the solar plasma. No modeling of the solar plasma is included in the data processing, so the plasma effects appear as increased noise. Tracking data were processed during that period but the arcs have large Doppler RMS and the drag coefficients significant uncertainties. In this study, we only show the results for data posterior to the solar

conjunction ($DOY_{2006} \geq 307$, where DOY_{2006} indicates the time elapsed in days since Jan 0 2006).

The time evolution of the orbit is shown in Figure 4.3. In a previous study (Mazarico et al. [2007]), we identified a strong anti-correlation between the scale factor for the solar radiation during the Mars Odyssey POD (C_R) and β. This angle β is the angle between the orbit and the Earth-Mars line. Here, β does not vary as much and is average (near 45°). Another important variable is the angle α, similar to β but seen from the Earth. α displays increasingly low values, which correspond to a "edge-on" orbit viewing geometry. The line-of-sight component of the spacecraft velocity is maximum, and the determination of the along-track accelerations such as the atmospheric drag is optimal.

4.3 Methods and modeling improvements

4.3.1 POD Method

The Precision Orbit Determination method was presented in detail in Chapter 2 (Section 2.3.3). In this study, we also use the GEODYN orbit determination program developed at the NASA GSFC (Pavlis et al. [2006]), and the setup is very similar to the work done for Mars Odyssey, but some of the models used are different.

The theoretical ephemerides of the Martian moons were updated to numerically integrated orbits fitted to recent high-precision spacecraft observations (Jacobson and Rush [2006]).

We also use more recent inversions of the Mars gravity field. We started by using the JPL model 'jgm95j01' and its related new Mars orientation (Konopliv et al.

[2006]). We then used preliminary results of the MRO Radio Science Team. In particular, the 'momgm0023c' solution is a 100x100 field obtained by adding the MRO tracking data available through August 30, 2007 to the normal equations derived from MGS data (Lemoine, personal communication).

4.3.2 Spacecraft physical model

Following the scheme developed by Marshall and Luthcke [1994], we constructed a macro-model of the spacecraft. The spacecraft properties were taken from Wynn [2004], except for the optical properties. The reflectivity coefficients (diffuse and specular) of the various panels were obtained from the MRO navigation team (Highsmith [2005]), which estimated post-launch values from an energy balance experiment while the spacecraft was on cruise to Mars.

With the large size of its high-gain antenna (~3m in diameter) and of both its solar arrays (about 5m long by 2.5m wide), MRO experiences a significant amount of self-shadowing. During the calculation of the spacecraft cross-sectional area, a surface element can obstruct the view of another panel. If not taken into account, this can lead to important overestimates of the areas of the various plates. A self-shadowing algorithm has been developed and implemented in GEODYN (Chapter 5).

4.3.3 Albedo radiation modeling

We tested a new model for the albedo radiation acceleration (i.e., the reflected solar radiation; we did not modify the planetary thermal radiation models). Previously, zonal seasonal maps of the albedo based on Viking IRTM data were used (Lemoine [1992]). The new model enables higher accuracy by using longitude/latitude albedo maps of arbitrary resolution. Small regions with large

albedo contrasts such as the area surrounding the Hellas basin can be resolved. With the former spherical harmonic description, a very high expansion degree would have been necessary, but at an unacceptable computational cost.

Each sunlit grid node visible by the spacecraft contributes to the total albedo acceleration. In addition to the albedo spatial information, the vectorial summation of the many small accelerations leads to a more precise total acceleration direction. This allows GEODYN to better discriminate between the sources of the observed spacecraft movements.

The albedo maps used here were obtained from MOLA radiometer data (G. Neumann, personal communication). The MOLA measured irradiances were fitted to the TES dataset in order to 'calibrate' the MOLA albedos to the absolutely-calibrated TES albedos. More detail is given in Chapter 6.

4.4 Arc convergence

In this section, we discuss the convergence of the trajectory arcs, i.e. how well the physical models included in GEODYN fit the tracking data observations. We tried different model configurations, varying the tracking data types used, the arcs, the *a priori* spherical harmonics gravity field, the self-shadowing and the albedo model.

In general, the convergence is good and the differences between the various runs small. The RMS of the Doppler residuals is less than 1mm/s for the 2- and 3-way data and below 4mm/s for the 1-way. The RMS of the Range is on the order of 1.5 meters. The adjusted scale coefficients for the solar and albedo radiations (C_R) are well-behaved and close to the expected value of 1.0, indicating that the radiation pressure non-conservative accelerations are modeled appropriately.

However, the C_R time series shows a secular increase, discussed in Section 4.4.6. The most important adjusted parameter is the drag coefficient C_D, because it directly scales our density measurements. The physical value of the aerodynamic drag coefficient of the MRO spacecraft is ~2.15, and was calculated using computational fluid dynamics simulations (Wynn [2005]). Thus, when the computational C_D coefficient is adjusted by GEODYN at a value of 2.15, the measured density is equal to the model density.

$$\rho_{measured} = \rho_{\mathrm{mod}\,el} \cdot \frac{C_D}{2.15} \quad (1)$$

The estimation of the drag coefficients is very stable in general, and provides acceptable estimates down to timescales of two MRO orbits (about 4h). When we tried to obtain more frequent measurements (every orbit), the solution was sensibly degraded and the drag coefficients cannot be trusted physically. The formal uncertainties associated with both C_D and C_R are much larger.

4.4.1 Influence of 1-way data

Contrary to 2- or 3-way Doppler tracking data, where the source of the frequency carrier is a high-accuracy, high-stability clock on Earth, the 1-way Doppler data are derived from an oscillator onboard the spacecraft. The accuracy of MRO's Ultra-Stable Oscillator (USO) is sufficient to use this data type during POD, although we assign them a higher *a priori* uncertainty. Unknown clock biases have to be estimated for each pass and each station, so we only included the 1-way data when 2- and 3-way data gaps were longer than 1 hour to avoid destabilizing the solution. We also added this noisier dataset only once the arc had converged with Range and 2- and 3-way Doppler data.

To assess the importance of 1-way Doppler to the overall arc convergence, we used the "long" arc set because the majority of the data gaps longer than 1h (i.e.,

when 1-way data is used) do not appear in the "short" arc set. The trajectory changes are moderate (~meter-level), but much larger than the differences due to the modeling of the cross-section (Figure 4.5). The 1-way data seem to improve the POD sensibly, although the closed-loop Doppler RMS is basically unchanged and the radiation coefficient C_R is only slightly modified. On the other hand, the drag coefficients are generally better determined, and those occurring during Doppler data gaps can now be adjusted based on actual observations and not simply based on their influence on other drag coefficients.

4.4.2 Arc set comparison

Formal uncertainties in the adjusted C_R are smaller for longer arcs. This is not surprising given that we adjust only one coefficient per arc, whatever its duration; naturally, with a longer arc, more observations are included and the signal to noise (SNR) is improved. The C_R time series shows less scatter with the "long" arc set, although this can be expected because longer adjustment periods will tend to smooth short timescale variations.

Other indicators of POD accuracy tend to favor the "short" arcs, although not considerably. The Doppler residual RMS is also improved with the "short" arcs (0.76±0.10mm/s vs 0.93±0.27mm/s,;1-σ values).

We have no measure of the distance of each of the two orbits to 'truth', given that we can only observe the position differences between the two trajectories. However, we favor the use of the "short" arc set in the remainder of the paper. Indeed, the C_Ds are slightly better determined in the shorter arcs, presumably because of the better overall coverage. Without the 1-way data, the "short" arcs have data coverage of ~44% compared to ~37% for the "long" arcs. After the inclusion of the 1-way data, the difference is less significant (52% vs 50%), but the closed-loop data are preferable. Due to their shorter length, the cumulative errors in the modeling of the non-conservative forces are smaller, and do not affect

the orbit reconstruction as much. Figure 4.6 shows that for the same modeling variations, the orbit changes are smaller in the "short" arc set compared to the "long" arc set. Another example is related to the time period between DOY_{2006}~500 and DOY_{2006}~620, which displays a significant RMS increase due to unmodeled atmospheric density enhancement (discussed later, see Section 4.5.2). Long arcs show RMS values up to 4mm/s whereas the short arcs keep moderate values (~2mm/s).

4.4.3 Influence of the *a priori* gravity field

The fact that MRO orbits at a much lower altitude than MGS and Mars Odyssey makes it more sensitive to gravity perturbations than the other spacecraft. Of course, this is one of the main interests of the mission for the Radio Science gravity experiment (Zuber et al. [2007a]), because higher spatial resolution can be attained during field inversion. The use of older gravity fields as *a priori* can leave gravitational perturbations unaccounted for, which can lead to higher RMS of fit and to errors in the converged trajectory. In addition, it can deteriorate the recovery of desired estimable parameters through leakage. The main adjustable accelerations are the atmospheric drag and the radiation pressure, so the measured densities can be affected.

Figure 4.7 shows the orbit differences between identical arcs using different gravity fields as *a priori*: 'mgm1041c' (Lemoine [2004]), 'jgm95j01' (Konopliv et al. [2006]), 'mromgm0020g' (Zuber et al. [2007b]) and 'mromgm0023c'. Table 4.1 gives a summary of the data used in the various gravity field inversions. The 'mgm1041c' field was obtained in a different, older Mars orientation frame, so the comparison is maybe not entirely appropriate. Nevertheless, the changes in the new Mars orientation frame (Konopliv et al. [2006]) are small. Not surprisingly, the solutions using the two fields inverted with some MRO data ('mromgm0020g'

and ‘mromgm0023c’) have the smallest orbit differences. Although ‘jgm95j01’ performs well, the orbit differences are greater by several meters. Using a gravity solution containing MRO data is also important because it accounts for the resonances to which the MRO orbit is most sensitive.

From the differences induced in the atmospheric drag and solar radiation coefficients, C_D is clearly not as affected as C_R (Figure 4.8). The radial components of the solar radiation, with a direction nearly fixed in inertial space during each arc, appear to be more strongly affected by the gravity anomalies. The variance of C_R around its running mean is improved (reduced) with the newer gravity fields. Moreover, while the variance of C_D, which is intrinsically greater than for C_D, is not uniformly reduced, it can be observed that it is usually lower for ‘mromgm0020g’ and ‘mromgm0023c’ than for ‘jgm95j01’. Consequently, for the atmospheric results presented here, we used the most recent ‘mromgm0023c’, which is best for avoiding aliasing of gravity anomaly perturbations into the atmospheric drag.

4.4.4 Influence of self-shadowing

As discussed in Section 4.3.2, the modeling of the spacecraft self-shadowing during the calculation of the non-conservative accelerations is important because any computational error can be either directly (overestimated atmospheric drag) or indirectly (smearing of the mismodeled solar radiation) translated into a density measurement error.

In terms of orbit differences (Figure 4.9), the addition of self-shadowing does not significantly affect the trajectory, on the order of ~10cm. The “short” arcs show slightly smaller changes, which is reasonable because the impact of non-conservative force mismodeling is proportional to arc length.

Accounting for self-shadowing will always diminish the cross-sectional areas used in the calculation, so in order to have the same adjusted force magnitude the adjusted scaling coefficients will in general have to be larger. As a result, most of the C_D and C_R values are increased, as well as their absolute variance (Figure 4.10). However, some of them are actually decreased, which indicates that the use of self-shadowing can help the POD program balance the various forces in a different, superior way.

4.4.5 Influence of albedo

The albedo model described in Section 4.3.3 was under development until recently, so it was not used as the default model in this study. It is expected to be fully implemented in GEODYN for the processing of the Lunar Reconnaissance Orbiter (LRO) tracking data. With no atmospheric drag, the albedo radiation pressure will be a more important acceleration in that mission.

In the case of MRO, the changes brought to the albedo acceleration could be overshadowed by mismodelings in the density model. Indeed, the modeling improvements only affect the orbit reconstruction very slightly. The radiation coefficient, which is the most sensitive parameter to the new albedo model, is changed by less than 2%, while the C_D varies by only ~0.5%. The orbit differences are also very small, with only ~1mm, ~15cm and ~6cm in the radial, transverse and normal directions respectively. However, while the radial and normal orbit differences are approximately constant, the transverse component shows a tenfold increase. Even though the cross-track is usually sensitive to the direct solar radiation, and the C_R coefficient increases with time as well, the C_R variation is much smaller in amplitude, so this sensible cross-track orbit difference could be related to a better seasonal modeling of the albedo. While potentially valuable for future studies with other spacecraft, we choose not to implement the

new albedo model for the remainder of this study, given its computational cost compared to the potential benefits to the current work.

4.4.6 "Best run"

After the various assessments described in the previous sections, we selected what appears to be the best of the datasets and models. We used the 1-way data to supplement the closed-loop tracking, which improves the estimation of the drag coefficients. The "short" arcs are better adapted to the purpose of this study, because the cumulative errors in the modeling of the non-conservative forces are smaller. Similarly, to prevent orbit perturbations due to gravity anomalies from altering the retrieved densities, we needed to consider the most recent gravity field expansion. The use of self-shadowing is the most critical when it comes to the estimated C_D values, because those coefficients directly scale to the cross-sectional area. As noted previously, we do not use the algorithm for albedo acceleration calculation because it is currently very expensive computationally compared to the induced changes.

The convergence is good, with RMS generally lower than 2 meters for the Range measurements, and near 0.8mm/s for the closed-loop Doppler (Figure 4.12). The open-loop Doppler RMS, not shown in the figure, is poorer, but still reasonably good (less than 2 mm/s). The scaling coefficients for the non-conservative forces, C_D and C_R, are shown in Figure 4.13, along with their formal uncertainties. The radiation coefficient does not adjust to unity, although it is reasonably close. That means that unmodeled accelerations are incorporated as radiation pressure. That could potentially compromise the confidence in the retrieved drag coefficient values. However, by reconverging a number of arcs (between DOY_{2006}~527 and DOY_{2006}~634) while fixing C_R to 1.0, the drag coefficients were only changed by 0.30±0.24%. That shows quite clearly that although the POD force modeling

could be improved further, the density measurements are undoubtedly robust, because of the low orbital altitude and the resulting high SNR.

During the period from DOY_{2006}~500 to DOY_{2006}~630 (L_S~235 to L_S~320), the Doppler RMS increased dramatically. Several other parameters show what could be called a "regime change". In particular, the C_D variance, even in relative terms (Figure 4.11), increases sharply near DOY_{2006}~540. As it will be shown in Section 4.6.3, this can be clearly attributed to the dust storm activity in summer 2007 in the Southern Hemisphere.

4.5 Derived density time series

As discussed earlier, the drag coefficient is adjusted by the POD program to scale the atmospheric drag acceleration in order to obtain the integrated trajectory to best fit the tracking observations. The drag coefficients themselves are not useful with regard to the atmospheric density, but they do provide a measure of how well the *a priori* atmospheric model used predicts the actual (measured) density. Using Equation (1), we can easily obtain a density time series from the obtained C_D values.

While the full time series of scaled densities could be useful in terms of data assimilation by numerical models such as GCMs, we need to choose a reference to present the results here and evaluate the density changes.

As seen in Section 4.2.2, the orbit of MRO is polar, with a frozen periapsis near the South Pole. The primary contribution to the total atmospheric drag occurs in Southern latitudes, within a few scale heights of the periapsis altitude, and on the day side, because of the higher density levels.

We think a point 250km above the South Pole is a convenient reference for monitoring the atmospheric density, for several reasons. First, it removes any direct ties to the MRO orbit, so resonant perturbations to the eccentricity, changes in periapsis altitude or local solar time (Figure 4.1) will not add unnecessary dependencies and complexity to the density time series, which will only reflect atmosphere-related changes. The fact that the South Pole density is not affected by a solar time factor also simplifies the result interpretation. Second, even though MRO never actually orbits over the South Pole, it passes through the South Pole region every orbit (about two hours). In contrast, it will only orbit over a region near the equator once a day. Using the South Pole as a density reference ensures that the measurement is based on the predicted densities that the spacecraft actually encountered. Finally, the South Pole was already chosen successfully as a reference for Mars Odyssey (Mazarico et al. [2007]), and choosing it for MRO as well could be useful for future comparison studies.

The derived time series were "cleaned", in the sense that the few obviously wrong measurements and the data from poorly-converged arcs were discarded. Figure 4.14 shows the obtained density time series, with drag estimations every two orbits (~4h). Even at the highest measurement frequency, results show low uncertainties and great consistency, with the scatter primarily due to atmospheric variability (Section 4.6.1).

4.5.1 *a priori* atmospheric models used and assessment

The main *a priori* model used during POD is the Stewart model (Stewart [1987]), also shown in Figure 4.14. This model is also the default model in GEODYN, and was used successfully in previous studies of MGS and Mars Odyssey data. In the context of atmospheric drag studies the model was described in detail in Mazarico et al. [2007]. In short, it is a semi-analytical model developed in the late 1980s

based on Viking and Mariner 9 data, mostly acquired near solar minimum. It does include a dependence on the 81-day averaged $F_{10.7}$ proxy through the exospheric temperature, and takes into account the various diffusive properties of nine molecular or atomic species in the heterosphere. Some of those properties have a dependence on local solar time and latitude. To account for dust storms and seasonal surface pressure changes, a reference height bias is used. In Figure 4.14, we can see that while the measured density follows the model during the first ~200 days, it is not driven by it. The slope of the seasonal increase is different, and near DOY_{2006}~450, when the model predicts a very sharp density enhancement related to dust storm activity, the measurement trend is unaffected. This further shows the robustness of our density time series. The Stewart model also seems to slightly overestimate the density outside of dust storm activity (Section 4.5.2).

To provide an independent comparison, we also used the Mars Climate Database v4.2 (MCD4.2, Forget et al. [2007]) as an *a priori*. MCD4.2 is a database of results from numerous GCM runs, and it calculates by interpolation the values of many atmospheric parameters for a given set of inputs (L_S or time, position, dust opacity scenario, solar activity scenario). This model captures a number of atmospheric processes not present in more simple semi-analytical models. This makes it difficult to represent by a single value like for the Stewart model, because it does not have spherical (pseudo-)symmetry. The South Pole is not a reliable reference because of the perturbations that can affect that region without being present along the spacecraft trajectory. In addition to this reference issue, which makes the comparison with the Stewart model very difficult, we find that the RMS of the fit increases, and actually worsens the retrieval of C_R. The added complexity in the density estimates time series does not improve the fit to the tracking observations. MCD4.2 is known to have issues in the South Winter polar night, which corresponds to the beginning of our analysis. The model density is significantly overestimated (by close to one order of magnitude). After POD, the

adjusted densities are reduced and comparable to the values obtained using the Stewart model. The time series shows significant scatter, principally due to the reference issue mentioned above. As a result, we do not discuss the significance in terms of atmospheric science of the results obtained using MCD4.2. Figure 4.15 presents the various densities as well as the predictions of the Mars-GRAM 2000 model (Justus et al. [2000]).

4.5.2 Dust Storm activity

Apart from the seasonal density, the major feature in the time series is the large density enhancement between DOY_{2006}~540 and DOY_{2006}~600 (L_S~260 to L_S~330). This density increase is clearly related to a major dust storm.

The Summer 2007 dust storm occurred in the Southern Hemisphere and was observed and monitored by the THEMIS instrument on Mars Odyssey (Christensen et al. [2004]). The increase in the lower atmosphere heat capacity due to dust loading increased its temperature significantly, resulting in an upward expansion of the high-density lower layers, which lead to global thermospheric density increase.

Several parameters indicate that this period is unusual, with poorer Doppler residual RMS. We observe higher variance of the C_D and C_R coefficients (Figure 4.10) and larger orbit differences (Figure 4.9). The observed density increase also matches a period of higher tracking data residuals, with RMS values up to 3mm/s (Figure 4.12). However, the RMS starts increasing around DOY_{2006}~500, more than a month before the dust storm was visually observed. This could mean that the poorer RMS are due to the higher density levels, at least in part. However, the RMS goes back to nominal values at relatively low densities, after DOY_{2006}~650, which corresponds to DOY_{2006}~400-450 in terms of density. The Stewart model

used is also inadequate as it does not include unusual seasonal atmospheric structures.

To account for such unmodeled features of the drag acceleration, we adjusted empirical along-track accelerations during the orbit determination. These accelerations are periodic, with one cycle per orbit. We solve for the amplitude of one cosine and one sine term, which is equivalent to a cosine with a phase with respect to the angle to periapsis (true anomaly). The RMS is dramatically reduced (Figure 4.12). The densities are relatively unchanged, given the magnitude of the excess acceleration included in these empirical accelerations, and they are arguably improved. However, the adjustment of both these accelerations and the radiation coefficient C_R led to significant changes in C_R compared to the values obtained previously, and to acceleration magnitudes larger than anticipated from the RMS values. This is due to the high correlation with the empirical acceleration and the radiation coefficient. Thus, for each arc, we fixed C_R to the value obtained previously without the empirical acceleration.

Figure 4.16 shows the amplitude and phase of the cyclic along-track accelerations. The shape is reminiscent of the density times series, with a large very sharp jump near DOY_{2006}~540. Interestingly, the adjusted amplitudes grew and became consistent earlier, near DOY_{2006}~480. Prior to this time, the accelerations were very small, which was expected, and changed significantly from arc to arc. Looking at the phase, there seems to be some structure from the start of the time series and even at low amplitudes. After DOY_{2006}~460, the scatter in both amplitude and phase was reduced and the phase remained small. This indicates that the empirical accelerations reach maximum near periapsis (where the maximum drag acceleration occurs), so they contribute to add to the already-modeled atmospheric drag.

Additionally, the large RMS decrease back to nominal levels shows that these empirical accelerations capture virtually all of the unmodeled atmospheric drag. To correct the previous underestimated results we converted the obtained acceleration amplitudes to density. Rigorously, we would add the model drag acceleration and the empirical acceleration in vector form for every timestep along the spacecraft trajectory, divide those accelerations by the appropriate scale ($A/2m C_D V^2$). However, in practice this approach is non-optimal because we essentially add densities at the South Pole at a fixed altitude to densities along the spacecraft trajectory.

Thus, we explored another simplified method. We scaled the previously obtained density values by the ratio of the acceleration amplitude over half the peak-to-peak variation of the drag acceleration. This is reasonable because of the good phasing of both accelerations. The resulting total density (Figure 4.17) displays a sharper density increase due to the dust storm, as well as a greater peak density. In the remainder of the paper, we use this total density.

4.5.3 Increasing the measurement temporal resolution

In the previous atmospheric studies with data from MGS (Forbes et al. [2006]) and Mars Odyssey (Mazarico et al. [2007]), the temporal resolution of the density was very limited. Rather noisy estimates could be obtained once a day (Mazarico et al. [2007]), but generally C_D adjustments were done once per 4-5-day arc.

The lower orbiting altitude of MRO and the increased atmospheric drag (by about two orders of magnitude) enable the accurate recovery of density measurements at unprecedented frequency. Indeed, the C_D estimation periods *need* to be greatly reduced, because the orbit reconstruction deteriorates with periods greater than ~12h. At the start of the MRO primary science phase, corresponding to early

Southern Winter, the density was low, so at the outset density estimates could not be made at very high frequency. However, moving out of winter, the density time series temporal resolution could be significantly improved. The start and stop time of each drag parameter estimation was chosen close to apoapsis, which ensures that periods of high atmospheric drag (near periapsis) do not exhibit discontinuities.

Figure 4.18 shows the density time series obtained for estimations at frequencies of 2, 3, 4 and 6 orbits (one orbit is ~2h). Smoothed, they are virtually indistinguishable, but their variances change significantly. This is indicative of the variability of the atmosphere in the region MRO orbits on such timescales (Section 4.6.1). On the other hand, the C_R and the RMS do not change appreciably, denoting that the POD convergence is consistent.

The temporal resolution directly translates into spatial resolution. Each ~2h orbit corresponds to a density averaging over ~30 degrees of longitude. For MGS and Mars Odyssey, with estimation periods of at least one day, the measurements were globally averaged. Here, for the higher frequencies (one estimation every 2 or 3 orbits), the measurement is confined to a rather small longitudinal region. With larger densities on the dayside due to the day-to-night density contrast, our measurements are more sensitive to the dayside, which provides further localization. In Section 4.6.5, we take advantage of this unprecedented spatial resolution in the total density at 250km altitude.

4.6 Results and Interpretation

In this section, we discuss and interpret the results presented above, and their significance for the knowledge of the Martian lower exospheric region. The high quality of the density time series, both temporally and spatially, enables us to

study new aspects of the atmospheric structure, which was impossible in the case of Mars Odyssey and MGS.

4.6.1 Variability

Because of the slow changes in the predicted South Pole density (Figure 4.17), the trends in the absolute density variance are comparable to the CD variances shown in Figures 4.8, 4.10 and 4.11. However, the atmospheric variability is expressed relative to the mean density. We calculated it by taking a running standard deviation of the residuals to the smoothed density time series. In Figure 4.19, we show the results (smoothed with a 30-day running mean for clarity) for the various time series. The variability at greater periods cannot be measured because drag estimations longer than ~12 hours increase the Doppler residual RMS.

As expected, the atmosphere is less turbulent on longer time scales. This is not an artifact of the longitudinal sampling (see Section 4.6.5), nor of the measurement uncertainty (formal relative sigmas are less than 1% for the 4-hour estimates). After averaging those density variations over longer periods, the obtained time series is smoothed and the observed variability is reduced. The density changes significantly on a timescale of less than 2 orbits (4h). This is consistent with results of Keating et al. [1998] during MGS aerobraking, who found large thermospheric density changes from one orbit to the next. The general level of variability is smaller than observed at the lower MGS aerobraking altitudes (110-160km), although Figure 5 of Keating et al. [1998] shows the two-sigma variability and has an extreme temporal resolution compared to our measurements. Indeed, while the observations were spaced by 27–33 hours (orbital period of MGS), the periapsis densities were measured on very short arcs (<10 minutes). While the largest variability that we observe is about 15% on average, they measured 40-80% background variability. The main difference with Keating et al.

[1998] is the behavior of the variability during the dust storm. Along with increased density, they observed a very large variability augmentation, to about 200%. On the contrary, to first order, the dust storm period does not appear to be very different in our measurements. The variability observed at the MRO altitude is related primarily to the density level, with a strong anti-correlation. With peak densities during the dust storm, the relative variability is actually at a minimum. The high-frequency features produced by the dust storm in the lower atmosphere and up to altitudes comparable to the MGS aerobraking periapses (110 – 130 km) seem to disappear at MRO orbital altitude. The exobase could play a role in regulating the density changes, because of the importance of molecular conduction in the upper atmosphere and of the solar heating in governing the diffusive scale heights of the various molecular species. However, after a study of the complete MGS aerobraking dataset, Withers et al. [2003] found values more consistent with our results, with a sol-to-sol variability at 125 km of 15–20 % not directly attributable to zonal variations.

It is interesting to note that the order of the curves is modified during the dust storm (Figure 4.19, roughly DOY_{2006}~550 to DOY_{2006}~620). The variability levels at 4, 6 and 8 hours are nearly identical (~8%), while the 12-hour variability is not affected (~5%). In order to look in more detail at the dependence of the variability on timescale, we performed a series of linear fits of the variability to the measurement duration, in a sequence of 5- or 10-day time windows. The linear fit is in general very good, and adding a quadratic term does not improve the residuals. The slope of this linear fit is always negative (more variability at shorter timescales). It slowly decreases in absolute value, by 80%, until DOY_{2006}~500-600 before reincreasing rapidly. The fact that the variability seems to decrease linearly with the measurement duration means that the atmosphere is variable on a timescale of less than four hours. The estimation a single density value over a longer duration will average out the short-period features and

decrease the amplitude changes of the recovered density time series. This could be verified with future MRO data if the densities are much higher (for instance with higher solar activity), which would improve the accuracy and stability of 2-hour measurements. If the variability does not increase further at that timescale, it would establish the intrinsic variability timescale and amplitude. Indeed, with only the 4-hour measurements, we cannot rule out that the actual atmospheric variability is greater.

4.6.2 Solar activity

The exosphere is very sensitive to the heating by the solar flux (mainly extreme UV radiation), because molecular species are not in thermal equilibrium. With the very low density, collisions are too rare to homogenize the temperatures.

In addition to the seasonal variations, the density levels are controlled primarily by the solar activity. The previous studies focused on the Martian exosphere, with MGS (Forbes et al. [2006]) and Mars Odyssey (Mazarico et al. [2007]), reported observations of the solar rotation effects on the upper atmosphere densities. Slowly-changing active regions on the Sun produce a radiation forcing on Mars with period equal to ~26 days.

In the density time series obtained here, we do not observe any such period. The lower exospheric region should be sensitive to variations in the incoming solar flux because that is where most of the EUV (Extreme UV) radiation absorption occurs. The energy is then transported upwards, isothermally. Various mitigating factors could explain this non-observation. First, the exobase is located near 200km, so most of the heating energy would be deposited at lower altitudes than where the MRO measurements are made (by a few scale heights). Second, our measurements are very short compared to the solar rotation period, so the intrinsic

density variability could potentially obscure the solar effects. Indeed, the solar flux variations are very small in absolute value during the study period, which corresponds to solar minimum. The relative changes can reach up to 20%, but the absolute solar EUV flux changes by less than 7 s.f.u. (solar flux unit). With the scaling relationships found by Forbes et al. [2006], this would translate to a density change of about 10%, smaller than the atmospheric variability discussed in Section 4.6.1 (except during the dust storm period, but increased dust opacity changes complicate the isolation of the solar rotation effect).

On longer timescales, the exospheric density is controlled primarily by the level of solar radiation. We performed a least-squares regression on the density time series to find its dependence on $F_{10.7}$ and L_S. However, the results are poorly constrained. Indeed, our measurement baseline, about 1 year, is short compared to a Martian year (~668 days) and the solar cycle (11 years). The best-fit phase of the cosine dependence on L_S does not agree with recent results by Forbes et al. [2008] using MGS data. In addition, because the studied period is during solar minimum, the solar activity was very low and did not display a specific signature which could have helped the fitting.

Based on the density results, we can estimate the exospheric temperature, which is the temperature of the nearly isothermal neutral atmosphere above ~220km. To enable the transformation from density to temperature, we assume that we can use the *a priori* atmospheric model. For each arc, we calculate the model density for $F_{10.7}$ values 10 s.f.u. above and 10 s.f.u. below the actual value. As an intermediary step in the density calculation, the exospheric temperature T_{exo} is estimated at each of those solar flux values. We then use a linear interpolation through those three values to match the measured density to an adjusted temperature. As a result, the temperatures we obtain are highly correlated to the density estimates. It should also be noted here that we reprocessed the data with a

modified Stewart model, from which we removed the two 'dust storms'. Indeed, those dust storms were modeled through a reference radius increase, while the model exospheric temperature was unaffected (only dependent on $F_{10.7}$). This perturbed the interpolation significantly during the model dust storm periods. For instance, it lead to an artificial temperature decrease near DOY_{2006}~450 because a large density adjustment was necessary to remove the effect of the first model dust storm, when actually the exospheric temperature estimate was reasonable (the model density without the dust storm was comparable to the measured density).

Figure 4.20 shows the corrected temperatures T_{exo} obtained from the "no dust storm" Stewart model. At the start of the time series, the values are lower than predicted by both the Stewart [1987] and Bougher et al. [1990], but are more consistent after DOY_{2006}~450. The dust storm occurring between DOY_{2006}~540 and DOY_{2006}~600 corresponds to a large temperature enhancement of 60K from ~200K to ~260K (~25%). With a dust opacity of ~0.4 with peak values greater than 1.0 (Michael Smith, personal communication), this is consistent with past observations, such as those by Mariner 9 with an anomaly of ~75K (Bougher et al. [1993]) after a dust storm of peak opacity ~1.5 (Fenton et al. [1997]) and by MGS with an increase in T_{exo} of ~30K after the small 1998 dust storm (Bougher et al. [2000]) with a dust opacity of ~0.3 (Keating et al. [1998]). Here again, due to the limited time series duration, the fit of temperature with respect to $F_{10.7}$ and L_S is not satisfying.

4.6.3 Scale Height

In the analysis of Mars Odyssey tracking data, Mazarico et al. [2007] used a method to calculate analytically the best-fit scale height near the periapsis, based on a series of POD convergences that assumed an exponential density profile, varying the *a priori* scale heights. The estimated scale heights were well-

constrained and stable when some of the *a priori* scale heights were not included in the calculation.

We reiterated this method with MRO data, but the retrieved scale heights were poorly determined and unstable. This indicates that the atmosphere near 250km does not behave as a simple exponential atmosphere. However, as noted in Section 4.5.2, the simple Stewart model performs well in terms of POD modeling compared to recent, more sophisticated models. One way to reconcile these two points is that the Stewart model may capture the critical processes of the exospheric region, i.e. differential diffusion of the various atmospheric species and solar time dependence (day-to-night density contrast).

The first approach we used to obtain estimates of an effective scale height near 250km was to assume that the exospheric temperature entirely sets the density profile. Atomic oxygen is the major component of the atmosphere at MRO's orbital altitude (Stewart [1987], Krasnopolsky [2002]), so to first order we used the diffusion scale height of atomic oxygen, estimated from the exospheric temperature through:

$$H = {kT}/{Mg} \tag{4}$$

where k is the gas constant, M is the mean molecular mass (M_O=16g.mol^{-1}) and g the gravitational acceleration.

The values we obtain are very large (~35km) and rather dubious with regards to the predictions of the model (20-25km). Rather than M=16g.mol^{-1}, we used M~20g.mol^{-1} which corresponds to a mixture of ~83% O, ~8% CO_2 and ~8% N_2 (in relative number density, based on Figure 1 of Krasnopolsky [2002]), but the results were not improved significantly.

As we observed after using the King-Hele method, the atmosphere does not seem to behave like simple exponential atmosphere where atmospheric scale height and

temperature are closely related. Thus, we used the density values at 240 and 260km (adjusted by C_R like our measurements at 250km) to estimate the effective sale height (Figure 4.21). Similarly to the density, the dust storm plays a significant role in increasing the scale height, showing that the upper atmosphere is not simply responding to an increased density level at the exobase as a boundary condition, but is modifying its structure as well.

4.6.4 Dust storm

In the previous sections, we already presented the increases in density, temperature and scale height which are indicative of the Summer 2007 dust storm. The densities suggest a dust storm stronger than those observed by Viking upon which the Stewart model is based (Figure 4.17). Indeed, the dust opacity at 9μm reached values greater than 1.5 (Michael Smith, personal communication), compared to ~3 for the second Viking dust storm (Hunt [1979]) and >2 peak values for the 2001 dust storm (Michael Smith, personal communication).

The timing of the exospheric density increase upper atmosphere is also interesting to better understand the coupling between lower and upper atmosphere. The first thermal observations of the dust storm by the MCS instrument on MRO occurred on June 24-25, 2007 (DOY_{2006}=540-541), and within 6 days the lower atmosphere warmed up by 20-40K (Kass et al. [2007]).

We observe almost no time lag at the onset of the dust storm, with the density increase starting near DOY_{2006}=540. However, the density increase seems to last longer, with a first very sharp initial rise from ~7.10^{-13}kg.m^{-3} to ~$12.x10^{-13}$kg.m^{-3} between DOY_{2006}=540 and DOY_{2006}=550, and a slower increase from $1.2.10^{-12}$kg.m^{-3} to $1.35.10^{-12}$kg.m^{-3} in the following 10 days. The typical dust storm implemented in the Stewart model does not show such break in the slope and

reaches maximum density after less than 15 days, with a faster growth at the beginning of ~5.10^{-13}kg.m^{-3} in 6 days. By the end of our analysis period, the dust storm density enhancement has not completely subsided. The exponential decay time is approximately 50 days/sols, comparable to previous estimates (Cantor [2007]).

Another interesting feature is the decrease in density just before the dust storm occurs. It is not currently explained, but it is presumably not linked to the dust storm itself. It may be the long-tail of an earlier dust phenomenon starting near DOY_{2006}~450 visible in Figure 4.22; dust opacity is also observed to decrease just prior to the dust storm by the THEMIS instrument (Michael Smith, personal communication).

4.6.5 Longitudinal structure

The 4-hour density time series contains about 1500 separate density estimations, which span almost a year. We can use this dataset to study details of the atmospheric structure, taking advantage of the spatial and temporal resolutions, unprecedented in POD atmospheric studies at high altitude.

The adjusted densities are weighted towards the Southern hemisphere due to the slightly eccentricity of MRO orbit and to the periapsis location near the South Pole. Because of the day-to-night density contrast, the measurements are also weighted towards the dayside hemisphere. Thus, we assume here that the density values are representative of the densities at the dayside equator-crossing longitudes. Moreover, the range of longitudes sampled by the spacecraft from pole to pole is small (about 7 degrees), as well as the difference in longitude from equator to the periapsis of course. Other time series with lower estimation

frequencies than 4 hours are not appropriate for this study because they measure the density over too large a region to resolve longitudinal differences.

In the 4-hour time series, we examined the longitudinal density variations in various time periods. We used the relative density residuals, obtained after removing the density general trend (from a 20-day running mean) and dividing by the mean value of the density in this time period (the results are unchanged if we use the smoothed value).
The time periods for the fits must be long enough in order to obtain a reasonable sampling in longitude and to mitigate the large density variability (Section 4.6.1), but not too long to avoid excessive temporal smoothing of the time-dependent wave structures. We varied the duration of the time periods and found that a 60-day window is a good compromise. The patterns are robust and very consistent with the estimates obtained from longer duration windows in periods where the wave structures appear stable. In addition, there are generally 10 to 15 data points in each 15° longitude bin. With lower durations, mean values are not well determined and compromise the results of the fit.

We then fitted a wave pattern to those density residuals (and not the binned mean values; the results would be nearly identical). In addition to the very prominent ‘wave 2’ signal, we solved for ‘wave 1’ parameters because it decreased the misfits substantially (more than 50% at times), unlike higher orders. We note that Keating et al. [1998] also found that wavenumbers 1 and 2 provided a good fit to the density wave observed at 125km (their Figure 6).

Even though the 60-day window used necessarily leads to slow changes in those parameters, they are persistent and thus not due to random residual distribution. This is clearly visible in Figure 4.23, where we show two examples for time periods centered at DOY_{2006}=420 and DOY_{2006}=570 respectively. In the first one,

the relative variability was much higher (Figure 4.19) so the wave pattern is not obvious from the raw density measurements. However, the mean values are well-behaved and well fitted by the two waves. In the second period with lower variability, the 'wave 2' periodic sign is obvious (even though wave 1 is important to have a good fit).

Figure 4.24 shows the least-squares best-fit values for the amplitude and phase of the two waves. We also estimated their uncertainties from the bootstrap method. The estimates are generally accurate, except at the beginning of the time series (until DOY_{2006}~410). Both amplitude and phase are poorly constrained when the amplitude is small. More interestingly, at those times, the wave seems to change polarity. The 'wave 2' just has one such reversal, but 'wave 1' experiences three, plus one failed reversal near DOY_{2006}~360. From the amplitudes, we can see that 'wave 2' is dominant, but 'wave 1' is significant after DOY_{2006}~460. 'Wave 1' is very stable in phase during non-zero periods, contrary to 'wave 2' which experiences a continuous drift.

Figure 4.25 shows that the agreement between the measurements and the wave fit is good over the whole period. The 'noise' level (due to the variability) is much higher in the first half and at the very end of the studied period (anti-correlated with the density level), and the structure in the second half is more complex.
The most visible feature is the brutal phase shift (more than 120° in ~10 days) near DOY_{2006}~460. It is not related to changes in the local solar time of the spacecraft orbit (which would change the phase observed): the mean solar time is constant and the true solar time is almost monotonically increasing (Figure 4.3). This shift occurs on a timescale much shorter than the 60-day window used for the curve fitting, so its abruptness is certainly an artifact of the fitting. As shown in Figure 4.26, even though the binned longitude values changed little over 8 days, the fit seems to be in transition between two regimes, by going though a minimum in

fitted amplitude. This feature is also seen with different window durations (40-day, 80-day). If there are indeed fast changes in amplitude and phase in the actual density, they cannot be visible in this study.

Atmospheric waves that appear standing from a nearly Sun-synchronous orbit were previously observed in the Martian atmosphere. The primary source of measurements indicating wave activity has been the accelerometer data during aerobraking of recent Mars orbiters. Keating et al. [1998] reported the first observations and interpreted the waves as standing. However, Withers et al. [2003] notes that this is unlikely as it would require an implausible zonal wind structure in the lower hemisphere. Forbes and Hagan [2000], Wilson [2000] and Joshi et al. [2000] proposed the alternative explanation of non-migrating waves resulting from the interactions between the thermal tides (diurnal and semidiurnal) and atmospheric waves (such as gravity waves resulting from interaction with the topography). Some waves have large enough vertical wavelengths that they can propagate to high altitudes without too much dissipation (Withers et al. [2003]), because the diurnal solar forcing in the thermosphere is rather weak. Bougher et al. [1993] observed that the semidiurnal tidal contribution could propagate to the exobase near solar minimum. Diffusive processes can then carry the wave structure upwards (but without the relative amplitude increase with altitude due to energy conservation like in the lower layers). The period of MRO tracking studied here corresponds to the best-case scenario for observing those waves at very high altitude: solar minimum (and small solar rotation effects), dust storm season (L_S~270°) and local solar time near 3pm where temperatures peak (Bougher et al. [1993], Bruinsma and Lemoine [2002]).

The determination of exactly which wave interaction with the thermal tides is responsible for the observed waves is out of scope of the current study. However, based on Withers et al. [2003] (his Figure 17 and Table 4), there are four Hough modes (Chapman and Lindzen [1970]) most likely to contribute to density waves

at the highest levels: one would produce a zonal wavenumber at fixed solar time of 1 (σ=2, s=1, n=1), two a wavenumber 2 (σ=2, s=0, n=2 and σ=1, s=-1, n=1) and one for wavenumber 4 (σ=2, s=-2, n=2). At lower altitude, from MGS aerobraking accelerometer data, wavenumber 3 had been observed to contribute significantly (Withers et al. [2003], Wilson [2002], Forbes et al. [2002]), but the associated modes have a short vertical wavelength and must have dissipated at MRO altitude. The amplitudes measured here are much lower than observed at 125km by MGS (by a factor of 3–4). They could thus be consistent with earlier observations, although further modeling work is needed to account for the phase changes and dissipations effects between 125 and 250km (e.g., Forbes and Hagan [2000] with Mars-GSWM).

4.7 Conclusion and future work

In this paper, we obtained an unprecedented dataset of density measurements of Mars atmosphere near 250km altitude. The high temporal and spatial resolutions were made possible by the low orbit of MRO, and inform us on the Martian upper atmosphere with greater accuracy and more spatial and temporal detail than previously possible. We could estimate the variability of the atmosphere and its dependence on other atmospheric phenomena from drag coefficients adjusted at various frequencies. Thanks to the occurrence of a seasonal dust storm, we could also determine that the upper atmosphere is very quickly affected by the lower atmosphere dust opacity enhancement. Although all our measurements were done near solar minimum, which is not optimal to constrain the dependence of the density to the solar EUV flux input, our results are consistent with studies performed on MGS higher in the exosphere. Finally, we observed important longitudinal variations coherent over long timescales, which we interpret as atmospheric waves resulting of interaction with the thermal tides.

The Stewart atmospheric model performs surprisingly well compared to more recent models, although it is based on the only spacecraft measurements at high altitude near solar minimum available until recently. However, the inclusion of two higher opacity periods in the 'average year', while interesting when compared to actual dust storm events, is rather counter-productive when wanting to evaluate scale heights and exospheric temperatures based on density adjustments. It would be best to use the Stewart model without any of the fixed dust storm events, because the strength and timing of actual events varies so much year-to-year.

The prospects for future work are also interesting. On the measurement side, even though the density is now decreasing, the solar activity should pick up because the solar cycle is transitioning out of solar minimum. This could potentially enable the recovery of stable and accurate density values every orbit (~2h). With higher solar activity, the atmospheric waves could be overwhelmed by the *in situ* diurnal forcing (UV-EUV heating). Nevertheless, the solar activity level at which this happens could prove important to learn about the processes at play in the exosphere (solar effects, dissipation, molecular conduction). An extended baseline of the density measurements will also be important to study seasonal, inter-annual and solar-related variations. On the modeling side, further localization of the measurements to study targeted issues could be valuable. For instance, shortening the estimation periods to half an orbit, separating dayside from nightside, and doing a join estimation of several of those coefficients could help better constrain the day-to-night ratio and improve our understanding of the neutral upper atmospheric processes.

4.8 References

Bougher S. W., C. G. Fesen, E. C. Ridley and R. W. Zurek (1993), Mars mesosphere and thermosphere coupling: Semidiurnal tides, Journal of Geophysical Research, 98(E2), pp. 3281–3295.

Boynton W. V., W. C. Feldman, S. W. Squyres, T. H. Prettyman, J. Brückner, L. G. Evans, R. C. Reedy, R. Starr, J. R. Arnold, D. M. Drake, P. A. J. Englert, A. E. Metzger, Igor Mitrofanov, J. I. Trombka, C. d'Uston, H. Wänke, O. Gasnault, D. K. Hamara, D. M. Janes, R. L. Marcialis, S. Maurice, I. Mikheeva, G. J. Taylor, R. Tokar, C. Shinohara (2002), Distribution of Hydrogen in the Near Surface of Mars: Evidence for Subsurface Ice Deposits, Science, 297, pp. 81–85.

Bruinsma S. and F. G. Lemoine (2002), A preliminary semiempirical thermosphere model of Mars: DTM-Mars, Journal of Geophysical Research, 107(E10), 5085.

Cantor, B. A. (2007), MOC observations of the 2001 Mars planet-encircling dust storm, Icarus, 186, 60–96, doi: 10.1016/j.icarus.2006.08.019.

Chapman S. and R. S. Lindzen (1970), Atmospheric Tides, D. Reidel, 200pp.

Christensen P. R., B. M. Jakosky, H. H. Kieffer, M. C. Malin, H. Y. McSween Jr., K. Nealson, G. L. Mehall, S. H. Silverman, S. Ferry, M. Caplinger and M. Ravine (2004), The Thermal Emission Imaging System (THEMIS) for the Mars 2001 Odyssey mission, Space Science Reviews, 110, pp. 85–130, doi:10.1023/B:SPAC.0000021008.16305.94

Fenton L. K., J. C. Pearl and T. Z. Martin (1997), Mapping Mariner 9 Opacities, Icarus, 130, pp. 115–124.

Forbes J. M. and M. E. Hagan (2000), Diurnal Kelvin wave in the atmosphere of Mars: Towards an understanding of 'stationary' density structures observed by the MGS accelerometer, Geophysical Research Letters, 27, pp. 3563–3566.

Forbes, J. M., S. Bruinsma, and F. G. Lemoine (2006), Solar rotation effects in the thermospheres of Mars and Earth, Science, 312, 1366 – 1368.

Forbes, J. M., F. G. Lemoine, S. L. Bruinsma, M. D. Smith and X. Zhang (2008), Solar rotation effects in the thermospheres of Mars and Earth, Geophysical Research Letters, accepted for publication.

Forget, F., E. Millour, F. González-Galindo, A.Spiga, S. R. Lewis, L. Montabone, P. L. Read, M. A. López-Valverde, G. Gilli, M.-C. Desjean, J.-P. Huot and the MCD/GCM development team (2007), The new (version 4.2) Mars Climate Database, Seventh International Conference on Mars, Abstract 3098.

Highsmith D. (2005), MRO Approach/MOI/AB Navigation Readiness Review.

Hinson, D. P., R. A. Simpson, J. D. Twicken, G. L. Tyler, and F. M. Flasar (1999), Initial results from radio occultation measurements with Mars Global Surveyor, Journal of Geophysical Research , 104, 26,997–+.

Hunt G. E. (1979), On the opacity of Martian dust storms derived by Viking IRTM spectral measurements, Journal of Geophysical Research, 84, pp. 8301–8310.

Jacobson R.A. and B. Rush (2006), Ephemerides of the Martian Satellites – MAR063, Jet Propulsion Laboratory Interoffice Memorandum, 343R-06-004.

Joshi M. M., J. L. Hollingsworth, R. M. Haberle and A. F. C. Bridger (2000), An interpretation of Martian thermospheric waves based on analysis of a general circulation model, Geophysical Research Letters, 27, pp. 613-616.

Justus, C. G., B. F. James, S. W. Bougher, A. F. C. Bridger, R. M. Haberle, J. R. Murphy, and S. Engel (2002), Mars-GRAM 2000: A Mars atmospheric model for engineering applications, *Advances in Space Research*, 29, 193–202.

Kass D. M., D. McCleese, T. Schofield, A. Kleinboehl, R. Zurek, N. Bowles (2007), MCS Views of the 2007 Global Dust Storm, American Astronomical Society, DPS meeting 39, Abstract 17.02.

Keating, G. M., S. W. Bougher, R. W. Zurek, R. H. Tolson, G. J. Cancro, S. N. Noll, J. S. Parker, T. J. Schellenberg, R. W. Shane, B. L. Wilkerson, J. R. Murphy, J. L. Hollingsworth, R. M. Haberle, M. Joshi, J. C. Pearl, B. J. Conrath, M. D. Smith, R. T. Clancy, R. C. Blanchard, R. G. Wilmoth, D. F. Rault, T. Z. Martin, D. T. Lyons, P. B. Esposito, M. D. Johnston, C. W. Whetzel, C. G. Justus, and J. M. Babicke, “The Structure of the Upper Atmosphere of Mars: In Situ Accelerometer Measurements from Mars Global Surveyor,” Science, 279, 1998, p.1672.

Konopliv, A. S., C. F. Yoder, E. M. Standish, D.-N. Yuan, and W. L. Sjogren (2006), A Global Solution for the Mars Static and Seasonal Gravity, Mars Orientation, Phobos and Deimos Masses, and Mars Ephemeris, Icarus.

Krasnopolsky, V. (2002), Mars' upper atmosphere and ionosphere at low, medium, and high solar activities: Implications for evolution of water, Journal of Geophysical Research, 107, 11–+.

Lemoine, F. G. (1992), The dynamics of orbitings satellites and gravity model development, Ph.D. thesis, University of Colorado at Boulder, Bouler, Colorado.

Lemoine, F. G (2003), 'mgm1041c' gravity field solution, Planetary Data System, Geosciences Node, http://pds-geosciences.wustl.edu/geodata/mgs-m-rss-5-sdp-v1/mors_1021/sha/.

Malin M. C., G. E. Danielson, A. P. Ingersoll, H. Masursky, J. Veverka, M. A. Ravine and T. A. Soulanille (1992), The Mars Observer Camera, Journal of Geophysical Research, 97, pp. 7699–7718, doi:10.1029/92JE00340.

Marshall, J. A., and S. B. Luthcke (1994), Modeling radiation forces acting on TOPEX/Poseidon for precision orbit determination, Journal of Spacecraft and Rockets, 31, 99–105.

Mase, R. A., P. Antreasian, J. L. Bell, T. L. Martin-Mut, and J. C. J. Smith (2005), Mars Odyssey Navigation Experience, Journal of Spacecraft and Rockets, 42 (3), 386–393.

Mazarico, E., M. T. Zuber, F. G. Lemoine and D. E. Smith (2007), Martian exospheric density using Mars Odyssey radio tracking data, Journal of Geophysical Research, 112, 5014.

McCleese D. J., J. T. Schofield, F. W. Taylor, S. B. Calcutt, M. C. Foote, D. M. Kass, C. B. Leovy, D. A. Paige, P. L. Read and R. W. Zurek (2007), Mars Climate

Sounder: An investigation of thermal and water vapor structure, dust and condensate distributions in the atmosphere, and energy balance of the polar regions, Journal of Geophysical Research, 112(E05), doi:10.1029/2006JE002790.

Pavlis, D. E., S. G. Poulose and J. J. McCarthy (2006), GEODYN operations manuals, contractor report, SGT Inc., Greenbelt, Maryland.

Smith, D. E., M. T. Zuber, and G. A. Neumann (2001), Seasonal Variations of Snow Depth on Mars, *Science*, 294, 2141–2146, doi:10.1126/science.1066556.

Stewart, A. I. F. (1987), Revised time dependent model of the Martian atmosphere for use in orbit lifetime and sustenance studies, Tech. Rep. JPL PO NQ-802429, University of Colorado.

Tyler, G. L., G. Balmino, D. P. Hinson, W. L. Sjogren, D. E. Smith, R. A. Simpson, S. W. Asmar, P. Priest and J. D. Twicken (2001), Radio science observations with Mars Global Surveyor: Orbit insertion through one Mars year in mapping orbit, Journal of Geophysical Research, 106(E10), 23327-23348, doi:10.1029/2000JE001348.

Wilson, R. J. (2002), Evidence for nonmigrating thermal tides in the Mars upper atmosphere from the Mars Global Surveyor Accelerometer Experiment, Geophysical Research Letters, 29(7), 1120.

Withers P., S. W. Bougher and G. M. Keating (2003), The effects of topographically-controlled thermal tides in the martian upper atmosphere as seen by the MGS accelerometer, Icarus, 164, pp.14–32.

Wynn J. (2004), MRO Surface Property Data for Navigation and ACS Analysis, Interoffice Memo # 0115_MRO_AC_04 Rev 1, Lockheed Martin.

Zuber, M. T., F. G. Lemoine, D. E. Smith, A. S. Konopliv, S. E. Smrekar, S. W. Asmar (2007a), Mars Reconnaissance Orbiter Radio Science Gravity Investigation, Journal of Geophysical Research, 112(E05), doi:10.1029/2006JE002833

Zuber, M. T., R. J. Phillips, J. C. Andrews-Hanna, S. W. Asmar, A. S. Konopliv. F. G. Lemoine, J. J. Plaut, D. E. Smith and S. E. Smrekar (2007b), Density of Mars' South Polar Layered Deposits, Science, 317, pp.1718–1719, doi: 10.1126/science.1146995

Zurek, R. W. and S. E. Smrekar (2007), An overview of the Mars Reconnaissance Orbiter (MRO) science mission, Journal of Geophysical Research, 112, E05S01, doi:10.1029/2006JE002701.

4.9 Tables

Gravity field	MGS data	ODY data	MRO data	Reference
mgm1041c	209 arcs *(incl. 1-way)* hiatus, SPOs + 1999/02 → 2002/05	-	-	Lemoine [2004]
jgm95j01	476 arcs *(incl. 1-way)* 1998/03 → 2004/12	217 arcs 2002/01 → 2004/12	-	Konopliv et al. [2006]
mromgm0020g	348 arcs *(incl. 1-way)* 1999/04 → 2004/12	-	107 arcs 2006/09 → 2007/04	Zuber et al. [2007b]
mromgm0023c	348 arcs *(incl. 1-way)* 1999/04 → 2004/12	-	186 arcs *(incl. 1-way)* 2006/09 → 2007/08	unpublished

Table 4.1 Summary of the data used during the inversion of the various gravity fields used in Section 4.4.3.

4.10 Figures

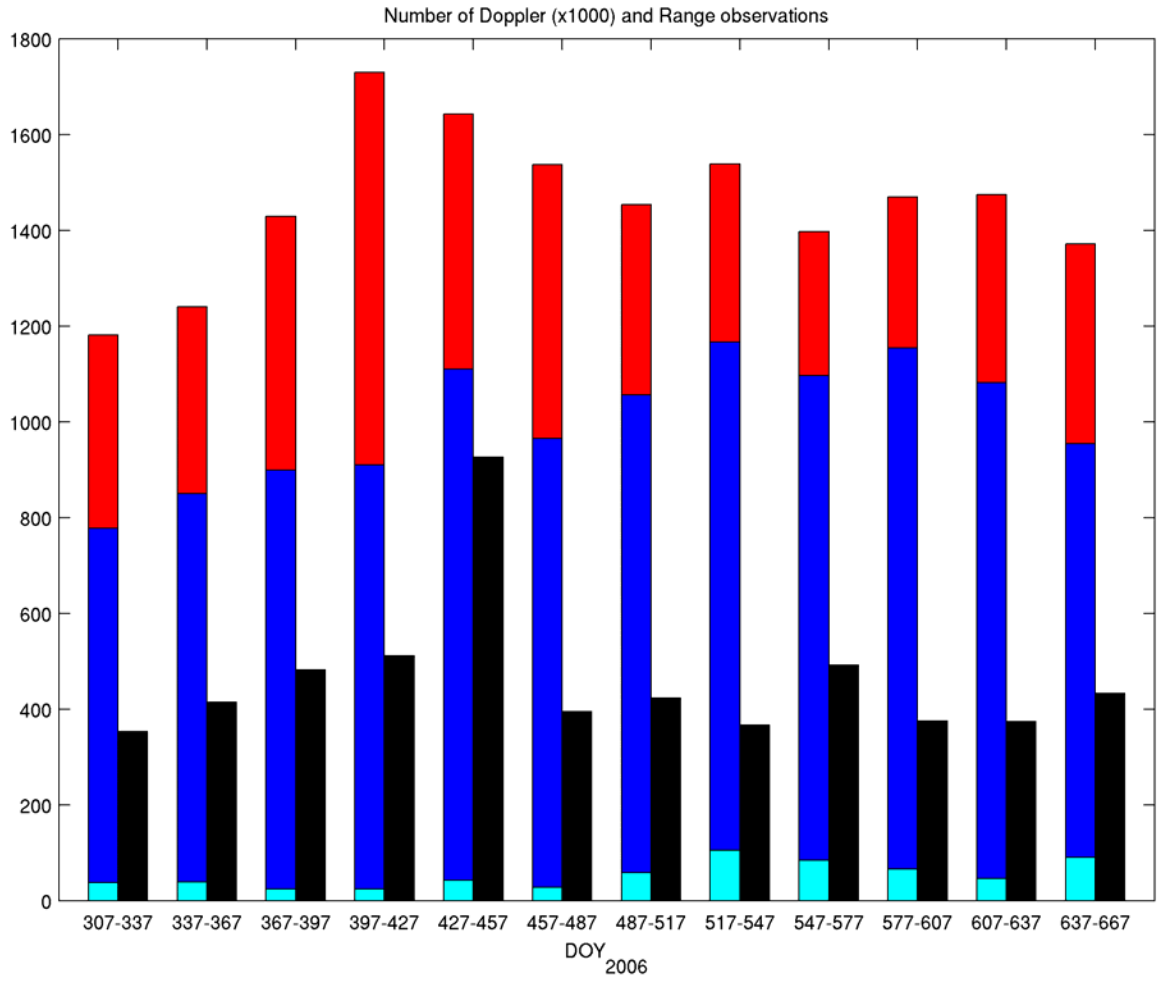

Figure 4.1 Number of Doppler (1-way in red, 2-way in blue, 3-way in cyan) and Range observations (in black) in successive 30-day windows spanning ~1 year. Note that the number of Doppler observations has been scaled down by a factor 1000.

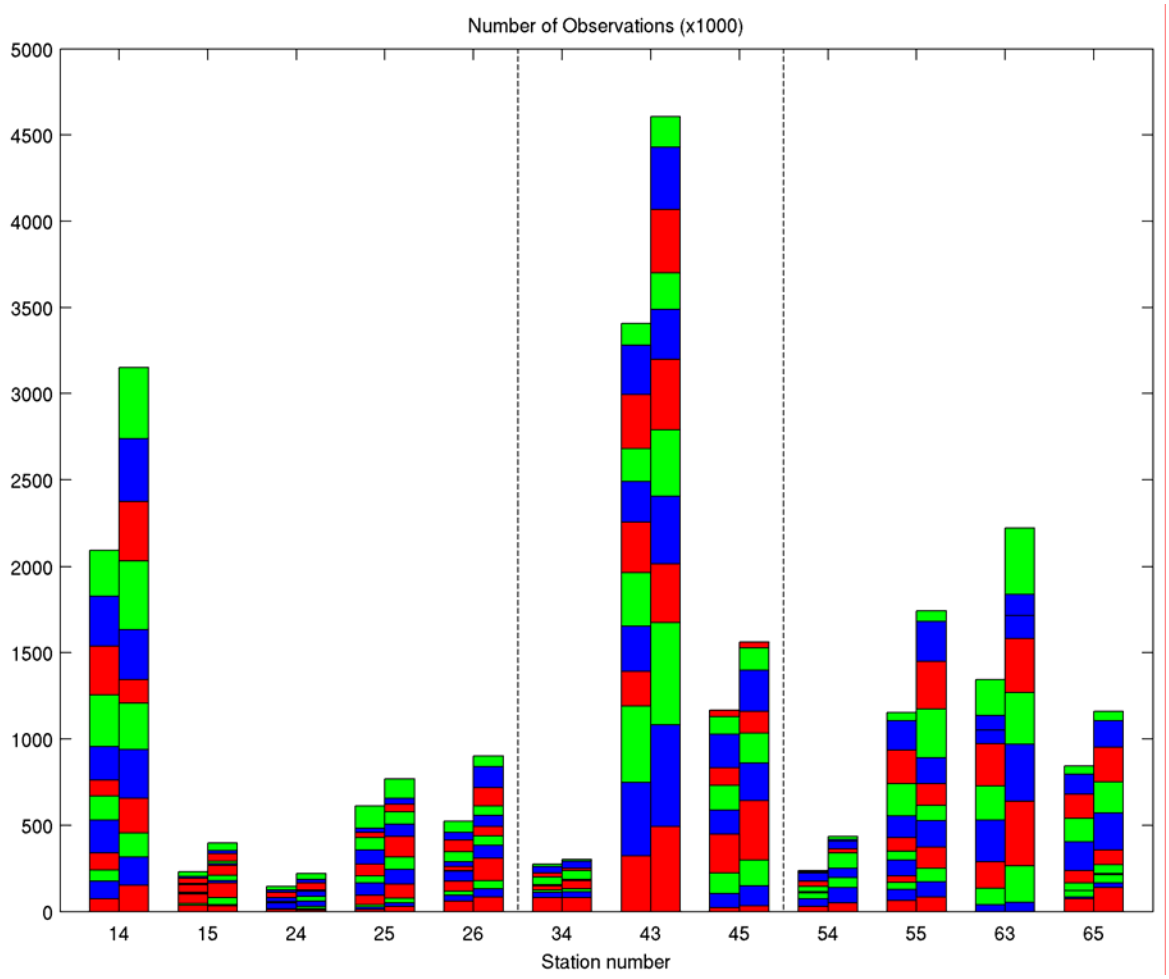

Figure 4.2 Number of radio tracking observations transmitted (left column) and received (right column) at the participating ground stations of the NASA Deep Space Network. The various colors alternate between the different 30-day time windows (as in Figure 4.1). The dashed lines separate the three DSN complexes: Goldstone in California (stations numbers: 14, 15, 24, 25 and 26); Canberra in Australia (34, 43 and 45); and Madrid in Spain (54, 55, 63 and 65). The larger number of received observations is due to 1-way tracking, when the spacecraft is the transmitter. The main antennae used to track MRO project are the 70-meters in Goldstone (14) and Canberra (43).

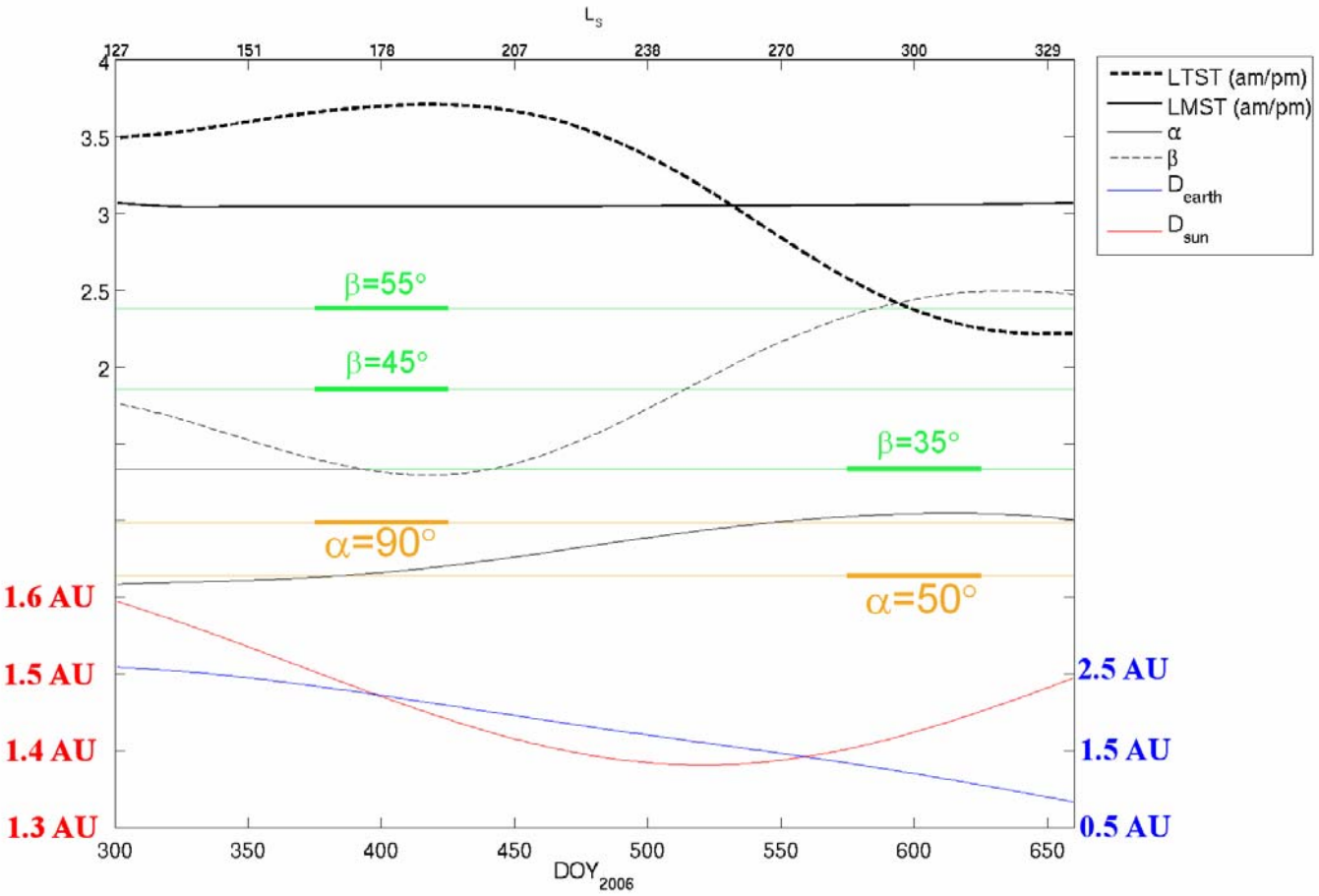

Figure 4.3 Evolution of the main characteristics of the orbits of Mars and MRO: the distance of Mars to the Sun and the Earth; the orbit viewing angle of the spacecraft orbit from the Earth (α) and from the Sun (β); the local mean solar time (LMST) and the local true solar time (LTST). With a time span of about half a Martian year, it is not obvious from the figure that MRO is on a nearly-sun-synchronous orbit at ~3am/pm. At DOY_{2006}~300, the Earth and Mars are in conjunction, with a distance greater than 2.5AU.

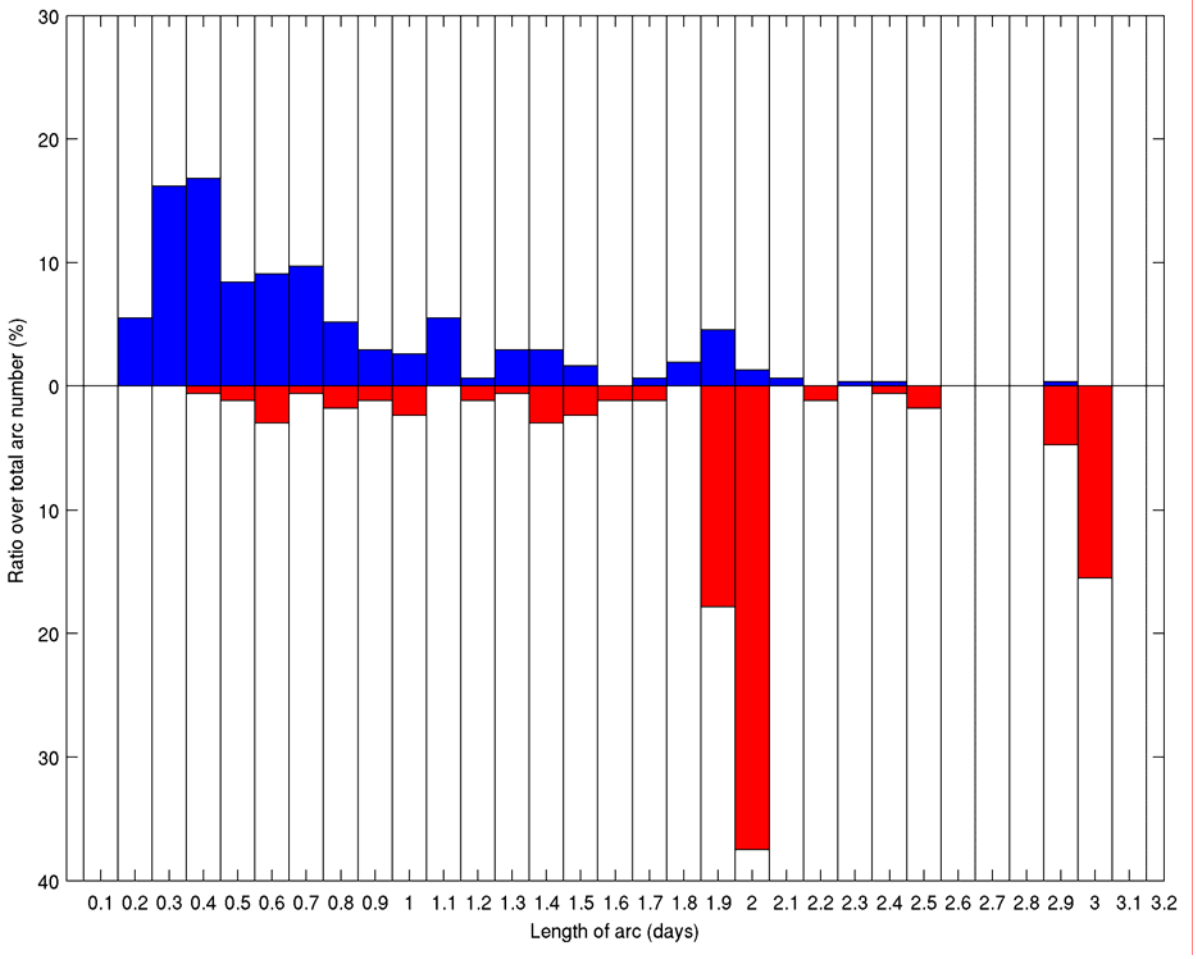

Figure 4.4 Distribution of arc length for the two different set of arcs used in this study. The values plotted correspond to the ratio of the arcs of a set within a duration range over the total number of arcs in the set. In red, the "long" arc set: the arcs were cut directly after an AMD maneuver (cf. Section 4.2.1) and just before the next one. This leads to a very sharp distribution at 2 and 3 days, chosen by the MRO navigation team as preferred AMD temporal separation. In blue, the "short" arc set: the arcs were "cut" specifically to avoid any 2-3 way tracking gap greater than 5 hours, as well as the maneuvers. The much smoother distribution shows that there are a number of such data gaps. There are 305 arcs in the "short" arc set and 166 in the "long" arc set.

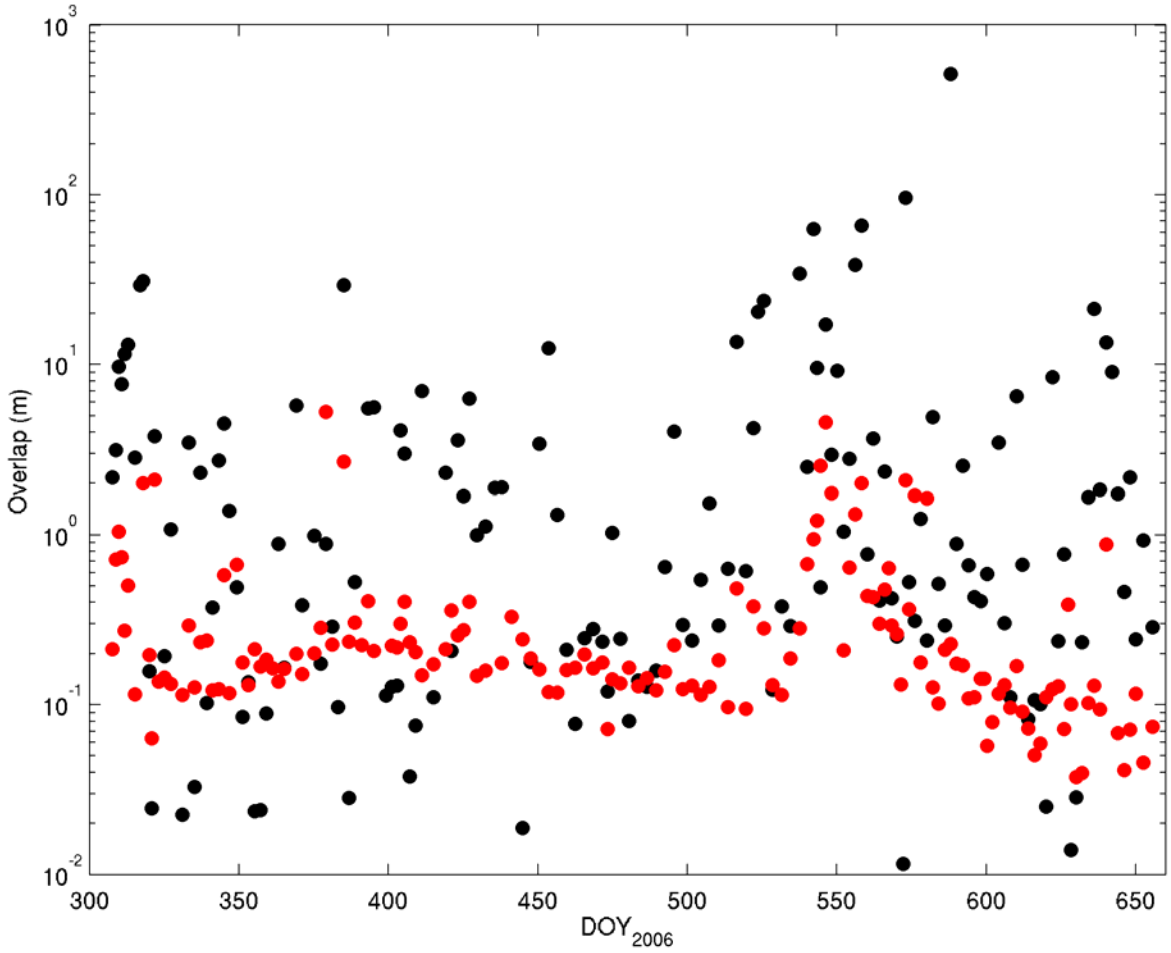

Figure 4.5 Total orbit difference between two runs of "long" arcs with and without 1-way Doppler data (black). For reference, the total orbit difference between two runs of "long" arcs (with the 1-way data), with and without self-shadowing (red). The differences increase significantly, and show that not using the 1-way Doppler data during data gaps deteriorates the solution.

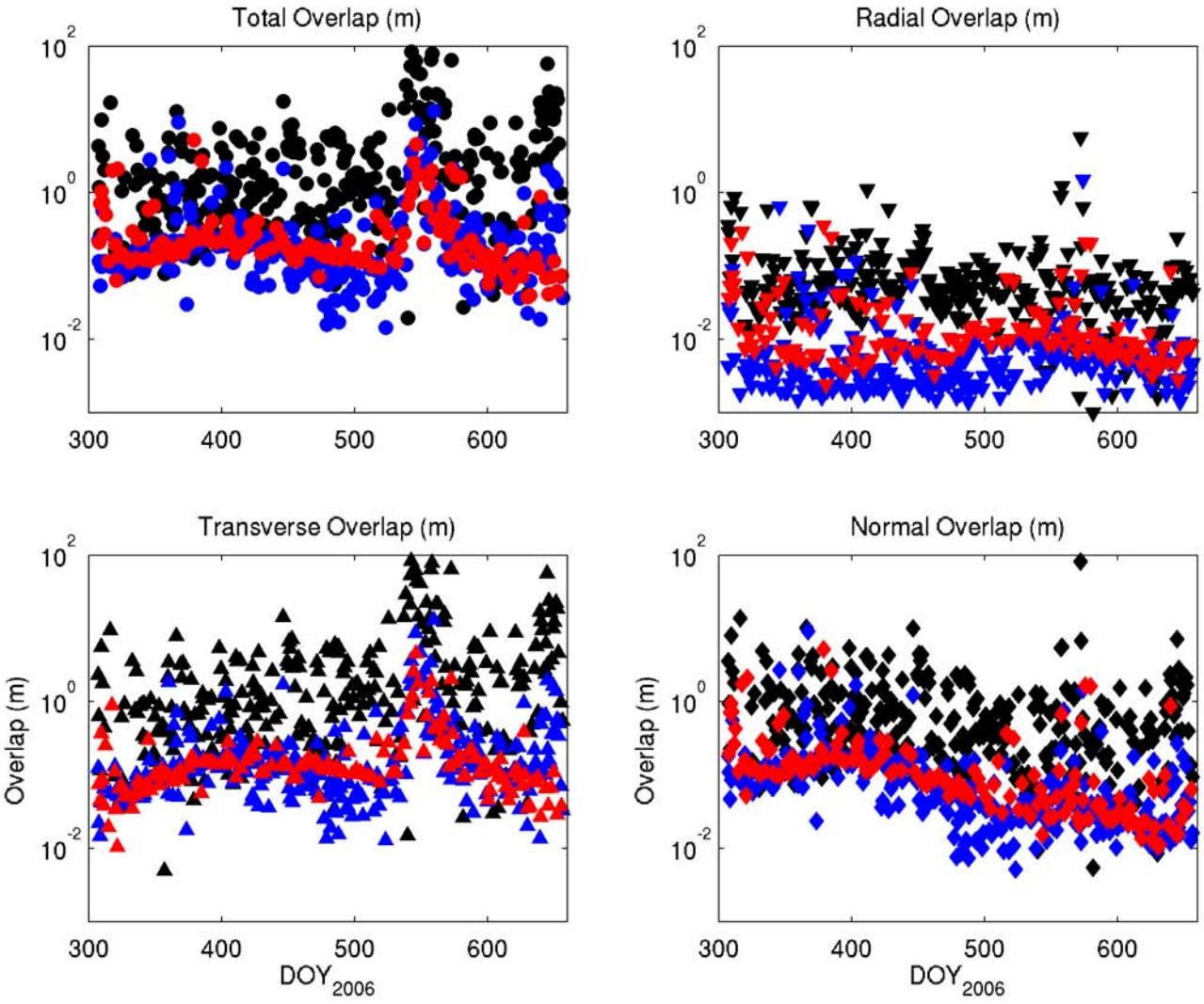

Figure 4.6 In black we show the orbit differences between "long"–arc and "short" –arc runs (with 1-way Doppler data and self-shadowing). The red and blue symbols are the difference between two runs of "long" and respectively "short" arcs (with the 1-way data), with and without self-shadowing.

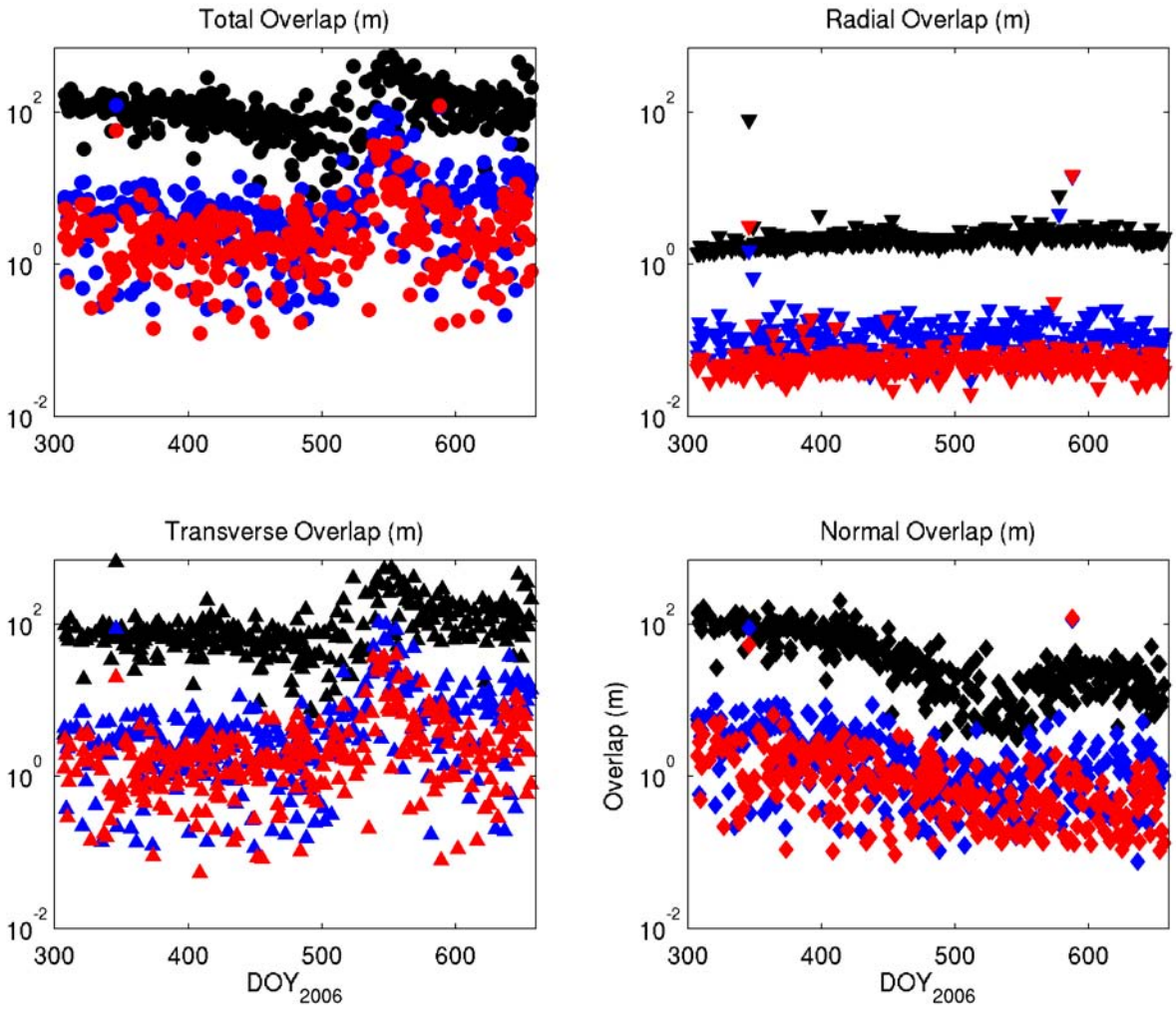

Figure 4.7 Orbit differences between arcs converged using the *a priori* gravity field 'mromgm0023c' and arcs converged with 'mgm1041c', 'jgm95j01' and 'mromgm0020g' (respectively in black, blue and red). Part of the large changes in the 'mgm1041c' orbit could be due to the different Mars orientation used at inversion.

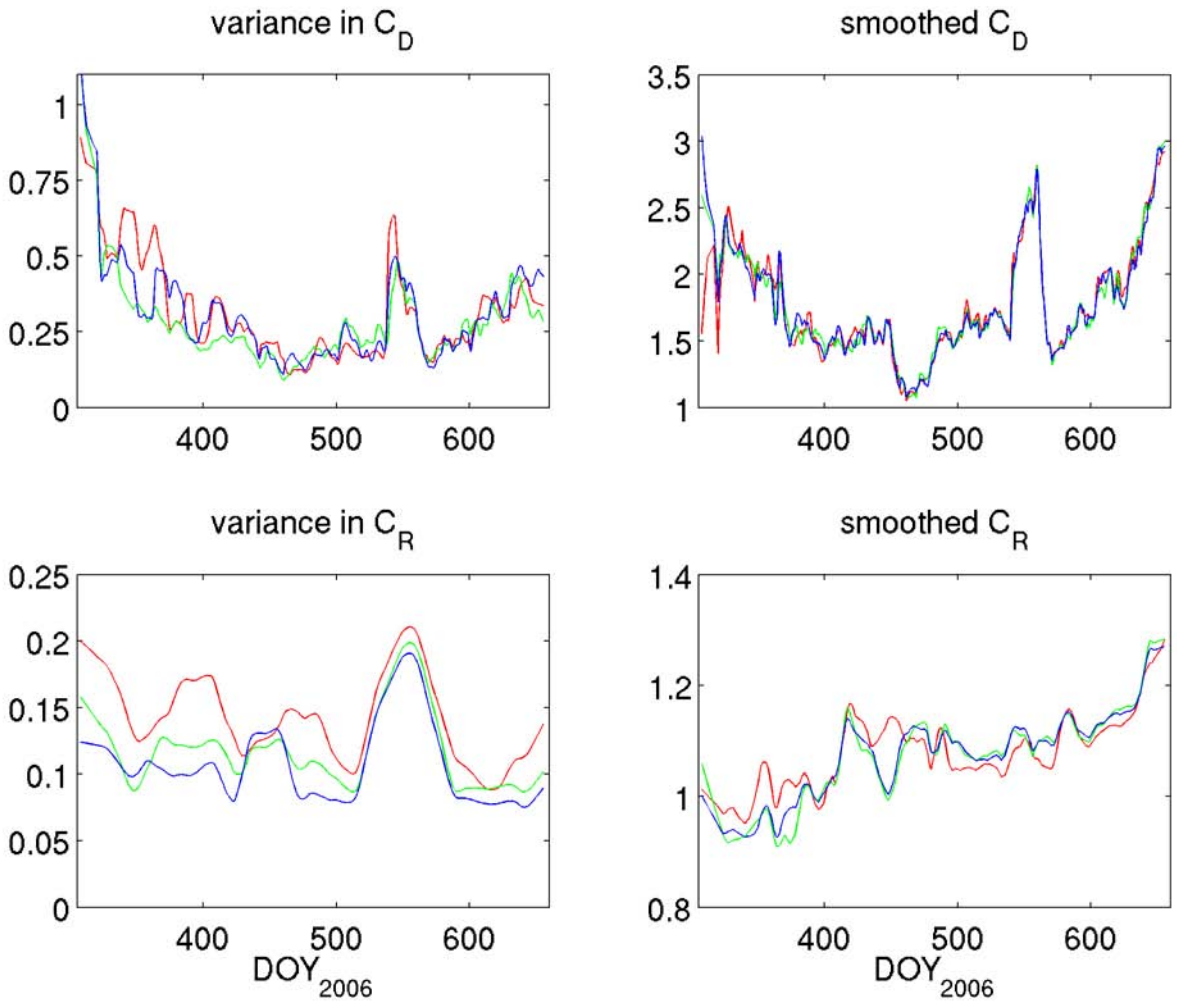

Figure 4.8 Differences induced in C_D and C_R by the change in *a priori* gravity field used. The right column shows the variance of the obtained CD (top) and CR (bottom) values, around their running mean (right column). The gravity fields shown are 'jgm95j01' (red), 'mromgm0020g' (green) and 'mromgm0023c' (blue).

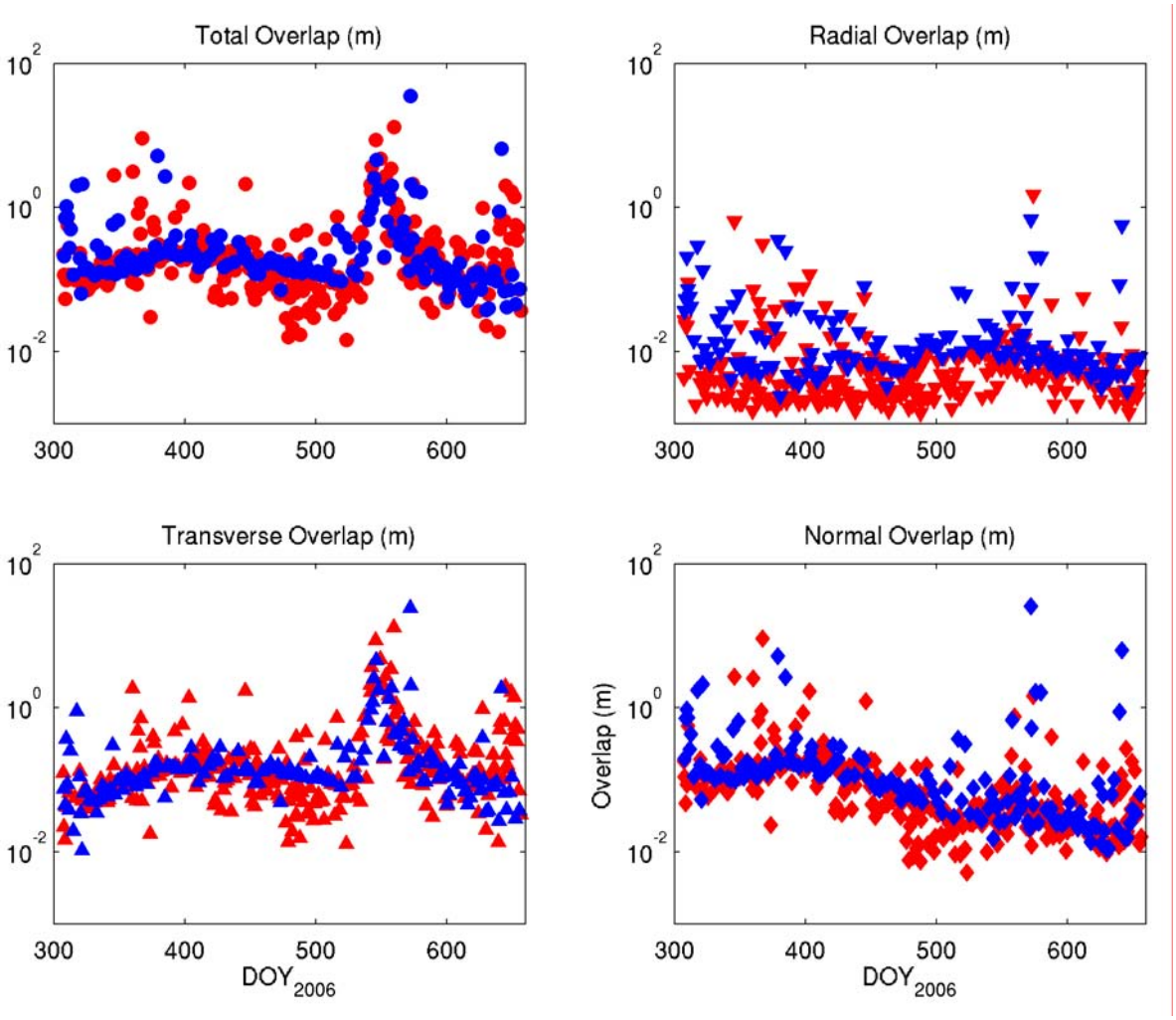

Figure 4.9 Orbit differences between arcs converged with and without the use of the self-shadowing during cross-section computations for the non-conservative forces. It is Results are shown for both the "short" (red) and "long" (blue) arc sets.

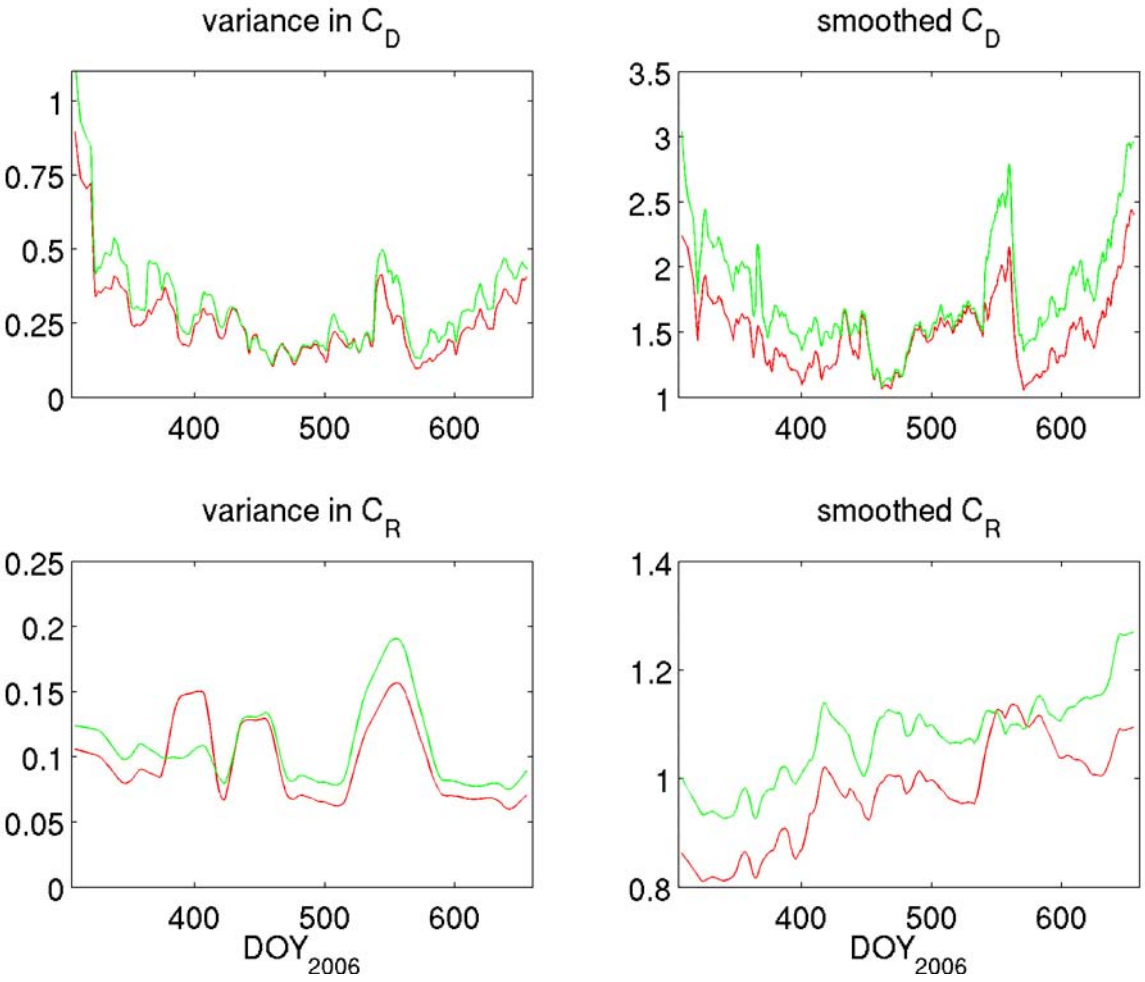

Figure 4.10 Same as Figure 4.8, but for the differences induced in C_D and C_R by the use of self-shadowing. The red curves show the non-shadowing case, while the green denotes its use.includes the effet.

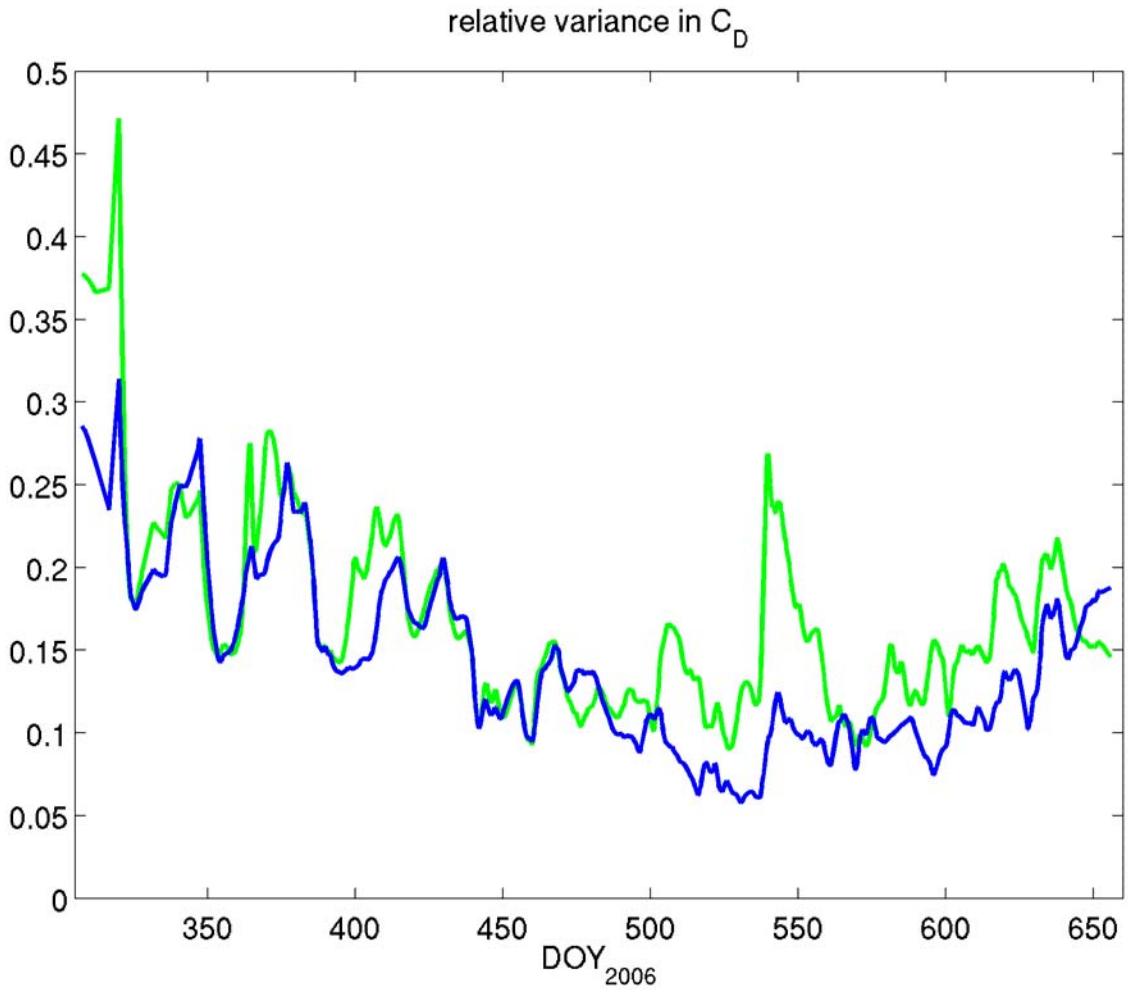

Figure 4.11 Relative variance in the drag coefficient time series. The green curve shows the same set of parameters as the green curve of Figure 4.10. The blue curve shows the results of the addition of a cyclic empirical acceleration to mimic the atmospheric drag unaccounted for by the *a priori* atmospheric model.

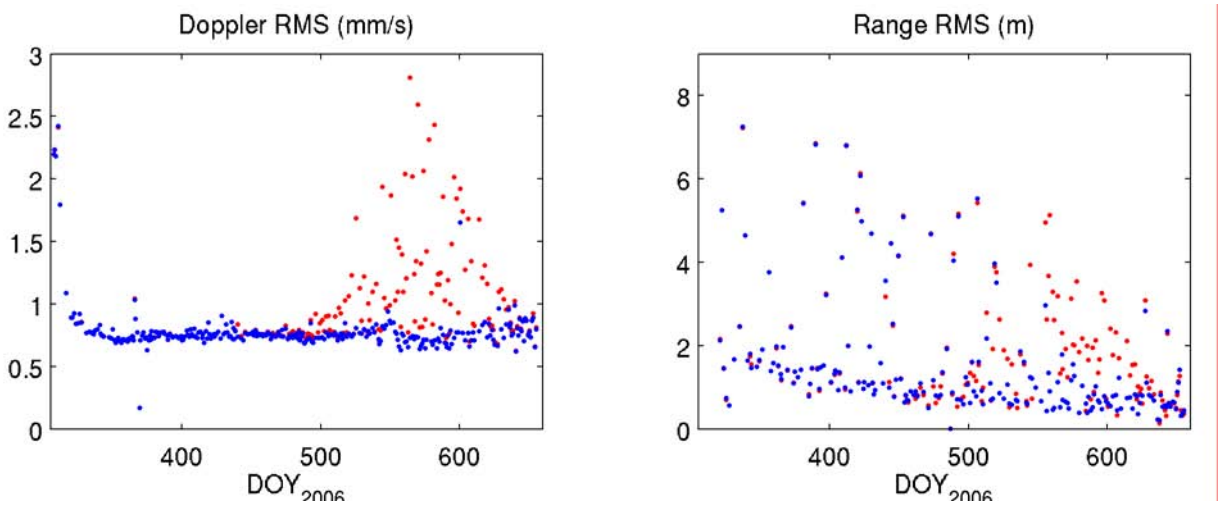

Figure 4.12 Root-Mean Squares (RMS) of the residuals of the Doppler observations (left) and of the Range observations (left). The overlying blue dots are with the adjustment of empirical accelerations. Both time series are nearly indistinguishable for $DOY_{2006}<500$.

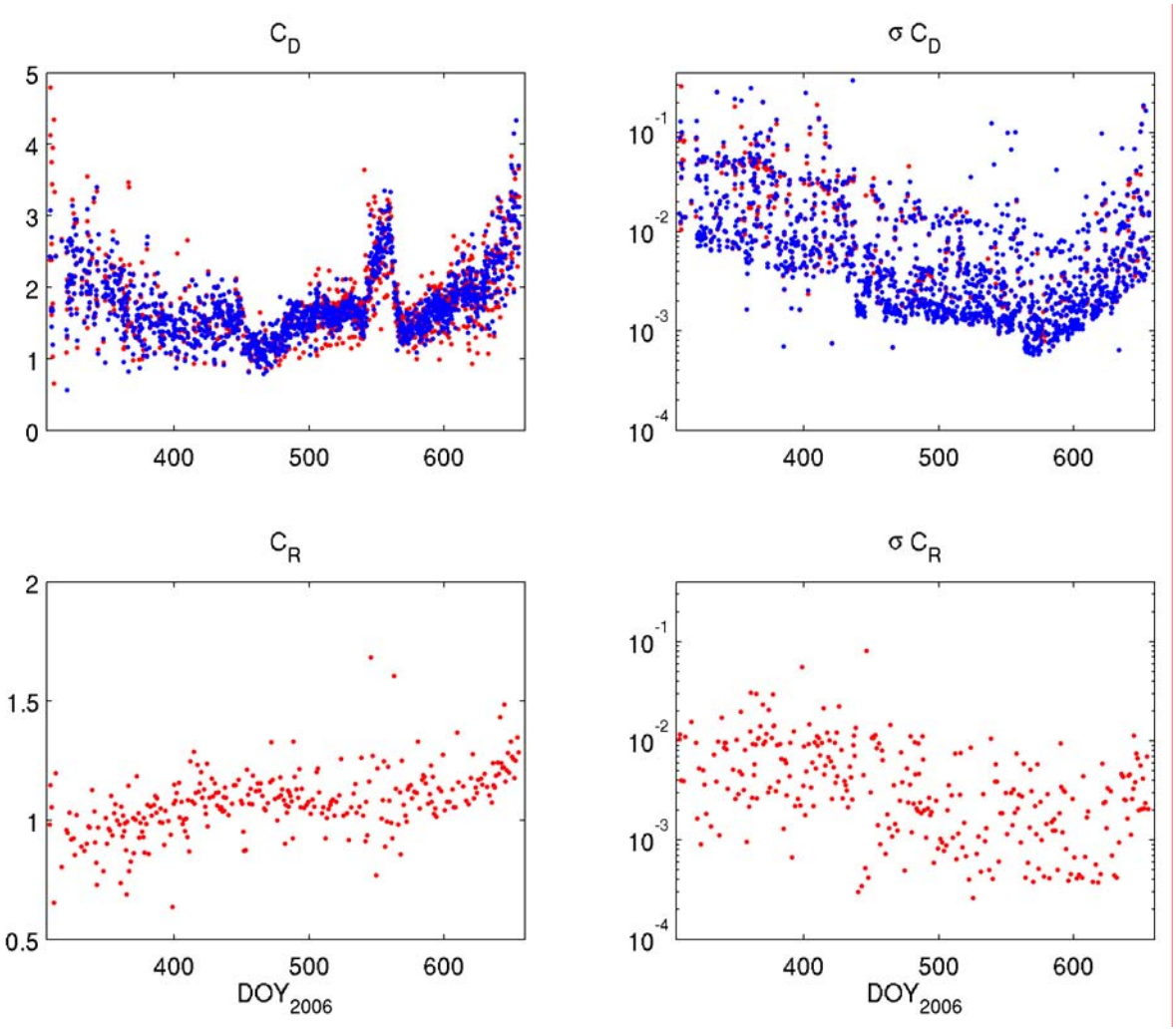

Figure 4.13 Time series of the obtained drag (C_D, top) and radiation (C_R, bottom) coefficients, and their formal uncertainties (right column). As in Figure 4.12, the blue dots are for arcs with added empirical accelerations, where the radiation coefficient was fixed.

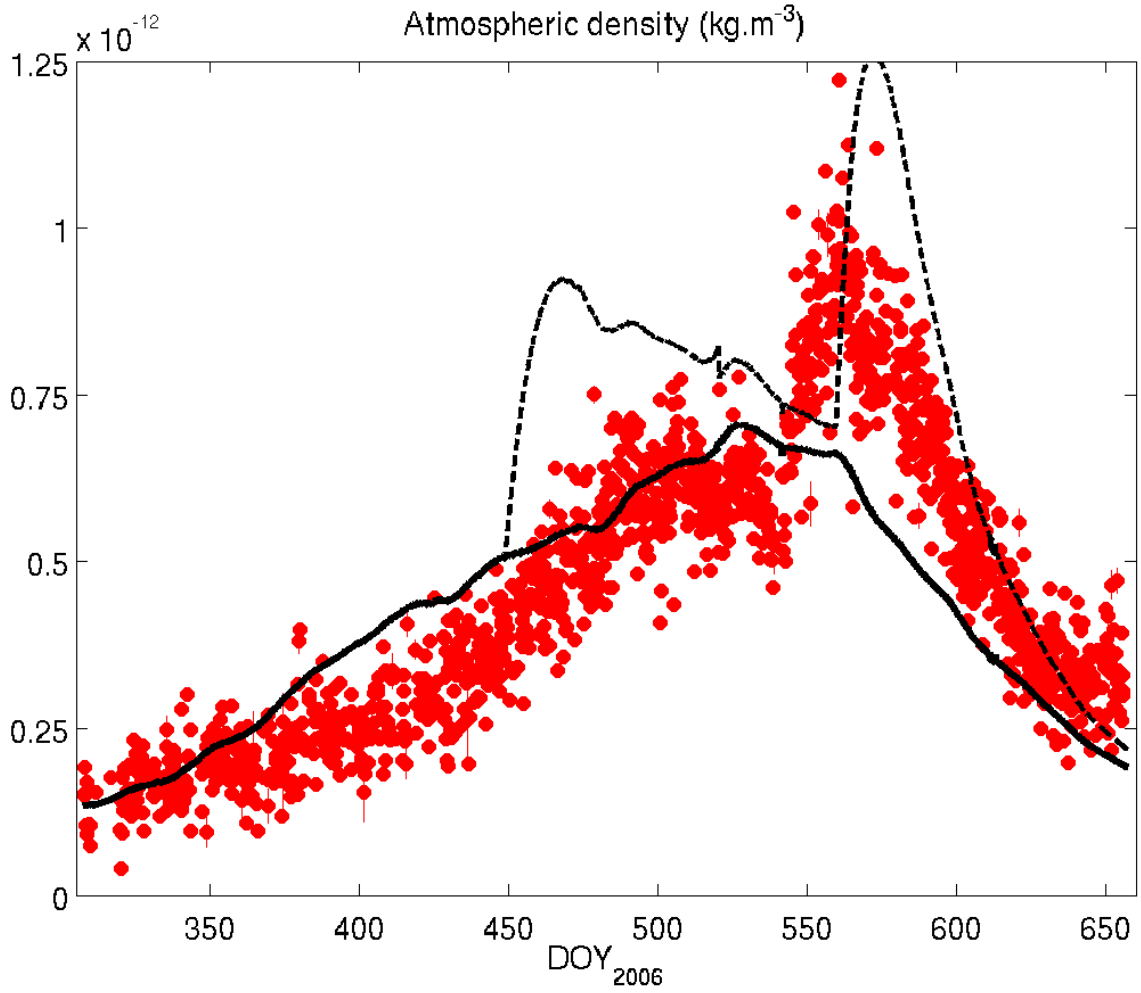

Figure 4.14 Density time series for measurements every 2 orbits (~4h). The vertical lines show the measurement uncertainty (most are too small to be visible). The black lines show the densities predicted by the Stewart model. The thick line shows the normal seasonal and solar variations, and the dashed line shows the effect of the two dust storms included in an average year of the Stewart model (based on the Viking lander observations).

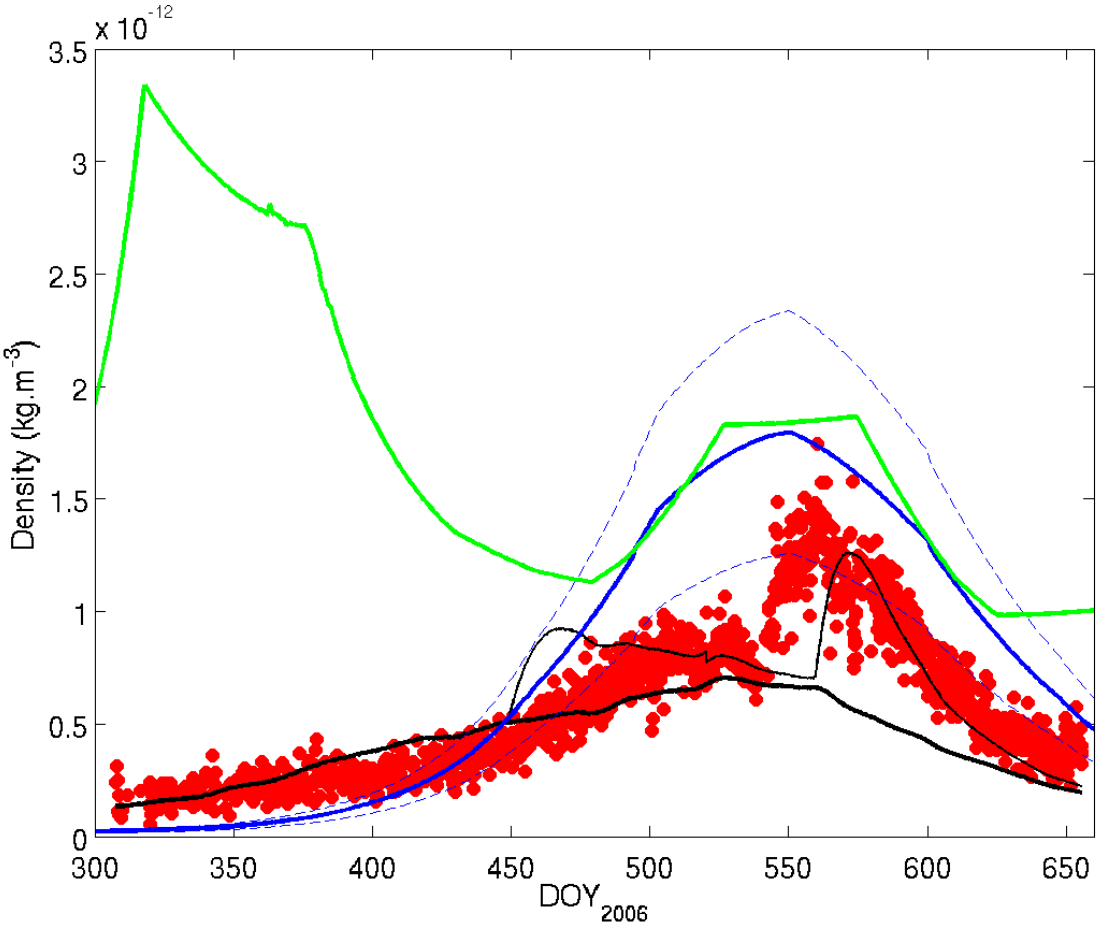

Figure 4.15 4-h density measurements (red dots) and predictions of various models: Stewart 1987 with and without Viking-type dust storms (thick black line and thin black line respectively); MCD4.2 (thick green line); and Mars-GRAM 2000 along with confidence limits (thick blue line and dashed blue lines). MCD4.2 considerably overestimates the densities during the Southern late winter and spring. Both MCD4.2 and Mars-GRAM 2000 overestimate the density during Southern summer.

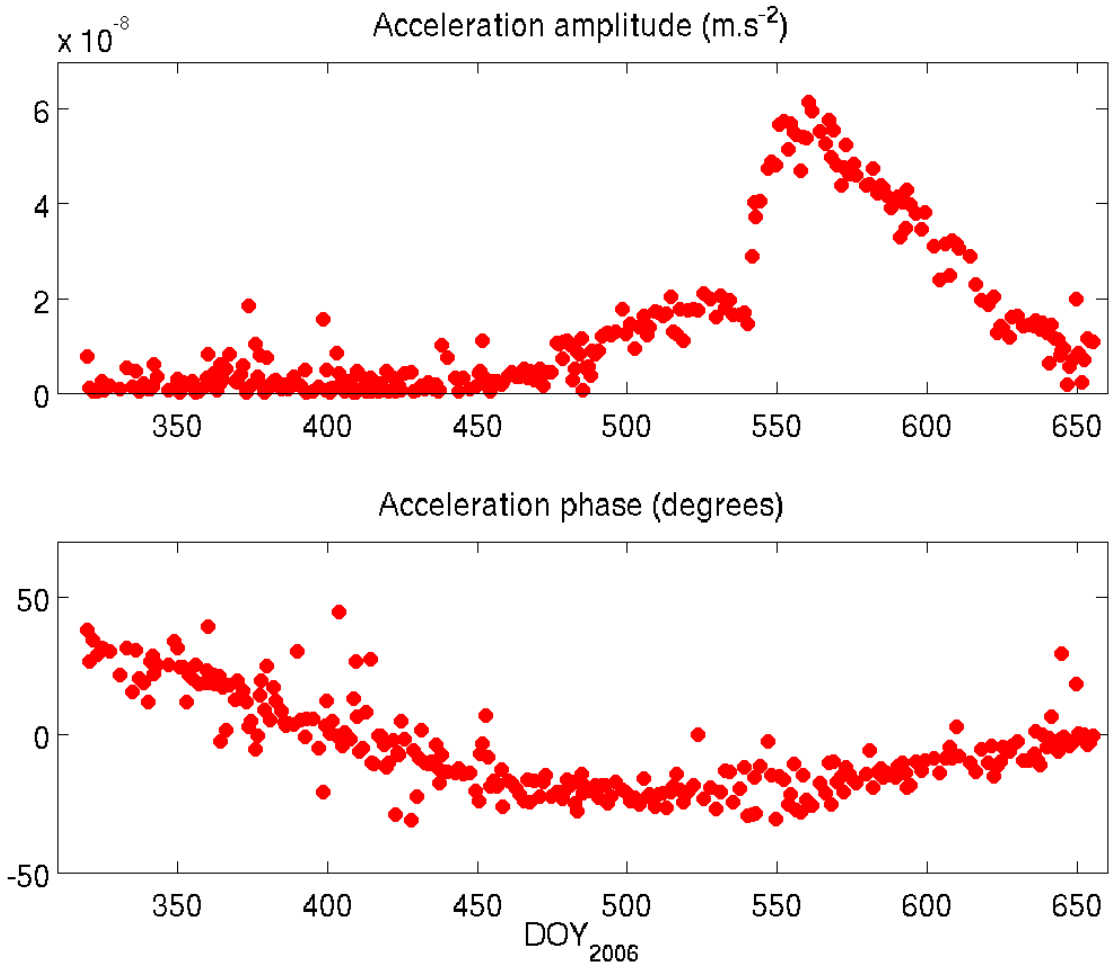

Figure 4.16 Time series of the amplitude and the phase of the empirical along-track accelerations. The phase is relative to the periapsis, so the low values indicate that the maximum acceleration occurs near the South Pole, where we expect a density enhancement due to the dust storm.

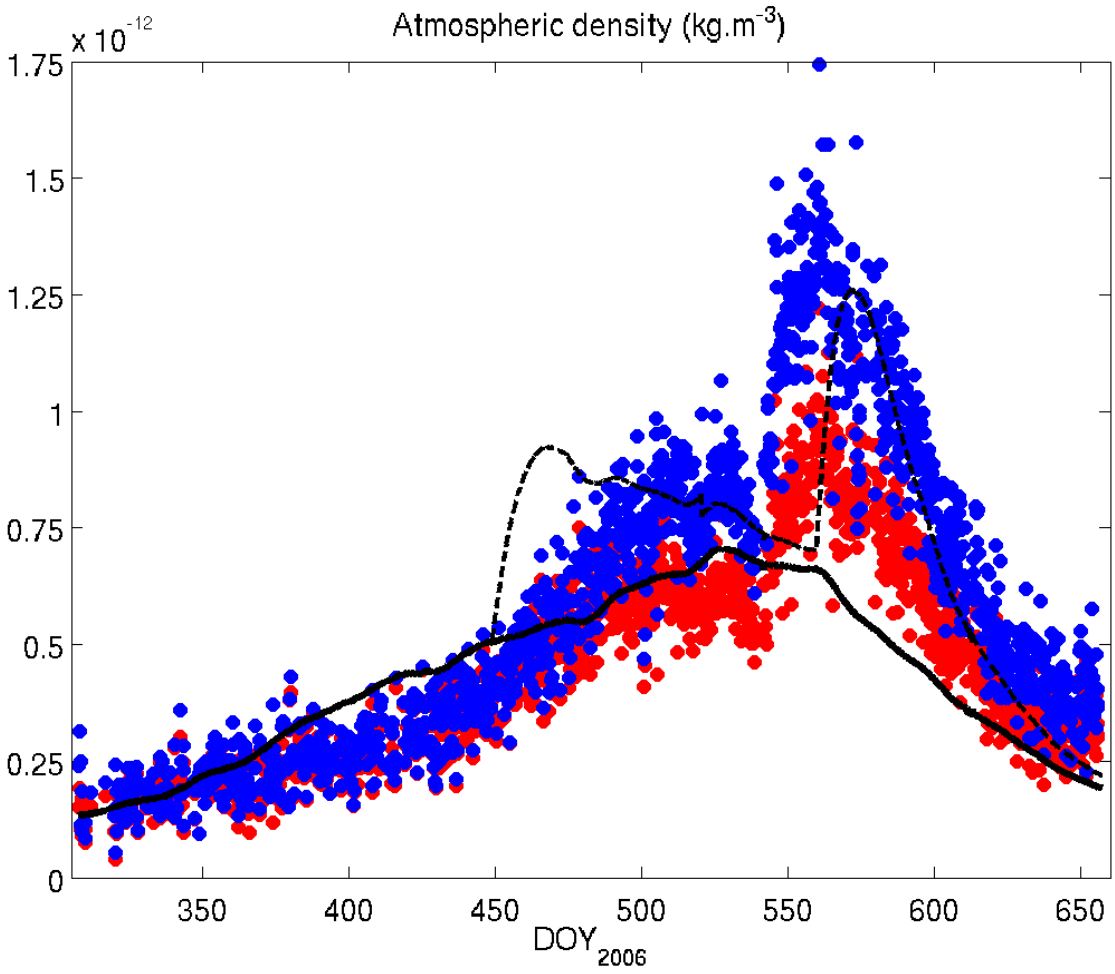

Figure 4.17 Density time series for measurements every 2 orbits (~4h). The blue dots show the previous density values (red, also in Figure 4.14) corrected by the addition of the contribution from the empirical along-track accelerations. As in Figure 4.14, the black lines show the densities predicted by the Stewart model with (dashed) and without (thick) high dust opacity periods.

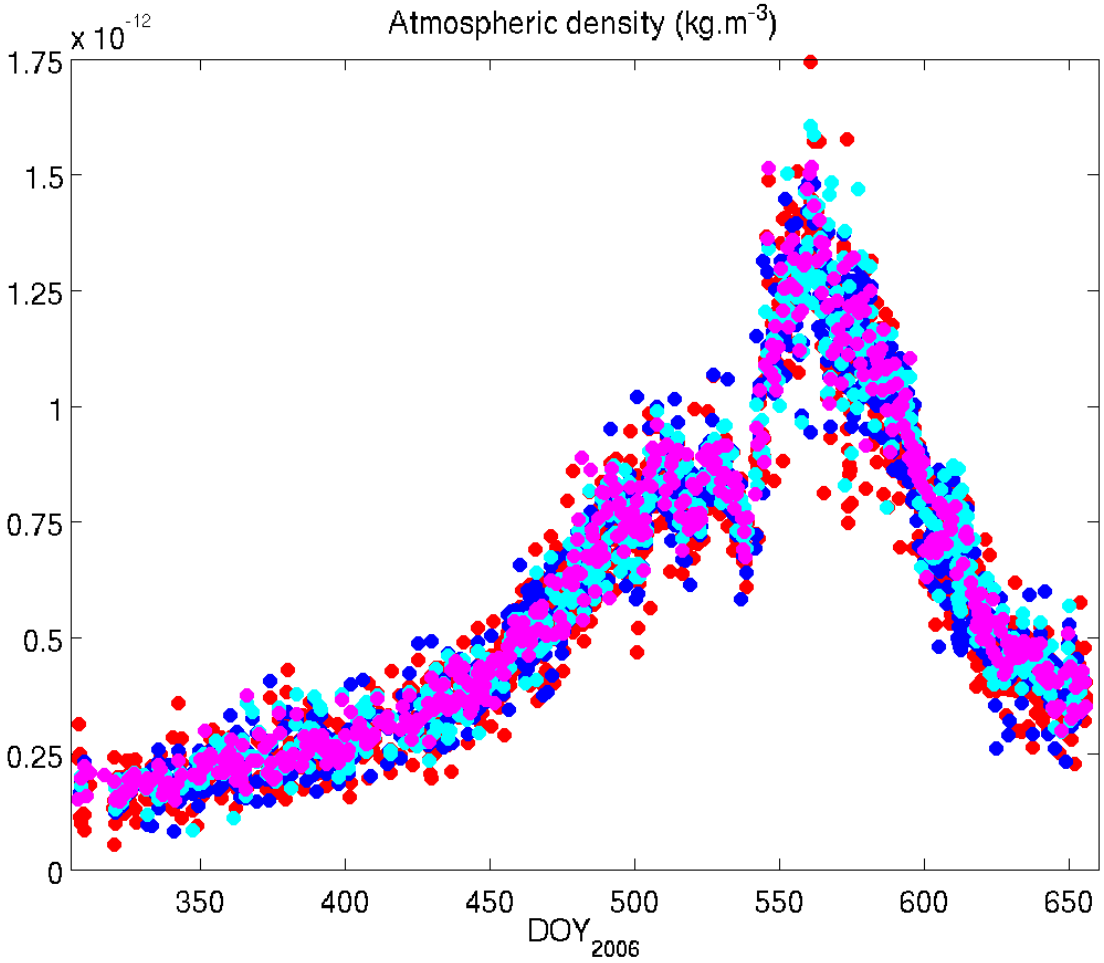

Figure 4.18 Time series of density at 250km, estimated at various frequencies: once every 2 (red), 3 (blue), 4 (cyan) and 6 (magenta) orbits.

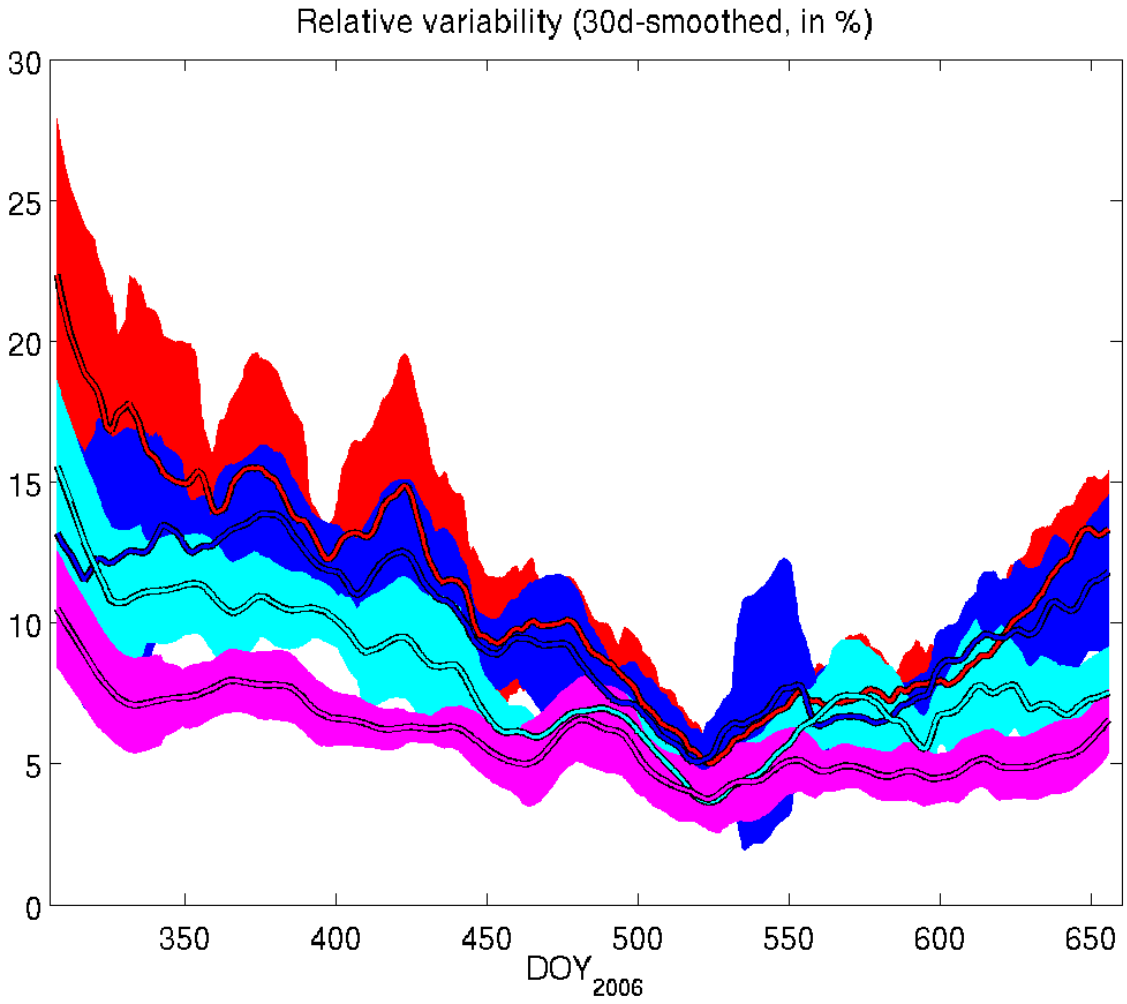

Figure 4.19 Relative density variability for various estimation timescales (same as Figure 4.17). The curves are smoothed by a 30-day running mean for better clarity. The surfaces show the standard deviation of the instantaneous variability around those smoothed curves, and can be regarded as error estimates of the variability.

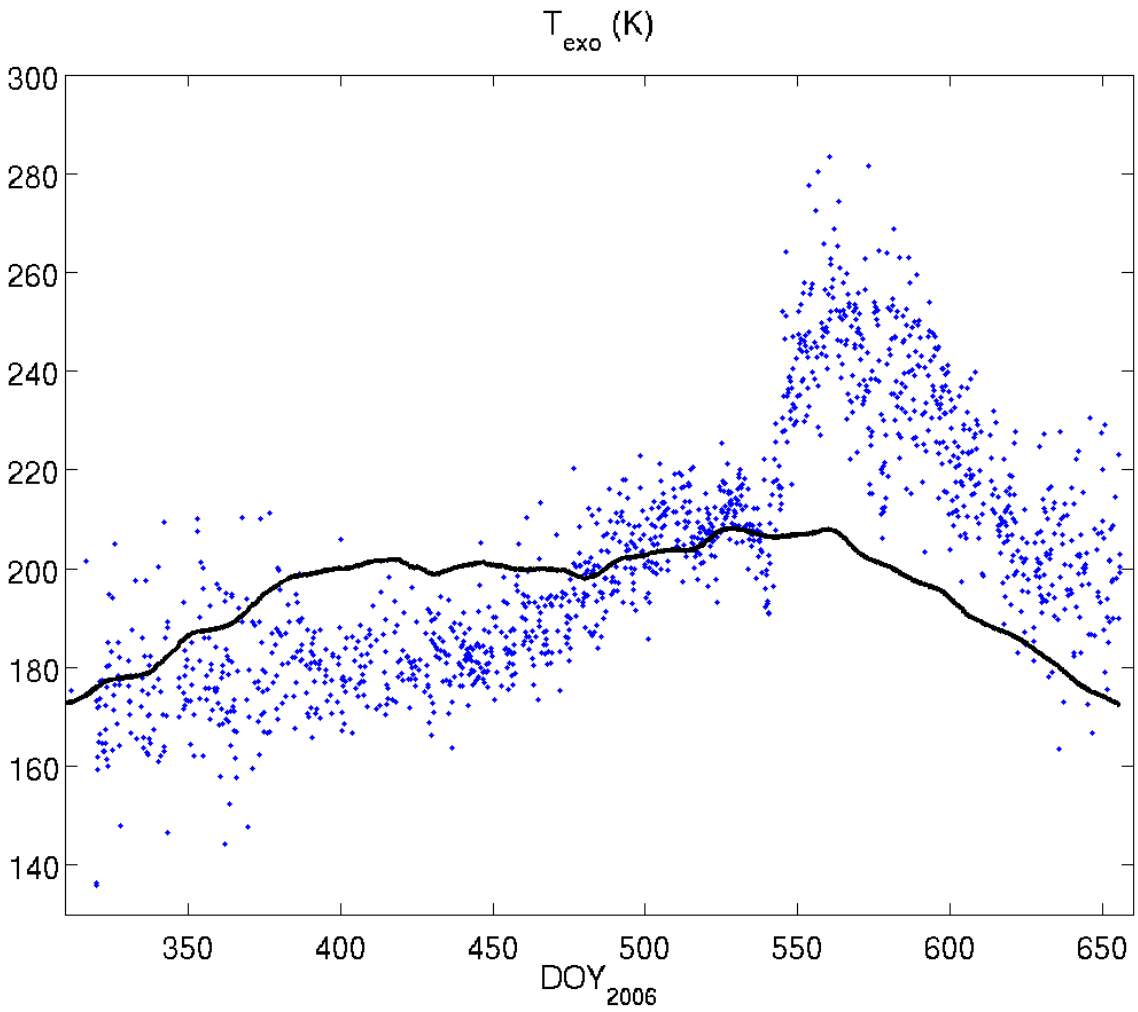

Figure 4.20 Exospheric temperature estimates obtained from interpolation. The temperatures predicted by the model are shown in black.

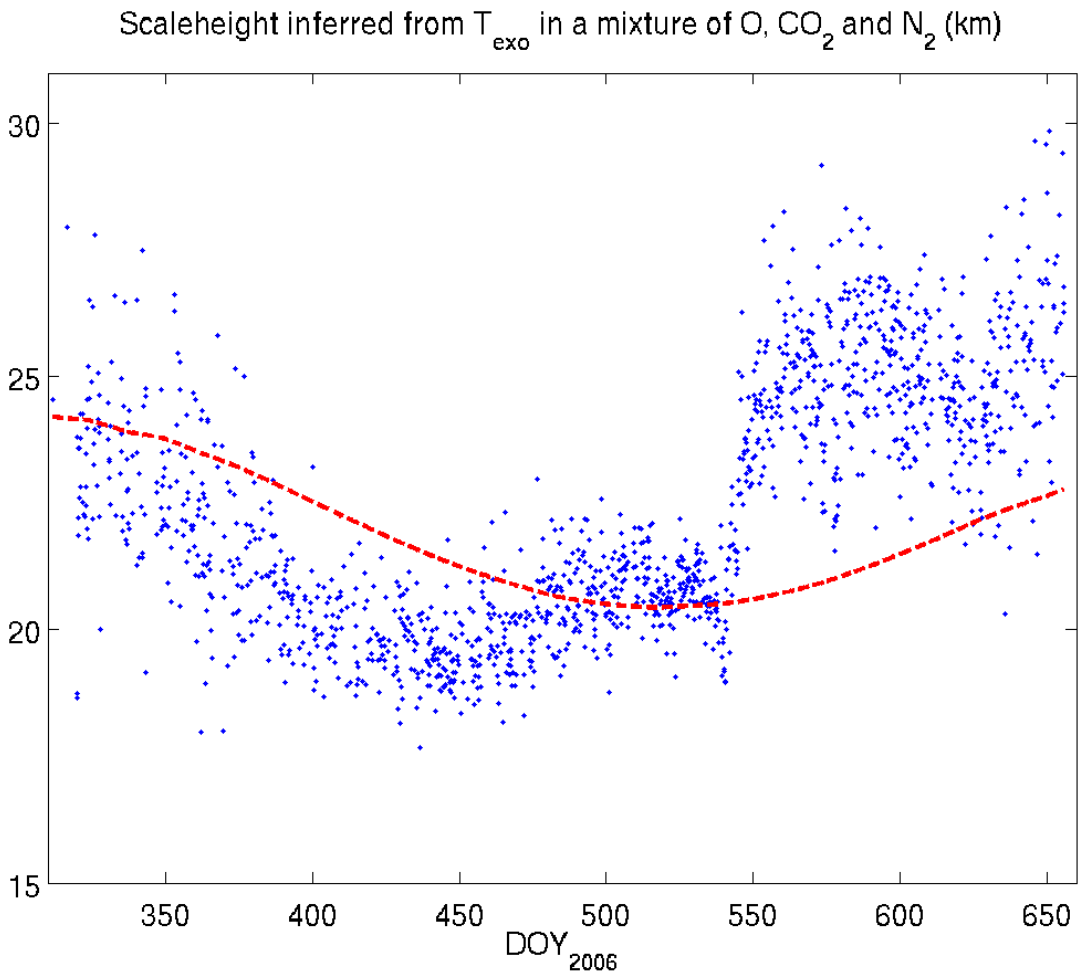

Figure 4.21 Scale height inferred from the exospheric temperature estimates. In black, the scale height inferred from the model exospheric temperature. In red, the scale height calculated from densities 240 and 260km above the South Pole.

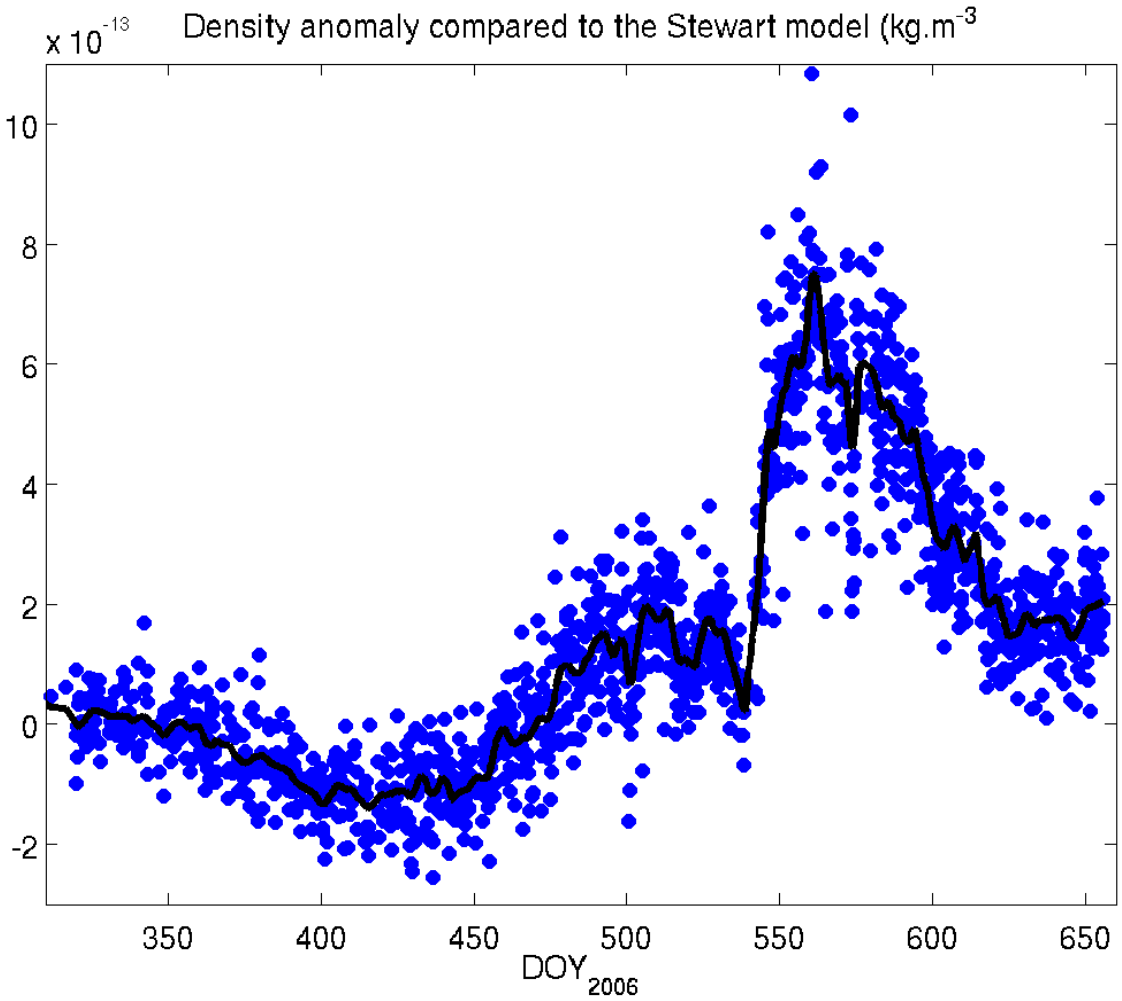

Figure 4.22 Difference between the measured total density and the prediction by the Stewart model without dust storms. For clarity, the black line shows the same times series smoothed over 30 days.

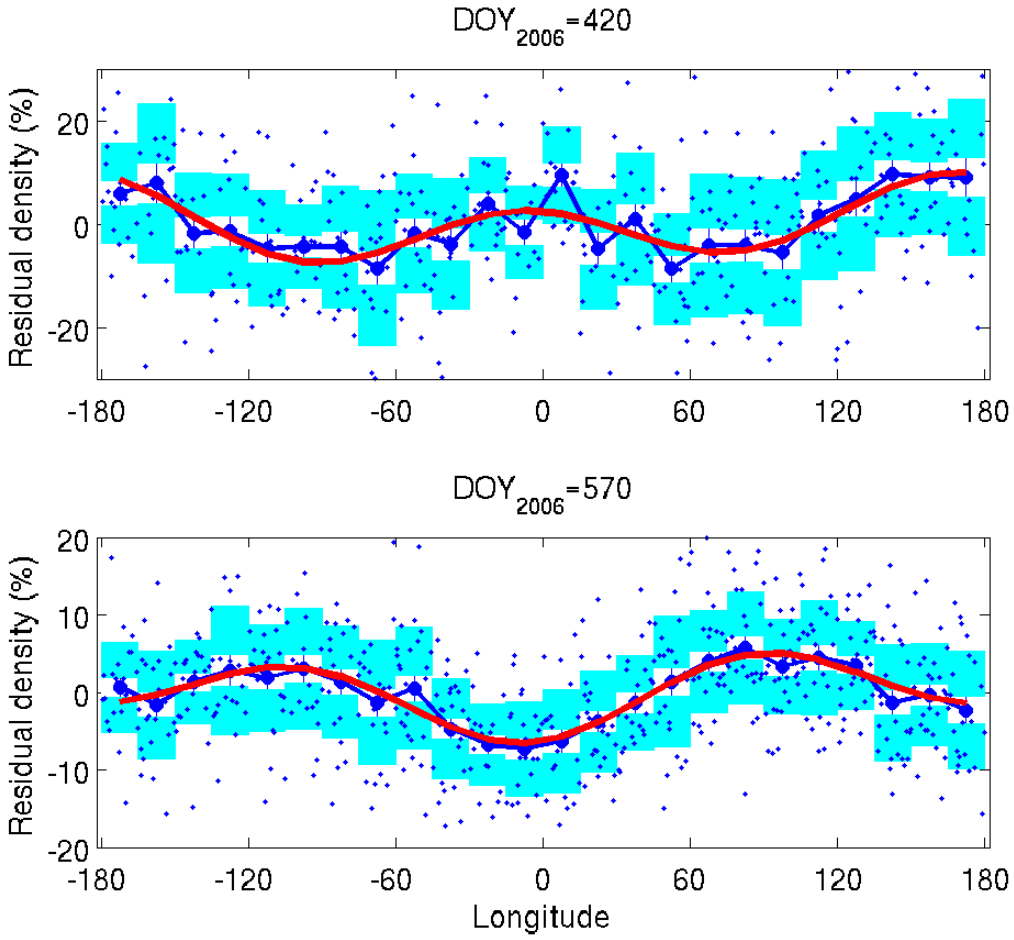

Figure 4.23 Density residuals (small blue dots) plotted according to their dayside equator-crossing longitude. The mean density in each 15° longitude bin is shown by a large blue dot, with its associated uncertainty shown as a white box. The cyan box shows the standard deviation of the density residuals around the mean. The thick red line shows the best fit using two waves (wavenumbers 1 and 2). The two plots correspond to data from two 60-day periods centered on DOY_{2006}=420 and DOY_{2006}=570.

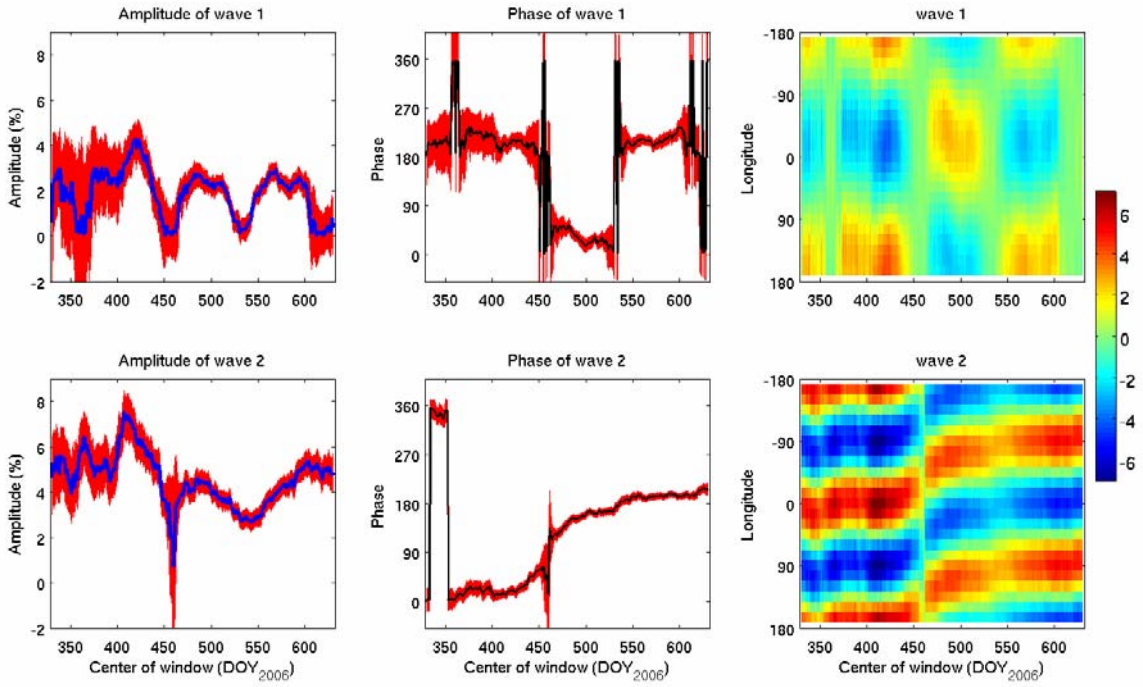

Figure 4.24 Amplitude (left; in % of the mean in the 60-day time period), phase (center; in degrees) and fitted wave field (right; also in % relative to the mean). Large changes in phase occur only during periods when amplitudes are small, which is expected from the smoothing of the fitting process in the transition between two different states.

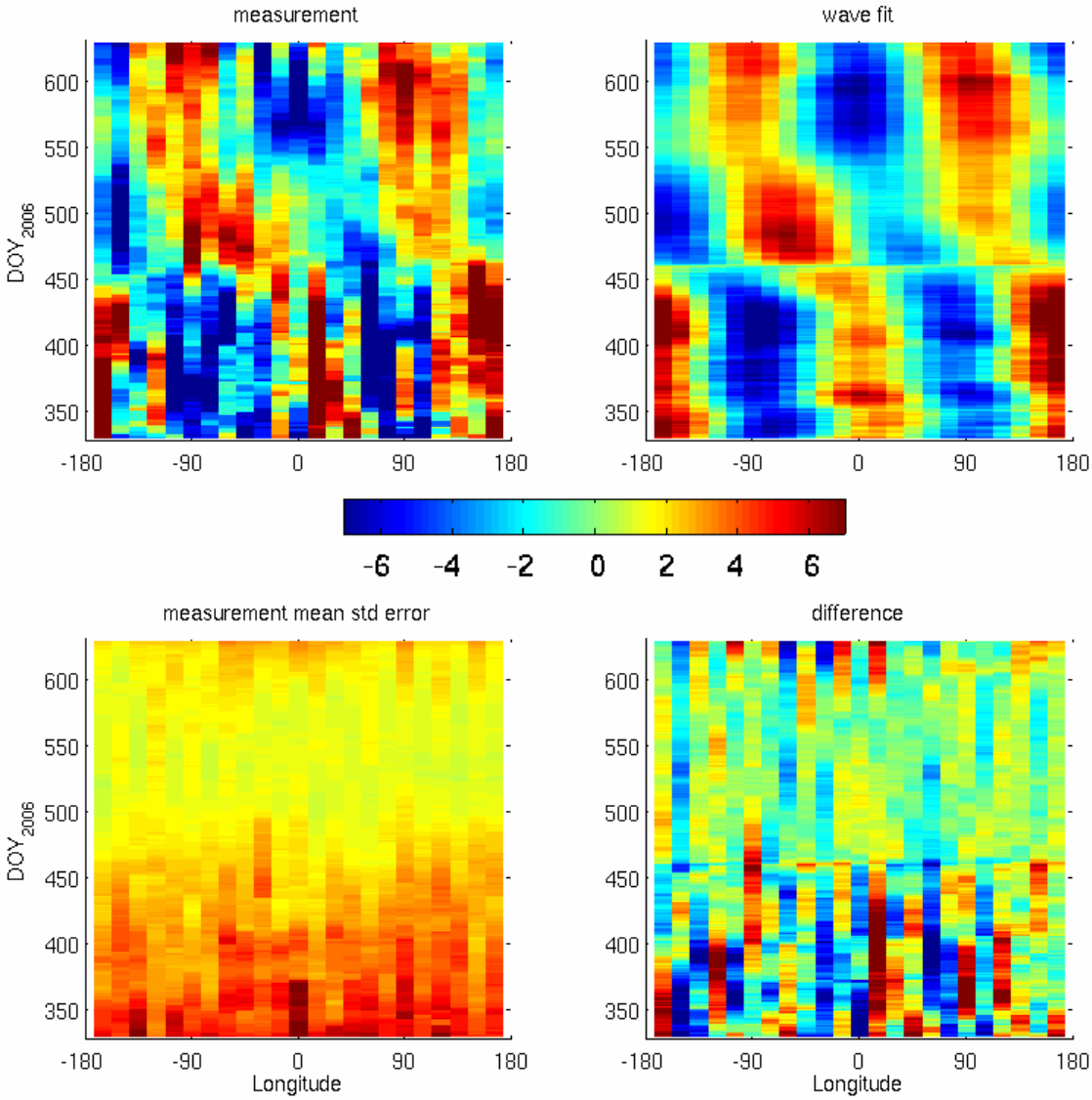

Figure 4.25 Checkerboard plots of: **(a)** the density residuals over 60 days averaged in 15° longitude bins (the time shown on the left axis is the center of the window); **(b)** the density fitted with two waves (wavenumbers 1 and 2); **(c)** the standard error of the residuals shown in (a); **(d)** difference of (a) and (b) showing the mistfits. The colorbar is the same for four plots (-7 to 7, in %).

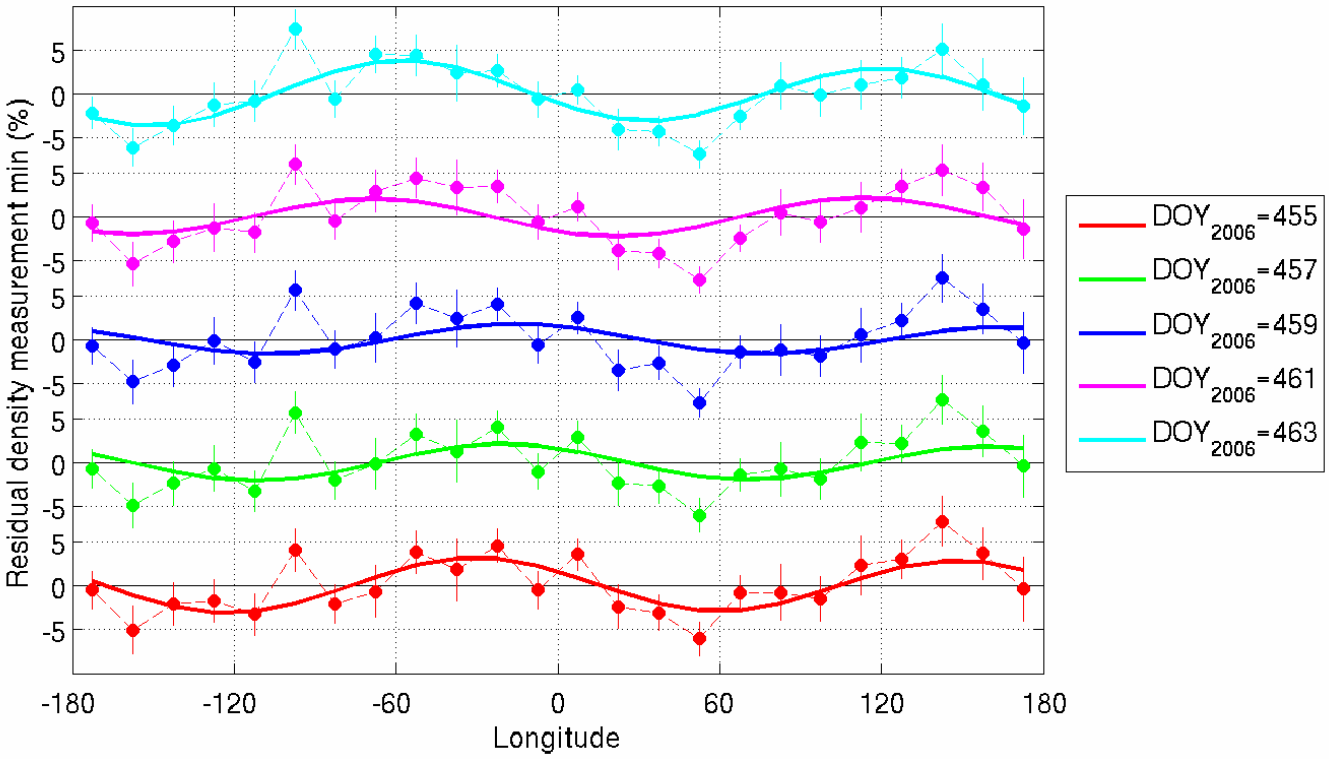

Figure 4.26 Plot of the density residual averages in 15° longitude bins (solid circles joined by a dashed line) and the best-fit wave structure (wavenumbers 1 and 2, thick line) for five different 60-day windows centered on DOY_{2006} = 455, 457, 459, 461 and 463. Each set is shifted for clarity. The binned averages do not vary significantly, but the fits show rapid and large phase shifts.

[THIS PAGE INTENTIONALLY LEFT BLANK]

Chapter 5

Non-conservative force modeling: self-shadowed cross-sections

5.0 Introduction

In this chapter, we give an overview of the updated algorithm for the calculation of the cross-sectional areas during the non-conservative force estimations (atmospheric drag, direct solar radiation, albedo and thermal planetary radiation).
After describing what self-shadowing is and its importance, we will present the existing cross-section calculation method and explain its limitations. Then we will describe the algorithm for an improved modeling and show how it can be integrated in the current GEODYN program structure. Finally, we will test the algorithm on data from the Mars Reconnaissance Orbiter (MRO), in terms of computational cost and of modeled force changes. We will also mention a further enhancement to the use of self-shadowing during POD.

5.1 What is self-shadowing?

Few artificial satellites have such simple geometries as Sputnik or Starlette (sphere) or micro-satellites (box). In general, capable spacecraft have at least an external antenna and a solar array panel attached to the main bus. When those are movable, they can create a large variety of configurations depending on the position of the ground station on Earth, the Sun and the object observed. Those more complex geometries can necessarily affect the POD work in two ways.
First, the physical geometry change can shift the center of mass and modify the moments of inertia of the spacecraft, which alters how it will respond to external

forces and torques. The majority of the spacecraft mass is usually located inside the main bus, so this effect is small in general. However, in the case of MRO, fast movements of the large high-gain antenna are clearly visible in the Doppler residuals when the center of gravity movement is not considered (Figure 5.1). Those rapid antenna jerks are associated with the antenna turning completely around its gimbals to avoid the “forbidden solid angle” that would endanger or break the rotating gimbal mechanism.

Second and more importantly than the center-of-mass shifts, the non-conservative forces, which are a major focus of this thesis work, are strongly affected by complex geometries. Indeed, they all include a spacecraft cross-sectional area in their formula. This area can be rapidly modified by changing spacecraft orientation in space, so a good attitude model is important. But it is equally important for some spacecraft to account for self-shadowing. Some surface elements facing the right direction (for example, the direction of the Sun in the case of solar radiation), can be partially obstructed by another surface element. Over the course of an orbit, depending on the spacecraft geometry and orientation, this effect can significantly change not only the magnitude of the total calculated acceleration, but also its direction.

If the “self-shadowing effect” is constant, then only the magnitude of the acceleration will be overestimated. Thus, it can be correctly modeled with GEODYN by adjusting a scale factor, and it will not introduce aliasing in the POD. On the other hand, if the self-shadowing effect varies significantly during one orbit, the modeled acceleration pattern is very different from what it would have been not taking self-shadowing into account. It is easy to see that the numerical adjustment of the various accelerations by GEODYN can be significantly modified. Aliasing is introduced; for instance, if during part of the orbit a whole bus plate is shadowed by the antenna, not taking this fact into account could lead GEODYN to assign a higher solar radiation scale factor and underestimate the

atmospheric drag scale factor, while trying to balance the various accelerations to better fit the data measurements.

The inclusion of self-shadowing during the calculation of the spacecraft cross-sectional area can be very important, depending on the spacecraft geometry and orbit. The situation is different for the two spacecraft studied in this work. In the case of Mars Odyssey, the only significant shadowing was for the atmospheric drag (i.e., for the spacecraft cross-sectional area observed from the velocity vector), but it was constant and could thus be taken into account *a posteriori* by applying a correction factor. On the other hand, Mars Reconnaissance Orbiter showed a more significant and time-variable shadowing effect for both the direct solar radiation and the atmospheric drag. The direct solar radiation shadowing is mostly the consequence of the large high-gain antenna obscuring from view a bus plate. The shadowing of the drag cross-section is more variable, and the inclusion of the self-shadowing effect for POD more desirable.

5.2 Earlier cross-section calculation schemes

The simplest method of estimating the spacecraft cross-section is to assume it constant. This is a very good approximation for spherical satellites, of which there are a few, but it is usually a poor assumption. Indeed, the spacecraft cross-sectional area can be very variable depending on the viewpoint: the area for the solar radiation is in general much larger than the one for atmospheric drag, because the solar panels are oriented accordingly. Significant errors are introduced if we use a single value for all these configurations. It is not possible in GEODYN to specify one constant cross-section for each non-conservative force, although it could be implemented easily, if there was any need for it.

Rather, when no attitude telemetry is available, analytical attitude models are used, such as specifying that the solar arrays point towards the Sun, the high-gain antenna towards the Earth and the instrument bus panel towards the planet (nadir). This kind of model requires the description of the spacecraft in a series of surface elements, called “plates”. All the plates of this “macro-model” are oriented in space and the total area is calculated by performing simple dot-products between the plate normal and the viewing vector and adding all the visible plate areas weighted by the obtained values. This method has the interest of being very efficient computationally and of being an important improvement compared to the constant cross-section assumption.

In reality, for the radiation pressure acceleration calculations, the individual plate cross-sections are not lumped together directly, because each of them has particular diffuse and specular reflectivity coefficients. The contribution of each plate to the total acceleration is thus calculated in sequence.

5.3 Self-shadowing model: a truly 3D spacecraft model

It can be noted here that the macro-model description of the spacecraft is not three-dimensional. Only the normal vector and the area of each plate need to be set, and their relative position is not necessary. In order to generalize the cross-section model to take the self-shadowing into account, a new way of describing the spacecraft in three dimensions needs to be devised. Obviously, the spatial arrangement of the plates is critical to be able to determine which are in front or behind. Solving the self-shadowing problem cannot be a simple add-on to the existing simple framework.

In the current scheme, the cross-section of each visible plate is calculated individually, in order to evaluate its contribution to the spacecraft acceleration.

This is necessary for the radiation pressure accelerations because of the heterogeneous radiative properties of macro-model plates. Thus, the new self-shadowing scheme should also provide as output the shadowed area of individual plates. To allow for compatibility with older GEODYN inputs, but also to make it possible to easily switch between cross-section algorithms, it is also desirable that the macro-model and the new 3D-model match (same plates). This also greatly reduces the error sources in the new code, as the self-shadowing scheme just becomes an add-on feature that does not change the normal course of the program execution but is called when precise cross-sectional areas are needed.

5.3.1 3D-model description

Here we describe the format of the new "geometry file".

After a first line of comment, the total number of nodes defining the spacecraft plates is followed by the Cartesian coordinates in the spacecraft frame (in meters) of all those nodes:

```
* NODES
26
001      1.000000  -1.500000   1.500000
002      1.000000  -1.500000  -1.300000
…
026      1.500000  -2.910000  -1.407100
```

Each plate is then defined as follows:

```
* BUS plate #1  -  X+
001    0  4
001     1.000000   0.000000   0.000000
001    001 002 006 005
```

The number on the left column is the plate number, which must match the macro-model. The two integers on the first line are respectively a flag set to *true* if the plate is movable (e.g., solar array, antenna) and the number of nodes which define the plate. The plates do not need to be rectangular, and can be any (flat) convex polygonal shape.

The following line gives the normal to the plate, providing orientation information. For non-movable plates (bus), a plate just has a “front”, i.e. if viewed from behind it will not be taken into account. This reduces the number of useless polygonal intersections to be considered, given that for example with a simple box, for any viewing angle only three faces are visible. In the case of a movable object, only one plate needs to be defined for every physical surface element (antenna, solar panel). Depending on the viewing angle, the obtained area will be assigned to either the front- or the back-side plate of the macro-model. The last line shown defines the nodes of the plate/polygon. The order is important, and the first three nodes are used to check the normal vector.

In the case of movable panels, one extra line defines the position (still in the spacecraft frame) of the gimbals.

```
* HGA
011    1  8
011     0.000000   0.000000   1.000000
011    019 020 021 022 023 024 025 026
        0.000000  -3.150000  -1.520000
```

5.3.2 Algorithm description

Upon the first call to the self-shadowing subroutine, the geometry file is read. (If it is not found, rather than continuing the execution without shadowing, the program is aborted.)

The spacecraft is then ‘oriented’, i.e. we rotate each plate into position according to the attitude information (quaternion file). If the plate is movable, we first perform a rotation of the plate nodes around the gimbal with the appropriate rotation matrix. Then, the rotation from the spacecraft frame to the True-of-Date frame is applied for all the plates (Figure 5.2)

The next step is to project all the plates on the *projection plane*, defined by the viewing vector (oriented towards the spacecraft; for example Sun→spacecraft

vector). In addition to the new two-dimensional coordinates of each node on that plane, each plate is assigned a *depth*, equal to the mean of the node-to-projection plane (signed) distances of the appropriate nodes (Figure 5.3). This depth information enables the ordering from farthest to closest of all the projected plates with respect to one another, from the viewpoint of the input vector.

At that point, we iteratively calculate how each plate is shadowed by the ones standing in front. We start with the plate with the greatest *depth* (farthest). This is done by finding the intersection of the considered polygon with the plates having larger depth values. Those intersections are themselves convex (because the intersection of two convex polygons is another convex polygon).

Due to the nature of the problem, we cannot rule out complicated intersection geometries and we do not know *a priori* if intersections of intersections occur. In the simple example shown below, in order to obtain the correct shadowed area of plate C, we need to add the area of ABC after having subtracted BC and AC (Figure 5.4).

The algorithm that will give this sort of behavior in the general case is not obvious. It turns out to be simple to implement, but can potentially be computationally expensive, due to the unavoidable multiple intersection testing.

Each intersection polygon is added at the end of the pool of polygons, originally only consisting of the ‘physical’ spacecraft plates. It is assigned the depth of the shadowing plate, so that it can shadow again subsequent polygons. In addition, we need to keep track of the sign of the contribution of the intersection. This is done by assigning a value of +1 to the original spacecraft plates, and assigning to each new intersection polygon the inverse of the product of the values of the two intersecting plates forming it. The area of the intersection polygon, multiplied by this sign value, is added to the total area of the spacecraft plate considered.

The algorithm is summarized below in pseudo-code:

```
orient spacecraft

project spacecraft

sort all the spacecraft polygons: P_i [i=1...N_sc] with
      area sign S_i = 1
      depth     D_i      (D_i < D_i+1; i=1 is 'farthest')

N=N_sc

loop through original polygons i = 1 to N_sc
     A_i = area ( P_i )
     N_iter = N
     loop through polygons j = 1 to N_iter
          if ( D_j<D_i ) and ( P_i ∩ P_j )
               N = N + 1
               add intersection to the pool: P_N with
                    S_N = – S_i.S_j
                    D_N = D_j
               A_i = A_i + D_N . area ( P_N )
          endif
     endloop
endloop
```

5.3.3 Implementation

The algorithm was written out in FORTRAN to provide a set of subroutines directly integrated in GEODYN. It requires setting up new logical flags at the start of GIIE, which turn on or off the use of the self-shadowing. The source files are provided at the end of this chapter. Here we will quickly describe the various functions.

The only subroutines GEODYN need to call are: **extattSS** and **getSHADOW**. **extattSS** is called by **f**, the function that calculates the forces acting on the spacecraft. It supersedes **extatt**; in addition to reading the quaternion information

for the current timestep and constructing the resulting rotation matrices, it fills the ROTMAT three-dimensional array which provides attitude information to be used to orient the spacecraft. **getSHADOW** returns the shadowed and unshadowed areas of the various plates given an input direction vector and the unit number of the geometry input file. In the full self-shadowing implementation, **getSHADOW** is called by modified versions of **bwsolr**, **bwalbd** and **bwdrag**.

ANGLE_2P	calculates the angle between two 2D vectors
EXTATTSS	sets the ROTMAT array for use in ROTATEPOINT
FORM_POLY	forms convex polygon exterior to a cloud of points
GETAREAPOLY_IND	calculates the area of a polygon given its index in the polygon pool
GETSHADOW	main function; calculates vector of shadowed and unshadowed plate areas given input 3D vector
INSIDE_POLY	returns true if a point is inside a polygon
INTER_PT	returns the intersection between two segments described as four points
INTERS_POLY	creates a polygon which is the intersection of two convex polygons
ORIENT_SPACECRAFT	rotates the spacecraft plates according to the attitude data in ROTMAT
PROJECT_SPACECRAFT	projects the spacecraft nodes on a plane perpendicular to the input 3D vector; creates the corresponding 2D points with a 'depth' parameter
READGEOMETRY	reads the geometry input file, stored in a fort.UNIT file
REMOVE_DOUBLONS	removes identical points in a polygon
ROTATEPOINT	rotates a point around a reference point given the index of the ROTMAT to be used
SORT_ALL	sorts a set of polygons according to their depth property (farthest, i.e. largest depth value, to closest)

5.4 Computational Efficiency

To evaluate the computational cost of using the self-shadowing scheme during POD, we used a short 4-hour arc of Mars Reconnaissance Orbiter, starting on April 25 2007 at 20:14 UTC. The arc was not actually converged, but simply integrated once, i.e. without the iterative adjustment of the initial state to achieve best fit. The self-shadowing subroutine was used to calculate the atmospheric drag and direct solar radiation in every case, but its use was turned on and off for the

albedo (and thermal) radiation. Because the albedo acceleration calculation makes multiple calls to **getSHADOW** in order to add the contribution of multiple surface spots, it provides a better duration measurement of the self-shadowing part of execution (the overheads of starting/stopping GIIE and calculating the other forces and measurement correction are reduced in relative terms). For instance, with the standard albedo model, **getSHADOW** was actually called 43 times. As noted earlier, in general the use of self-shadowing for the albedo acceleration is not necessary, so the computational cost for drag and direct solar radiation would be about 20 times smaller than the numbers below.

The standard GEODYN run is the “no shadowing – standard albedo” one. Other albedo models will be discussed in **Chapter 6**, but they obtain the albedo acceleration estimate from a variable number of surface points (the grid nodes of a constant-resolution albedo map that are visible to the spacecraft). With a 5-degree map resolution, about 50 grid points are visible at any given time; this increases to ~150 for 3-degree resolution and ~1000 for the 1-degree map. The program execution duration results are presented in Table 5.1. The interpolated shadowing results will be discussed in **Section 5.7.1**.

Clearly, the addition of self-shadowing to the POD creates a computational bottleneck, as the execution time increases tremendously with self-shadowing as the number of source points for cross-section, when the execution time does not grow significantly without self-shadowing.
The computational cost due to shadowing only is shown in Figure 5.5.

Another way to look at those results is to plot the relative increase in computation time (Figure 5.6). The cross-section calculations using the **getSHADOW** function account for an increasing part of the total runtime.

As a result, while the use of self-shadowing during the non-conservative force estimation can be valuable as it will be shown in the next section (Section 5.6), it is clearly a computational burden, and should be used carefully. For instance, it is best to converge the arcs completely without it, and process the tracking data with more careful cross-section modeling only for the final product creation, be it drag coefficients like in this work or normal equations for gravity field inversion for potential future studies.

5.5 Application with MRO

5.5.1 3D model

A 3D model of the spacecraft was constructed using information from the available documentation, while making it most compatible with the existing macro-model.

```
GEOM FILE for the MRO spacecraft
* NODES
 26
001      1.000000  -1.500000   1.500000
002      1.000000  -1.500000  -1.300000
003     -1.000000  -1.500000  -1.300000
004     -1.000000  -1.500000   1.500000
005      1.000000   1.500000   1.500000
006      1.000000   1.500000  -1.300000
007     -1.000000   1.500000  -1.300000
008     -1.000000   1.500000   1.500000
009      1.050000  -1.550000  -1.350000
010     -0.499302  -2.444490  -1.350000
011     -4.445109  -1.387214  -1.350000
012     -3.790297   1.056578  -1.350000
013      0.155510  -0.000698  -1.350000
014     -1.050000  -1.550000  -1.350000
015     -1.944490  -3.099302  -1.350000
016     -5.890297  -4.156578  -1.350000
017     -6.545109  -1.712786  -1.350000
018     -2.599302  -0.655510  -1.350000
019      1.500000  -1.910000  -1.407100
020      0.500000  -0.910000  -1.407100
021     -0.500000  -0.910000  -1.407100
022     -1.500000  -1.910000  -1.407100
023     -1.500000  -2.910000  -1.407100
024     -0.500000  -3.910000  -1.407100
025      0.500000  -3.910000  -1.407100
026      1.500000  -2.910000  -1.407100
* BUS plate #1  -  X+
001    0  4
001     1.000000   0.000000   0.000000
001    001 002 006 005
* BUS plate #3  -  Y+
003    0  4
003     0.000000   1.000000   0.000000
003    005 006 007 008
* BUS plate #4  -  Y-
004    0  4
004     0.000000  -1.000000   0.000000
004    001 004 003 002
* BUS plate #5  -  Z+
005    0  4
005     0.000000   0.000000   1.000000
005    001 005 008 004
* BUS plate #6  -  Z-
006    0  4
006     0.000000   0.000000  -1.000000
006    002 003 007 006
* SAP front
007    1  5
007     0.000000   0.000000   1.000000
007    013 012 011 010 009
        1.050000  -1.550000  -1.350000
* SAM front
009    1  5
009     0.000000   0.000000  -1.000000
009    014 015 016 017 018
       -1.050000  -1.550000  -1.350000
* HGA
011    1  8
011     0.000000   0.000000   1.000000
011    019 020 021 022 023 024 025 026
        0.000000  -3.150000  -1.520000
* END
comments
```

The macro-model is given here for reference. The plates in both models correspond and have very similar surface areas (2nd line of each plate, after normal vector). The macro-model defines the specular (3rd line) and diffuse (4th line) reflectivity coefficients to be used in the radiation pressure acceleration calculations.

```
PANEL   0  1 1   2005224            1.0D+00 +0.0000000D+00  0.00000D+00
PANEL   0  1 2   2005224          7.3400D+00
PANEL   0  1 3   2005224          0.5099D+00  1.0000000D-20
PANEL   0  1 4   2005224          0.0435D+00  1.0000000D-20
PANEL   0  2 1   2005224           -1.0D+00 +0.0000000D+00  0.00000D+00
PANEL   0  2 2   2005224          7.3200D+00
PANEL   0  2 3   2005224          0.4715D+00  1.0000000D-20
PANEL   0  2 4   2005224          0.0965D+00  1.0000000D-20
PANEL   0  3 1   2005224             0.0D+00 +1.0000000D+00  0.00000D+00
PANEL   0  3 2   2005224          6.3500D+00
PANEL   0  3 3   2005224          0.4427D+00  1.0000000D-20
PANEL   0  3 4   2005224          0.1026D+00  1.0000000D-20
PANEL   0  4 1   2005224             0.0D+00 -1.0000000D+00  0.00000D+00
PANEL   0  4 2   2005224          6.3400D+00
PANEL   0  4 3   2005224          0.5099D+00  1.0000000D-20
PANEL   0  4 4   2005224          0.0435D+00  1.0000000D-20
PANEL   0  5 1   2005224             0.0D+00 +0.0000000D+00  1.00000D+00
PANEL   0  5 2   2005224          6.3600D+00
PANEL   0  5 3   2005224          0.4187D+00  1.0000000D-20
PANEL   0  5 4   2005224          0.0458D+00  1.0000000D-20
PANEL   0  6 1   2005224             0.0D+00 +0.0000000D+00 -1.00000D+00
PANEL   0  6 2   2005224          6.4000D+00
PANEL   0  6 3   2005224          0.5255D+00  1.0000000D-20
PANEL   0  6 4   2005224          0.1128D+00  1.0000000D-20
PANEL   1  7 1   2005224             0.0D+00  0.0000000D+00  1.00000D+00
PANEL   1  7 2   2005224          12.740D+00
PANEL   1  7 3   2005224          0.0100D+00  1.0000000D-20
PANEL   1  7 4   2005224          0.1000D+00  1.0000000D-20
PANEL   1  8 1   2005224             0.0D+00  0.0000000D+00 -1.00000D+00
PANEL   1  8 2   2005224          12.740D+00
PANEL   1  8 3   2005224          0.0450D+00  1.0000000D-20
PANEL   1  8 4   2005224          0.0450D+00  1.0000000D-20
PANEL   1  9 1   2005224             0.0D+00  0.0000000D+00 -1.00000D+00
PANEL   1  9 2   2005224          12.740D+00
PANEL   1  9 3   2005224          0.0100D+00  1.0000000D-20
PANEL   1  9 4   2005224          0.1000D+00  1.0000000D-20
PANEL   1 10 1   2005224             0.0D+00  0.0000000D+00  1.00000D+00
PANEL   1 10 2   2005224          12.740D+00
PANEL   1 10 3   2005224          0.0450D+00  1.0000000D-20
PANEL   1 10 4   2005224          0.0450D+00  1.0000000D-20
PANEL   1 11 1   2005224             0.0D+00  0.0000000D+00  1.00000D+00
PANEL   1 11 2   2005224           7.130D+00
PANEL   1 11 3   2005224          0.1800D+00  1.0000000D-20
PANEL   1 11 4   2005224          0.2800D+00  1.0000000D-20
PANEL   1 12 1   2005224             0.0D+00  0.0000000D+00 -1.00000D+00
PANEL   1 12 2   2005224           6.500D+00
PANEL   1 12 3   2005224          0.0191D+00  1.0000000D-20
PANEL   1 12 4   2005224          0.0495D+00  1.0000000D-20
```

Telemetry quaternion data can be used with the 3D model presented above to reconstruct the spacecraft attitude. Figure 5.7 shows MRO on April 25th 2007 at ~19:40 UTC, seen from different viewpoints to be able to appreciate the three-dimensional configuration.

5.5.2 Results

The orbital arc chosen to show the effects of the self-shadowing on the force modeling is the arc **0165**, a ~5h-long arc starting on May 2nd 2007 at ~20:32 UTC. We processed the arc with full shadowing (i.e. also for the albedo radiation). The most direct effect of adding the self-shadowing is seen in the C_R and C_D parameters. C_R, the radiation coefficient, is a scale factor of the incoming solar radiation, and as such shows a reasonable convergence for values close to unity. Adding the self-shadowing, its adjusted value increases from ~0.866 to ~0.923, a sign of improved convergence. The single C_D coefficient changes from 1.576 to 1.622.

Figure 5.8 shows the changes induced in the magnitude of the non-conservative forces. While the shadowing of the albedo radiation remains approximately constant at a low value (~6%), the effect is much more variable and significant for the direct solar radiation. The peak value is close to 25% shadowing, and occurs at maximum acceleration (fully sunlit). Clearly, such an effect is important to take into consideration if we want to avoid aliasing of the solar radiation into the atmospheric drag, which is highly desirable in the current work. In the present case, the shadowing related to the drag, although it reaches high percentage values (40%), is located during a period of low atmospheric density (far from periapsis). However, this is dependant on geometry and can change with time (Figure 5.11).

In addition to magnitude changes, it is also interesting to look at the modifications in the direction of the resulting accelerations. Figure 5.9 shows that the

atmospheric drag is basically unchanged (still along-track), while the albedo is the most sensitive to self-shadowing, with about 10% moving from Along-track and Radial to Cross-track. The solar radiation also sees about 5% of its Cross-track component shift Radial.
Figure 5.10 displays the angular distances between the before- and after-accelerations. The changes are small, but could be significant for the albedo. Combined with updated surface maps of the albedo, the modeling of that force could be improved and in turn impact the recovery of atmospheric drag.

In addition to the detailed effects of the self-shadowing on one arc, we can also look at their time evolution. Using simple statistical properties (minimum, mean, maximum, standard deviation) of the parameters discussed above, we can see in Figures 5.11, 5.12 and 5.13 that the general characteristics are unchanged.
The atmospheric drag is the most sensitive to the spacecraft attitude changes. The period from DOY_{2006}~430 to DOY_{2006}~540, when the solar array pointing was modified, is clearly visible and reduced significantly the amplitude of the self-shadowing: the mean value and the standard deviation are decreased. Nevertheless, the standard deviation is generally quite high, indicating that the drag self-shadowing is very variable along the orbit. Ignoring it would lead to sensible mismodeling of the non-conservative forces.

5.6 Model improvements

5.6.1 Cross-section interpolation

As shown in Section 5.5, the use of self-shadowing can be very costly computationally, in particular for the albedo radiation pressure because of the numerous surface spots that we need to consider. To really improve the acceleration modeling, higher-resolution albedo models (**Chapter 6**) will further

increase this computation load. This can result in unacceptable execution times (Figure 5.5).

To solve this problem, and make possible the use of algorithms more demanding of cross-section calculations, we developed an interpolation scheme. The number of cross-sections to be evaluated at each iteration can be controlled and does not depend on the resolution of the albedo map used. As shown in Figure 5.6, the relative cost of using self-shadowing with high-resolution albedo maps is greatly reduced.

First, we use an orthographic projection centered on the spacecraft for the chosen source points. We then calculate the radius of a regular polygon containing all those two-dimensional coordinates, to insure that the interpolation behaves normally. The number of faces of this polygon is arbitrary, as well as the number of inner polygons, but of course they define the total number of cross-sections to be computed at each timestep. The preferred distribution is shown in Figure 5.14; it seems to be optimal for MRO, but not necessarily in other cases (e.g. different altitude).

The cross-sections are then calculated from the viewpoint of every interpolation node using **getSHADOW**. The results for all the nodes are combined for the interpolation at all the original source points. This is done one plate at a time, so we obtain interpolated individual plate cross-sections at each source point.

As evident in Figure 5.14, this interpolation scheme works very well, with errors usually below 5%. The largest relative errors occur at low cross-section values and outside of the region contributing most to the total acceleration.

5.6.2 Future work

Many improvements could be made to the current implementation of the self-shadowing, which is a first step towards a more accurate modeling of the non-conservative forces.

- Additional rotations are sometimes necessary as a complement to the quaternion information in order to coincide with the spacecraft frame definitions. Such rotations before or after the quaternion operations could be defined in the geometry input file.
- The plate normal vector could be removed from the input geometry file, as it is redundant with some of the calculations made by **getSHADOW**. However, it currently acts like a check for the user.
- If we use the interpolation scheme with only the albedo (no thermal), during the periods of day/night transitions, cross-sections are calculated at the interpolation nodes even when the number of visible source points is smaller. A simple modification could be made so that in such cases the cross-sections at the actual source points are used instead.
- Currently the algorithm cannot be used when a whole hemisphere of the planet is visible from the spacecraft, as it will try to get interpolation outside of that globe, but still on the surface… Solving this would enable the interpolation for eccentric orbits.
- A memory of the previous iteration results could be implemented to speed up the calculations. It would need to be carefully evaluated if for instance, only a small number of interpolation node cross-sections can be updated at each timestep, and the rest inferred. Rates of change of the spacecraft attitude quaternions (especially high-gain antenna) would need to be considered. Indeed, the high-gain antenna on MRO can rotate quickly over most of the solid angle.

- The reprogramming of the whole algorithm to make use of already-made 3D libraries would probably be very beneficial computationally. For instance, illuminating a 3D model of the spacecraft and counting the number and luminosity of each pixel would be very efficient with OpenGL on an average workstation with dedicated graphics card.

5.7 Conclusion

Chapters 2, 3 and 4 of this Thesis showed that with accurate models for the major forces acting on the Mars-orbiting spacecraft, especially gravity anomalies, now available, it is possible to extract more subtle information from the radio tracking data. The atmospheric drag is the most immediate, and is very interesting because it provides density information in the region of the atmosphere were measurements are scarce. However, the density estimations are directly dependent on the adjustment of the non-conservative forces. In the present study, a good amount of effort has been put into improving the modeling of those accelerations. In this chapter, we discussed the issue of the cross-section. A mismodeling the cross-section translates into a mistaken estimate of the instantaneous acceleration. In the case of the Mars Reconnaissance Orbiter, the omission of self-shadowing can lead to large overestimates of the calculated cross-sectional areas. In terms of magnitude, the effect on the albedo acceleration is small, but both for the direct solar radiation and the atmospheric drag, the changes are greater than 15-20%. In addition, the drag self-shadowing is very variable over one orbit (from 0% over half an orbit up to peaks near 70%), so not taking it into account can fundamentally change its ‘signature’ on the spacecraft trajectory perturbations. As a result, the numerical POD program could assign some of the actual drag to the solar radiation or vice-versa, leading to an under- or over-estimate of the actual density. In terms of directional changes, the effects are negligible for the atmospheric drag and small for the direct solar radiation (~1 degree). However, for

the albedo acceleration, the change in the direction of acceleration is much larger (~7 degrees), which can affect the resulting orbital perturbations.

The self-shadowing implementation presented here allows the accurate computation of the cross-section for a spacecraft, arbitrarily-defined as a set of polygonal plates. This significant improvement in modeling comes to a cost computationally, which impedes its use for the albedo acceleration. Given that in the case of MRO, the albedo force is sensibly modified due to the self-shadowing, we developed a cross-section interpolation scheme to overcome this issue.

5.8 Tables

Execution time (s)	standard albedo	new albedo (5deg)	new albedo (3deg)	new albedo (1deg)
no shadowing	9	9	10	31
interpolated shadowing	109	59	70	164
full shadowing	69	77	145	997

Table 5.1

5.9 Figures

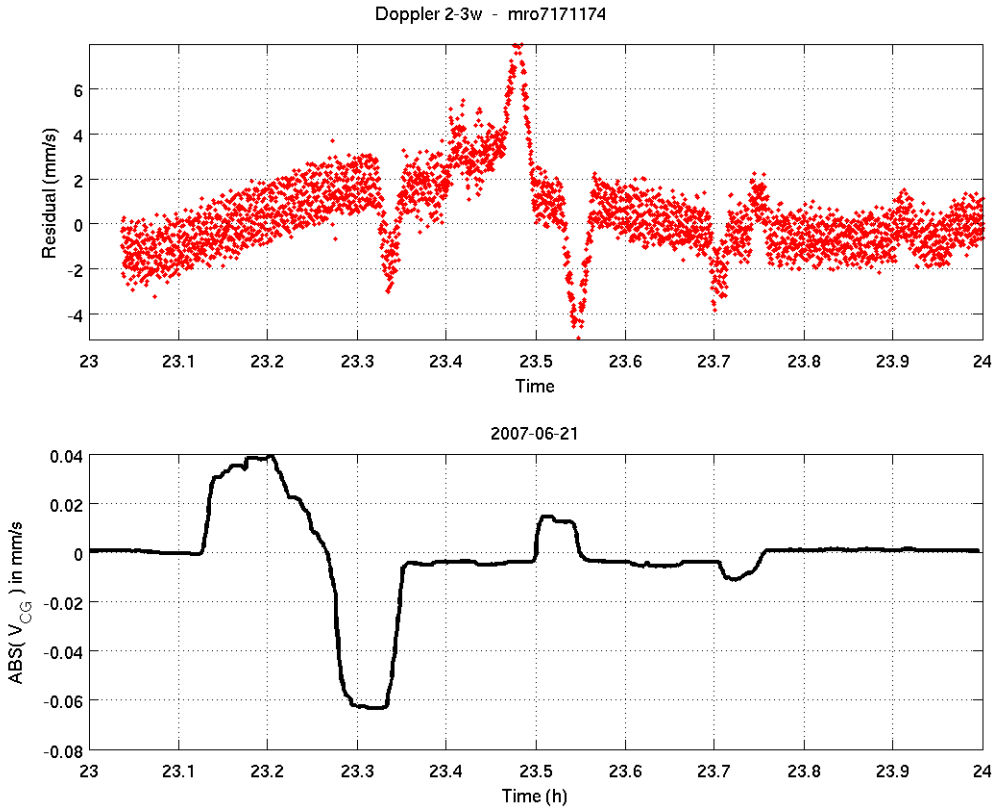

Figure 5.1 Line-of-sight velocity of MRO center-of-mass (bottom, shown for arc *mro7171174*) seems to be the source of sudden short-lived excursions in the Doppler residuals (top). The temporal shift corresponds to the Earth-Mars time delay. The residual anomalies appear to be anti-correlated with the velocity derivative (e.g., the first positive center-of-mass step produces one negative and one negative residual spikes.

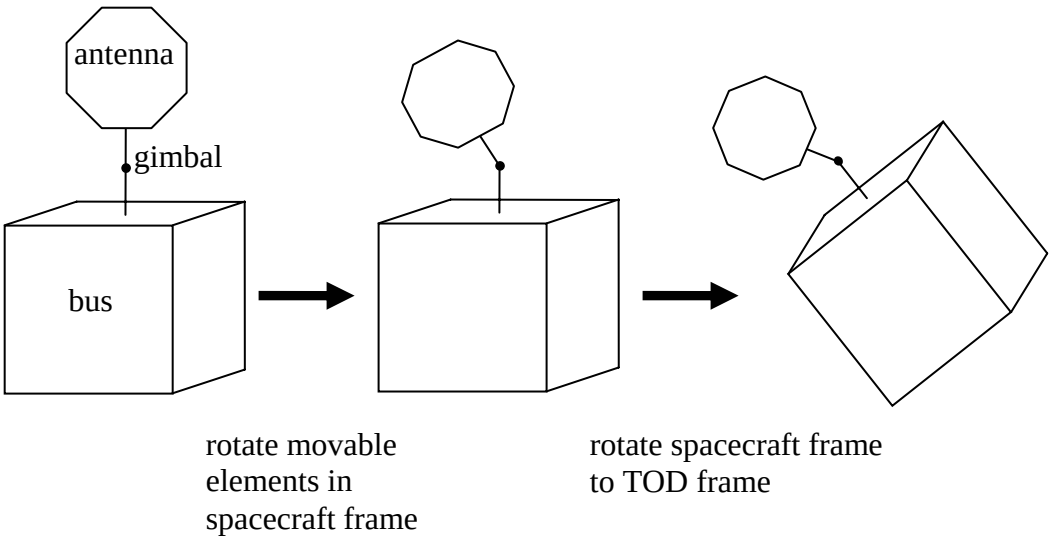

Figure 5.2 Illustration of the steps to reconstruct the spacecraft attitude.

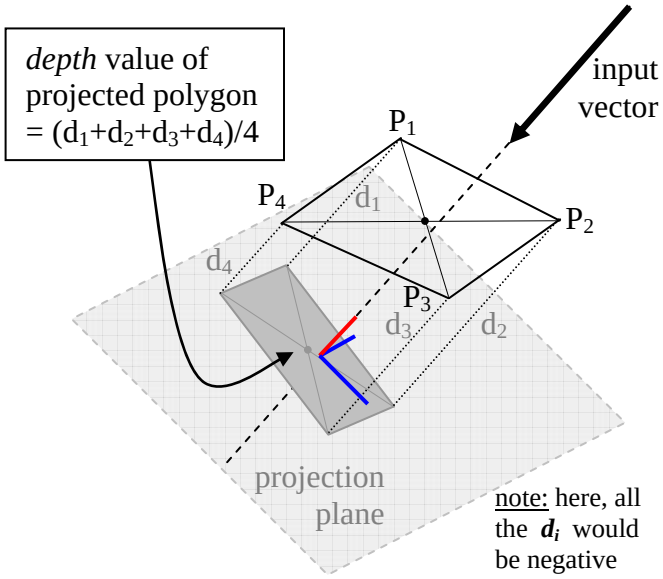

Figure 5.3 Flattening one 3D polygon onto the projection plane. The resulting projected polygon (dark gray) is assigned a *depth* value which is the average of the distances necessary to bring the original points (P_i) to the projection plane using the normalized input vector.

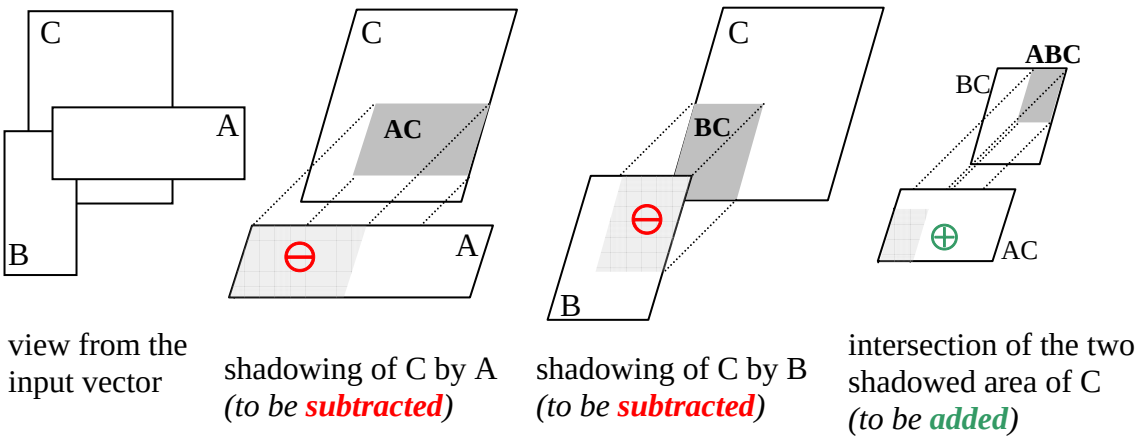

Figure 5.4 Simple case showing that secondary intersections need to be considered in order to obtain the correct shadowed areas. This involves adding the polygons AC and BC to the polygon pool, so that they can intersect.

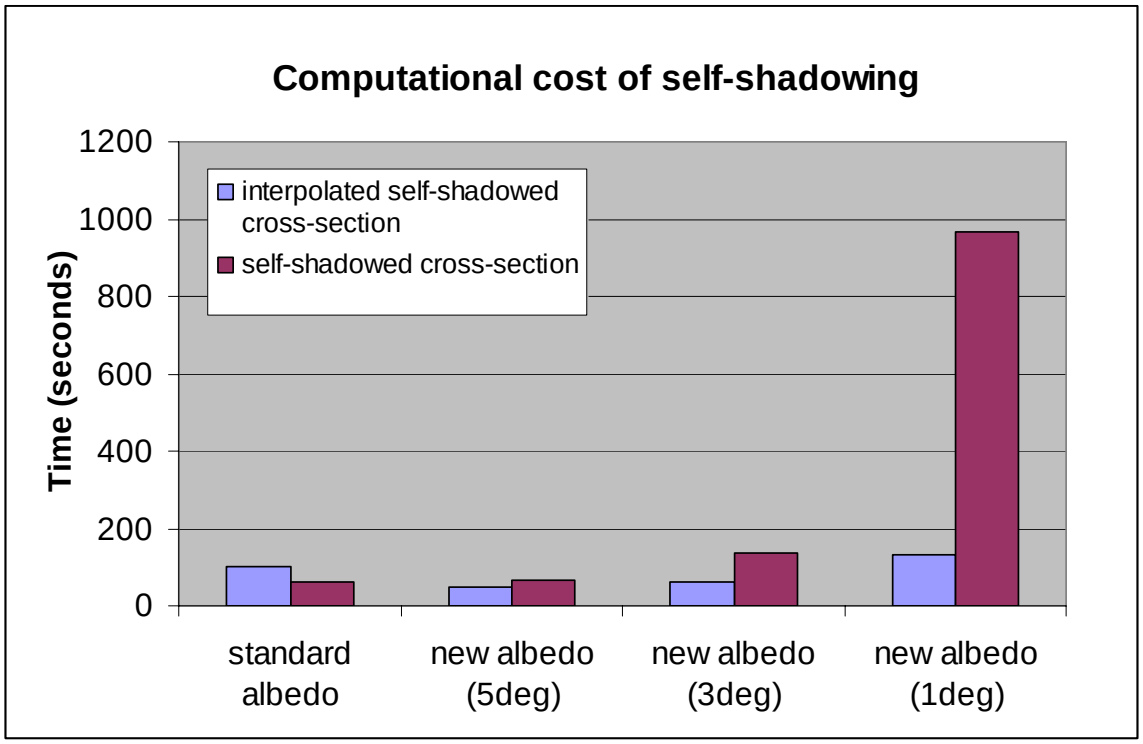

Figure 5.5 Absolute computational cost $t_{shadowing}$-$t_{noshadowing}$ of using self-shadowing for different albedo model cases.

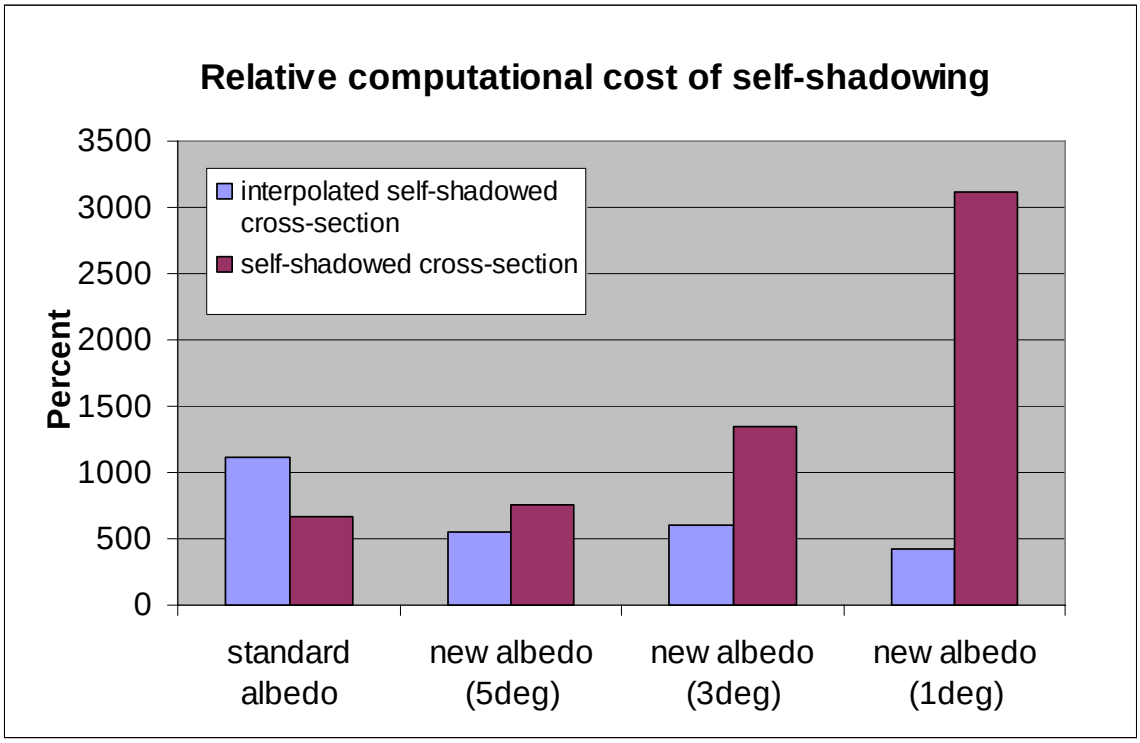

Figure 5.6 Relative cost $(t_{shadowing}-t_{noshadowing})/t_{noshadowing}$. Using full self-shadowing for the high-resolution albedo cases is very detrimental to efficiency. On the other hand, using the interpolation optimization, the relative cost remains acceptable.

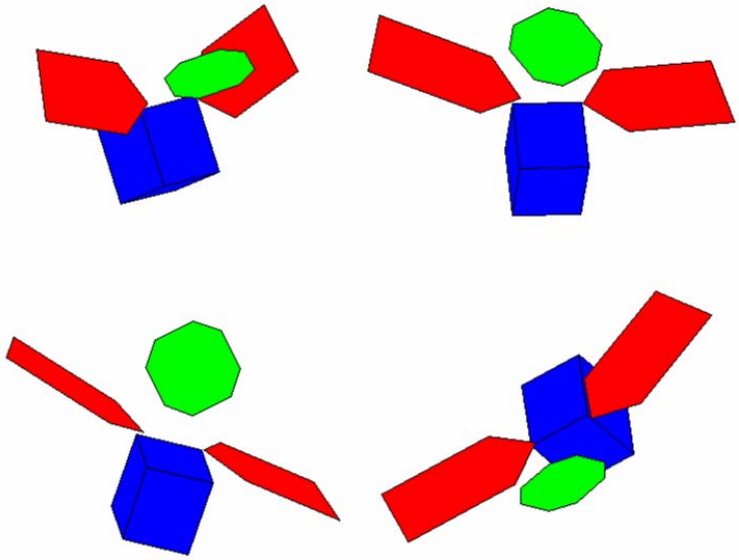

Figure 5.7 MRO spacecraft seen from 4 different view points. The bus is in blue, the solar arrays in red and the high-gain antenna in green.

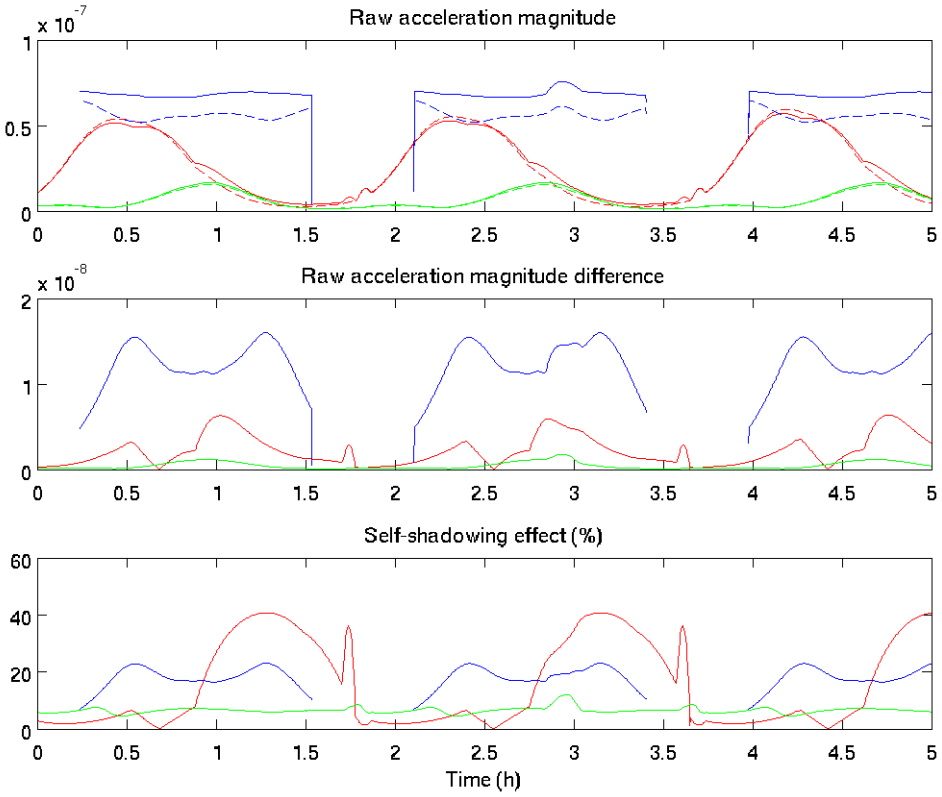

Figure 5.8 Comparison of raw (C_D and C_R coefficients removed) acceleration magnitudes displaying the effects of the self-shadowing modeling. Red shows the atmospheric drag, blue the solar radiation and green the albedo+thermal radiation.

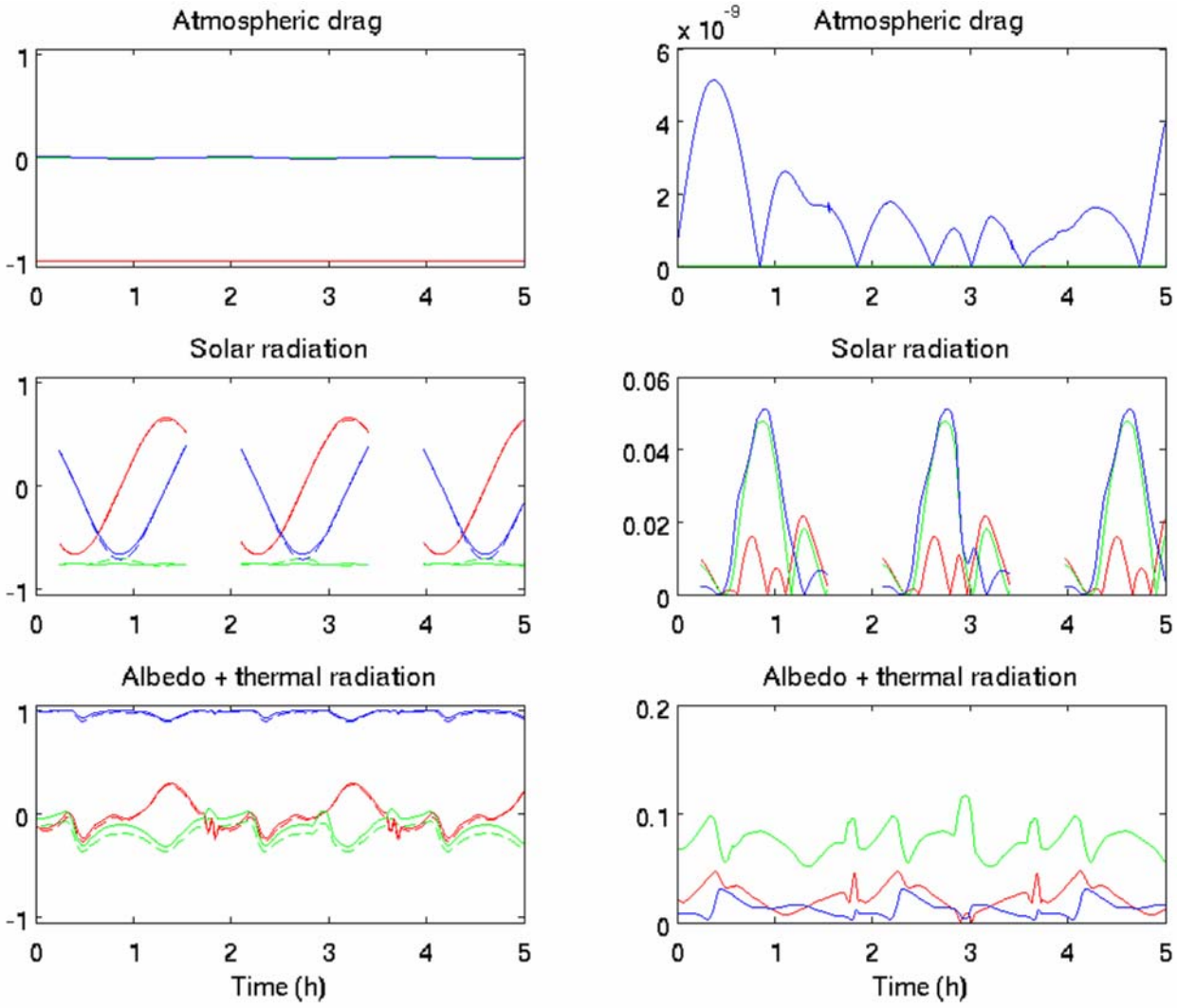

Figure 5.9 Distribution of the non-conservative accelerations in the ACR frame. Red is for Along-track, green for Cross-track and blue for Radial. The left column shows the ratio of the ACR components to the acceleration magnitude, with the dashed line indicating the self-shadowing case. On the right column, the difference between those two line is plotted.

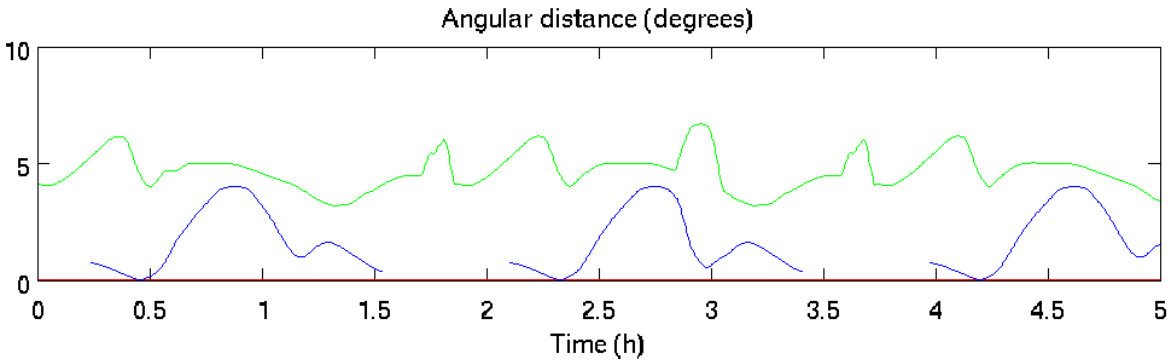

Figure 5.10 Angular distance between the acceleration vectors of the non-self-shadowed and the self-shadowed cases. [red = atmospheric drag; blue = solar radiation; green = albedo+thermal radiation]

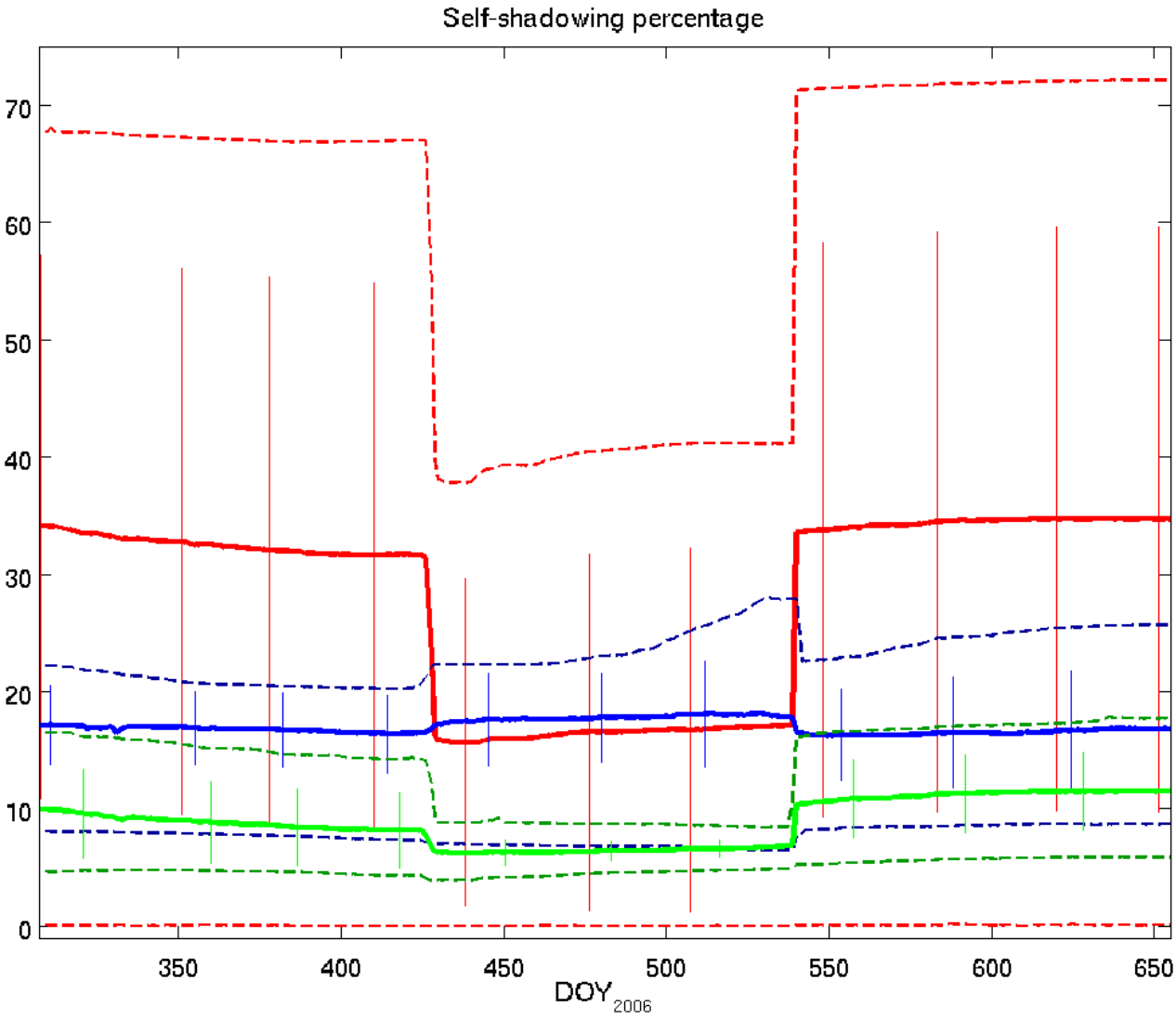

Figure 5.11 Mean (thick line), minimum/maximum (dashed line) of the self-shadowing effect for the atmospheric drag (red), solar radiation (blue) and albedo radiation (green). The vertical lines are indicators of the standard deviation.

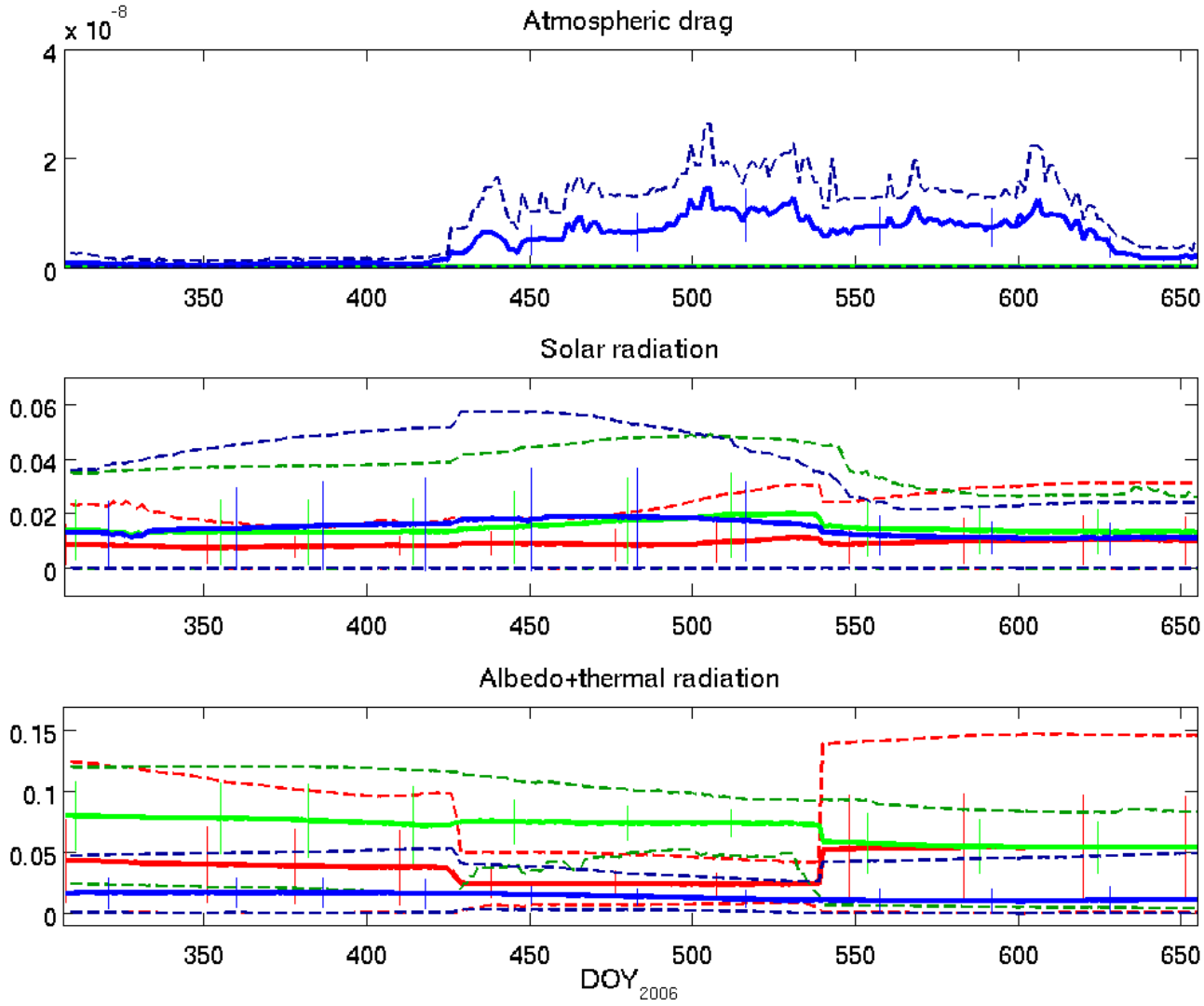

Figure 5.12 Mean (thick line), minimum/maximum (dashed line) of the self-shadowing effect for the along-track (red), cross-track (blue) and radial (green) components of the acceleration changes. The vertical lines are indicators of the standard deviation.

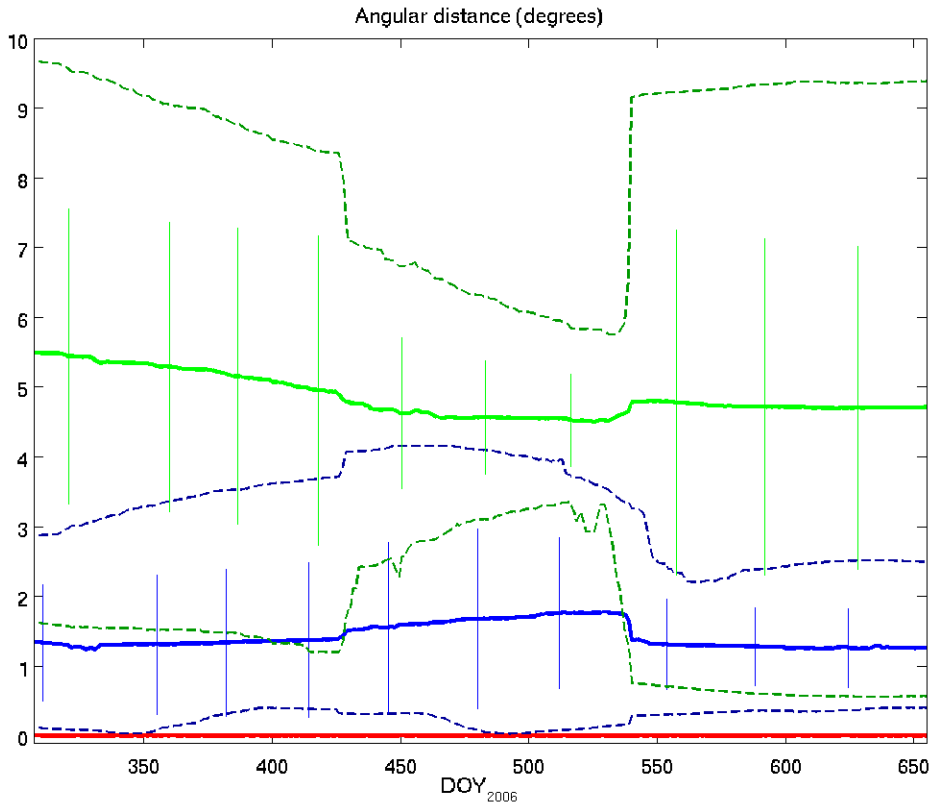

Figure 5.13 Mean (thick line), minimum/maximum (dashed line) of the acceleration direction angular changes for the atmospheric drag (red), solar radiation (blue) and albedo radiation (green). The vertical lines are indicators of the standard deviation.

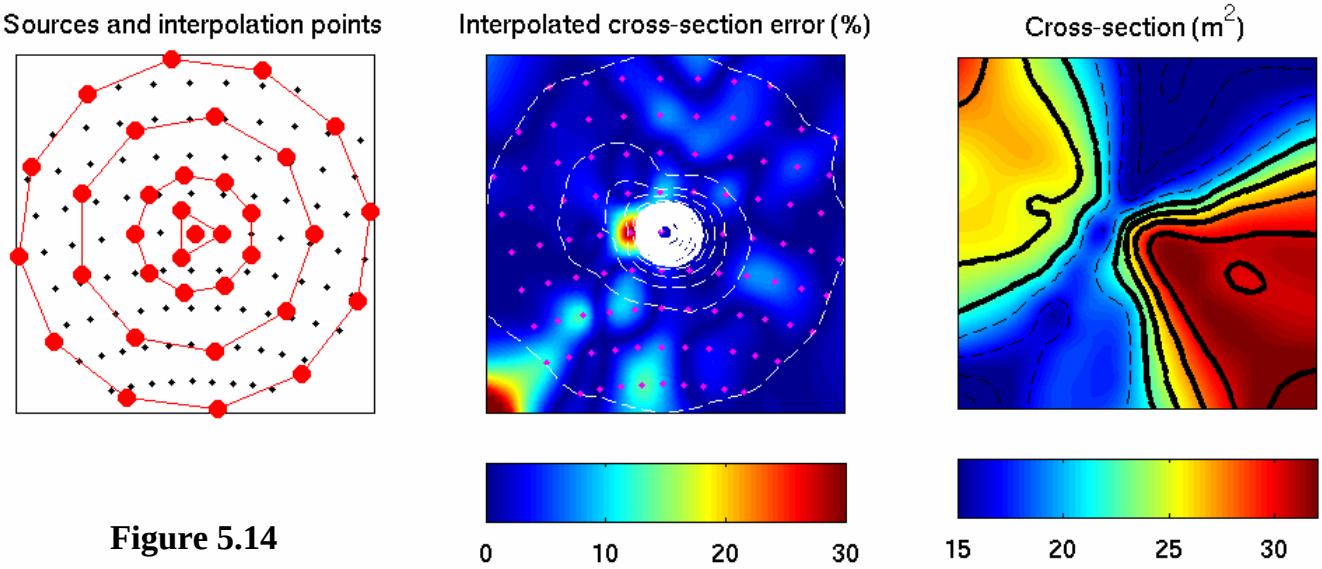

Figure 5.14

[left] Original source points (black dots) and interpolation nodes (red circles) in the projected plane. The preferred spot distribution has four rings with respectively 3, 9, 9 and 12 nodes at radii 1/6, 1/3, 2/3 and 1 of the maximum projected radius.

[center] Relative error (in %) in the interpolated total cross-section. The interpolation is satisfactory in the visible region, and larger than average errors tend to occur in regions contributing little to the total acceleration. The white contours show the ratio of the individual node acceleration contribution to the maximum (contours are every 10%; <50% are dotted, >50% thick).

[right] Total spacecraft cross-section, shown with contours.

[THIS PAGE INTENTIONALLY LEFT BLANK]

[THIS PAGE INTENTIONALLY LEFT BLANK]

Chapter 6

Non-conservative force modeling: high-resolution albedo radiation pressure

6.0 Introduction

Studies such as those conducted in Chapters 2, 3 and 4 were made possible by the improved modeling of small perturbing accelerations on the spacecraft. Indeed, while only the adjusted drag coefficient is used to obtain the density time series, robust estimates would not be possible without accurate modeling of the other accelerations.

In addition to the continuing improvement of the Mars gravity field made possible with the Mars Reconnaissance Orbiter radio tracking data, the non-conservative forces are currently the most challenging to model.

In Chapter 5, an algorithm to calculate the spacecraft cross-sectional area more accurately was presented in detail. It benefits the computation of all the non-conservative accelerations. Except for new estimates of the aerodynamic drag coefficient C_D (assumed to be equal to 2.15 for MRO following Wynn [2004]), only a better atmospheric density model would improve the atmospheric drag estimation. The goal of this Thesis being to make this possible by providing new density measurements, we will not consider this option here.

The optical properties of the spacecraft surface elements enter the calculation of all the radiation pressure accelerations. The estimation of the reflectivity coefficient values is difficult and can usually only be achieved during cruise (Highsmith [2005]) or with a long tracking data temporal coverage: Lemoine et al. [2006] used normal equations built from more than 6 years of MGS POD arcs to

solve for the most important of those coefficients. While this can definitely improve the orbit reconstruction, it can only be applied in some particular cases.

An improvement of the direct solar radiation would require considering second-order effects such as the inter-panel re-reflections. With the uncertainties in the values of the reflectivity coefficients, the potential benefits are not obvious. Thus, we choose to concentrate our modeling efforts on the albedo radiation pressure. By albedo, we mean the reflected solar radiation. In this chapter, we do not try to model the planetary thermal radiation pressure (infrared blackbody radiation from Mars).

As pointed out in Lemoine [1992], the thermal radiation is often larger than the albedo acceleration, so using the thermal data from the TES (Christensen et al. [2001]) and THEMIS (Christensen et al. [2004]) spectrometers could be worthwhile for future work. However, the surface temperatures depend mostly on the local solar time, with a maximum near the subsolar point (solar bulge). On the dayside, the temperature anomalies resulting from heterogeneous thermal inertia are not significant compared to the idealized temperature structure (shown on Figure 6.1 with TES data). On the nightside, the relative temperature differences are greater (Figure 6.2), but the thermal radiation pressure is much lower than on the dayside (the contrast between dayside and nightside thermal emission fluxes is more than five, Lemoine [1992]). During global dust storms, the thermal flux changes dramatically due to the increased atmospheric dust opacity. The surface is not visible and the temperature is homogenized. The completion of the current thermal radiation model to account for such effects could improve the orbit reconstruction during those periods.

On the other hand, the albedo can vary considerably on short lengthscales, and it experiences large seasonal changes in the polar regions due to the non-permanent caps. Here, we propose a different method of calculating the albedo acceleration than the one available in GEODYN (Pavlis et al. [2006]).

6.1 Existing albedo model

The force model for the planetary albedo radiation pressure currently implemented in GEODYN follows Knocke et al. [1988]. Briefly, the planetary surface visible from the spacecraft is divided in a number of elements, whose individual contributions are summed vectorially. The albedo value of each element is obtained from a spherical harmonic expansion. In the case of Mars, Lemoine [1992] produced albedo maps based on limited data from the Infrared Thermal Mapper (IRTM) instruments on the two Viking orbiters. Zonal expansions were created to reduce the data gaps and because Lemoine [1992] found that the effect of longitudinal variations on POD was not significant for short arc durations compared to the overall albedo variation. In addition, zonal models have been used satisfactorily for the Earth. However, the main shortcoming of the spherical harmonic method resides in the albedo representation near the poles. A low expansion degree tends to smooth out the high-albedo features near the poles, which are important for spacecraft in a polar orbit such as MGS, Mars Odyssey and MRO. Indeed, in the course of one day, whereas any equatorial region is in visibility only a few times, the MRO spacecraft orbits each pole about 13 times. It also spends more time in the North Pole region where apoapsis is located.

An increase in resolution using the current models is not practical. The computation time for this algorithm scales linearly with the number of surface elements used, but if we want to increase the resolution of the underlying albedo map, the dependence is steeper because it depends on the spherical harmonic expansion degree. The computational cost rises quickly (typically for a 3-day arc, nearly 1 million albedo values need to be evaluated). To achieve high spatial resolution (less than 5 degrees) with the current method would hinder the POD process by slowing it down considerably.

6.2 New albedo model

6.2.1 Data

Data from recent spacecraft missions (MGS, Mars Odyssey) with their good global and seasonal coverage provide an opportunity to improve the force modeling of the albedo and thermal accelerations.

Although TES onboard MGS produced albedo maps (Christensen et al. [2001]), we choose to use data from the MOLA instrument (Zuber et al. [1992]). In addition to serving as a laser altimeter, from which high-resolution, high-accuracy, global-coverage topography was obtained (Smith et al. [1998]), MOLA also acts as a passive radiometer and can be used to estimate the albedo at the laser wavelength (1064nm, Sun et al. [2006]). Over the course of the MGS mission, about 75 million albedo measurements were collected (the data were provided by G. Neumann, NASA/GSFC). From this impressive dataset we can build maps at very high-resolution. The Mars albedo has been observed to change after dust storm events due to the redistribution of dust (Neumann et al. [2006]), so constructing maps in specific time windows would be preferable. However, given that the MRO and the MGS missions only had a small temporal overlap, we constructed seasonal maps of an “average year”.

The MOLA instrument measured the radiance at 1064nm, the wavelength of the onboard laser used in altimetry mode. The majority of the energy radiated by the Sun and reflected off Mars is in the visible wavelengths. We need to regularize the MOLA measurements to obtain more appropriate bolometric albedo values for the acceleration calculation. We perform a normalization using the TES measurements. The TES and the MOLA instruments both flew on the Mars Global

Surveyor spacecraft, so this is reasonable. In addition, while the MOLA was not absolutely calibrated, the TES instrument had an absolute calibration source in both thermal IR and visible/near-IR (Christensen et al. [2001]). Figure 6.3 is a plot of the raw MOLA power observations (P_{MOLA}, in $mW.m^{-2}.sr^{-1}.nm^{-1}$) compared to the albedo values obtained by TES (figure from G. Neumann, personal communication). We derive a linear regression, which we use to obtain MOLA (pseudo-)albedo values (a_{MOLA}):

$$a_{MOLA} = 0.078087 + 0.0045618 \, . \, P_{MOLA} \quad (1)$$

6.2.2 Constructed albedo maps

We created albedo maps separated by 15 degrees of L_S, but each encompassing a "Martian month" of data (30 degrees of L_S). This is comparable to the temporal resolution of the seasonal zonal maps used previously (20 to 25 degrees of L_S), and removes the problem of sharp discontinuities at the boundaries. Such a timescale is sufficiently short to capture the albedo changes with season, and sufficiently long to ensure good spatial coverage and averaging.

Figure 6.4 shows the 24 maps spanning a whole Mars year. The obtained maps are in good agreement with the albedo map of Christensen et al. [2001], although the polar regions lack coverage in certain seasons (of course, during the polar night, the MOLA instrument data cannot measured reflected light). In each seasonal map, no pole has data polewards of ~87° due to the orbit inclination; for those latitudes we use the average of neighboring values. Although it is not necessary because the region is in constant shadow during the considered season, the other (larger) gaps are filled with the average of the 5-degree band with data closest to the winter pole.

Figure 6.5 shows a comparison of the albedo maps from various dataset and representations. The differences between the two dataset are important (Figure 6.5, a and c). In other time periods (not shown), the results are similar. The main

discrepancy between the spherical harmonic (zonal or not) and the full grid representations occurs near the poles. The asymmetry of the polar features cannot be fully captured after expanding the maps obtained with the new MOLA data into low-degree spherical harmonic expansions. Figures 6.5b and 6.5c show that there is an improvement when using a full expansion (i.e., not just zonal), but part of the polar region shows errors greater than 0.10 (i.e., >25% locally) with a 9x9 expansion.

6.2.3 Algorithm

The algorithm itself is straightforward, as simple as the spherical harmonic expansion method. As presented in Figure 6.5, we use a simple map representation of the albedo in longitude/latitude coordinates (with the pixel convention rather than the node convention, i.e. we give albedo values at the center of small surface elements). The resolution of these maps is arbitrary (but limited in practice to 1 degree in both longitude and latitude).

At each timestep, we only consider the surface elements which are sunlit. We calculate the incidence and emission angles (Figure 6.6) of those visible from the spacecraft, and add their contribution to the total acceleration vector. According to first principles and assuming a Lambertian reflection of the solar radiation on the planetary surface, the individual contribution of the area element *i* is:

$$d\vec{a}_i = \frac{C_R}{m.c.\pi}.\frac{F_{sun,1AU}}{D_{sun}^2}.\tau_{i,sun}.\tau_{,surfi}.\frac{\cos(\Theta_s).\cos(\alpha)}{d_i^2}.a_i.\Sigma_i.$$

$$\sum_j A_{i,j}\left[\left(1-R_{j,spec}\right)\vec{u}+\left(\frac{2}{3}R_{j,diff}+R_{j,spec}\left(\vec{u}\bullet\vec{n}_j\right)\right).\vec{n}_j\right] \qquad (2)$$

The parameters entering this equation are:

- C_R: the radiation coefficient, a scale factor which also enters the calculation of the direct solar and the planetary thermal radiations
- m: mass of the spacecraft (in kg)

- c: speed of light (c=299792458m.s^{-1})
- $F_{sun,1AU}$: solar flux at 1 AU (=1376W.m^{-2})
- D_{sun} : distance to the Sun (in AU)
- $\tau_{i,sun}$: visibility factor of the area element from the Sun ($0 \leq \tau_{i,sun} \leq 1$)
- $\tau_{i,surf}$: visibility factor of the area element from the spacecraft ($0 \leq \tau_{i,surf} \leq 1$)
- Θ_s: incidence angle of the sunlight on the area element (in radians)
- α: emission angle from the area element to the spacecraft (in radians)
- d_i: distance from the area element to the spacecraft (in m)
- a_i: albedo of the surface element
- Σ_i: area of the area element (m^2)
- $\vec{u}$: unit vector from the center of the area element to the spacecraft
- j : index of the spacecraft macro-model plate
- $\vec{n}_j$: unit normal vector of the from the center of the area element to the spacecraft
- $A_{i,j}$: cross-section of the spacecraft observed from the surface element (i.e., with the direction $\vec{u}$) (in m^2)
- $R_{j,spec}$: specular reflectivity of spacecraft plate j
- $R_{j,diff}$: diffuse reflectivity of spacecraft plate j

With a coarse albedo map resolution, area elements can suddenly come into view or disappear. To smooth the acceleration time series, it is possible to calculate the visibility ratio from the Sun ($\tau_{i,sun}$) and from the spacecraft ($\tau_{i,surf}$) for a small number of elements: respectively, those within a small angular distance of the terminator, and those at the fringe of the portion of the planet visible from the spacecraft. To calculate these visibility ratios, we project the surface element nodes using an orthographic projection centered on the spacecraft position, and assume they form a rectangle. Further assuming that the boundary of visibility is linear in the projected space, we can simply calculate the resulting intersection,

and obtain the ratio of the area of the polygon on the visible side of the visibility boundary to the total area of the surface element. In practice, these two assumptions are always reasonable for the Sun visibility. For the spacecraft visibility, if the region in view is small (low altitude), the curvature of the boundary cannot be ignored. Nevertheless, the resulting errors should be relatively small and would not impact the albedo modeling sensibly. Moreover, low altitudes responsible for such cases would probably be only reached during aerobraking, a phase where atmospheric drag completely dominates the other non-conservative forces.

6.2.4 Testing

We tested the new albedo force model with the Mars Reconnaissance Orbiter (MRO) spacecraft. We focus on the short arc "0192" (2007-06-03 11:47:00 to 2007-06-05 00:28:00). That time period corresponds to L_S~244°, in the late Southern Spring. For more details on the orbit of MRO, see Chapter 4.

We processed the tracking data using two versions of GEODYN (Pavlis et al. [2006]), with and without the new albedo modeling, and we obtained two acceleration time series (Figure 6.7). Of course, the former zonal model produces accelerations which are nearly identical from orbit to orbit. The albedo accelerations calculated from the MOLA albedo map is more complex and more variable, with significant differences compared to the previous case.

On Figure 6.8, we show the effect of varying the albedo map resolution on the acceleration magnitude. The relatively coarse 5° resolution (although equivalent to a prohibitive degree and order ~70 spherical harmonic expansion with the older acceleration scheme) shows important oscillations, which disappear with the 2° and 2.5° maps. These oscillations are not due to the scintillation of the area elements suddenly appearing and disappearing, because the use of the 'visibility factor' does not eliminate them. The differences in the results produced from the

2° and 2.5° maps are small, and they both are in good agreement with the accelerations obtained using the 1° map (not shown). Given the computational cost of using the 1° map (Chapter 5), these two maps represent a good compromise in practice.

More complex albedo distributions are expected to not only change the albedo acceleration amplitude but also their direction. On Figure 6.9, we illustrate how the albedo acceleration evolves along three orbits. For clarity, the longitude is 'unwrapped' in this longitude-latitude plot. The color coding indicates the acceleration amplitude. With the three viewing directions included, it is clear that in addition to the changes in acceleration from orbit to orbit when above the same latitude range, the direction of the acceleration is also modified (the asymmetry in longitude is due to the Sun movement while the tilt away from the South Pole is due to that region contributing most of the albedo radiation). Figure 6.10 shows the first of those three orbits, but emphasizes the directionality of the albedo acceleration by focusing on its three components (here, North, East and Radial to match the longitude-latitude horizontal axes). Figure 6.11 displays the same information for the albedo acceleration obtained from the spherical harmonics albedo model. Clear differences are visible, in the total magnitude, in the magnitude of the individual components and also in the acceleration direction. These are shown in Figure 6.12. The differences, while small overall, reach up to 25% of the MOLA albedo map accelerations. The radial component is not affected much compared to the North direction, which also experiences significant changes over short wavelengths.

To assess the importance of the acceleration changes on the orbit reconstruction, we now look at the components in the ACR frame (Along-track, Cross-track, Radial). The cumulated values over the whole arc are a proxy for the orbital perturbations resulting from the albedo acceleration. The radial component dominates, contributing over 92% if the total acceleration; the cross-track accounts

for ~8%, while the along-track is negligible due to its symmetric contribution. Indeed, while the mean of the cross-track and radial components are about -18% and 30% of their respective maximum absolute value, the along-track has a mean of ~0.7% of its peak value. The relative differences in the cumulated values of the albedo accelerations obtained with the former zonal expansion model and the MOLA albedo map are ~130% in the along-track, ~12% in the cross-track and ~2.6% in the radial directions. Given their respective importance, the resulting effect is small, but still corresponds to an angle change of ~2.5° in direction.

6.3 Conclusion and Future work

As presented here and in Chapter 4 in the case of the Mars Reconnaissance Orbiter, the effects resulting from the change in albedo force modeling are small. At MRO orbital altitude, the albedo acceleration is much smaller than the atmospheric drag and the direct solar radiation, and below the thermal radiation level over at least half of the orbit. The inclusion of this new force model for the orbit reconstruction with atmospheric density retrieval as a goal is not a necessity. Nevertheless, given that the features in the Mars albedo seasonal maps are robust and would appear nearly stationary (except for the obvious day/night differences), they could become important to model precisely in the future in order to obtain higher resolution gravity fields. The leaking of albedo features into the gravity field could be a problem, especially for sun-synchronous orbits which see the planet surface with a nearly constant Sun incident angle.

In addition, it could be valuable in the case of future lunar missions. Indeed, without atmospheric drag, the radiation forces will be among the largest sources of orbital errors, along with the gravity anomalies of course. The lower temperature of the Moon and the higher solar flux near 1AU will also contribute in reducing the difference between the albedo and the thermal radiations.

The use of a recent dataset (MOLA radiometry) enabled the creation of albedo maps with better spatial and temporal resolutions. In the case of the Mars Reconnaissance Orbiter, the effects on the resulting albedo accelerations can be as high as 25% near the poles, which are especially important for polar orbiters because those regions are bright and contribute at every single orbit. The induced changes in direction appear to be quite small (near 2.5°) and are principally due to the previously neglected longitudinal albedo variations. Nevertheless, the improvements in the albedo modeling do not affect the orbit reconstruction significantly (on the order of ~20cm; Chapter 4, Section 4.3.3), because the albedo force is small in general and because the high-frequency perturbations due to the drag (density anomalies not predicted by the *a priori* models) affect the orbit reconstruction to a greater degree.

The current model is rather simple, and could be improved in various ways. First, we could implement non-Lambertian reflections. On the Moon, the assumption of isotropic re-radiation of the area elements is not as reasonable because of the large backscattering observed.

Second, we could extend the current gridded map algorithm to thermal radiation modeling. In the case of the Moon or other airless bodies, the surface temperature of area elements could be computed from the Sun/spacecraft geometry and maps of albedo and thermal inertia. We attempted to implement this idea for Mars using look-up tables for parameters describing the local solar time temperature dependence as a function of albedo and thermal inertia, but the interpolation scheme was not leading to reasonable estimates over the whole globe. A semi-analytical model needs to be more carefully constructed. In addition, the Martian atmosphere can complicate the thermal radiation by its own contribution.

The computational cost of this new albedo calculation can become very high when used in conjunction with a full self-shadowing calculation. In addition to the interpolation scheme presented in Chapter 5, more advanced techniques could reduce the number of spacecraft cross-sectional areas to be calculated. Given that

the spacecraft attitude changes slowly compared to the timestep duration (except for MRO during short periods of fast antenna movement), the cross-section values would also be slowly variable and may not need to be evaluated at every timestep. The idea of an interpolation based on a pool of regularly updated cross-sectional areas could be explored.

Finally, the format of the albedo map used as input could be generalized to allow polygonal area elements. This could prove invaluable near the poles, by considerably reducing the number of the contributing area elements.

6.4 References

Christensen P. R., J. L. Bandfield, V. E. Hamilton, S. W. Ruff, H. H. Kieffer, T. N. Titus, M. C. Malin, R. V. Morris, M. D. Lane, R. L. Clark, B. M. Jakosky, M. T. Mellon, J. C. Pearl, B. J. Conrath, M. D. Smith, R. T. Clancy, R. O. Kuzmin, T. Roush, G. L. Mehall, N. Gorelick, K. Bender, K. Murray, S. Dason, E. Greene, S. Silverman and M. Greenfield (2001), Mars Global Surveyor Thermal Emission Spectrometer experiment: Investigation description and surface science results, Journal of Geophysical Research, 106, pp. 23823–23872.

Christensen P. R., B. M. Jakosky, H. H. Kieffer, M. C. Malin, H. Y. McSween Jr., K. Nealson, G. L. Mehall, S. H. Silverman, S. Ferry, M. Caplinger and M. Ravine (2004), The Thermal Emission Imaging System (THEMIS) for the Mars 2001 Odyssey mission, Space Science Reviews, 110, pp. 85–130, doi:10.1023/B:SPAC.0000021008.16305.94

Highsmith D. (2005), MRO Approach/MOI/AB Navigation Readiness Review.

Knocke P. C., J. C. Ries, B. D. Tapley (1988), Earth Radiation Pressure Effects on Satellites, Proceedings of the AIAA/AAS Astrodynamics Conference, pp. 577-586, Minneapolis, Minnesota, August 15-17, 1988.

Lemoine F. G. (1992), The dynamics of orbitings satellites and gravity model development, Ph.D. thesis, University of Colorado at Boulder, Bouler, Colorado.

Lemoine F., S. Bruinsma, D. Chinn and J. Forbes (2006), Thermospheric Studies with Mars Global Surveyor, Proceedings of the AIAA/AAS Astrodynamics Conference, Abstract 6395, Keystone, Colorado, Aug. 21-24, 2006.

Neumann G. A., S. Byrne, D. E. Smith and M. T. Zuber (2006), Mars 1064-nm Albedo Changes Seen by the MOLA Instrument, and the 2001 Dust Storm, Eos Trans. AGU, 87(36), Jt. Assem. Suppl., Abstract P31A-03.

Pavlis, D. E., S. G. Poulose and J. J. McCarthy (2006), GEODYN operations manuals, contractor report, SGT Inc., Greenbelt, Maryland.

Smith D. E., M. T. Zuber, H. V. Frey, J. B. Garvin, J. W. Head, D. O. Muhleman, G. H. Pettengill, R. J. Phillips, S. C. Solomon, H. J. Zwally, W. B. Banerdt and T. C. Duxbury (1998), Topography of the northern hemisphere of Mars from the Mars Orbiter Laser Altimeter, Science, 279, pp. 1686-1692.

Sun X., G. A. Neumann, J. B. Abshire and M. T. Zuber (2006), Mars 1064 nm spectral radiance measurements determined from the receiver noise response of the Mars Orbiter Laser Altimeter, Applied Optics, 45, pp. 3960-3971.

Wynn J. (2004), MRO Surface Property Data for Navigation and ACS Analysis, Interoffice Memo # 0115_MRO_AC_04 Rev 1, Lockheed Martin.

Zuber M. T., D. E. Smith, S. C. Solomon, D. O. Muhleman, J. W. Head, J. B. Garvin, J. B. Abshire and J. L. Bufton (1992), The Mars Observer laser altimeter investigation, Journal of Geophysical Research, 97, pp. 7781–7797.

6.5 Figures

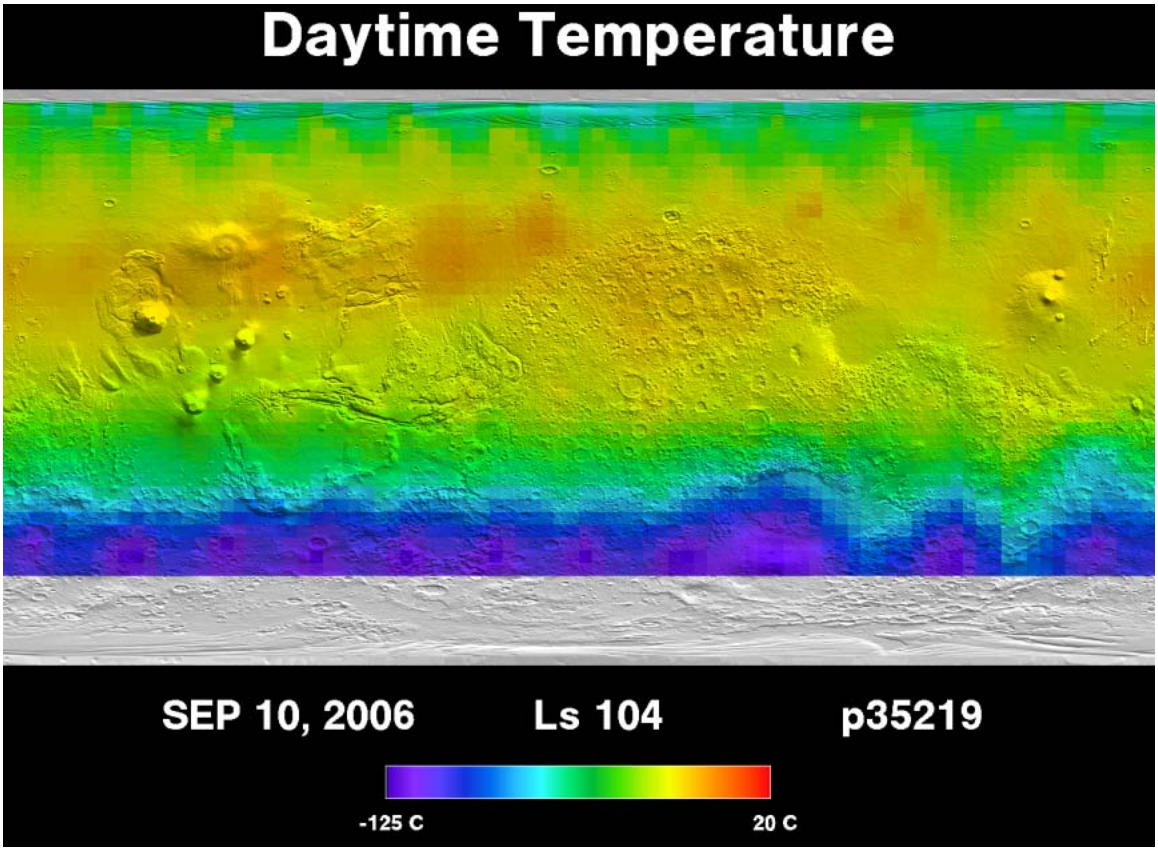

Figure 6.1 Global daytime temperatures obtained from the TES instrument (Christensen et al. [2001]).[1]

[1] This daily image was obtained from http://tes.asu.edu/tdaydaily.png on December 03, 2007.

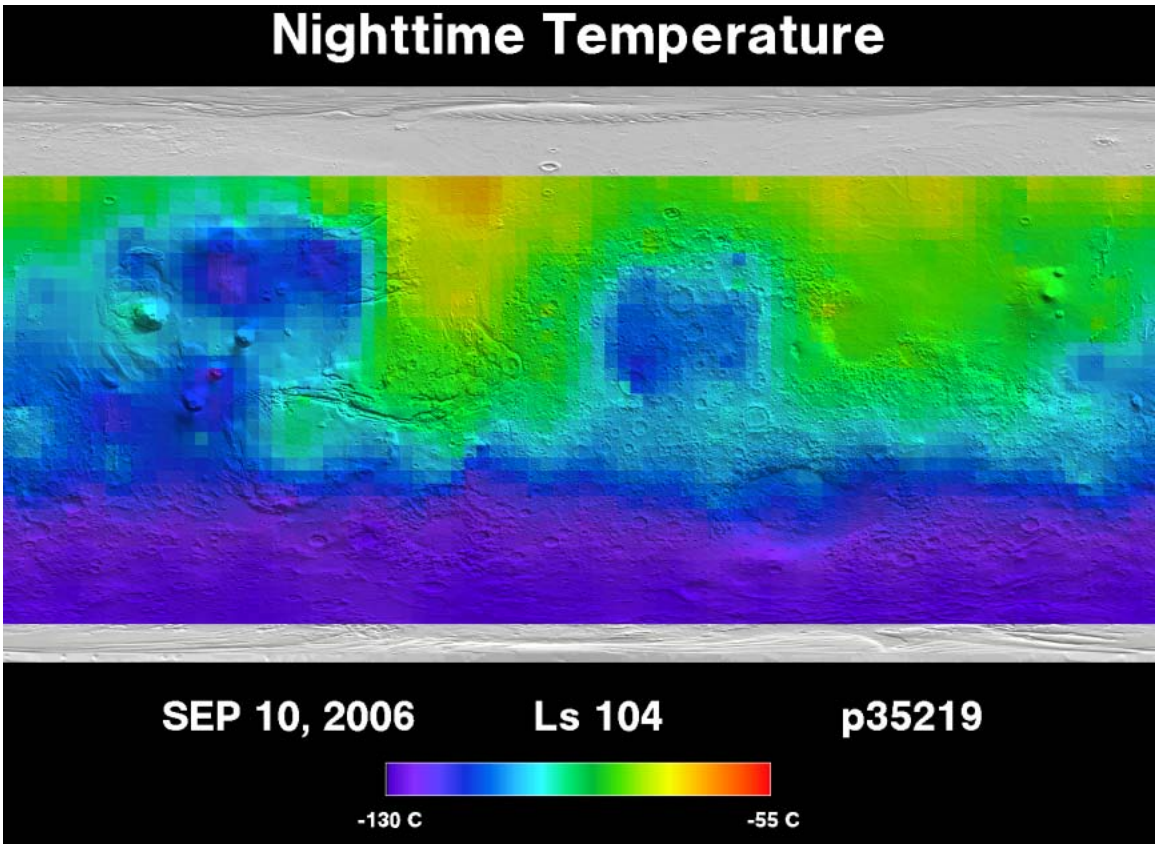

Figure 6.2 Global nighttime temperatures obtained from the TES instrument (Christensen et al. [2001]). Note the lower temperature values of the Tharsis rise and of Arabia Terra compared to other areas in the same latitude range (because of MGS orbit, the solar time is constant in this map). They are due to the lower thermal inertia in these two regions.[2]

[2] This daily image was obtained from http://tes.asu.edu/tnightdaily.png on December 03, 2007.

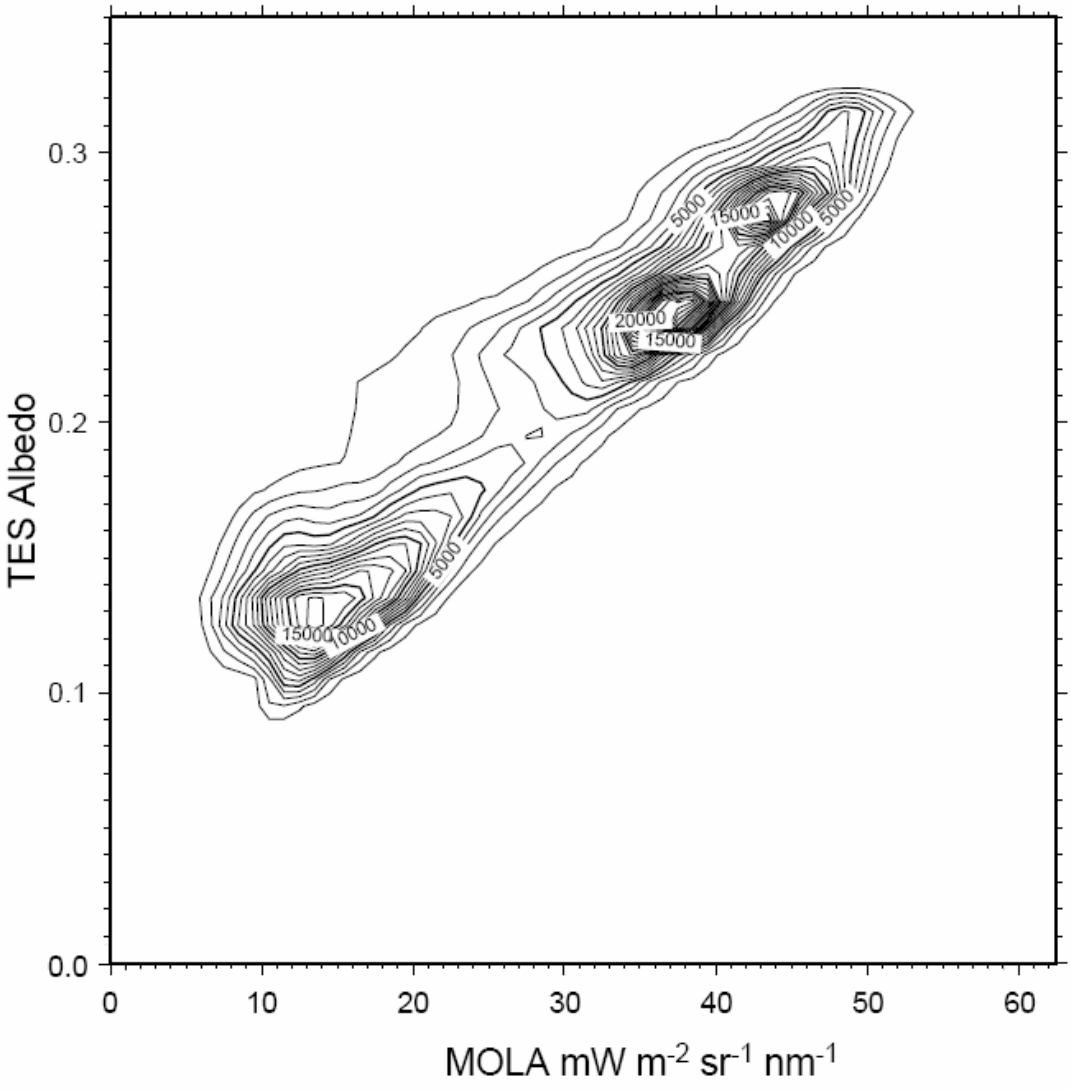

Figure 6.3 Density plot of the MOLA measurements versus the albedo values obtained by the TES instrument.

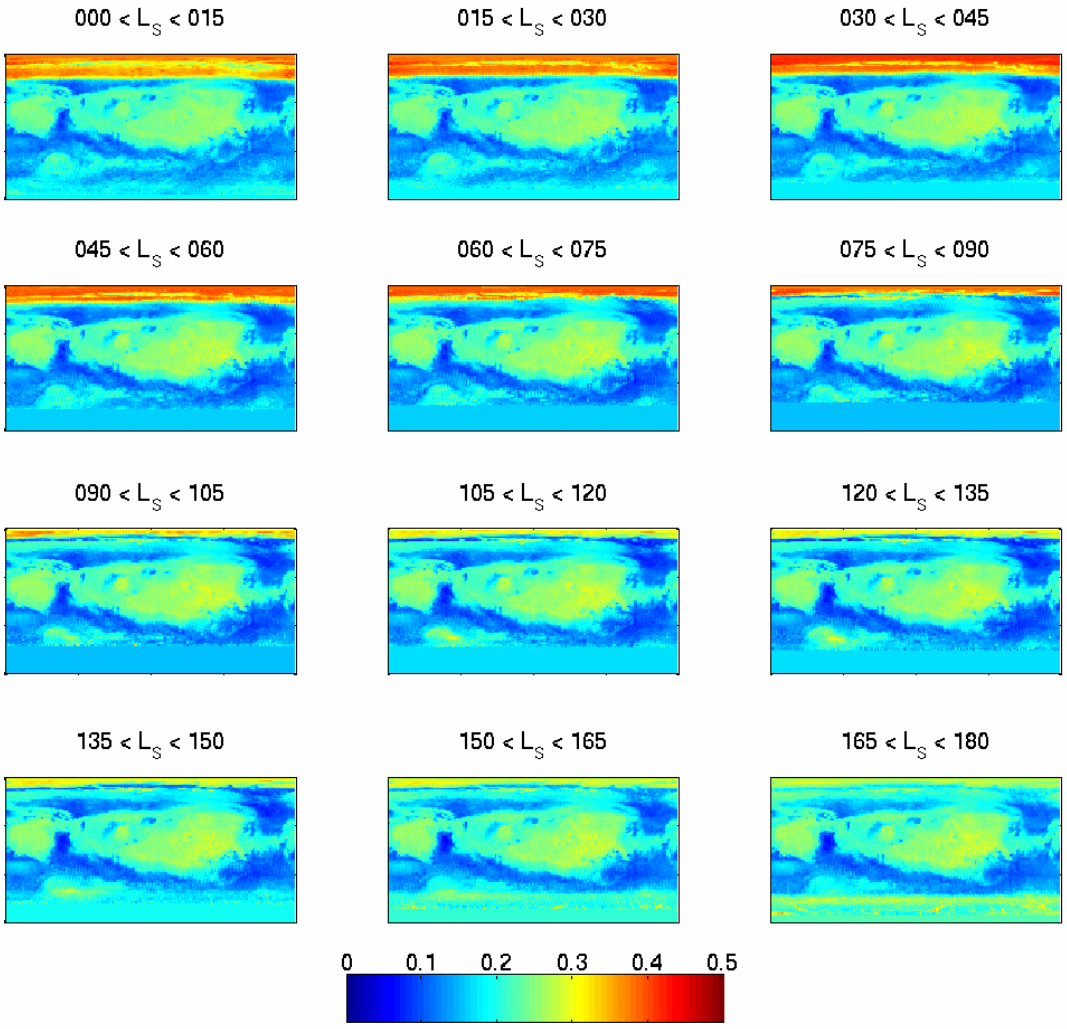

Figure 6.4a Seasonal albedo maps obtained from MOLA radiometry (after TES calibration) [L_S=0° to L_S=180°]. In each map, the albedo value assigned to a pixel is calculated from the mean of all the MOLA observations falling in range spatially and temporally. We chose to construct overlapping maps. For instance, the 105°-120° map includes data between 97.5° and 127.5° and the 120°-135° includes data between 112.5° and 142.5°. This way, the map differences at the boundaries are reduced.

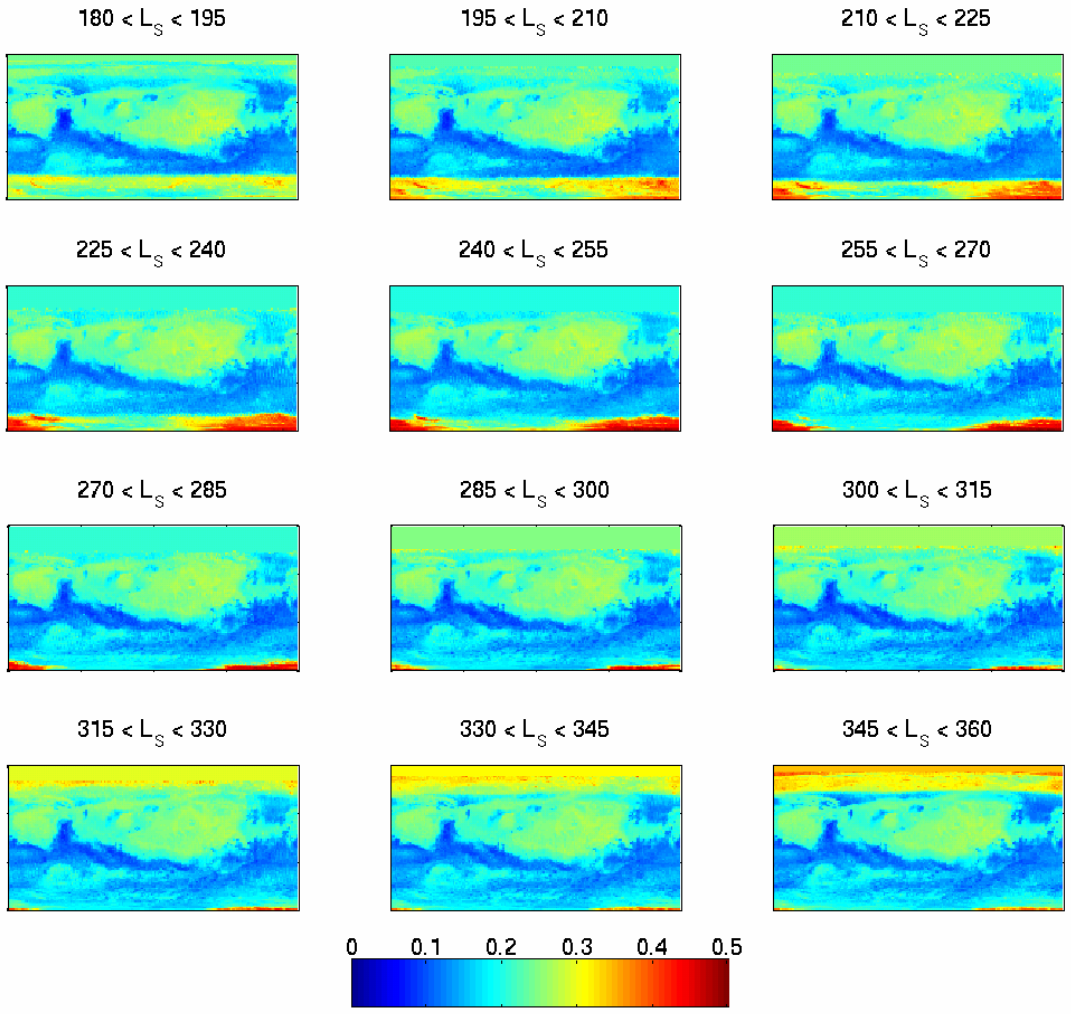

Figure 6.4b Same as Figure 6.4a but for the L_S=180° to L_S=360° range.

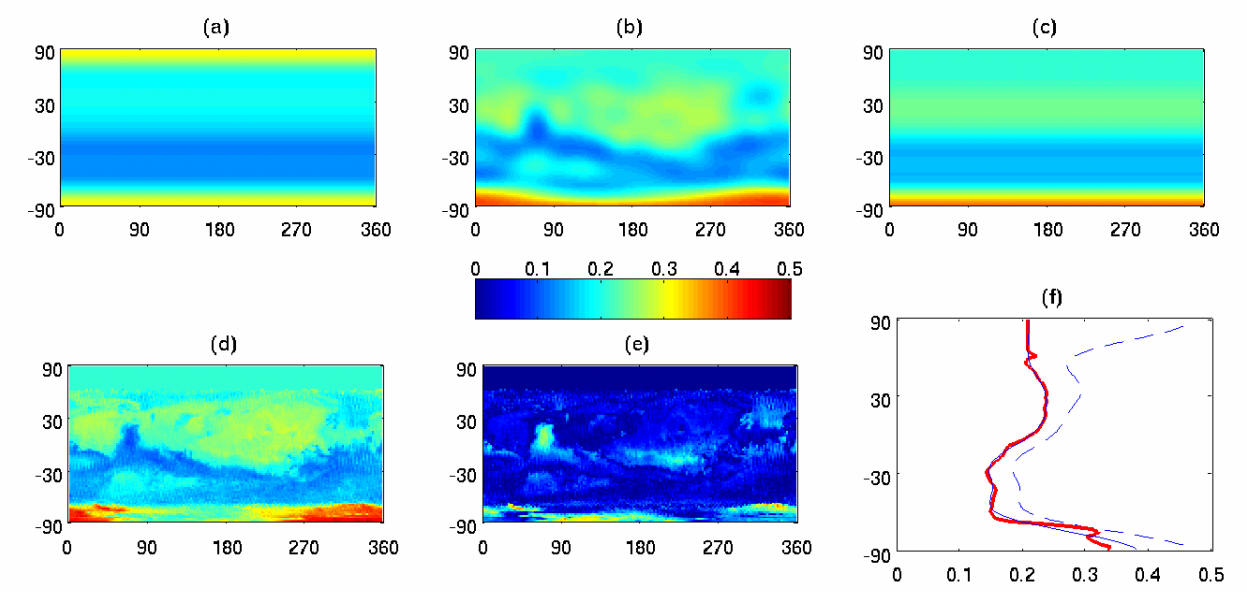

Figure 6.5 Comparison of albedo representations for the period L_S~225 to L_S~240. (a) shows the degree 9 spherical harmonic zonal map from Lemoine [1992]. The scale was adjusted by 50% (i.e., the scale is from 0.00 to 0.75) because of a general albedo level discrepancy compared to the MOLA data; (b) full harmonic expansion up to degree 9 (and order 9) of the MOLA albedo map; (c) zonal harmonic expansion up to degree 9 of the MOLA albedo map; (d) high-resolution (2 degrees in both latitude and longitude here) map derived from the MOLA data; (e) absolute difference between the (c) and (d) with a scale of 0.00 to 0.25; (f) zonal albedo (horizontal axis) versus latitude (vertical axis): (d) in red, (c) in blue and (a) in dashed blue.

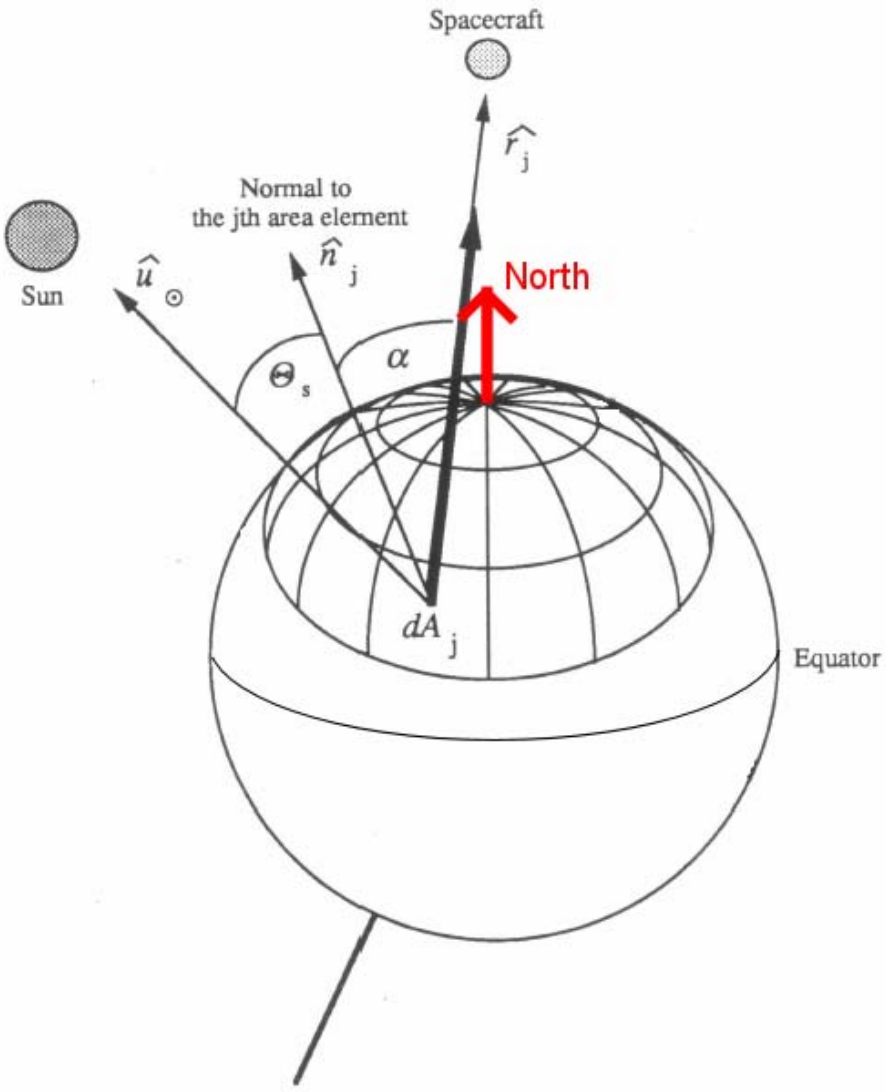

Figure 6.6 Geometric configuration of the spacecraft around a planet. The incidence (Θ_s) and emission (α) angles of a surface element are shown. Only the visible area elements of the albedo map are considered. In this particular case, the spacecraft is above the North pole. (adapted from Lemoine [1992]).

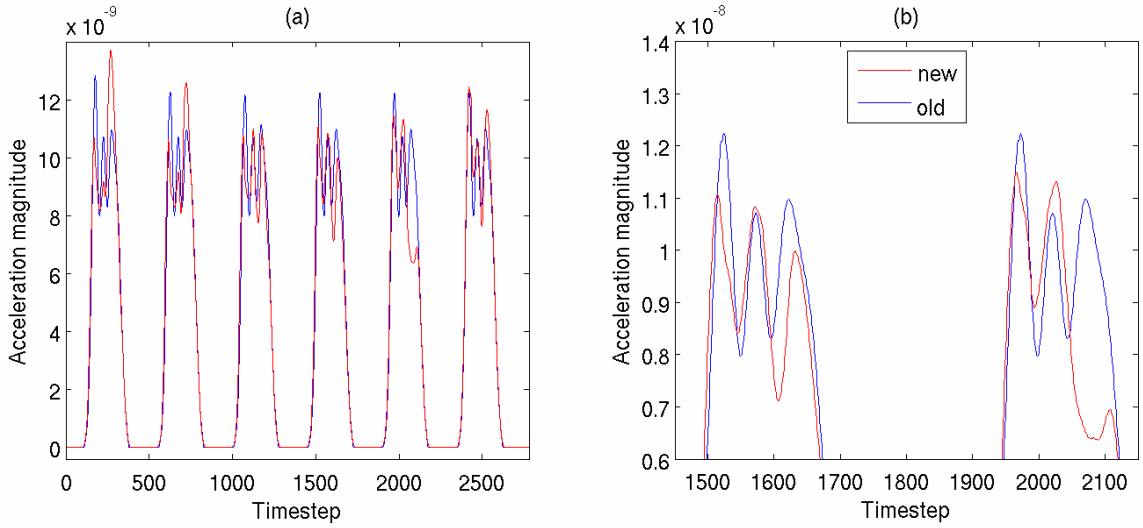

Figure 6.7 Comparison of the albedo acceleration magnitudes using the two albedo force models. With the zonal model, the pattern is repeated every orbit (blue). Using the albedo map derived from MOLA data, large differences from orbit to orbit are introduced. (the time step is equal to 15 seconds)

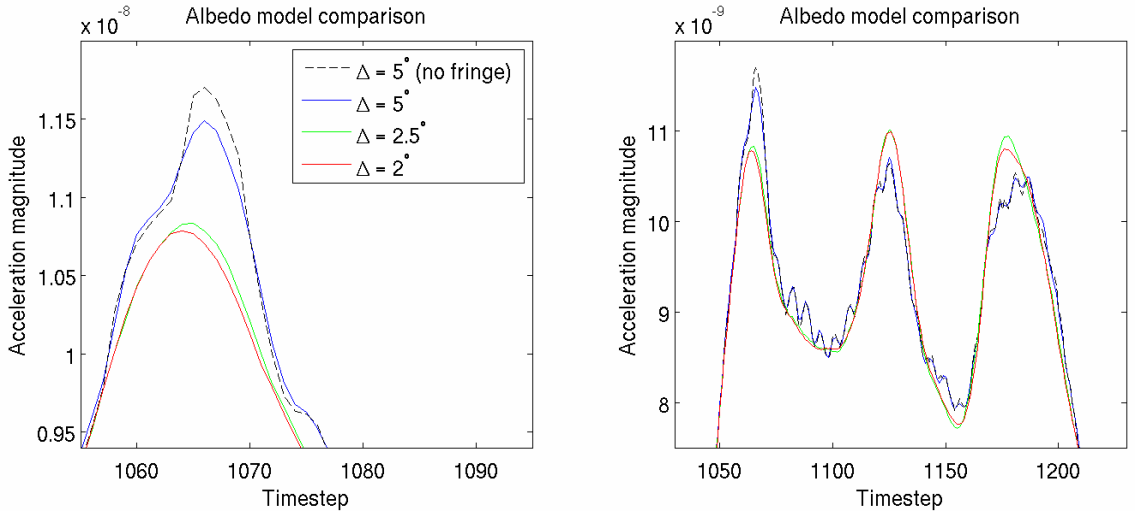

Figure 6.8 Effect of the grid resolution on the albedo acceleration. The partial visibility of the area elements has a sensitive but small influence in general (black dashed line), and could reasonably be ignored. In addition, with increased map resolution, its effect is further reduced.

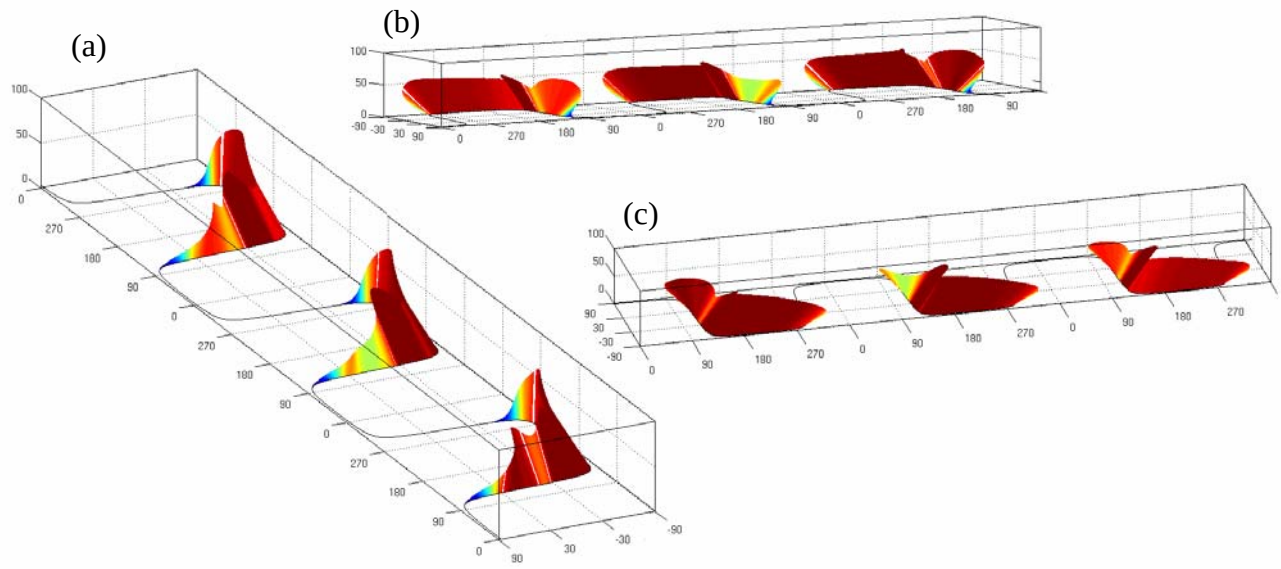

Figure 6.9 Evolution of the albedo acceleration with time. The horizontal axes show longitude and latitude. The acceleration vectors (scaled appropriately) are plotted starting on the spacecraft trajectory groundtrack. The three-dimensional orientation is given by the North, East and Radial components, while the color indicates the magnitude. On view (a), the spacecraft moves from the bottom to the top. Different views are shown in (b) and (c) to illustrate the tilt of the 'surface' away from the South Pole region which contributes most of the albedo radiation (high albedo during Southern Summer). The vertical axis shows the ratio (in percent) to the maximum magnitude.

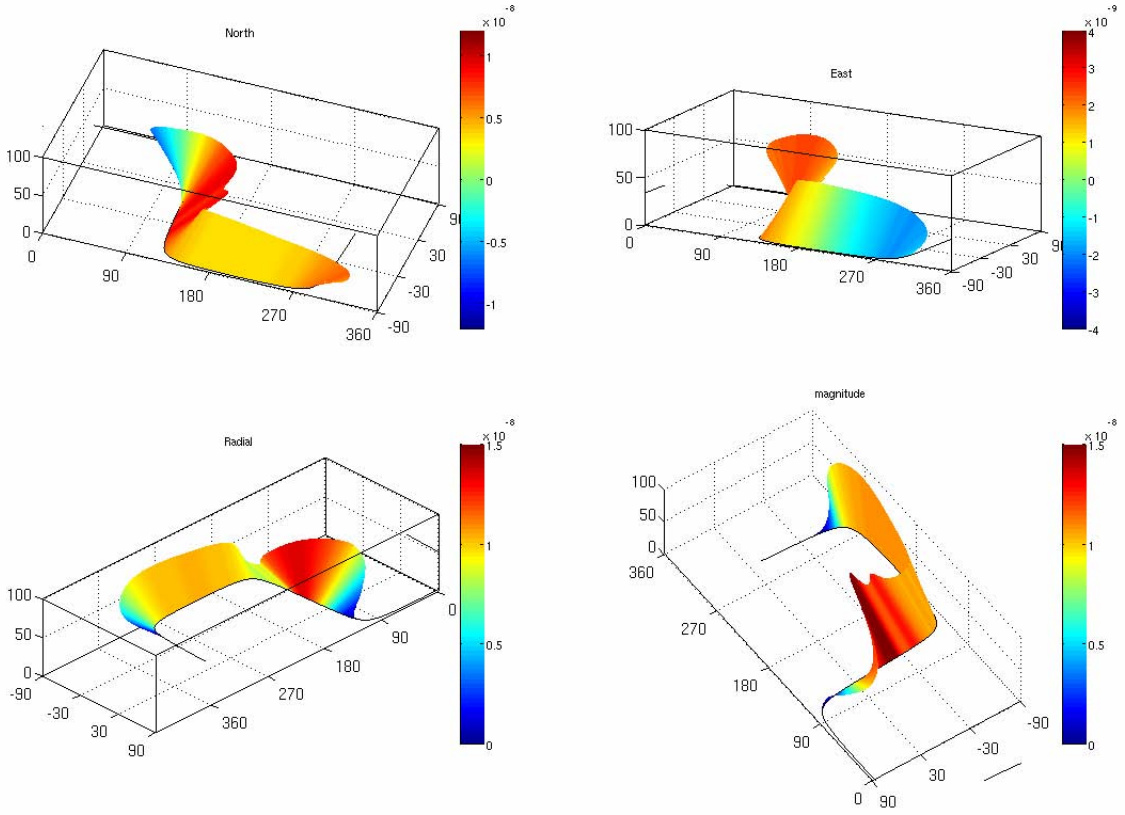

Figure 6.10 Same as Figure 6.9, but for just one orbit. The surface represents the acceleration vector, and does not vary from plot to plot. However, each plot focuses on either a component of the albedo force (North, East, Radial) or on its magnitude, with a specific colormap (units: $m.s^{-2}$).

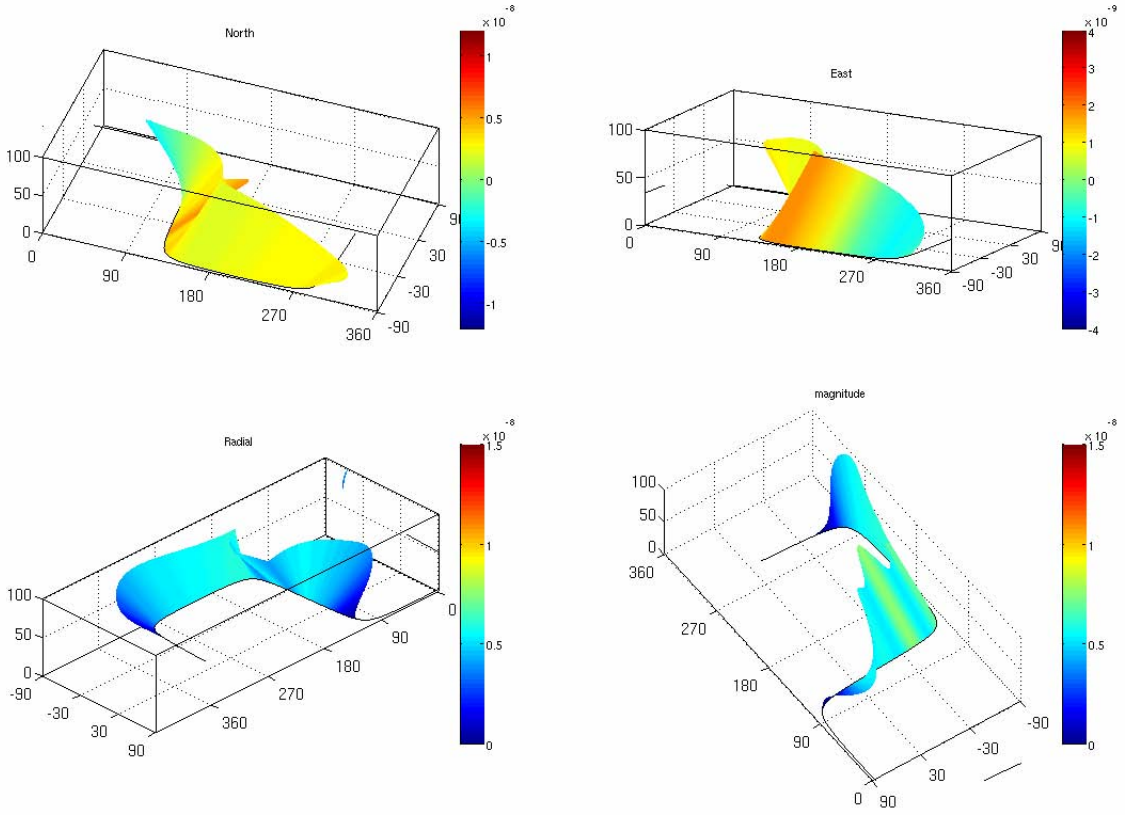

Figure 6.11 Same as Figure 6.10 but with the albedo acceleration obtained from the spherical harmonic model. The colormaps are identical, showing there are significant differences.

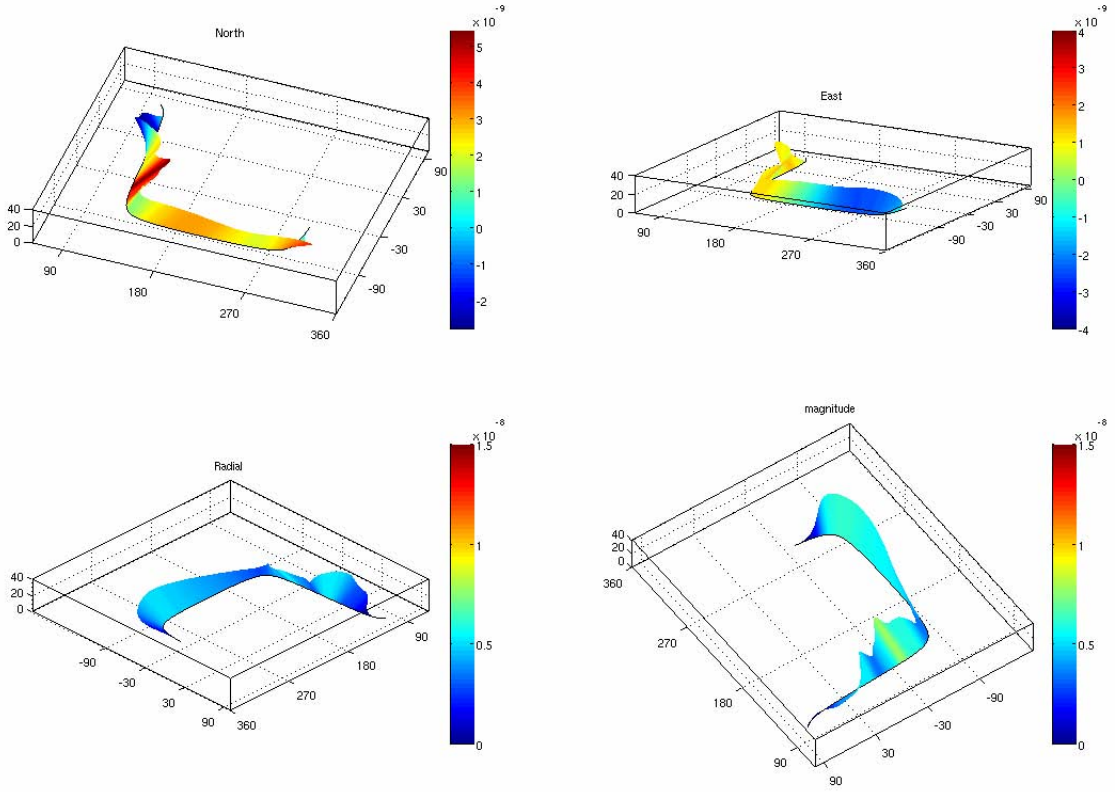

Figure 6.12 Same as Figure 6.10 but for the difference between the albedo accelerations obtained with the MOLA albedo map and with the older zonal map. Here, the vertical axis shows ratio in percent to the maximum magnitude of the MOLA map albedo acceleration.

[THIS PAGE INTENTIONALLY LEFT BLANK]

Chapter 7

Conclusion

7.1 Summary of results

In this Thesis, we obtained density measurements from analyzing the radio tracking data of two spacecraft, in three different density environments: the middle atmosphere (Chapter 3), the lower exosphere (Chapter 4), and the upper exosphere (Chapter 2).

We complemented the tremendous accelerometer dataset by estimating the density and scale height near the orbit periapses during the aerobraking phase of Mars Odyssey, and enabled the assessment of that complex region from a navigational perspective. Using Precision Orbit Determination (POD) on short arcs (just one orbit), we obtained periapsis densities very consistent with the *in situ* direct accelerometer measurements. We also found that in that environment very perturbed by atmospheric waves, the conventional scale height would underestimate the orbital energy lost by friction at each aerobraking pass. Our effective scale heights display a nearly constant 1-km bias.

With the radio tracking data of Mars Odyssey during its mapping orbit, we could monitor the density changes over a long baseline (about two Martian years, or four Earth years). Some issues in solar radiation modeling were shown not to contaminate the density recovery. Due to the very low density levels (around 10^{-14}kg.m^{-3}), reasonable estimates could only be obtained using several days of tracking data. This was sufficient to observe the effects of solar activity and season on the upper atmosphere. The obtained values were compared to two atmospheric

models. The agreement with the Stewart model (used as *a priori*) is good during the second Mars year, but density values in the first year show a better fit to the Mars-GRAM predictions. A signature of the solar rotation was detected in the time series through frequency analysis, but our results are less clear than observed for the MGS spacecraft, which has an orbital periapsis ~20km lower. Based on just two Martian years, the seasonally-variable scale height does not seem to display notable inter-annually variability and, more surprisingly, is not very sensitive to solar activity. A number of accurate daily densities could be used to estimate the atmospheric variability, important for engineering purposes in addition to the expected interest from the modeling community.

Lower in the exosphere, near 250km, we could estimate the atmospheric density with unusual temporal resolution for the POD method because of the higher density level. This high temporal resolution enabled a much more detailed study than previously possible. Although the MRO primary mission started just over one year ago, a nearly global dust storm occurred in late June 2007. In addition to observing the relative decrease of atmospheric variability during the dust storm period, we also estimated the warming effect in the exosphere. However, the most interesting result is the apparent observation of atmospheric waves in the exosphere. The period was ideal, with low solar activity and southern summer. These density oscillations, fixed in longitude from the perspective of MRO's Sun-synchronous orbit, could potentially be the result of the vertical propagation of the non-migrating waves first observed during the aerobraking of MGS.

In addition to the analysis of the radio tracking data, we worked to improve the *a priori* physical models used as integral parts of the POD process. We improved the macro-model description of the spacecraft to make it truly three-dimensional, enabling the calculation of the spacecraft cross-sectional area to include inter-plate shadowing (self-shadowing), which is important for a better modeling of the non-

conservative forces. Accurate modeling of these small non-conservative accelerations was especially important to us because the Thesis focused on one of them, the atmospheric drag. The second model improvement consisted in using recent data from the MOLA instrument on MGS to obtain high-resolution seasonal maps of Mars surface albedo. We modified the existing algorithm based on spherical harmonic expansions in order to use gridded longitude/latitude maps, which improves the computational efficiency when going to high resolution. While not necessary for obtaining the Mars Reconnaissance Orbiter results, it could prove important for future spacecraft missions, and in particular for the Lunar Reconnaissance Orbiter due to launch in October 2008 because of the lack of atmospheric drag on the Moon.

7.2 Future work

In addition to the assimilation of these exospheric density measurements into numerical General Circulation Models, the presented results warrant continued research efforts.

Natural directions for continuing modeling improvements are to improve the computational efficiency of the self-shadowing and albedo models. The rise of GPU computing (i.e., deferring intensive floating point calculations to a dedicated graphical card) opens interesting new ways of thinking about optimization. The Radio Science investigations on the upcoming lunar missions could also benefit from these small force models. Particularly important for the lunar environment, the albedo acceleration should be modified to account for non-Lambertian reflection due to the strong backscattering. Building upon the framework of the albedo model, a thermal radiation model should be the next step. A thermal inertia map, coupled with the albedo map and a simple thermophysical model of the surface temperature, could estimate the thermal emission at high resolution.

Theoretical and computational calculations on the propagation of various atmospheric waves would help understand the nature of the atmospheric density oscillations observed by MRO. An important question to answer would be whether our results are consistent with the waves discovered by MGS, in particular during the second aerobraking phase (the same Martian season as our measurements). The large phase change in the wave field also needs to be investigated, because it could be linked to changes in the wind structure in the lower atmosphere and might tell us about the coupling between lower and upper atmosphere.

For both Mars Odyssey and Mars Reconnaissance Orbiter, we need to pursue the data processing to extend the baseline of the measurements. Mars Odyssey, after an additional Martian year with poor density recovery due mainly to the unfavorable orbit geometry, should lead to new density measurements in the near future. In conjunction with densities obtained from MRO tracking data, the simultaneous response of the upper atmosphere to solar activity at different altitudes could be studied. With just one year of MRO data, we could not confidently separate the contributions of solar activity, season and dust opacity to the total neutral density at 250km. With a full Martian year or more, this will certainly become possible. In addition, the continued observation of the atmospheric waves, and in particular their disappearance with increasing solar activity, will inform us on the various processes affecting the upper atmosphere energy balance.

[THIS PAGE INTENTIONALLY LEFT BLANK]

[THIS PAGE INTENTIONALLY LEFT BLANK]